



HAL
open science

Multi-scale modeling and asymptotic analysis for neuronal synapses and networks

Claire Guerrier

► **To cite this version:**

Claire Guerrier. Multi-scale modeling and asymptotic analysis for neuronal synapses and networks. Analysis of PDEs [math.AP]. Université Pierre et Marie Curie - Paris VI, 2015. English. NNT : 2015PA066518 . tel-01314124

HAL Id: tel-01314124

<https://theses.hal.science/tel-01314124>

Submitted on 10 May 2016

HAL is a multi-disciplinary open access archive for the deposit and dissemination of scientific research documents, whether they are published or not. The documents may come from teaching and research institutions in France or abroad, or from public or private research centers.

L'archive ouverte pluridisciplinaire **HAL**, est destinée au dépôt et à la diffusion de documents scientifiques de niveau recherche, publiés ou non, émanant des établissements d'enseignement et de recherche français ou étrangers, des laboratoires publics ou privés.



École Doctorale de Sciences Mathématiques de Paris Centre

THESE DE DOCTORAT

pour obtenir le grade de docteur de l'Université Pierre et Marie Curie (PARIS VI)

Discipline : Mathématiques Appliquées

présentée par

Claire GUERRIER

Multi-scale modeling and asymptotic analysis for neuronal synapses and networks

dirigée par David HOLCMAN

après avis des rapporteurs

M. Gilles LEBEAU Université Nice Sophia-Antipolis
M. Michael J. WARD The University of British Columbia

soutenue le 17 décembre 2015 devant le jury composé de

M. Vincent CALVEZ	Ecole Normale Supérieure de Lyon	examineur
M. Vincent HAKIM	Ecole Normale Supérieure	examineur
M. David HOLCMAN	Ecole Normale Supérieure	directeur de thèse
M. Ivan KUPKA	Ecole Normale Supérieure	examineur
M. Gilles LEBEAU	Université Nice Sophia-Antipolis	rapporteur
M. Lorenzo ZAMBOTTI	Université Paris VI	examineur

Remerciements

Je tiens tout d'abord à remercier David Holcman pour son accueil au laboratoire Applied Mathematics and Computational Biology au département de biologie de l'Ecole Normale Supérieure.

J'ai pu, à son contact, avoir une approche concrète de nombreux domaines de mathématiques appliquées tels que les équations aux dérivées partielles, l'analyse asymptotique ou encore les processus stochastiques. Il m'a également initié à la modélisation mathématique en biologie, et m'a fait découvrir de nouvelles perspectives dans le monde de la recherche. Enfin, il m'a accordé une grande liberté dans les choix de mes différents projets, et dans la gestion de mon travail au quotidien.

Je remercie également les membres de l'équipe que j'ai côtoyés tous les jours au laboratoire, pour leurs discussions ainsi que la bonne entente qui y règne. Je remercie Jüergen Reingruber pour ses nombreux conseils et remarques, notamment en lab meeting, ainsi que Nathanaël Hozé, Assaf Amitai, Khanh Dao Duc et Jing Yang pour toute l'aide qu'ils m'ont apportée pendant ma thèse. Je remercie tout particulièrement Jérôme Cartailier pour nos nombreuses discussions enrichissantes et passionnées, qui m'ont permis de surmonter les quelques périodes de doute et de découragement qu'un thésard peut rencontrer. Je remercie enfin Ofir Shukron et Pierre Parutto, et leur souhaite une grande réussite pour leur futur doctorat.

J'ai également eu la chance de rencontrer des chercheurs de spécialités que je connaissais mal, qui m'ont fait découvrir une manière différente d'aborder les problèmes de recherche, ce qui m'a permis de mettre en perspective la modélisation mathématique. Je remercie particulièrement Gilles Fortin et John Hayes pour leur collaboration très enrichissante, ainsi que Jérémie Sibille pour m'avoir fait découvrir le quotidien de la recherche en électrophysiologie.

Je tiens également à remercier les professeurs Gilles Lebeau et Michael J. Ward pour avoir accepté de relire ma thèse. Leurs remarques ont grandement amélioré le manuscrit. Je remercie Vincent Calvez, Vincent Hakim, Ivan Kupka et Lorenzo Zambotti pour m'avoir fait l'honneur de faire partie de mon jury.

Enfin, je remercie toute ma famille pour leur présence et leur soutien. Merci à mes parents pour leur écoute et leur patience pendant mes longues années d'études, pour leur soutien sans failles et leurs encouragements. Merci également à ma belle-famille pour leur gentillesse et leur patience ces dernières années, ainsi que pour le soutien logistique apporté pendant la dernière phase de rédaction de ce manuscrit. Et enfin, merci à Nicolas, sans qui la vie serait moins belle !

Publications

Published

- Guerrier C and Holcman D “Search time for a small ribbon and application to vesicular release at neuronal synapses” *SIAM MMS* **13(4)**, pp 1173-1193 (2015)
- Guerrier C, Hayes JA, Fortin G and Holcman D “Robust network oscillations during mammalian respiratory rhythm generation driven by synaptic dynamics. ” *Proc. Natl. Acad. Sci.* **112(31)**, pp 9728-9733 (2015)
- Guerrier C and Holcman D “Brownian search for targets hidden in cusp-like pockets: Progress and Applications” *European Physical Journal ST* **223**, pp 3273-3285 (2014)
- Guerrier C, Korkotian E and Holcman D “Calcium Dynamics in Neuronal Microdomains: Modeling, Stochastic Simulations and Data Analysis” In Jaeger D. jung R (eds.) *Encyclopedia of Computational Neuroscience*, pp 1-37 (2014) Springer New York Heidelberg Dordrecht London

Submitted

- Guerrier C and Holcman D “Multi-scale methods and simulations of Brownian particles reaching small targets to compute the time distribution of vesicular release at neuronal synapses”

Résumé

Dans cette thèse, nous étudions plusieurs structures neuronales à différentes échelles allant des synapses aux réseaux neuronaux. Notre objectif est de développer et analyser des modèles mathématiques, afin de déterminer comment les propriétés des synapses au niveau moléculaire façonnent leur activité, et se propagent au niveau du réseau. Ce changement d'échelle peut être formulé et analysé à l'aide de plusieurs outils tels que les équations aux dérivées partielles, les processus stochastiques ou les simulations numériques.

Dans la première partie, nous calculons le temps moyen pour qu'une particule brownienne arrive à une petite ouverture définie comme le cylindre faisant la jonction entre deux sphères tangentes. La méthode repose sur une transformation conforme de Möbius appliquée à l'équation de Laplace. Nous estimons également, lorsque la particule se trouve dans un voisinage de l'ouverture, la probabilité d'atteindre l'ouverture avant de quitter le voisinage. De nouveau, cette probabilité est exprimée à l'aide d'une équation de Laplace, avec des conditions aux limites mixtes. En utilisant ces résultats, nous développons un modèle et des simulations stochastiques pour étudier la libération vésiculaire au niveau des synapses, en tenant compte de leur géométrie particulière. Nous étudions ensuite le rôle de plusieurs paramètres tels que le positionnement des canaux calciques, le nombre d'ions entrant après un potentiel d'action, ou encore l'organisation de la zone active.

Dans la deuxième partie, nous développons un modèle pour le terminal pré-synaptique, formulé dans un premier temps comme un problème de réaction-diffusion dans un microdomaine confiné, où des particules browniennes doivent se lier à de petits sites cibles. Nous développons ensuite deux modèles simplifiés. Le premier modèle couple un système d'équations d'action de masse à un ensemble d'équations de Markov, et permet d'obtenir des résultats analytiques. Dans un deuxième temps, nous développons un modèle stochastique basé sur des équations de taux poissonniens, qui dérive de la théorie du premier temps de passage et de l'analyse précédente. Ce modèle permet de réaliser des simulations stochastiques rapides, qui donnent les mêmes résultats que les simulations browniennes naïves et interminables.

Dans la dernière partie, nous présentons un modèle d'oscillations dans un réseau de neurones, dans le contexte du rythme respiratoire. Nous développons un modèle basé sur les lois d'action de masse représentant la dynamique synaptique d'un neurone, et montrons comment l'activité synaptique au niveau des neurones conduit à l'émergence d'oscillations au niveau du réseau. Nous comparons notre modèle à plusieurs études expérimentales, et confirmons que le rythme respiratoire chez la souris au repos est contrôlé par l'excitation récurrente des neurones découlant de leur activité spontanée au sein du réseau.

Abstract

In the present PhD thesis, we study neuronal structures at different scales, from synapses to neural networks. Our goal is to develop mathematical models and their analysis, in order to determine how the properties of synapses at the molecular level shape their activity and propagate to the network level. This change of scale can be formulated and analyzed using several tools such as partial differential equations, stochastic processes and numerical simulations.

In the first part, we compute the mean time for a Brownian particle to arrive at a narrow opening defined as the small cylinder joining two tangent spheres. The method relies on Möbius conformal transformation applied to the Laplace equation. We also estimate, when the particle starts inside a boundary layer near the hole, the splitting probability to reach the hole before leaving the boundary layer, which is also expressed using a mixed boundary-value Laplace equation. Using these results, we develop model equations and their corresponding stochastic simulations to study vesicular release at neuronal synapses, taking into account their specific geometry. We then investigate the role of several parameters such as channel positioning, the number of entering ions, or the organization of the active zone.

In the second part, we build a model for the pre-synaptic terminal, formulated in an initial stage as a reaction-diffusion problem in a confined microdomain, where Brownian particles have to bind to small target sites. We coarse-grain this model into two reduced ones. The first model couples a system of mass action equations to a set of Markov equations, which allows to obtain analytical results. We develop in a second phase a stochastic model based on Poissonian rate equations, which is derived from the mean first passage time theory and the previous analysis. This model allows fast stochastic simulations, that give the same results than the corresponding naive and endless Brownian simulations.

In the final part, we present a neural network model of bursting oscillations in the context of the respiratory rhythm. We build a mass action model for the synaptic dynamic of a single neuron and show how the synaptic activity between individual neurons leads to the emergence of oscillations at the network level. We benchmark the model against several experimental studies, and confirm that respiratory rhythm in resting mice is controlled by recurrent excitation arising from the spontaneous activity of the neurons within the network.

Contents

Introduction	13
Abbreviations and notations	39
I Mathematical modeling of synapses at the molecular level	41
1 Brownian search for targets hidden in cusp-like pockets: Progress and Applications	43
1.1 Introduction	43
1.2 Examples for the search of a hidden target in cellular and molecular biology	45
1.2.1 Mother-daughter cell	45
1.2.2 Finding a binding site in a protein: The example of hemoglobin	47
1.2.3 Rotation of a needle in a confined band	47
1.2.4 Cusp activation between a vesicle and the pre-synaptic membrane of a neuron	47
1.3 Classification of the NET and DST in dimension two and three	48
1.3.1 Stochastic equation	48
1.3.2 Dire strait formula in dimension 2	48
1.3.3 Dire strait formula in dimension 3	52
1.3.4 Derivation of the DST for a three-dimensional cusp located at the end of a funnel	52
1.3.5 Dire strait to a ribbon	54
1.4 Conclusion	55
2 Search time for a small ribbon and application to vesicular release at neuronal synapses	57
2.1 Introduction	57
2.2 Search for a small two-dimensional cusp located between two tangent spheres	59
2.2.1 Asymptotic computation of the mean time in two dimensions	60
2.2.2 A three-dimensional escape to a narrow ribbon	63
2.3 Diffusion to proteins located underneath a pre-synaptic vesicle	67
2.3.1 Splitting probability of a Brownian ion to hit a vesicular ribbon versus entering the pre-synaptic bulk	67

2.4	Discussion: estimation of the vesicular release probability	72
2.5	Conclusion	74
2.6	Appendix A : Revisiting the Dire Strait Search in a three-dimensional cusp located at the end of a funnel	75
2.6.1	Mapping the cusp domain with a Möbius transformation into a narrow Banana	76
2.7	Appendix B: Simulating the NET in two and three dimension.	79
2.7.1	Simulating Brownian trajectory using Euler scheme in confined domains.	79
2.7.2	Choosing the optimal time step Δt	80

II Coarse-grained multiscale simulations of molecular dynamics 83

3	Multi-scale methods and simulations of Brownian particles reaching small targets to compute the time distribution of vesicular release at neuronal synapses	85
3.1	Introduction	85
3.2	Multi-scale model of diffusing ions in pre-synaptic terminal	87
3.2.1	Modeling calcium dynamic in the pre-synaptic terminal	87
3.2.2	Reaction-diffusion equations for calcium in pre-synaptic terminal	89
3.3	Markov-Mass action model for bridging the discrete-continuum levels	91
3.3.1	Model of target site organization at the AZ	91
3.3.2	A Markov chain to describe target activation	93
3.3.3	The Mass action equations for the ion in the bulk	95
3.3.4	Solving the coupled Markov equations	96
3.4	Exhaustive Brownian simulations of ions	97
3.4.1	Stochastic simulations	97
3.4.2	Coarse-grained stochastic dynamics with Poissonian rates . . .	100
3.4.3	Stochastic simulations with the Poissonian rate and the Markov-Mass action law models	102
3.4.4	Computing the distribution of release times for a uniform channel distribution	102
3.4.5	Computing the distribution of release times for a uniform channel distribution	105
3.5	Discussion and Conclusion	107
3.6	Tables	108
3.7	Appendix A: A refined model of diffusing ions in the pre-synaptic terminal	111
3.7.1	PDEs description	111
3.7.2	Markov-Mass action model	112
3.8	Appendix B: Detailed computation of the mean fraction of particles reaching any target, F_{ions} presented in section 3.4.4	115

**III Modeling bursting oscillations in neuronal networks
for the genesis of pre-Bötzinger Complex rhythms 117**

4 Robust network oscillations during mammalian respiratory rhythm generation driven by synaptic dynamics 119

4.1 Introduction 120

4.2 Results 121

 4.2.1 Robust rhythmic activity generated in the model network. . . 121

 4.2.2 Rhythmic activity depends on the number and strength of connected neurons. 123

 4.2.3 Depolarizing neurons increases the rhythm frequency. 125

 4.2.4 Few active neurons are sufficient to trigger population bursts. 125

 4.2.5 Short-term synaptic plasticity in the preBötC inspiratory rhythm generator. 126

4.3 Discussion 128

 4.3.1 Can bursting oscillations be generated in neuronal networks without any intrinsically rhythmic neurons? 128

 4.3.2 Local network structure and dynamics. 129

 4.3.3 Role of synaptic depression in burst termination. 130

4.4 Materials and Methods 131

 4.4.1 Electrophysiology. 131

 4.4.2 Mathematical Modeling. 131

4.5 Complement on the Material and Methods 133

 4.5.1 Experimental procedure 133

 4.5.2 Hodgkin-Huxley Model of the membrane potential 134

 4.5.3 Model of the synaptic dynamics 134

 4.5.4 Computing the synaptic current I_{syn} 136

 4.5.5 Constructing the network connectivity 137

 4.5.6 Summary of the network dynamics 137

4.6 Complementary simulations 139

 4.6.1 Decreasing the network connectivity gradually suppresses the endogenous rhythm. 139

 4.6.2 Histograms of the interburst interval for four different network realizations. 140

 4.6.3 Influence of the synaptic properties on the network. 143

 4.6.4 Modification of the spiking frequency during a burst. 146

 4.6.5 Effect of deleting random neurons on the network activity. . . 147

 4.6.6 Consequences of gradually decreasing the synaptic strength. . 149

 4.6.7 Depolarizing neurons increases the rhythm frequency. 151

 4.6.8 Minimal number of stimulations for burst induction. 155

 4.6.9 Inspiratory drive currents. 155

4.7 Movie 156

 4.7.1 Movie S1: 156

 4.7.2 Movie S2: 156

 4.7.3 Movie S3: 156

 4.7.4 Movie S4: 156

4.7.5	Movie S5:	156
4.7.6	Movie S6:	156
4.7.7	Movie S7:	157
Conclusion		161
Appendix A Calcium dynamics in neuronal microdomains: modeling, stochastic simulations and data analysis		167
A.1	Definition	167
A.2	Detailed Description	168
A.2.1	Neuronal microdomains	168
A.2.2	Diffusion in neuronal microdomains: stochastic modeling . . .	169
A.2.3	Modeling the interaction of calcium ion with surface or receptors	174
A.2.4	Stochastic simulation of calcium in a dendritic spine	179
A.2.5	Diffusion laws in microdomains with small openings	182
A.2.6	Calcium extrusion along a cylinder: Homogenization of hole into a killing rate	193
A.2.7	Calcium cascade initiating cellular activation	198
A.2.8	Discussion and conclusion	201
Bibliography		205

Introduction

Recent mathematical physics, stochastic modeling and analysis are now actively concerned with questions related to cellular biology and neuronal structures. Synaptic microdomains are an example which is at an intermediate scale between the molecular and the neuronal network level. These neuronal structures are underlying fundamental and yet not completely understood functions, such as learning and memory, breathing, sleeping, and many more.

Motivated by understanding and analyzing these structures, which are continuously investigated in both experimental and theoretical neuroscience, I developed in this PhD thesis various models, asymptotic analysis and numerical simulations to study how properties at the molecular level (synapse) propagate to the network level (neural networks). I developed and analyzed mathematical models using methods based on asymptotic of partial differential equations, stochastic processes and numerical simulations.

In the introduction I will first present the mathematical framework that I used, then I will briefly introduce the biological background, and finally I will present the main results that I obtained in this PhD.

Part I: Mathematical modeling of synapses at the molecular level

Diffusion properties of molecules searching for small targets or narrow passages have been studied under the generic term of narrow escape problems that I now summarize. I will then briefly present the biological background for synaptic transmission, followed by my model to compute the release probability.

The narrow escape problem

The narrow escape problem in diffusion theory is to calculate the narrow escape time (NET) of a Brownian particle to a small absorbing window on the otherwise reflecting boundary of a bounded domain (Fig. 1). It was first introduced in the context of the theory of sound [200, 157], and was applied more recently for the determination of biological cells function to take into account the cells particular geometrical structures [85]. Indeed, the NET is ubiquitous in molecular and cellular biology, including stochastic models of chemical reactions [80, 35], modeling the early steps of viral infection in cells [115, 86], the regulation of diffusion between the mother and daughter cells during division [65, 61], and many other models [84].

The main goal in the NET problem is to develop asymptotic methods to compute

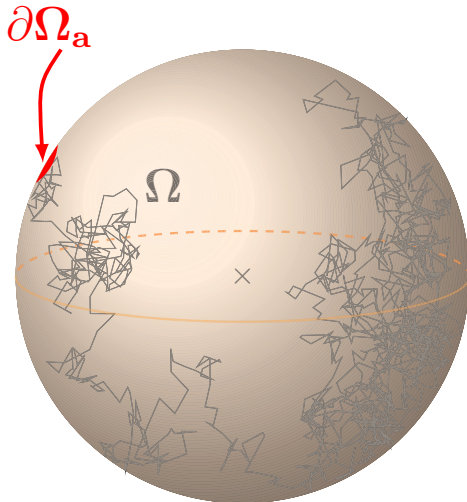


Figure 1: **The narrow escape problem.** A Brownian trajectory is reflected on the boundary of a spherical domain Ω , and is absorbed at a small circular target site $\partial\Omega_a$ (red).

the NET explicitly in various geometries of cellular structures. A Brownian particle is described by the stochastic equation

$$\dot{\mathbf{X}} = \sqrt{2D}\dot{\mathbf{w}} \quad (1)$$

where D is the diffusion coefficient and $\dot{\mathbf{w}}$ is white noise. The mean time $\langle \tau \rangle(\mathbf{x})$ for a Brownian particle starting at position \mathbf{x} to reach at small absorbing domain $\partial\Omega_a$ located on the boundary $\partial\Omega$ is the solution of the mixed boundary value problem for the Laplace equation [85]

$$\begin{cases} D\Delta u_\varepsilon(\mathbf{x}) = -1 & \text{for } \mathbf{x} \in \Omega \\ \frac{\partial u_\varepsilon}{\partial n}(\mathbf{x}) = 0 & \text{for } \mathbf{x} \in \partial\Omega \setminus \partial\Omega_a \\ u_\varepsilon(\mathbf{x}) = 0 & \text{for } \mathbf{x} \in \partial\Omega_a. \end{cases} \quad (2)$$

The difficulty here is to construct an asymptotic solution $u_\varepsilon(\mathbf{x})$, in the limit when the ratio

$$\varepsilon = \frac{|\partial\Omega_a|}{|\partial\Omega|} \quad (3)$$

tends to zero. The NET diverges as the absorbing part of the boundary shrinks, thus rendering the computation a singular perturbation problem. The computation is related to the calculation of the principal eigenvalue of the mixed Dirichlet-Neumann problem for the Laplace equation [85, 84, 174].

Asymptotic analysis of the narrow escape problem

There are two different approaches to solve equation 2 that I discuss now.

A first approach is based on the Neumann's function, and Helmholtz integral equation [174]. To calculate the NET (eq. 2) in domain Ω , this method uses the Neumann function $N(\mathbf{x}, \xi)$, solution of the boundary value problem:

$$\begin{cases} \Delta_{\mathbf{x}} N(\mathbf{x}, \xi) = -\delta(\mathbf{x} - \xi) \text{ for } \mathbf{x}, \xi \in \Omega \\ \frac{\partial N(\mathbf{x}, \xi)}{\partial n(\mathbf{x})} = -\frac{1}{|\partial\Omega|} \text{ for } \mathbf{x} \in \partial\Omega, \xi \in \Omega. \end{cases} \quad (4)$$

Using Green's identity to derive an integral representation for u_ε for ξ in Ω , we have the representation,

$$u_\varepsilon(\xi) = \frac{1}{D} \int_{\Omega} N(\mathbf{x}, \xi) d\mathbf{x} + \int_{\partial\Omega_a} N(\mathbf{x}, \xi) \frac{\partial u_\varepsilon}{\partial n} dS_{\mathbf{x}} + \frac{1}{|\partial\Omega|} \int_{\partial\Omega} u_\varepsilon(\mathbf{x}) dS_{\mathbf{x}}, \quad (5)$$

and the average of the NET over the boundary is solution of the Helmholtz integral equation

$$\int_{\partial\Omega_a} N(\mathbf{x}, \xi) \frac{\partial u_\varepsilon}{\partial n} dS_{\mathbf{x}} = -\frac{1}{|\partial\Omega|} \int_{\partial\Omega} u_\varepsilon(\mathbf{x}) dS_{\mathbf{x}} \text{ for } \xi \in \partial\Omega_a. \quad (6)$$

For ξ outside of the boundary layer located near the absorbing hole $\partial\Omega_a$, this representation allows computing the leading order approximation of the NET. For example, the NET in a three-dimensional domain Ω , when the target is a circular absorbing window $\partial\Omega_a$ of radius a centered at $\mathbf{0}$ on the boundary $\partial\Omega$ (Fig. 1), is given by [85]

$$u_\varepsilon(\mathbf{x}) = \frac{|\Omega|}{4aD} \left[1 - \frac{L(\mathbf{0}) + N(\mathbf{0})}{2\pi} a \ln a + O(a) \right], \quad (7)$$

where $L(\mathbf{0})$ and $N(\mathbf{0})$ are the principal curvatures of the surface at the center of the absorbing boundary $\partial\Omega_a$. The third order asymptotic expansion can be found when Ω is a sphere [27] using the matched asymptotic approach (see below). When the absorbing window is located at a corner of angle α in dimension 2, then [85]

$$u_\varepsilon(\mathbf{x}) = \frac{|\Omega|}{D\alpha} \left[\ln \frac{1}{\varepsilon} + O(1) \right]. \quad (8)$$

This method has also been extended to the NET on Riemannian manifolds [181, 179, 180, 87].

In [201, 202] an asymptotic framework, based on combining matched asymptotic expansions and potential theory, was developed to analyze PDE problems with strong local changes in the boundary conditions. In this approach, a boundary layer solution is constructed near the absorbing the boundary of small size ε [201, 202]. This approach requires a sufficiently smooth boundary in a neighborhood of the absorbing window. The method consists in stretching the domain near the absorbing window, which allows expanding the solution in power of ε and reveals the leading-order boundary layer solution. The solution in the outer region

(outside the boundary layer) can then be matched with the boundary layer solution to find the asymptotic solution of the NET. This method was developed mainly in [27, 201, 202, 203, 107]. In three dimensions, the method was used in [202], where the boundary layer problem is computed from the classical electrified disk problem [91].

Brownian escape through a small cusp: The dire strait problem

Contrary to freely accessible small targets (Fig. 1), the mean time of a Brownian particle to reach a target located within a narrow cusp, the Dire Strait Time (DST), is much longer [83] (Fig. 2). Finding asymptotic expressions for such search times

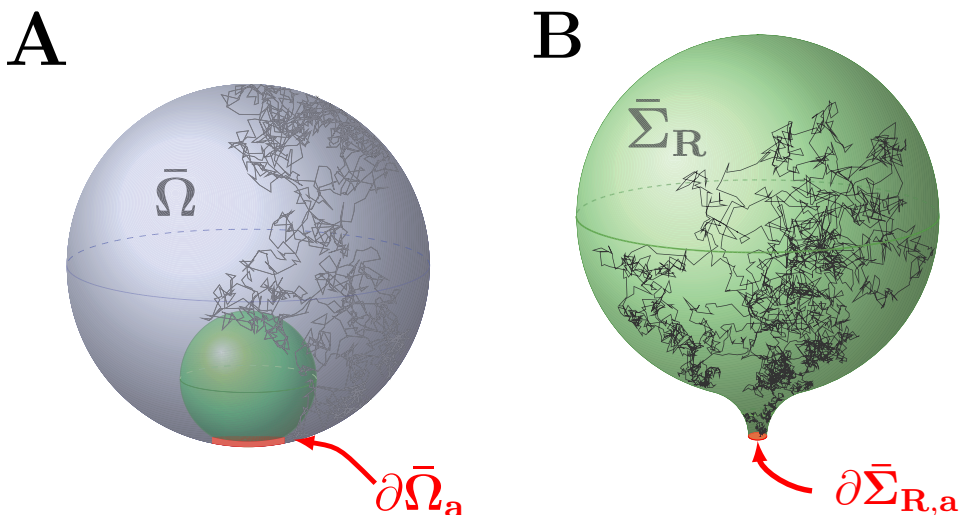


Figure 2: **Brownian trajectories escaping through a small absorbing window at cusp-like geometries.** **A:** A Brownian trajectory is reflected between two tangent spheres (blue and green), and is absorbed at a small absorbing ribbon (red) at the end of a cusp-like geometry. **B:** The domain is a ball connected smoothly to a funnel-shaped cusp, with radius of curvature R at the cusp.

remains challenging both numerically and analytically. Numerically, because it requires very long simulations, leading to many inaccuracies, and this is not even sufficient to guess asymptotic formulas. From an analytical point of view, the classical methods developed for the narrow escape problems do not apply. Indeed, the cusp geometry at the small hole creates singularity that prevents the use of Neumann's functions [84, 85, 86]. To circumvent this difficulty, the cusp can be de-singularized using conformal mapping, which allows using the matched asymptotics approach in the image domain to determine the solution [82, 75]. An overview of the main results for the NET/DST are presented in chapter 1.

Asymptotic solution of the dire strait problem

The new results presented in chapter 2 of this thesis relies on the construction of an asymptotic solution of equation 2 when the small absorbing target is located at the end of a cusp (see Fig. 2A-B). The analytical computation of these search times presents several difficulties due to their particular cusp-like geometry, that I overcame using the Möbius conformal mapping and asymptotics of elliptic PDEs. The first result is the asymptotic approximation of the NET in the domain of Fig. 2A delimited by two tangent spheres, where the target is a small ribbon of height ε joining the two spheres (red). For the 2D problem, I used the following Möbius map

$$f(\mathbf{x}) = \frac{1}{\mathbf{x}} = \omega, \quad (9)$$

to send the cusp region in the initial domain Ω into a long rectangular domain $\tilde{\Omega}$. Using matching asymptotics in $\tilde{\Omega}$, I obtained the expansion of the solution

$$u_\varepsilon(\mathbf{x}) = \frac{\sqrt{2R}|\Omega|}{2D\sqrt{\varepsilon}} \left(1 - \sqrt{2R\varepsilon} \frac{\text{Re}(\mathbf{x})}{|\mathbf{x}|^2} \right), \quad (10)$$

where R is the radius of the green ball (Fig. 2A). We found the leading order term

$$\langle \tau \rangle = \frac{\sqrt{2R}|\Omega|}{2D\sqrt{\varepsilon}} (1 + o(1)). \quad (11)$$

For the three-dimensional problem in domain $\bar{\Omega}$ (Fig. 2A), the rotational symmetry of the problem allows the reduction to a two-dimensional one in the previous domain Ω . Using again the mapping function f (eq. 9) and setting $u_\varepsilon(\mathbf{x}) = v_\varepsilon(\omega)$, I obtained the mapped equation in domain $\tilde{\Omega}$:

$$\begin{aligned} |\omega|^4 \Delta v_\varepsilon(\omega) &+ \frac{|\omega|^2}{\text{Re}(\omega)} \left((\text{Im}(\omega)^2 - \text{Re}(\omega)^2) \frac{\partial v_\varepsilon}{\partial s}(\omega) + 2 \text{Re}(\omega) \text{Im}(\omega) \frac{\partial v_\varepsilon}{\partial t}(\omega) \right) \\ &= -\frac{1}{D} \text{ for } (\omega) \in \tilde{\Omega} \\ \frac{\partial v_\varepsilon}{\partial n}(\omega) &= 0 \text{ for } \omega \in \partial\tilde{\Omega} \setminus \partial\tilde{\Omega}_a \\ v_\varepsilon(\omega) &= 0 \text{ for } \omega \in \partial\tilde{\Omega}_a. \end{aligned} \quad (12)$$

Using matching asymptotics, I determined the asymptotic formula for the DST of a Brownian particle to a small ribbon that connects a ball and its tangent plane (Fig. 2A):

$$\langle \tau \rangle = \frac{|\bar{\Omega}|}{4\pi D\varepsilon}, \quad (13)$$

where $|\bar{\Omega}|$ is the volume of the 3D domain and ε is the height of the ribbon, whose surface is $S_{rib} = \sqrt{2R}\varepsilon^{3/2}$. This formula is valid for a general domain, as long as the cusp geometry is preserved.

The second result corrects the formula for the search time for a Brownian particle

to escape through a narrow cusp located at the end of a funnel in a three dimensional bounded domain $\bar{\Sigma}_R$ (eq. 2, FIG. 2B) [83]. The radius of curvature at the cusp is R , and the absorbing boundary is a small disk of radius ε . The rotational symmetry of the domain in cylindrical coordinates (ρ, ϕ, z) allows again the reduction to a two-dimensional problem in the domain $\Sigma_R = \bar{\Sigma}_R \cup \{\phi = 0\}$:

$$\begin{aligned} \frac{\partial^2 u}{\partial \rho^2}(\rho, z) + \frac{1}{\rho} \frac{\partial u}{\partial \rho}(\rho, z) + \frac{\partial^2 u}{\partial z^2}(\rho, z) &= -\frac{1}{D} \text{ for } (\rho, z) \in \Sigma_R \\ \frac{\partial u}{\partial n}(\rho, z) &= 0 \text{ for } (\rho, z) \in \partial \Sigma_R \setminus \partial \Sigma_{R,a} \\ u(\rho, z) &= 0 \text{ for } (\rho, z) \in \partial \Sigma_{R,a}. \end{aligned} \quad (14)$$

In the domain Σ_1 , with radius of curvature one at the cusp, the Möbius transformation is given by:

$$\begin{aligned} f(\xi) &= \frac{\xi - \alpha_\varepsilon}{\xi + \alpha_\varepsilon}, \\ \alpha_\varepsilon &= \sqrt{\varepsilon(1 + \varepsilon/4)}, \end{aligned} \quad (15)$$

which maps Σ_1 into a narrow banana-shaped domain Γ . Setting $\omega = f(\xi) = re^{i\theta}$, Equation (14) is mapped into

$$\begin{aligned} \frac{|1 - \omega|^4}{4\alpha_\varepsilon^2} \Delta v_\varepsilon + \frac{|1 - \omega|^2}{\alpha_\varepsilon(1 - |\omega|^2)} \left[\frac{\partial v_\varepsilon}{\partial r} \frac{\partial r}{\partial \rho} + \frac{\partial v_\varepsilon}{\partial \theta} \frac{\partial \theta}{\partial \rho} \right] &= -\frac{1}{D} \text{ for } \omega \in \Gamma \\ \frac{\partial v_\varepsilon}{\partial n}(\omega) &= 0 \text{ for } \omega \in \partial \Gamma \setminus \partial \Gamma_a \\ v_\varepsilon(\omega) &= 0 \text{ for } \omega \in \partial \Gamma_a. \end{aligned} \quad (16)$$

Solving asymptotically equation (16) using matching asymptotics gives the solution in the image domain

$$\begin{aligned} v_\varepsilon(\theta) &= \frac{|\bar{\Sigma}_1|}{D\pi\varepsilon\sqrt{\varepsilon}} (\sin(\theta) + \pi - \theta) \\ &+ \frac{\alpha_\varepsilon^2}{15D} \left[2 \ln \left(\frac{1 - \cos(\theta)}{2} \right) - 2(1 + \cos(\theta)) + \frac{3}{\cos(\theta) - 1} + \frac{3}{2} \right]. \end{aligned} \quad (17)$$

The new formula for the NET is:

$$u_\varepsilon = \frac{|\bar{\Sigma}_R|\sqrt{R}}{D\varepsilon\sqrt{\varepsilon}} + O(1), \quad (18)$$

where R is the radius of curvature at the cusp.

Because the DST is a rare event, the probability density function of the time spent in a domain prior to escape, in the limit of small target size, is dominated by a single exponential decay [175]. The exponential rate is therefore the flux into the absorbing target. This single exponential result allows coarse-graining microscopic model of reaction-diffusion into Markovian jump processes, where the rate is the flux on the absorbing boundary equal to the reciprocal of the DST. Before showing how the asymptotic computations presented here are applied in the neurobiological question I was interested in, I shall now briefly introduce some basic notions about synaptic transmission.

Background for synaptic transmission and neuronal organization

There are about 10^{11} neurons in the human brain, each containing about 10^3 synapses, a structure that permits a neuron to pass an electrical or chemical signal to another cell. Synapses are essential to neuronal functions. Chemical synapses are divided into three different parts, the pre-synaptic terminal (a portion of the signal-passing neuron), the synaptic cleft, and the post-synaptic terminal (a portion of the target neuron) (Fig. 3). The role of the various geometries of synapses is still unclear, though their morphological changes in cognitive pathology such as in epilepsy and autism spectrum disorders, indicate that they may be involved in regulating elaborated neuronal functions. The structure-function approach in modeling and analyzing these structures can possibly be the key to bridge the gap between the molecular and the cellular scales.

A chemical synapse transmits an electrical signal (an action potential, AP),

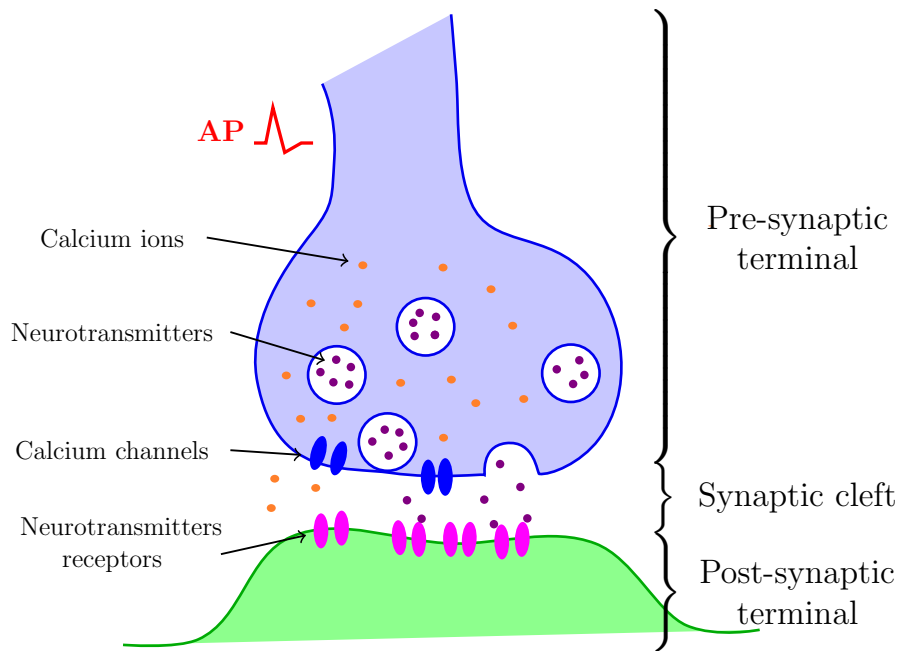


Figure 3: **Functional organization of chemical synapses.** The synapse is composed of a pre-synaptic terminal, where an incoming action potential leads to the opening of voltage gated calcium channels (blue). The consecutive entry of calcium ions (orange) triggers the fusion of vesicle with the synaptic membrane, and the liberation of neurotransmitters (purple) in the synaptic cleft. The neurotransmitters diffusing in the cleft can find specific receptors (fuschia) located in the post-synaptic terminal (green). The binding of neurotransmitters on these receptors triggers the conversion of the chemical signal into an electrical signal in the post-synaptic neuron.

driven by the quick rise and fall of the membrane potential of the presynaptic neuron, to the postsynaptic neuron through a complex molecular process. An incoming AP leads in the presynaptic terminal to the opening of voltage-gated-calcium-channels (VGCC) and to the entry of calcium ions. The VGCC are located at the Active Zone (AZ), a dense region apposed to the post-synaptic neuron, where some vesicles are attached to the presynaptic membrane, waiting for fusion (docked vesicles). The calcium ions must bind to specific molecules on the docked vesicles to trigger their fusion with the synaptic membrane, and the liberation of neurotransmitters in the synaptic cleft. The neurotransmitters diffusing in the cleft can bind specific receptors located in the post-synaptic terminal. The binding of neurotransmitters on these receptors triggers the conversion of the chemical signal into an electrical signal in the post-synaptic neuron.

The frequency at which neuronal APs are produced is known as the neuron's firing rate. This process of information transfer is stochastic, and the probability of vesicular release (the release probability) is a crucial factor in the regulation of signal propagation in neuronal networks. Indeed, the reliability of neurotransmitter release can be highly variable: experimental data from electrophysiological recordings, molecular and imaging studies have demonstrated that synaptic terminals can individually modify their neurotransmitter release probability dynamically, through local regulation.

Modeling the synaptic compartments

Modeling the synaptic terminals and the synaptic cleft has been a challenge for decades. The synaptic cleft is a small gap between the pre- and postsynaptic terminals, where neurotransmitters are released from the pre-synaptic vesicles and diffuse to bind to specific receptors located on the post-synaptic neuron. Computational studies using diffusion models have shown that the geometrical components of the cleft, such as cleft height and localization of vesicular release, shapes the post-synaptic current [207, 122]. More recent studies, using Monte-Carlo simulations [59] or narrow escape theory (NET) [86], have estimated the probability to bind to receptors on the post-synaptic neuron. This probability is very low, which is compensated by a large number of neurotransmitters [190].

Binding of neurotransmitters on receptors trigger the opening of channels located in the post-synaptic terminal. Models of diffusion in the post-synaptic terminal have accounted for its geometry such as a bulbous head connected to the dendrite through a thin neck. This microstructure can contain few to thousands of calcium ions, and its geometry allows to compartmentalize them, as shown by using coarse-grained reaction-diffusion models of Langevin equations [78, 88, 76].

The first empirical formula for estimating the release probability

In their pioneering work, the electrophysiologists Katz and Miledi [101, 102] succeeded to link the release probability P_r for a vesicle to the number of available

release sites N_F and the quantal size q , which is the smallest signal that can be transmitted to the post-synaptic neuron, coming from the release of a single vesicle:

$$P_r = qN_F, \quad (19)$$

and proposed a model for synaptic facilitation (SF) based on the accumulation of calcium in the pre-synaptic terminal. Further studies have shown that other biophysical mechanisms such as binding to calcium buffers would affect this model.

Several models [130, 150] are now based on reaction-diffusion equations that describe in details the chemical reactions involved in the terminal, and reproduce numerically some relevant aspects of transmission and plasticity. Nevertheless, these non-stochastic models ignore the spatial heterogeneity, temporal fluctuations or diffusional barriers. They do not account for the particular organization of the AZ, or the specific geometry of the terminal and the distribution of vesicles. A recent model of the AZ [103] uses Monte-Carlo simulations to understand how the organization of calcium channels influences the release probability, but without taking into account the geometry of the docked vesicles. They conclude that channels must be localized at some distance from the vesicles in order to agree with experimental data. The relative distribution of the vesicles compared to VGCC geometry remains poorly understood [150, 145, 169]

Toward a new model for the release probability based on the dire strait time computation

The major characteristics influencing the release probability at a synapse is thought to be the number and organization of the vesicles and VGCC at the AZ, and the number and types of calcium buffers, which are specific proteins in the terminal that bind calcium ions to regulate their concentration in the cell. The relative position of the calcium channels and the vesicles is not completely answered. Indeed, to observe their organization, a nanometer precision would be needed, which is not yet achieved even by the most advanced superresolution microscopy.

To address the question of the influence of the relative position of channels relatively to vesicles, I present in the second part of chapter 2 a model of vesicular fusion triggered by the diffusion of calcium ions in the pre-synaptic terminal. In the terminal, calcium ions enter mainly through calcium channels (N or P/Q-types) located within the AZ. They trigger the release of a docked vesicle by binding to target molecules (such as synaptotagmin) located close to a complex of proteins connecting the synaptic membrane and the vesicular membrane Fig. 4 (SNARE protein complex). The arrival of several ions at the target triggers the fusion of the vesicles with the terminal membrane, and ultimately to vesicular fusion, which models the synaptic response [186]. Although the binding of few calcium ions (from 4 to 8) is enough to trigger fusion, it is still an open question to understand how these ions find such small molecular sites and how the mean time and probability depends on the local geometry and calcium channel location. The organization of the AZ is thought to play a major role in modulating the synaptic response: are vesicles densely packed or far from each other? are channels clustered? Do they co-localize with vesicles? we have proposed several answers to these questions using analytical

solutions of the model equations and associated stochastic simulations.

To investigate the possible mechanism underlying the modulation of the synap-

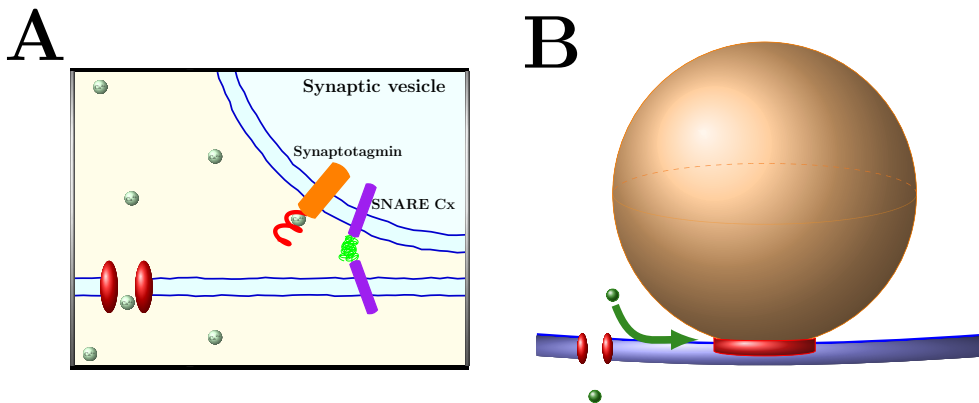


Figure 4: **Modeling SNARE complex activation by calcium ions.** **A:** Schematic representation of the protein organization connecting the vesicles and the pre-synaptic membrane. Calcium ions enter through ionic channels. They diffuse to activate key proteins such as synaptotagmin and SNARE Complex located between the vesicle and synaptic membrane. The binding of several ions is required to activate the SNARE Complex. **B:** Model of SNARE activation. The Brownian particle (green ball) has to find its target site (red cylinder) trapped between a plane (blue) and a tangent sphere (orange).

tic response, I built a diffusion model to estimate the first time for diffusing particles (calcium ions) to find small target molecules hidden in a cusp between the pre-synaptic terminal membrane and the vesicular membrane (geometry of Fig. 4B), depending on the AZ organization (Figure 5A). The novelty in my approach is to consider the particular geometry of the vesicles, attached to the synaptic membrane through the SNARE complex. I model this geometry using a sphere (the vesicle) tangent to a plane (the synaptic membrane).

To model calcium ions, I neglect their charge, and represent their motion using Brownian particles. The activation of the SNARE complex is modeled by the arrival of several Brownian particles under the vesicles, in a domain delimited by a small cylinder joining the sphere and the plan, and centered at their tangential point (Fig. 4B, target cylinder in red). With this configuration, the target site is located at the end of a cusp, and the activation time problem falls into the DST for the geometry presented above, eq. 13, Fig. 2. Because the distance of the calcium channels to the center of the vesicle can vary, I also investigated how this change can affect the probability of vesicular release, in a model of square lattice vesicular organization (Figure 5A).

Computing the release probability from the Splitting probability

The analysis of the DST reveals that equation 13 gives relevant results only when a Brownian particle starts outside a boundary layer (BL) near the cusp. Nevertheless,

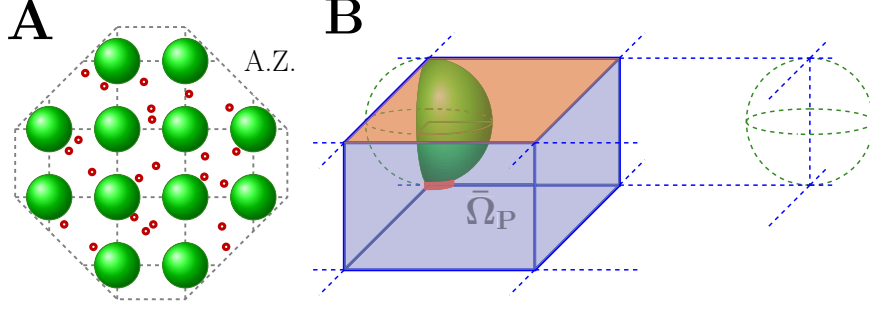


Figure 5: **Model of vesicular release activation in the pre-synaptic terminal.** **A:** Active Zone organization. Vesicles (green) are regularly distributed on a square lattice. Calcium channels (red) are uniformly distributed in the AZ. **B:** Elementary 3-dimensional domain representing the boundary layer around the vesicle. I compute the splitting probability for an ion starting in the bottom of the domain, to reach the target (red) before leaving the BL through the orange boundary. The other boundaries are reflecting.

the co-localization of channels and vesicles was observed at several synapses [133] and is thought to be an important source of heterogeneity in the release probability.

In complement with the formula 13, I investigated the time and proportion of particles reaching the target when the initial position starts in a boundary layer close to the target. Using analysis and numerical approximations, I computed the splitting probability $p(\mathbf{x})$ for a Brownian particle starting at point \mathbf{x} inside the BL to reach its target, before leaving the BL. The splitting probability $p(\mathbf{x})$ satisfies the mixed boundary-value Laplace equation [100, 174, 189]:

$$\begin{cases} \Delta p(\mathbf{x}) = 0 & \text{for } \mathbf{x} \in \bar{\Omega}_P \\ p(\mathbf{x}) = 1 & \text{for } \mathbf{x} \in \partial\bar{\Omega}_{P,a} \\ p(\mathbf{x}) = 0 & \text{for } \mathbf{x} \in \partial\bar{\Omega}_{P,out} \\ \frac{\partial p}{\partial n}(\mathbf{x}) = 0 & \text{for } \mathbf{x} \in \partial\bar{\Omega}_P \setminus (\partial\bar{\Omega}_{P,a} \cup \partial\bar{\Omega}_{P,out}), \end{cases} \quad (20)$$

where $\bar{\Omega}_P$ (Fig. 5B) represents the elementary BL domain, $\partial\bar{\Omega}_{P,a}$ (red) is the part of the boundary representing the target, and $\partial\bar{\Omega}_{P,out}$ (orange) the border by which the particle leaves the BL.

Using asymptotic analysis and numerical approximation, I found an analytical approximation $p_s(r)$ for the splitting probability to reach the absorbing window before leaving $\bar{\Omega}_P$:

$$p_s(r) = 1 - \frac{1 - 9.8 \frac{R^2 \varepsilon}{H^3}}{1 - \frac{2R\varepsilon}{H^2}} \left(1 - \frac{2R\varepsilon}{r^2} \right), \quad (21)$$

where r is the distance between the channel and the vesicle, R is the radius of a vesicle, $2H$ is the distance between two vesicles and ε is the height of the ribbon

target. Numerical simulations show a nice agreement between the asymptotic formula and Brownian simulations for different values of R , H and ε .

By neglecting the dynamics of calcium ion unbinding events, I was able to compute the release probability of a vesicle, $p_{act}(r, N)$, which is the probability to find at least T particles inside the target, when N particles enter through a channel located at a distance r from the vesicle. Because the probability to find exactly k ions out of N follows the Binomial distribution $\mathcal{B}(N, p(r))$, I obtain that

$$p_{act}(r, N) = 1 - \sum_{k=0}^{T-1} \binom{N}{k} p(r)^k (1 - p(r))^{N-k}, \quad (22)$$

where p is the probability for one particle to reach the target before leaving $\bar{\Omega}_P$. Using the approximation eq. (21), I found an explicit expression for the probability of activation $p_{act}(r, N)$ after a single channel opens.

In conclusion, these formulas indicate that the probability of vesicular release depends drastically on the calcium channel location, decreasing from 1 to practically 0 in only few nanometers. Moreover, the vesicular organization of the AZ is also a determinant factor, due to the local geometry of the target underneath a vesicle. When channels are uniformly distributed, a sparse distribution of vesicles at the AZ requires a high number of entering ions in order to trigger fusion. However, when channels are co-localized with vesicles, the activation probability is significantly increased. A reliable synapse requires a nanometer precision of the channel location, but this high requirement can be compensated by increasing the initial number of ions.

Part II: Coarse-grained multiscale simulations of molecular dynamics

Reaction-diffusion problems in confined microdomains where particles have to bind to small target sites can be coarse-grained into Markovian jump processes [79] using the NET/DST approximation. This approach takes advantage of the fact that the arrival process of Brownian particles moving in a large bounded domain to a small absorbing target is Poissonian, with a rate equals to the total flux in the absorbing boundary [138, 174, 175]. This rate is the reciprocal of the NET/DST, and captures many of the geometrical features of the domains. Coarse-graining binding and unbinding using a Markov jump approach is a key step for analyzing stochastic chemical reactions, circumventing inherent difficulties of the full reaction-diffusion, formulated as coupled partial differential equations that are much harder to solve.

Performing stochastic simulations of diffusion processes at a molecular level in confined microdomains is also challenging. Few to many particles have to be simulated and tracked and several spatial scales are involved and in particular when they have to bind small targets. Naive stochastic simulations of Brownian particles are inefficient, due to the long time for finding a small target, which is a rare event. Following simultaneously all diffusing particles prevents an effective use of an adaptive time step near the small target, which leads to endless simulations. On the other hand, solving the associated partial differential equations is difficult due to the time dependent boundary conditions. In chapter 3, I propose two different approaches to simulate effectively diffusion processes in microdomains, based on the NET/DST presented in chapter 2, and on the coarse-graining into Markovian jump processes.

Modeling calcium dynamics in neuronal synapses

In chapter 3, I use my model for the release probability (chapter 2) in the context of a more general model for the pre-synaptic terminal that I shall describe now. Following an AP, VGCCs located at the AZ open, leading to the entry of calcium ions in the terminal. These ions diffuse in the terminal and reach different targets such as synaptotagmin located underneath a vesicle, or some calcium buffers. They can otherwise be extruded from the terminal by pumps, or leave through the neck. As previously explained, the binding of 4 to 8 calcium ions on the small molecular targets located underneath a docked vesicle activates a complex molecular machinery, which leads to fusion. As presented in chapter 2, the success of this process depends on the relative position between the vesicles and the channels, and their organization at the surface.

At equilibrium, calcium concentration is very low in the terminal, containing only a few ions. The entry of thousands of ions leads to a transient peak of calcium, leading to vesicular fusion. The concentration goes back to equilibrium in tens of ms. The release probability depends mainly in the shape and amplitude of this peak, which motivates the study of this transient regime. However, the resolution of the reaction-diffusion system of equations that describes the evolution of the number of particles in the terminal and the associated release probability is not easy. To imple-

ment Brownian simulations, the terminal is modeled as a ball smoothly connected to a short cylinder (neck), and although calcium are charged ions, they are modeled as Brownian particles (Fig. 6). The small size of the targets and the particular cusp geometry at each vesicle prevent the efficient use of a naive Brownian simulation. To circumvent this difficulty, I built a stochastic description based on rate equations, and a system of mass-action equations coupled to a Markov chain. I shall describe first the reaction-diffusion system of equations that describes the evolution of the number of particles in the terminal.

The reaction-diffusion system of equation

The classical reaction-diffusion system of equations in the domain Ω representing the presynaptic terminal, describes the density of free particles in the terminal ($M(\mathbf{x}, t)$), the density of buffer sites with ($B^{(1)}(\mathbf{x}, t)$) and without ($B^{(0)}(\mathbf{x}, t)$) bound calcium ions and the density of targets with j bound vesicles: $S^{(j)}(\mathbf{x}, t)$, $j \in 0..T$, where T is the number of ions needed to trigger fusion. The system of equation is

$$\left\{ \begin{array}{l} \frac{\partial M(\mathbf{x}, t)}{\partial t} = -\nabla \cdot \mathbf{J}_M(\mathbf{x}, t) - k_0 M(\mathbf{x}, t) B^{(0)}(\mathbf{x}, t) + k_{-1} B^{(1)}(\mathbf{x}, t) \\ \quad - k_S M(\mathbf{x}, t) \sum_{j=0}^T S^{(j)}(\mathbf{x}, t) \\ \frac{\partial B^{(0)}(\mathbf{x}, t)}{\partial t} = -\nabla \cdot \mathbf{J}_B^{(0)}(\mathbf{x}, t) - k_0 M(\mathbf{x}, t) B^{(0)}(\mathbf{x}, t) + k_{-1} B^{(1)}(\mathbf{x}, t) \\ \frac{\partial B^{(1)}(\mathbf{x}, t)}{\partial t} = -\nabla \cdot \mathbf{J}_B^{(1)}(\mathbf{x}, t) - k_{-1} B^{(0)}(\mathbf{x}, t) + k_0 M(\mathbf{x}, t) B^{(1)}(\mathbf{x}, t) \\ \frac{\partial S^{(0)}(\mathbf{x}, t)}{\partial t} = -k_S M(\mathbf{x}, t) S^{(0)}(\mathbf{x}, t), \\ \frac{\partial S^{(i)}(\mathbf{x}, t)}{\partial t} = k_S M(\mathbf{x}, t) [S^{(j-1)}(\mathbf{x}, t) - S^{(i)}(\mathbf{x}, t)], i = 1..T-1 \\ \frac{\partial S^{(T)}(\mathbf{x}, t)}{\partial t} = k_S M(\mathbf{x}, t) S^{(T-1)}(\mathbf{x}, t), \end{array} \right. \quad (23)$$

where the fluxes are defined by

$$\mathbf{J}_X(\mathbf{x}, t) = -D\nabla X(\mathbf{x}, t), \text{ for } X \in \{M, B^{(0)}, B^{(1)}\}. \quad (24)$$

The constant k_0 (resp. k_{-1} , resp. k_S) represents the binding to the buffers (resp. the unbinding to the buffers, resp. the forward reaction rate on the target). The initial conditions for $B^{(0)}(\mathbf{x}, t)$, $B^{(1)}(\mathbf{x}, t)$ and $S^{(j)}(\mathbf{x}, t)$, $j \in 0..T$, are

$$B^{(0)}(\mathbf{x}, 0) = B_0(\mathbf{x}), \quad B^{(1)}(\mathbf{x}, 0) = 0. \quad (25)$$

$$S^{(0)}(\mathbf{x}, 0) = S_0(\mathbf{x}), \quad S^{(j)}(\mathbf{x}, 0) = 0 \text{ for } 1 \leq j \leq T. \quad (26)$$

and the boundary conditions are reflective on all the boundary $\partial\Omega$.

The initial and boundary conditions for $M(\mathbf{x}, t)$ are the initial reactant density

$c_0(\mathbf{x})$, absorption at the absorbing boundary, and flux given by the motion of the reflective boundary,

$$M(\mathbf{x}, 0) = c_0(\mathbf{x}) \quad \text{for } \mathbf{x} \in \Omega(t) \quad (27)$$

$$M(\mathbf{x}, t) = 0 \quad \text{for } \mathbf{x} \in \partial\Omega_a(t) \quad (28)$$

$$\mathbf{J}_M(\mathbf{x}, t) \cdot \boldsymbol{\nu}(\mathbf{x}) = 0 \quad \text{for } \mathbf{x} \in \partial\Omega_r(t) \setminus S_{AZ} \quad (29)$$

$$\mathbf{J}_M(\mathbf{x}, t) \cdot \boldsymbol{\nu}(\mathbf{x}) = \frac{J_{tot}(t)}{S_{AZ}} \quad \text{for } \mathbf{x} \in S_{AZ}. \quad (30)$$

J_{tot} is the flux of particles entering through the channels. The boundary of the domain Ω is partitioned into three parts: one containing the pumps and the bottom of the neck denoted $\partial\Omega_a(t)$, which absorbs particles, and the remaining surface of the domain, denoted $\partial\Omega_r(t)$. The surface S_{AZ} represent the AZ where vesicles are located near the small target. This ensemble of reaction-diffusion equations described the entrance of ions in a pre-synaptic terminal and the distribution of fused vesicles can be read in the variable $\int_{\Omega} S^{(T)}(\mathbf{x}, t) d\mathbf{x}$.

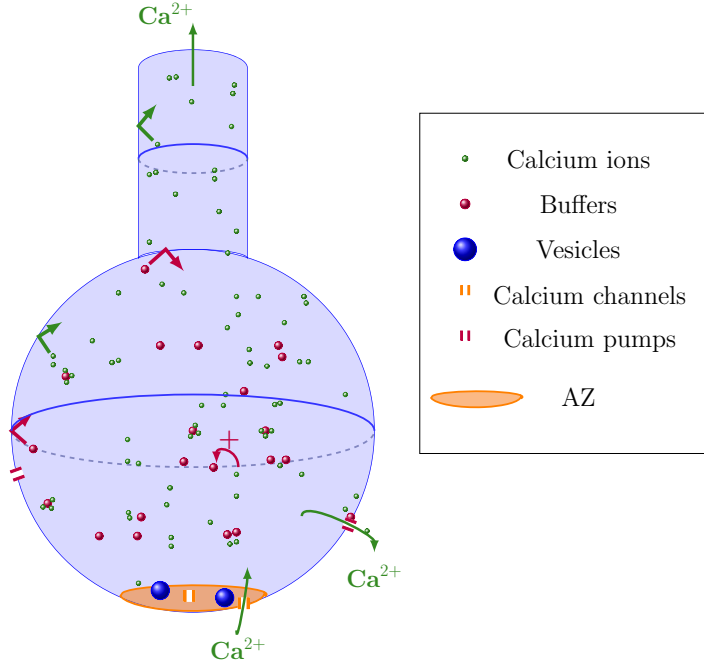


Figure 6: **Schematic representation of the pre-synaptic terminal.** The terminal is modeled as a sphere (head) connected to a cylinder (thin neck). Calcium ions are Brownian particles (orange spheres) that enter through calcium channels located at the AZ (orange). They are reflected everywhere on the boundary except at the pumps (red) and at the upper part of the cylinder. They can be extruded through pumps or bind buffers (green spheres) and the small targets underneath the vesicles (vesicles in blue).

Two reduced models for calcium dynamics in neuronal synapses

To reduce our full model of the pre-synaptic terminal, I used previous computations of the NET/DST [85, 70] and their consecutive Poissonian rates, to coarse-grain into rates the Brownian dynamics of particles and their arrival underneath vesicles, buffers, pumps and their exit through the neck.

Note that the arrival of a Brownian particle to a small target is not any more Poissonian when the particle starts in a boundary layer near the target. Hence, I cannot coarse-grain the entry of calcium through channels located at the AZ using a Poissonian rate. To circumvent this difficulty, I divided the domain into two separated compartments: the boundary layer surrounding the docked vesicles and the bulk outside of the boundary layer. The flux of ions between the two compartments can be deduced from the study in chapter 2, where I computed the probability to reach the target before reaching the bulk, and the DST to reach the target from the bulk. Using these considerations I built two reduced models that I described below, a stochastic model based on rates equations and a system of mass-action coupled to a Markov chain.

Stochastic description based on rate equations

The stochastic model allows stochastic simulations without entering into a full Brownian simulations. In the bulk compartment, the evolution of the number of free and bound particles, N_f and N_b , is computed using the following rates: the arrival of Brownian particles to a small target. The binding times are exponentially distributed with a rate λ equals to the reciprocal of the NET/DST τ :

$$\lambda = \frac{1}{\tau}. \quad (31)$$

When there are N independent Brownian particles in Ω , the rate constant for the first binding time T to a target site is $\lambda(N) = \lambda N$. I discretized the time with a step Δt (small enough), and at each time t , I replaced the simulation of the Brownian trajectories by the Poissonian arrival events τ_X to the small target X ($X \in \{\text{buffers, pumps, vesicles, exit}\}$). At each small site available, the rate is $\lambda N_f(t)\Delta t$, when there are exactly $N_f(t)$ free particles.

The conditional probability that a binding event occurs between time t and $t + \Delta t$ when there are $N_f(t)$ particles is:

$$\mathbb{P}(t \leq T < t + \Delta t | N_f(t)) = \frac{N_f(t)}{\tau_X} \Delta t. \quad (32)$$

Finally, the released rate of a particle to a buffer binding site is Poissonian with rate $k_{-1}\Delta t$.

In the boundary layer compartment, I considered the flux of particles entering through the channels, and separated the particles into the fraction reaching the bulk, and the fraction arriving underneath a vesicle, using the splitting probability presented in chapter 2. Specifically, at each discretized time t , zero to few particles are entering through the channels. Each particle can either arrive underneath a vesicle with probability $p_s(r)$ (eq. 21, Fig. 7), or go to the bulk compartment with

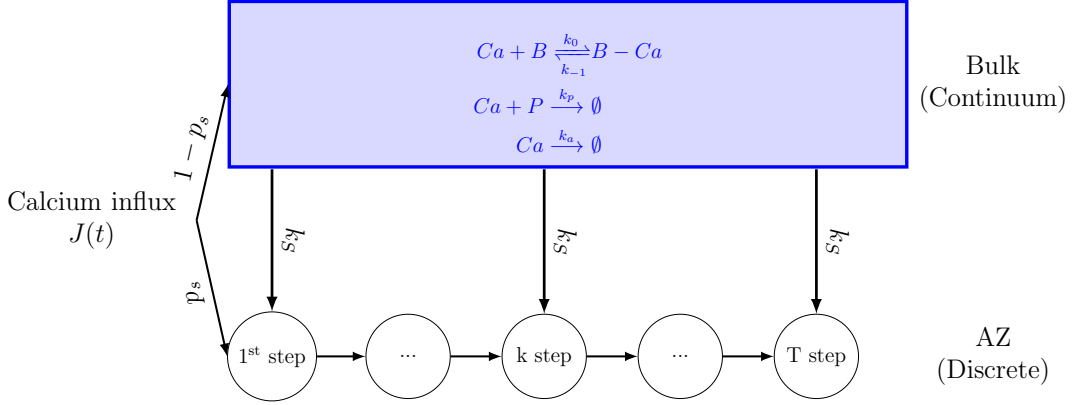


Figure 7: **Coarse-grained Markov-Mass action model:** the mass action equations in the bulk are coupled to the Markov chain in the AZ, that models the arrival of single particles to the target sites until the threshold T is reached. The influx of calcium ions $J(t)$ goes to the AZ with probability p_s (eq. 21), and to the bulk with probability $1 - p_s$.

probability $1 - p_s(r)$, which depends on the channel/vesicle organization. Using these two compartments, I tracked the number of particles bound on each vesicle and computed the stochastic release times for different parameters and AZ organization. This approach allows fast simulations that gives the same results but are much faster than naive and endless Brownian simulations.

A system of mass action equations coupled to a Markov chain

The second model couples a system of mass-action equations in the bulk, to a Markov chain in the boundary layer (Fig. 7). From this model, some analytical derivations are even possible. The number of free and bound particles in the bulk N_f and N_b are described by mass-action, which is a system of differential equations:

$$\left\{ \begin{array}{l} \frac{dN_f}{dt}(t) = k_{-1}N_b(t) - k_0(B_0 - N_b(t))N_f(t) + \sum_{l=1}^{l_V} (1 - p_s(\mathbf{x}^l)) J(t) \\ \quad - \left(k_p N_p + k_{es} + \sum_{i=1}^{N_{Dock}} (1 - p_T^i(t, (\mathbf{x}^l)_l)) k_S \right) N_f(t) \\ \quad + T \sum_{i=1}^{N_{Dock}} \left(\sum_{l=1}^{l_V} p_s(\mathbf{x}^l) q(\mathbf{x}^l, i) J(t) + k_S N_f(t) \right) p_{T-1}^i(t, (\mathbf{x}^l)_l) \\ \frac{dN_b}{dt}(t) = -k_{-1}N_b(t) + k_0(B_0 - N_b(t))N_f(t), \end{array} \right. \quad (33)$$

where $k_0 = \frac{1}{\tau_{buffers}}$, $k_p = \frac{1}{\tau_{pumps}}$, $k_S = \frac{1}{\tau_{vesicles}}$, $k_{es} = \frac{1}{\tau_{exit}}$. B_0 is the total number of buffer sites, k_{-1} is the unbinding rate from buffers, l_V is the number of channels,

N_p is the total number of pumps, N_{Dock} is the number of docked vesicles and $J(t)$ is the flux of particle entering through one channel. The term $\sum_{l=1}^{l_V} (1 - p_s(\mathbf{x}^l)) J(t)$ describes the flux of particles entered through the channels that join the bulk. The term $\sum_{i=1}^{N_{Dock}} (1 - p_T^i(t, (\mathbf{x}^l)_l)) k_S N_f(t)$ represents binding of particles coming from the bulk on the docked vesicles not yet released. Finally, the last term represents the flux of T ions entering the bulk after the fusion of vesicles.

In the boundary layer, the binding to the target sites located on the vesicles is described by a Markov Chain, where $p_k^i(t, (\mathbf{x}^l)_l)$, $k \in 0..T$ $i \in 1..N_{Dock}$ represents the probability to have k particles bound on vesicle i , and where channels are positioned at $(\mathbf{x}^l)_{l=1..l_V}$:

$$\left\{ \begin{array}{l} \frac{dp_0^i(t, (\mathbf{x}^l)_l)}{dt} = - \left(\sum_{l=1}^{l_V} p_s(\mathbf{x}^l) q(\mathbf{x}^l, i) J(t) + k_S N_f(t) \right) p_0^i(t, (\mathbf{x}^l)_l) \\ \frac{dp_k^i(t, (\mathbf{x}^l)_l)}{dt} = \left(\sum_{l=1}^{l_V} p_s(\mathbf{x}^l) q(\mathbf{x}^l, i) J(t) + k_S N_f(t) \right) \times \\ \quad (p_{k-1}^i(t, (\mathbf{x}^l)_l) - p_k^i(t, (\mathbf{x}^l)_l)) \\ \frac{dp_T^i(t, (\mathbf{x}^l)_l)}{dt} = \left(\sum_{l=1}^{l_V} p_s(\mathbf{x}^l) q(\mathbf{x}^l, i) J(t) + k_S N_f(t) \right) p_{T-1}^i(t, (\mathbf{x}^l)_l). \end{array} \right. \quad (34)$$

The term $\sum_{l=1}^{l_V} p_s(\mathbf{x}^l) q(\mathbf{x}^l, i) J(t)$ represents the fraction of particles binding to vesicle i immediately following their entry through channel l , summed over all the l_V channels. The initial conditions at time $t = 0$ are:

$$N_f(0) = 0 \quad (35)$$

$$N_b(0) = 0 \quad (36)$$

$$p_k^i(0, (\mathbf{x}^l)_l) = \delta_{k,0}. \quad (37)$$

Finally, the normalization is

$$\forall i \in [1, N_{Dock}], \sum_0^T p_k^i(t, (\mathbf{x}^l)_l) = 1. \quad (38)$$

The system of ODEs 33-34 allows to compute the release probability $p_T^i(t, (\mathbf{x}^l)_l)$ for vesicle i . I compared results of the two models in the case of a single channel and a single docked vesicle, for a uniform distribution of the channel and for different values of the total number of buffers B_0 (Fig. 8). I found a very good agreement between the two methods.

I solved analytically the system of equations 34 for each target site i , and for a channel distribution $(\mathbf{x}^l)_l$. I considered that the flux of particles entering in the boundary layer is $g^i(t, (\mathbf{x}^l)_l) = \sum_{l=1}^{l_V} p_s(\mathbf{x}^l) q(\mathbf{x}^l, i) J(t) + k_S N_f(t)$. The mean probability that k particles are bound at time t on vesicle i , averaged over the

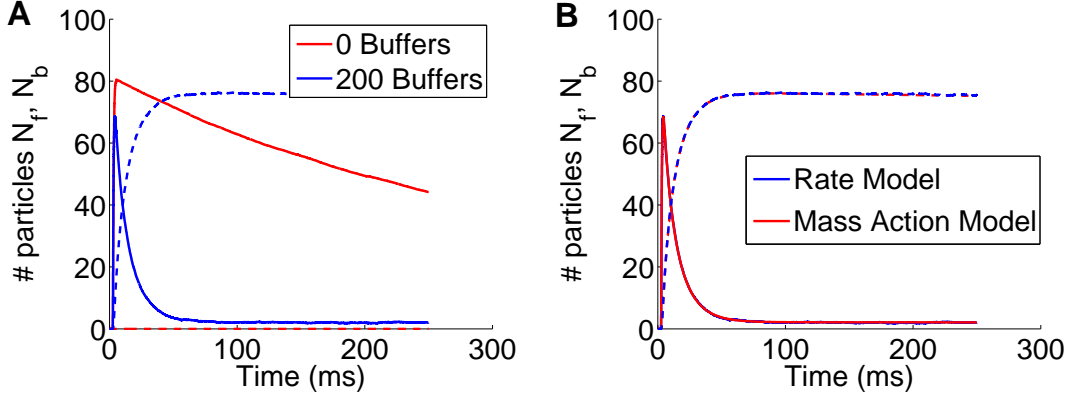


Figure 8: **Time course of calcium in the pre-synaptic terminal and target activation, in the case of a uniform distribution of channels.** **A:** Time evolution of the number of free calcium (normal line) and buffered calcium (dotted line) for different values of the number of buffer sites. **B:** Comparison between the stochastic model based on rates equations (red), and the system of mass-action coupled to a Markov chain (blue). I compare both the number of free (normal line) and buffered (dotted line) calcium for 200 buffer sites.

distribution of the channels, is given for $k \in [0, T - 1]$:

$$\begin{aligned} p_k^i(t) &= \langle p_k^i(t, (\mathbf{x}^l)_l) \rangle_{(\mathbf{x}^l)_l} & (39) \\ &= \int_{S_{AZ}^{lV}} \frac{1}{k!} \left(\int_{t_0}^t g^i(u, (\mathbf{x}^l)_l) du \right)^k \exp \left(- \int_{t_0}^t g^i(u, (\mathbf{x}^l)_l) du \right) f((\mathbf{x}^l)_l) d\mathbf{x}^1 \dots d\mathbf{x}^{lV}, \end{aligned}$$

and for $k = T$:

$$\begin{aligned} p_T^i(t) &= \langle p_T^i(t, (\mathbf{x}^l)_l) \rangle_{(\mathbf{x}^l)_l} & (40) \\ &= \int_{S_{AZ}^{lV}} \exp \left(- \int_{t_0}^t g^i(u, (\mathbf{x}^l)_l) du \right) \sum_{k \geq T} \frac{1}{k!} \left(\int_{t_0}^t g^i(u, (\mathbf{x}^l)_l) du \right)^k f((\mathbf{x}^l)_l) d\mathbf{x}^1 \dots d\mathbf{x}^{lV}, \end{aligned}$$

where $f((\mathbf{x}^l)_l)$ represents the probability density function of the repartition of channels.

In summary, I derived here for the first time a coarse-grained simulation based on the asymptotic computation of the DST, which allows replacing Brownian simulations by a Poissonian rate model. The second approach couples a continuum ensemble of particles with a discrete ensemble of events described by a set of Markov equations.

These two models of the presynaptic terminal reveals two different regimes in the release probability: a short-rime regime (< 10 ms) where a large fraction of vesicles are released due to the direct entry of calcium through the channels, and a long regime where the release probability is strongly dependent on calcium buffers. This approach can be used for any system of reaction, where the rare accumulation of few particles in a domain containing many of them can trigger a cellular event by binding to a fixed number of targets. These simple approaches allow running efficient simulations and even get analytical results.

Part III: Modeling bursting oscillations in neuronal networks for the generation of pre-Bötzinger Complex rhythms

This is the last section of my PhD that concerns modeling and simulations of synchronous oscillations, that emerge in a network of asynchronous neurons.

Models and oscillations in neural networks

Oscillatory activity in a group of neurons is characterized by a synchronization of their firing patterns that results in an almost periodic activity. This activity consists in bursting times, when all neurons fire together, followed by quiet times. Oscillations in neural networks are widespread within the brain, in different circuits such as the ones for breathing, chewing, swallowing, whisking, locomotion..., but also in circuits involved in behaviors such as memory, sleep or consciousness, and they may also play a role in neural development. How to generate oscillations in neural networks? How to synchronize the neurons? The first pioneering works in modeling neural network oscillations [196] are based on two complementary modeling techniques. Some models are highly detailed to capture the complexity of individual neurons [197, 195], and can contain several compartments (dendrite, soma, axon) and/or different types of voltage gated channels. This allows to integrate various stimulation conditions and inputs in a reasonable way. It is then possible to investigate many effects such as network size and connectivity.

Other models [44, 205, 28, 99] are based on reduced equations and simplified phenomenological equations. The reduction can affect the number and types of neurons or some characteristics of their anatomy, which leads ultimately to mean-field equations. The main challenge is to keep enough details about the physiological parameters, and to use the analysis to make predictions about the effects of parameter changes that can be tested experimentally.

In further modeling approaches, other distinctions were made between models, depending on whether the oscillations arise within the individual neurons and then synchronize across the network [17, 43, 23, 24, 16], or emerge at the population level [206]. These last models are usually minimal models, which are not informative about how the spike times of individual neurons relate to the network oscillations. More recent models present a combination of the two, based or not on Hodgkin-Huxley neurons [93, 194, 164, 22, 21].

Neural networks models for the pre-Bötzinger Complex

The pre-Bötzinger Complex (preBötC) is the neuronal network responsible for breathing at rest in mammals. This oscillatory network shows rhythmic activity in *in vitro* conditions, where bursting and silent periods alternate (Fig. 9). Although it has been discovered more than twenty years ago [184], the exact mechanism responsible for this neural activity remains controversial [53]. An early hypothesis was that the neuronal activity is initiated by pacemaker neurons synchronized via excitatory

synaptic connections [110]. Pacemaker neurons can be defined as neurons that can generate intrinsically oscillatory bursts of action potential, even when they are isolated from their neural network, in the absence of any synaptic input. For example, neurons that control the heart rate are pacemakers. In the modeling approach of the preBötC activity, the main minimal model for pacemaker neurons is based on a single-compartment Hodgkin-Huxley (HH) formalism, with the addition of a sodium current characterized by a fast activation and slow inactivation, that generates and terminates the bursting activity [166, 23, 24, 193].

However, electrophysiological studies have shown that inhibiting pacemaker

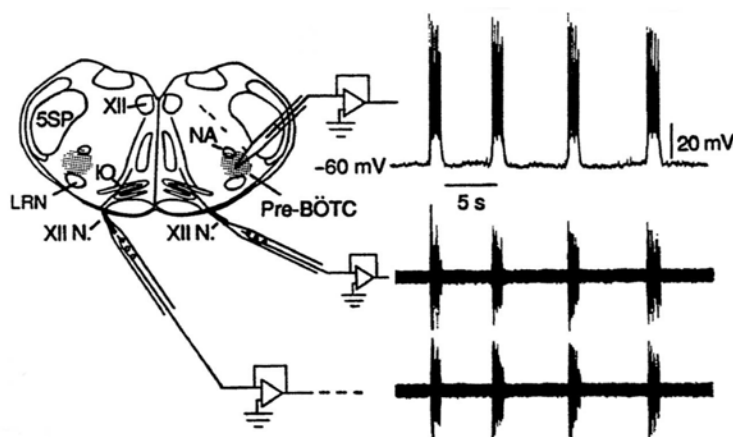


Figure 9: **Rhythmic activity in the pre-Bötzinger Complex.** Medullary slice containing the preBötC. Traces at right show a whole-cell recording from a rhythmically active neuron in the preBötC (upper), and inspiratory activity recorded from the hypoglossal nerve (lower). extract from [184]

neurons in the preBötC do not suppress bursting [46, 140]. This lead to the group-pacemaker hypothesis, where respiratory rhythm is thought to emerge from recurrent neuronal connections, without intrinsic neuronal bursting [53]. A first model [164, 176] tested this hypothesis and propose a mean-field model, where bursts are generated by the synaptic activation of a calcium current. The bursting activity of the network is then stopped by the slow inactivation of a sodium current, as modeled for pacemaker neurons. Nevertheless, to obtain an oscillatory rhythm, a regular spiking activity must be present in the neurons to activates the synaptic current. In my model that I shall describe below, I propose to test the group-pacemaker hypothesis at the preBötC, by generating emerging network oscillations without any regular activity at the neuronal level.

Model of robust network oscillations driven by synaptic dynamics in the pre-Bötzinger Complex

In chapter 4, I present a model to test the group-pacemaker hypothesis in the preBötC. This model captures the activity of individual neurons within the network and show how the spontaneous ectopic spiking of neurons leads to the emergence

of oscillations at the network level. The network oscillations and synchronization between neurons are only due to the synaptic dynamic at the neuronal level.

In our model, synaptic facilitation, that enhances neuronal excitability, converts ectopic spontaneous spiking of few neurons into synchronized spiking of the whole network through their recurrent connections, that creates bursting. Synaptic depression (SD), that decreases the synaptic strength of a neuron, is expressed by each neuron. SD stops their spiking activity, which silences progressively the network and stop the bursting event, to enter in a quiet period. Our model differs from previous efforts to test the pacemaker hypothesis [164]. In that model, the induction of bursts in the network is triggered by the regular spiking activity of a large fraction of the neurons. Moreover, burst termination and the quiescent period between bursts comes from the intrinsic property of neurons, through a current with slow inactivation expressed by all neurons, which recall the pacemaker neuron models. In our model, oscillations appear as a network property emerging from spontaneous neuronal activity without involving pacemaker neurons, or neurons expressing a rhythmic activity. This project has been carried out in collaboration with Gilles Fortin and John. A. Hayes (INAF) for the experimental part.

To test the emergence of a rhythm in the preBötC, I built a neuronal network where the electrical activity of each neuron is modeled using the classical Hodgkin-Huxley (HH) system for the voltage of the membrane potential (Eq. 41). Each neuron exhibits a spontaneous spiking activity represented by the addition of a noise source term $\sigma\dot{W}$ in the HH model. I considered a network of 400 neurons, which is in the range observed experimentally. For each neuron $k \in \llbracket 0, 400 \rrbracket$, the HH model is:

$$\left\{ \begin{array}{l} C \frac{dV^k(t)}{dt} = -I_{Na}(n^k, V^k) - I_K(n^k, V^k) - I_L(V^k) \\ \quad + \sum_{j \text{ connected to } k} I_{syn,j}(x^j, y_{free}^j, y_{dock}^j, V^j) + \sigma\dot{W} \\ \frac{dn^k(t)}{dt} = \alpha_n(1 - n^k) - \beta_n n^k, \end{array} \right. \quad (41)$$

where V^k represents the membrane potential of neuron k , and I_{Na} , I_K and I_L are respectively the classical sodium, potassium and leak currents. $\sum_{j \text{ connected to } k} I_{syn,j}$

represents the sum over all the neurons connected to neuron k , of the transmitted synaptic currents. To determine the neuronal connections, I ordered the neurons on a square lattice, and connected them sparsely within the network, using a connection probability $\mathbf{P}(i \rightarrow j)$ that decays with distance (Eq. 42, Fig. 10A):

$$\mathbf{P}(i \rightarrow j) = \exp(-d(i, j)^2 / (2s^2)). \quad (42)$$

The synaptic current $I_{syn,j}$ transmitted from neuron j to neuron k is proportional to the amount of fused vesicles at neuron j ' synapses. To compute this current, I derived a model of the pre-synaptic terminal based on the law of mass action (Eq. 44), that accounts for synaptic facilitation and depression. This model is based on the biological description of the time course of vesicles within the pre-synaptic terminal [186, 161].

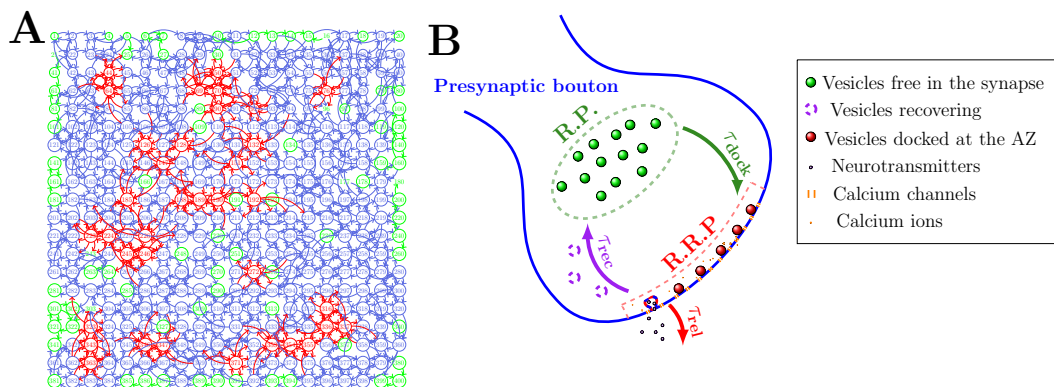


Figure 10: **Modeling the pre-Bötzinger Complex.** **A:** Example of a neuronal network (400 neurons) where neurons are located on a square lattice. The connections can be higher than 10 (red), between five and ten (blue), or less than five (green). Neurons with no input or output are marked in green, without any cycle around, such as number 16. **B:** Model of the synaptic vesicle cycle. Schematic representation of the pre-synaptic bouton: vesicles are divided into two pools, diffusing (green) and docked at the Active Zone (red) with transient ones (purple). After fusion, vesicles recover and enter the recycling pool.

To model the synaptic dynamic of the neurons, I used as a basis the classical facilitation-depression model of synapses [199, 198]. For the facilitation part, this standard model introduces a facilitation factor x , which is elevated by each spike by a certain amount and decays between spikes. The variable x could reflect, for example, the concentration of calcium ions (responsible for neurotransmitter release), that increases when a spike arrives in the presynaptic terminal and decreases because of calcium extrusion between two spikes. For each neuron j , the facilitation parameter $x^j(t)$ follows the dynamic:

$$\frac{dx^j}{dt} = \frac{X - x^j}{\tau_f} + k(1 - x^j)H(V^j - T).$$

I describe now our model for depression at synapses. Synaptic depression is described classically as the depletion of vesicles following activation [186]. The classical model for depression assumes that the synapse has a finite amount of resources, and the rate of synaptic depression depends on the resource's availability [199]. Each pre-synaptic spike activates a fraction of resources which then quickly inactivate. Nevertheless in this model, presynaptic stimulation through a spike train produces a regime of stationary EPSPs postsynaptically after a few spikes, which does not result in burst termination due to full depletion of available vesicles. To circumvent this difficulty, I built a model that account for the depletion of docked vesicles using a mass-action law model describing the state of the synaptic vesicles at time t .

In the terminal, vesicles can be in three different states: diffusing freely in the bulk (y_{free}^j), docked to the membrane (y_{dock}^j), or recovering after fusion (y_{rec}^j) (Fig. 10B). The amount of freely diffusing vesicles y_{free}^j is balanced between the inward flux of vesicles arriving from the recovery state, and the outward flux of vesicles binding to the membrane. This last flux is proportional to the fraction of available

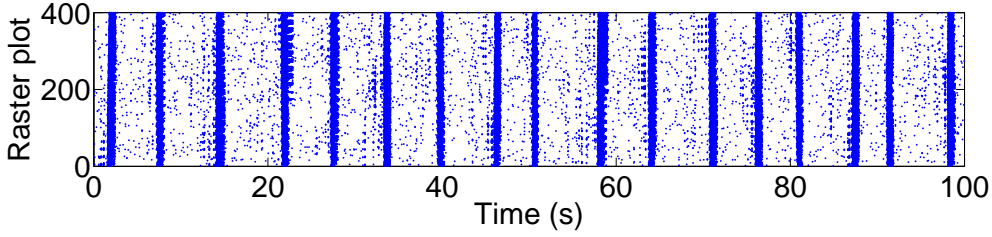


Figure 11: **Network rhythmic activity** Raster plot for the network generated in figure 10A. Each dot represent an AP. During 100 sec, the synchronous rhythmic patterns alternate between active and silent periods.

docking sites, and the fraction of vesicles freely diffusing. Similarly, the fraction of docked vesicles y_{dock}^j is given by the balance of inward vesicles binding to the membrane, and of the flux of released vesicles following a stimulation. Assuming that the total number of vesicles is fixed in the terminal, I get the conservation equation:

$$y_{\text{free}} + y_{\text{dock}} + y_{\text{rec}} = 1. \quad (43)$$

Finally, the complete system of equations is:

$$\left\{ \begin{array}{l} \frac{dy_{\text{free}}^j}{dt} = \frac{1 - y_{\text{free}}^j - y_{\text{dock}}^j}{\tau_{\text{rec}}} \\ \quad - \frac{1}{\tau_{\text{dock}}} (y_{\text{dock}}^{\text{max}} - y_{\text{dock}}^j) y_{\text{free}}^j \left[1 + \frac{x^j - X}{X} H(V^j - T) \right] \\ \frac{dy_{\text{dock}}^j}{dt} = \frac{1}{\tau_{\text{dock}}} (y_{\text{dock}}^{\text{max}} - y_{\text{dock}}^j) y_{\text{free}}^j \left[1 + \frac{x^j - X}{X} H(V^j - T) \right] \\ \quad - \frac{1}{\tau_{\text{rel}}} y_{\text{dock}}^j \frac{x^j - X}{X} H(V^j - T). \end{array} \right. \quad (44)$$

τ_{dock} (resp. τ_{rec} , resp. τ_{rel}) represents the mean time to attach to the membrane (resp. to recover, resp. to release the vesicles). The maximal number of vesicles attached to the membrane is $y_{\text{dock}}^{\text{max}}$, and H is the Heaviside function such that $H(V^j - T)$ is equal to one during an action potential, and zero otherwise. The synaptic current $I_{\text{syn},j}$ is proportional to the amount of fused vesicles during an action potential (starting at time t_0): $i_{t_0}(t) = (y_{\text{dock}}^j(t) - y_{\text{dock}}^j(t_0))H(V^j - T)$, see eq. 44. For each neuron, I obtain a system of five equations, and through the synaptic current transmitted from one neuron to another, the system contains 400×5 paired equations. I observe that neurons synchronize, and the network expresses oscillatory pattern (Fig. 11), with a frequency that depends on the various parameters of the system. The model predicts that synaptic dynamics, based on facilitation and depression, and spontaneous neuronal activity can generate periodic bursting patterns within populations of neurons that match *in vitro* preparations (Fig. 9, Fig. 11), without the need for underlying neuronal rhythms.

The model was benchmarked against several key experimental studies of the preBötC. First, I tested the robustness of the model by depolarizing the resting membrane potential of the entire network. For this procedure, the model accounts

for several experimental observations, and was able to reproduce the experimentally measured periods and burst duration reported in [142]. Second, I studied the effect of deleting random neurons on the network activity, and observed a decrease in the rhythm period that matches the experimental slow-down of the rhythm in the face of cumulative lesion of constituent neurons reported in [72]. The third step was to investigate the consequences of gradually decreasing synaptic strength, which mimic the application of the AMPA receptor blocker NBQX. Our model nicely reproduced the slow-down of the rhythm observed in [136]. Finally, I determined the minimal number of stimulations for burst induction in my model, and found that stimulating few neurons were sufficient to trigger a burst, a result that is in keeping with the observed preBötC ability to evoke ectopic bursts via focal stimulation of a few constituent neurons [96]. The good performance of the model in all these procedures confirms that the interburst interval is controlled by recurrent excitations arising from the remaining spontaneous activity within the network.

My collaborators have tested several predictions of the model to quantify depression in the preBötC, and they revealed by electrophysiological recordings that synaptic facilitation and depression occurs at preBötC synapses on time-scales that influence rhythmic population activity. They showed that a balance of facilitation and depression contributes to oscillatory synaptic activity on time-scales and intensities that affects respiratory rhythm generation.

Organization of the thesis

This thesis is organized as follows:

Part I, Chapter 1-2 In chapter 1, I present a rapid overview of the main results about the NET/DST in two and three-dimensions, and a new computations for the DST in cusp-like geometry. In chapter 2, I present the computation for the DST in a particular cusp-like geometry, where the small target is a ribbon connecting a sphere tangent to a plan. I apply this result to model vesicular release probability in the pre-synaptic terminal.

Part II, Chapter 3 In chapter 3, I build a stochastic model of calcium dynamics in the presynaptic terminal that I coarse-grain into a Poissonian rate Model, and a Mass-action model coupled to a Markovian equations. A complete review about modeling calcium dynamic in neuronal microdomains is presented in appendix to Part II.

Part III, Chapter 4 In chapter 4, I present a model of an oscillatory neuronal network in the pre-Bötzinger Complex. This model predicts that the oscillations at the network level are driven by synaptic properties of the neurons. The model was tested against several conditions experienced by the network. Our predictions concerning the synaptic dynamic of the neurons were confirmed experimentally [112].

Abbreviations and notations

AP: Action Potential

AMPA: α -amino-3-hydroxy-5-methyl-4-isoxazolepropionic

AZ: Active Zone

BD: Burst Duration

BL: Boundary Layer

CP: Cycle Period

EPSC: Excitatory Post-Synaptic Current

eEPSC: evoked Excitatory Post-Synaptic Current

EPSP: Excitatory Post-Synaptic Potential

DST: Dire Strait Time

$H(\cdot)$: Heaviside function

HH: Hodgkin-Huxley

IBI: Inter-Burst Interval

MFPT: Mean First Passage Time

NBQX: 2,3-dihydroxy-6-nitro-7-sulfamoyl-benzo[f]quinoxaline-2,3-dione

NET: Narrow Escape Time

Abbreviations and notations

preBötC: pre-Bötzinger Complex

PSD: Post-synaptic density

RP: Recycling Pool

RRP: Readily Releasable Pool

SD: Synaptic Depression

SF: Synaptic Facilitation

SNARE: Soluble N-éthylmaleimide-sensitive-factor Attachment protein Receptor

VGCC: Voltage Gated Calcium Channels

XIIIn: Hyppoglossal nerve

Part I

Mathematical modeling of synapses at the molecular level

Chapter 1

Brownian search for targets hidden in cusp-like pockets: Progress and Applications

*Published in Guerrier C and Holcman D “Brownian search for targets hidden in cusp-like pockets: Progress and Applications” European Physical Journal ST **223**, pp 3273-3285 (2014)*

We report here recent progress in computing the search time for a stochastic particle to find a small target hidden in cusp-like pockets. The target is a small segment in dimension two, a small hole or a narrow ribbon in dimension three, placed at the end of a cusp. The asymptotic analysis of the diffusion equation reveals the role of the local geometry, and a mathematical difficulty comes from the boundary layer near the target. The methods are conformal mapping and matching asymptotic. We present applications in cell biology where cellular activation occurs when a diffusing particle finds a hidden site. This is the case during vesicular fusion initiated after a protein located between the vesicular and cell membranes binds to several diffusing calcium ions. Another example is a drug activation site located inside a deep molecular pocket. The analytical formulas clarify the role of small parameters.

1.1 Introduction

Finding a small hidden target by a protein, an ion or a molecule is ubiquitous in molecular and cellular biology, and it represents a key limiting step for activation of a cellular process. For example, proteins need to find active sites hidden in the interior of a larger molecular complex. This is the case for the hemoglobin or the penicillin-binding proteins, and many others where active sites are hidden inside in the complex organization of α and β -sheet structures. For the hemoglobin, a ligand, such as β -lactam antibiotic, has to bind to a small site hidden inside the molecule and indeed, ligand recognition requires that strands should be antiparallel in the active site area [123]. Another example where finding a small target is relevant in cell biology is the diffusion of molecules, RNAs or proteins between the mother

and the daughter cell during cell division [84]. The diffusion time is controlled by the arrival of Brownian particles to the cylindrical neck connecting the two cells and it determines the amount of molecules that will be exchanged between them. Interestingly, the mean time for a thin rod to turn in a narrow tube or for a protein to rotate in a thin two-dimensional band is also very long and characterizes a strand to become parallel or anti-parallel.

Contrary to freely accessible small targets, the mean time for a Brownian particle to reach a target located at a narrow cusp is much longer. Finding asymptotic expressions for such search times remains challenging numerically and analytically. Numerically, because it requires very long simulations, leading to many inaccuracies, and this is not even sufficient to guess asymptotic formulas. From an analytical point of view, the classical methods developed for the narrow escape problems do not apply [84, 85, 86].

We report recent progress about asymptotic computation of the mean time for a Brownian particle diffusing in a bounded domain to find a small hidden target located at a cusp geometry on the boundary, which otherwise reflects the particle (Fig. 1.1). This time is referred in the literature as the Dire Strait Time (DST) [82, 83] and differs from the classical narrow escape time (NET), which is the time for a diffusing particle to find a small site located on a smooth part of the boundary. A major difference between the DST and the NET is reflected in the method for computing asymptotically each search time. In both cases, this computation involves solving the Poisson equation with small Dirichlet and large Neumann parts: the NET methods are matched asymptotic [201, 202, 203] or Green's function [85], but these methods fail to compute the DST because the cusp creates a new boundary layer. For the DST, the method mixes asymptotic analysis and conformal mapping. Furthermore, the analysis in dimension three is possible when there are symmetries that allow the analysis to two dimensions. However in both searches, because they are rare events, the probability density function of the time spent $\bar{\tau}$ in a compartment prior to escape, in the limit of small target size, is dominated by a single exponential decay

$$p_{\bar{\tau}}(t) \sim \bar{\tau}^{-1} \exp\{-t/\bar{\tau}\}. \quad (1.1)$$

The exponential rate $\bar{\tau}^{-1}$ is therefore the flux into the absorbing target. This single exponential result allows coarse-graining microscopic model of reaction-diffusion into Markovian jump processes, where the rate is the flux on the absorbing boundary equal to the reciprocal of $\bar{\tau}$. This rate encompasses the entire geometry to a single parameter, and can be used to simplify detailed stochastic simulations of biological pathways by replacing long stochastic trajectories with Poissonian injection rate. Finally, the local shape of the target does matter for the search time, as revealed both by analytical and numerical methods [8, 9, 38, 66, 81]. For example, an elliptic versus circular disc changes the leading order of the search time, and the exit time to two tangent discs versus a single disc of similar surface is different [85].

This report is organized as follows: in section 1.2, we present several examples motivated by cellular biology in which computing the DST is a key to understand the role of small targets. In section 1.3, we present a general classification for targets hidden in cusps. We also discuss the case of an absorbing band at the cusp between

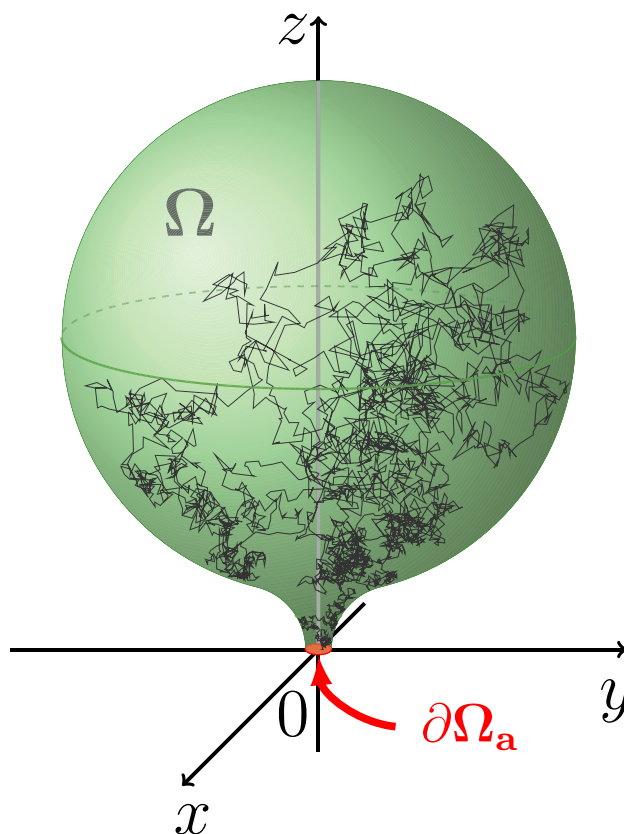


Figure 1.1: Schematic description of the exit search through a cusp.

a plane and a sphere (Fig. 1.2D).

1.2 Examples for the search of a hidden target in cellular and molecular biology

1.2.1 Mother-daughter cell

An intermediate stage during cell division consists of the asymmetric dumbbell shape (Fig. 1.2A) made between the mother and daughter cells, separated by a long connecting neck that can change over time. During this stage, some of the genetic material is transferred from the mother to the smaller daughter cell compartment. Diffusion through the cusps connecting the neck is the main determinant of the exchange rate and of the selection of fast diffusing particles during this transient regime [60]. Moreover, in the absence of any active mechanism, the back flow induced by diffusion from the daughter to the mother cell can be drastically slowed down, due to an asymmetry in the curvature of the connecting neck between cells. Thus the transition rates between the mother and the daughter can differ by several orders of magnitude as the geometry at the cusp changes. This asymmetrical diffusion effect can explain some of the findings reported experimentally in [60]: as the curvature at the connection between the cells and the neck varies over time, it changes the diffusion fluxes, as indicated by first passage time formulas that we shall

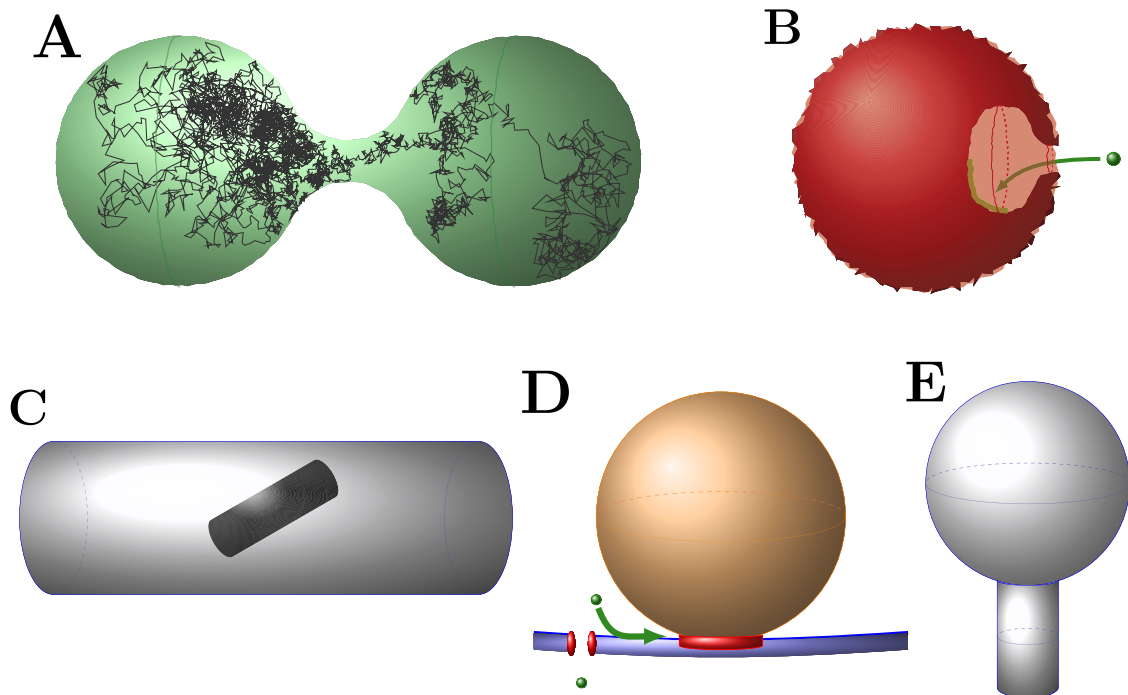


Figure 1.2: **Schematic cusp targets in cell biology characterized by the DST.** **A:** Model of diffusion between the mother and daughter cell through a cusp and narrow neck. **B:** Search by a molecule of a binding site, hidden in a cusp geometry. **C:** Rotation of a rod-like molecule in a cylindrical narrow domain. The rotation can only occur in an extreme position, representing a cusp in the phase space. **D:** The binding of several calcium ions (green) to a group of molecules located at the cusp (red) between the docked vesicle (orange) and the neuronal membrane (blue), induces vesicular release at the pre-synaptic terminal. **E:** The particular shape of the post-synaptic dendritic spine can be represented by a bulky head connected to a thin neck. Ions entering at the PSD on the top of the head escape the spine at the bottom of the neck.

describe below (see Eq. 1.18 and [84]). In conclusion, small asymmetric diffusion fluxes permit to isolate the mother from the daughter cells prior to reaching steady state. Had steady state diffusion been reached before the two cells separated, the probability density function of diffusing particles would be uniform in the domain, and the amount of particles in both cells would be proportional to their volumes.

1.2.2 Finding a binding site in a protein: The example of hemoglobin

Active sites of complex molecules, such as hemoglobin, can be hidden inside a complex molecular organization (Fig. 1.2B). To become activated, a ligand has to bind to a small site hidden inside the molecule and indeed, ligand recognition requires that strands are well positioned in the active site area. This phenomenon was observed for large antibiotic molecules such as the penicillin-binding proteins [123]: the catalytic funnel reveals an elongated binding cleft, where the active site is hidden. When the site can switch between an active and inactive state, the effective rate constant changes drastically [84].

1.2.3 Rotation of a needle in a confined band

A Brownian needle in a strip can model a stiff DNA fragment moving in a very confined chromatin structure. For example, under severe stress, the DNA of the bacterium *Deinococcus radiodurans*, the most radioresistant organism, undergoes a phase transition in reorganizing its genome into tightly packed toroids, which may facilitate DNA repair [119]. Three-dimensional analyses [120] reveal a complex network of double membranes that engulf the condensed DNA, suggesting that two-dimensional domains lying between parallel walls may play a significant role in DNA repair. The role of the distance between the parallel walls can be evaluated in the computation of the mean time for a needle to rotate in such environment (see Eq. 1.15). A similar example is a planar strip or a three dimensional cylinder: when a needle is only slightly shorter than the strip width, its turning around becomes a rare event, because there is not much room in the configuration space for the vertical position (Fig. 1.2C). Thus the computation of the mean time to turn around becomes a Dire Strait problem [85], which does not fall under the previously studied NET in planar geometry [85, 201, 202, 203, 66, 7, 30, 175].

1.2.4 Cusp activation between a vesicle and the pre-synaptic membrane of a neuron

Another illustration of cusp geometry that controls cellular processes from the molecular level is calcium diffusion near a vesicle located in the pre-synaptic terminal. Indeed calcium diffusion determines the probability of vesicular release (Fig. 1.2D), which should depend on the distance between the initial calcium entrance at channels and the docked vesicle position. Specifically, after ions enter the pre-synaptic terminal through calcium channels, they have to bind to specific proteins located at

the junction between the vesicle and the membrane that we shall modeled here as a ribbon (red in Fig. 1.2D). Interestingly, the probability of vesicular release can vary over six order of magnitude for the same synapse, a phenomenon that is still not clearly understood [106, 169]. The particular cusp geometry formed by the vesicle and the pre-synaptic membrane might be a key to resolve this drastic probability modulation [70].

1.3 Classification of the NET and DST in dimension two and three

1.3.1 Stochastic equation

A Brownian particle escapes through a narrow cusp located on the surface of a bounded domain Ω (see the example in Fig. 1.1). The motion is described by the stochastic equation

$$\dot{\mathbf{X}} = b(\mathbf{X}) + \sqrt{2\mathcal{D}}\dot{\mathbf{w}} \quad (1.2)$$

where b is the drift, \mathcal{D} is the diffusion coefficient and $\dot{\mathbf{w}}$ is white noise. We will consider $b = 0$ (for non-zero drift, new Non-Poissonian escape rates have recently been discussed in [37]). The DST $\bar{\tau}(\mathbf{x})$ for a particle starting at position \mathbf{x} is the solution of [173]

$$\begin{aligned} \mathcal{D}\Delta\bar{\tau}(\mathbf{x}) &= -1 \text{ for } \mathbf{x} \in \Omega \\ \frac{\partial\bar{\tau}}{\partial n}(\mathbf{x}) &= 0 \text{ for } \mathbf{x} \in \partial\Omega \setminus \partial\Omega_a \\ \bar{\tau}(\mathbf{x}) &= 0 \text{ for } \mathbf{x} \in \partial\Omega_a, \end{aligned} \quad (1.3)$$

where $\partial\Omega$ (resp. $\partial\Omega_a$) is the boundary (resp. the absorbing part of the boundary).

1.3.2 Dire strait formula in dimension 2

We now summarize classical results about the NET and DST from a domain Ω in the plane, for a small absorbing arc $\partial\Omega_a$ of length a of the boundary $\partial\Omega$. The ratio between the arclength of the absorbing boundary and the arclength of the entire boundary is a small parameter

$$\varepsilon = \frac{|\partial\Omega_a|}{|\partial\Omega|} = \frac{a}{|\partial\Omega|} \ll 1. \quad (1.4)$$

When $\partial\Omega_a$ is a sub-arc of a smooth boundary, the first order in ε of the NET from any point \mathbf{x} in Ω to $\partial\Omega_a$, denoted by $\bar{\tau}_{\mathbf{x} \rightarrow \partial\Omega_a}$, is independent of \mathbf{x} outside a small vicinity of $\partial\Omega_a$ (called a boundary layer), and we have

$$\bar{\tau}_{\mathbf{x} \rightarrow \partial\Omega_a} = \frac{|\Omega|}{\pi\mathcal{D}} \ln \frac{1}{\varepsilon} + O(1), \quad (1.5)$$

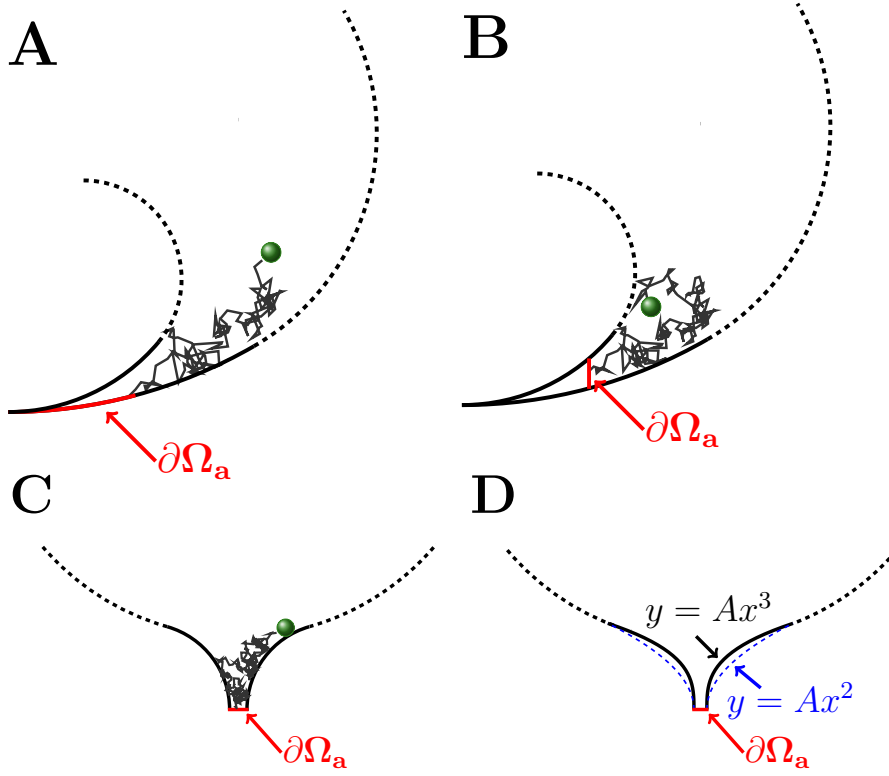


Figure 1.3: **Classification of cusp targets.** Target tangent **A**, perpendicular **B** and at the end **C** of a cusp. Changing the order of approximation of the cusp **D**.

where $O(1)$ depends on the initial distribution of \mathbf{x} [202, 175]. In particular, if Ω is a disc of radius R , then for \mathbf{x} at the center of the disc,

$$\bar{\tau}_{\mathbf{x} \rightarrow \partial\Omega_a} = \frac{R^2}{\mathcal{D}} \left[\ln \frac{\pi R}{a} + 2 \ln 2 + \frac{1}{4} + O(\varepsilon) \right], \quad (1.6)$$

and averaging with respect to a uniform distribution of \mathbf{x} in the disc [85]

$$\bar{\tau} = \frac{R^2}{\mathcal{D}} \left[\ln \frac{\pi R}{a} + 2 \ln 2 + \frac{1}{8} + O(\varepsilon) \right]. \quad (1.7)$$

Formula 1.5 indicates that the flux through a hole in a smooth wall on a flat membrane surface (e.g., a corral) is regulated by the following parameters: the area $|\Omega|$, the diffusion coefficient \mathcal{D} , and the aspect ratio ε (Eq. 1.4). This asymptotic formula can be used to estimate the residence time of a receptor inside the post-synaptic density, a main factor governing short-term synaptic plasticity [84].

For a Brownian motion on a sphere of radius R , described in the spherical coordinates (θ, ϕ) where $(x, y, z) = (R \sin \theta \cos \phi, R \sin \theta \sin \phi, R \cos \theta)$, the NET to an absorbing circle centered at the north-south axis ($\theta = 0$) near the south pole with a radius $a = R \sin \delta/2 \ll 1$, is given by

$$\bar{\tau}_{\mathbf{x} \rightarrow \partial\Omega_a} = \frac{2R^2}{\mathcal{D}} \ln \frac{\sin \frac{\theta}{2}}{\sin \frac{\delta}{2}}, \quad (1.8)$$

where $\delta \leq \theta \leq \pi$ [84]. Formula 1.8 can be used to estimate the rate of accumulation at one pole of proteins moving on the membrane surface during embryo development

[146] .

When the absorbing window in a plane is no longer on a smooth surface, but located at a corner of angle α , then ([85])

$$\bar{\tau}_{\mathbf{x} \rightarrow \partial\Omega_a} = \frac{|\Omega|}{\mathcal{D}\alpha} \left[\ln \frac{1}{\varepsilon} + O(1) \right]. \quad (1.9)$$

Formula 1.9 indicates that control of flux is regulated also by the access to the absorbing window afforded by the the angle of the corner leading to the window.

If the absorbing window is located at a cusp, then $\bar{\tau}_{\mathbf{x} \rightarrow \partial\Omega_a}$ grows algebraically, rather than logarithmically. In the domain bounded by two tangent circles (Fig. 1.3A), the lifetime is

$$\bar{\tau}_{\mathbf{x} \rightarrow \partial\Omega_a} = \frac{|\Omega|}{(d^{-1} - 1)\mathcal{D}} \left(\frac{1}{\varepsilon} + O(1) \right), \quad (1.10)$$

where $d < 1$ is the ratio of the radii [85]. Formula 1.10 indicates that a drastic reduction of flux can be achieved by putting an obstacle that limits the access to the absorbing window by forming a cusp-like passage. In addition, when $\partial\Omega_a$ is located at the end of a narrow neck with radius of curvature R_c (Fig. 1.3C-D), the DST is given in [84, 75] as

$$\bar{\tau}_{\mathbf{x} \rightarrow \partial\Omega_a} = \frac{\pi|\Omega|}{2\mathcal{D}\sqrt{a/R_c}} (1 + o(1)) \text{ for } a \ll |\partial\Omega|. \quad (1.11)$$

Formula 1.11 can be used to estimate the effective diffusion coefficient from a model of disk obstacles located on a lattice [84, 75].

The DST can also be computed on a surface of revolution generated by rotating a curve around an axis of symmetry. For example, the rotation of the curve in Fig. 1.3C around its axis of symmetry leads to a three dimensional domain similar to Ω in Fig. 1.1. We use the representation of the generating curve

$$y = r(x), \quad 0 < x < \Lambda$$

where the x -axis is horizontal with $x = \Lambda$ at the absorbing end \mathbf{AB} . We assume that the parts of the curve that generate the funnel have the form

$$\begin{aligned} r(x) &= O(\sqrt{|x|}) \text{ near } x = 0 \\ r(x) &= a + \frac{(x - \Lambda)^{1+\nu}}{\nu(1+\nu)\ell^\nu} (1 + o(1)) \text{ for } \nu > 0 \text{ near } x = \Lambda, \end{aligned} \quad (1.12)$$

where $a = \frac{1}{2}\overline{\mathbf{AB}}$ is the radius of the gap, and the constant ℓ has dimension of length. For $\nu = 1$ the parameter ℓ is the radius of curvature R_c at $x = \Lambda$. The DST from the head to the absorbing end \mathbf{AB} is given by the following algebraic decay [83]

$$\bar{\tau}_{\mathbf{x} \rightarrow \partial\Omega_a} \sim \frac{\mathcal{S}(\Lambda)}{2\mathcal{D}} \frac{\left(\frac{\ell}{(1+\nu)a} \right)^{\nu/(1+\nu)} \nu^{1/(1+\nu)}}{\sin \frac{\nu\pi}{1+\nu}}, \quad (1.13)$$

where \mathcal{S} is the entire unscaled area of the surface. In particular, for $\nu = 1$ the DST 1.13 reduces to

$$\bar{\tau}_{\mathbf{x} \rightarrow \partial\Omega_a} \sim \frac{\mathcal{S}}{4\mathcal{D}\sqrt{a/2\ell}}. \quad (1.14)$$

The case $\nu = 0$ corresponds to a conical funnel with an absorbing circle of small radius a (see [83]). For a sphere, Eq. 1.14 reduces to 1.8. Formulas 1.11–1.14 indicate that an efficient control of the flux can be achieved by putting the absorbing window at the end of a narrow symmetric or asymmetric funnel. This type of funnel can be formed by crowding obstacles on the membrane surface [75], which results in an effective coarse-grained diffusion coefficient on the surface, different from the microscopic diffusion coefficient. Finding the NET in the flat plane when the cusp locally behaves like $y(x) = Ax^\alpha + o(x^{\alpha+1})$ with $\alpha > 2$ remains an open problem (see Fig. 1.3C-D).

The turning around of a needle of length l confined to a planar strip which is only slightly wider (length l_0) than the length of the neck can be reduced to a two-dimensional DST problem through a funnel (see Fig. 1.2C and Sect. 1.2.3 for a specific description of biological motivations). The DST for the needle to turn 180° is given by [85]

$$\bar{\tau} = \frac{\pi(\pi/2 - 1)}{D_r l_0 \sqrt{\varepsilon}} \sqrt{\frac{D_X}{D_r}} (1 + O(\sqrt{\varepsilon})). \quad (1.15)$$

where $\varepsilon = \frac{l_0 - l}{l_0} \ll 1$, D_X is the longitudinal diffusion constant along the axis of the needle and D_r the rotational constant (see [71, 152, 153] for a specific description of the Brownian motion of anisotropic objects such as a needle in two dimensions). Formula 1.15 shows that when the free space between two planes decreases, the effective diffusion constant, proportional to the reciprocal of $\bar{\tau}$, experiences a second order phase transition characterized by a discontinuity of the derivative of the effective diffusion constant for the rotation. When the length l reaches and exceeds the critical value l_0 , the diffusion constant vanishes. This result explains the crucial role of the chromatin organization in maintaining the genome integrity after radiation. Another illustration of the DST can be found in the problem of diffusion escape from a dendritic spine membrane, or from cell during its division. Dendritic spines can be modeled as domains with a bulky head connected to an essentially one-dimensional strip (or cylinder) of small radius a and length L (Fig. 1.2E). The connection of the head (Ω_1) to the neck (Ω_2) can form either an angle or a smooth funnel. The boundary of the domain reflects Brownian trajectories and only the end of the cylinder $\partial\Omega_a$ absorbs them. In the three-dimensional case the Dirichlet boundary $\partial\Omega_a$ is a small absorbing disc at the end of the cylinder. The domain Ω_1 is connected to the cylinder at an interface $\partial\Omega_i$, which in this case is a circle. It was shown in [83] that the DST from $\mathbf{x} \in \Omega_1$ to $\partial\Omega_a$ is given by

$$\bar{\tau}_{\mathbf{x} \rightarrow \partial\Omega_a} = \bar{\tau}_{\mathbf{x} \rightarrow \partial\Omega_i} + \frac{L^2}{2\mathcal{D}} + \frac{|\Omega_1|L}{|\partial\Omega_a|\mathcal{D}}. \quad (1.16)$$

Formula 1.16 shows the role of the narrow neck in the diffusion flux regulation.

1.3.3 Dire strait formula in dimension 3

We recall now some known mean time asymptotic expressions for the NET in a three-dimensional domain Ω when the target is a circular absorbing window $\partial\Omega_a$ of radius a centered at $\mathbf{0}$ on the boundary $\partial\Omega$. It is given by [85]

$$\bar{\tau}_{\mathbf{x} \rightarrow \partial\Omega_a} = \frac{|\Omega|}{4a\mathcal{D}} \left[1 - \frac{L(\mathbf{0}) + N(\mathbf{0})}{2\pi} a \ln a + O(a) \right], \quad (1.17)$$

where $L(\mathbf{0})$ and $N(\mathbf{0})$ are the principal curvatures of the surface boundary at the center of the absorbing boundary $\partial\Omega_a$. The third order asymptotic expansion can be found on a sphere [27]. This formula is contrast with the DST asymptotics obtained for a target hidden in a three dimensional cusp. When the target is a small absorbing window $\partial\Omega_a$ of radius a located at the end of a funnel (Fig. 1.1), the asymptotics is

$$\bar{\tau}_{\mathbf{x} \rightarrow \partial\Omega_a} = \left(\frac{R}{a} \right)^{3/2} \frac{|\Omega|}{R\mathcal{D}} (1 + o(1)) \text{ for } a \ll R, \quad (1.18)$$

where the R is the radius of curvature of the rotated curve at the end of the funnel [83]. This formula corrects by a factor 1/2 the previous one reported in [84, 83]. The dependency in the radius of curvature at the cusp explains how geometry controls the diffusion flux from the mother to the daughter cell, as explained above in subsection 1.2.1. This asymptotics can also be used to estimate the search time for a hidden target inside a molecule (see Section 1.2.2)

Finally, the last asymptotic formula we shall present has application to estimate the probability of vesicular release at synapse for a model of calcium diffusion. The cusp-like geometry between a sphere and a surface (Section 1.2.4 and [70] and Fig. 1.2D). The two-dimensional projection near the cusp is represented in Fig. 1.3B. The DST a three-dimensional cusp, located at the end of a funnel when the absorbing cross section is perpendicular to the cusp is given by

$$\bar{\tau}_{\mathbf{x} \rightarrow \partial\Omega_a} = \frac{|\Omega|}{4\pi\mathcal{D}a} + O(1). \quad (1.19)$$

The absorbing boundary forms a small ribbon of height a with surface $S_{rib} = \sqrt{2 \frac{R_1 R_2}{|R_2 - R_1|}} a^{3/2}$ where R_1 and R_2 are the radii of curvature at the cusp. This result is presented below in subsection 1.3.5.

1.3.4 Derivation of the DST for a three-dimensional cusp located at the end of a funnel

We now present the main steps to compute the DST (formula 1.18) for a target located at the end of a cusp (Fig. 1.1). We use a conformal mapping to map the domain Ω that contains a small absorbing window $\partial\Omega_a$ of diameter a located at the end of the funnel, which is connected smoothly to a three dimensional ball. The radius of curvature at the funnel is R and the diffusion coefficient is \mathcal{D} . The symmetric cusp can be parameterized in cylindrical coordinates (ρ, z) (ρ is the distance to the $0z$ axis) by

$$\rho(z) = \frac{1}{R} z^2 + \frac{a}{2}, \quad (1.20)$$

for z small. In dimensionless variables $\mathbf{x} = R\mathbf{x}'$, $\bar{\tau}(\mathbf{x}) = u(\mathbf{x}')$, the domain Ω is mapped on Ω_{dless} , $\partial\Omega_a$ into $\partial\Omega_{\text{dless},a}$ and $|\Omega| = R^3|\Omega_{\text{dless}}|$, $a = R\epsilon$, $\mathcal{D} = R^2D$. The DST Eq. 1.4 becomes:

$$\begin{aligned} D\Delta u(\mathbf{x}') &= -1 \text{ for } \mathbf{x}' \in \Omega_{\text{dless}} \\ \frac{\partial u}{\partial n}(\mathbf{x}') &= 0 \text{ for } \mathbf{x}' \in \partial\Omega_{\text{dless}} \setminus \partial\Omega_{\text{dless},a} \\ u(\mathbf{x}') &= 0 \text{ for } \mathbf{x}' \in \partial\Omega_{\text{dless},a}, \end{aligned} \quad (1.21)$$

In cylindrical coordinates (ρ, ψ, z) , due to symmetry, the equation reduces to

$$\begin{aligned} \frac{\partial^2 u}{\partial \rho^2} + \frac{1}{\rho} \frac{\partial u}{\partial \rho} + \frac{\partial^2 u}{\partial z^2} &= -\frac{1}{D} \text{ for } (\rho, z) \in \Omega_{\text{dless}} \\ \frac{\partial u}{\partial n}(\rho, z) &= 0 \text{ for } (\rho, z) \in \partial\Omega_{\text{dless}} \setminus \partial\Omega_{\text{dless},a} \\ u(\rho, z) &= 0 \text{ for } (\rho, z) \in \partial\Omega_{\text{dless},a}. \end{aligned} \quad (1.22)$$

Using Mobius mapping

$$f(\xi) = \frac{\xi - \alpha_\epsilon}{\xi + \alpha_\epsilon}, \quad (1.23)$$

where $\xi = \rho + iz$, we map the two-dimensional domain $\Omega_{2D} = \Omega_{\text{dless}} \cap \{\psi = 0\}$ into Γ (Fig. 1.4), where $\alpha_\epsilon = \sqrt{\epsilon(1 + \epsilon/4)}$. The domain Ω_{2D} is thus mapped into two concentric circles, and the absorbing part of the boundary $\partial\Omega_{2D,a}$ into the segment $\partial\Gamma_a = [-1; -1 + \sqrt{\epsilon}]$ of length $\sqrt{\epsilon}$. The cusp is mapped on a narrow hot-dog shaped domain, and the other part of the domain is mapped on a small region, located at angle $O(\sqrt{\epsilon})$ (Fig. 1.4). Eq. 1.22 becomes in polar coordinates $\omega = r e^{i\theta} = f(\xi)$ with

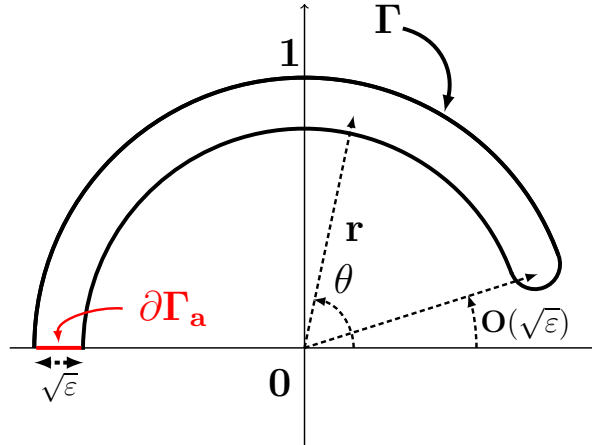


Figure 1.4: **Mapped Domain.** The two-dimensional projection Ω_{2D} of domain Ω_{dless} (dimensionless domain coming from Ω , Fig. 1.1) is mapped through the Mobius function $f(\xi) = \frac{\xi - \alpha_\epsilon}{\xi + \alpha_\epsilon}$ into Γ .

$$v(r, \theta) = u(f^{-1}(\omega)),$$

$$\frac{|1 - \omega|^4}{4\alpha_\epsilon^2} \Delta v + \frac{|1 - \omega|^2}{\alpha_\epsilon(1 - |\omega|^2)} \left[\frac{\partial v}{\partial r} \frac{\partial r}{\partial \rho} + \frac{\partial v}{\partial \theta} \frac{\partial \theta}{\partial \rho} \right] = -\frac{1}{D} \text{ for } (r, \theta) \in \Gamma. \quad (1.24)$$

To solve Eq. 1.24 in Γ , we proceed as in [75] and neglect the variation in the r -variable, because $r = 1 + O(\sqrt{\epsilon})$ and thus $v(r, \theta) \approx v(\theta)$ with absorbing boundary condition at π ($v(\pi) = 0$) and a boundary reflection is imposed on the upper part ($v'(c\sqrt{\epsilon}) = 0$), where the constant $c = O(1)$. We find

$$v''(\theta) + \frac{\sin(\theta)}{\cos(\theta) - 1} v'(\theta) = -\frac{\alpha_\epsilon^2}{D(\cos(\theta) - 1)^2}. \quad (1.25)$$

which is solved as [70]

$$v(\theta) = \frac{|\Omega_{\text{dless}}|}{D\pi\epsilon\sqrt{\epsilon}} (\sin(\theta) + \pi - \theta) + \frac{\alpha_\epsilon^2}{15D} \left[2 \ln \left(\frac{1 - \cos(\theta)}{2} \right) - 2(1 + \cos(\theta)) + \frac{3}{\cos(\theta) - 1} - \frac{3}{2} \right], \quad (1.26)$$

where $\alpha_\epsilon^2 = O(\epsilon)$. Thus, the mean first passage time $\bar{\tau}_{\mathbf{x} \rightarrow \partial\Omega_a}$ from a point \mathbf{x} inside the domain Ω located outside of the cusp to the absorbing target is obtained by placing the initial point at the angle $\theta = c\sqrt{\epsilon}$ in Eq. 1.26. We obtain

$$\bar{\tau}_{\mathbf{x} \rightarrow \partial\Omega_a} = \frac{|\Omega|\sqrt{R}}{\mathcal{D}a\sqrt{a}} + O(1), \quad (1.27)$$

where R is the curvature at the cusp, \mathcal{D} is the diffusion coefficient and $|\Omega|$ is the total volume of the domain. This formula corrects by a factor 2 the asymptotic expansion for the DST derived in [84, 85, 83].

1.3.5 Dire strait to a ribbon

To model the probability and the mean time for an ion to find a small target located between a membrane and a vesicle (Fig. 1.2D and Sects. 1.2.4 and 1.3.4), we approximate the local geometry by two tangent balls of radii R_1 and R_2 ($R_1 \ll R_2$). We summarize here recent progress on computing the escape time for a Brownian particle to a small ribbon, which consists of a cylinder with small height $a \ll 1$, located between the two spheres (see Fig. 1.2D and Fig. 1.3B for two-dimensional projection). In that context, the classical narrow escape results presented in the above sections do not apply. Using the symmetry of the domain, the analysis can be reduced to two-dimensions. In projection, the absorbing ribbon consists of a segment ($\partial\Omega_a$) joining the two discs (see Fig. 1.3B). Equation 1.4 in cylindrical coordinates (r, z) becomes

$$\begin{aligned} \frac{\partial^2 \bar{\tau}}{\partial r^2}(r, z) + \frac{1}{r} \frac{\partial \bar{\tau}}{\partial r}(r, z) + \frac{\partial^2 \bar{\tau}}{\partial z^2}(r, z) &= -\frac{1}{\mathcal{D}} \text{ for } (r, z) \in \Omega \\ \frac{\partial \bar{\tau}}{\partial n}(r, z) &= 0 \text{ for } (r, z) \in \partial\Omega \setminus \partial\Omega_a \\ \bar{\tau}(r, z) &= 0 \text{ for } (r, z) \in \partial\Omega_a. \end{aligned} \quad (1.28)$$

It is possible to obtain an analytical solution using the inversion mapping $\omega = f(\xi) = 1/\xi$ where $\xi = r + iz$ [70],

$$\bar{\tau}(r, z) = \frac{|\Omega|}{4\pi\mathcal{D}a} \left(1 - 2Ra \left(\frac{r}{r^2 + z^2} \right)^2 \right), \quad (1.29)$$

where $R = \frac{R_1 R_2}{R_2 - R_1}$. The DST is the mean first passage time $\bar{\tau}_{\mathbf{x} \rightarrow \partial\Omega_a}$ estimated for $r = 0$ in Eq. 1.29:

$$\bar{\tau}_{\mathbf{x} \rightarrow \partial\Omega_a} = \frac{|\Omega|}{4\pi\mathcal{D}a} + O(1). \quad (1.30)$$

This result is quite surprising: the leading order term does not depend on the curvature at the cusp and diverges like $\frac{1}{a}$, which is the divergence behavior obtained for a small circular hole. However, the difference is the surface of the ribbon equals to $S_{rib}(a) = \sqrt{2Ra}^{3/2}$.

1.4 Conclusion

We have summarized here results about the DST, which is the search time by a Brownian particle of a small target hidden in a cusp. These analytical formulas reveal the role of the local geometrical structure at a molecular level, and show the role of small parameters in controlling diffusion fluxes.

The computation of the DST for cusps of arbitrary shapes remains difficult and very few results exist so far. The presented formulas can be extended in some cases when a drift term is added [37], but in most cases it remains open. The drift term can account for both passive hydrodynamics flow or active transport, such as cargos transported by motors along microtubules. It can also represent the statistical transport driven by electro-diffusion forces.

Chapter 2

Search time for a small ribbon and application to vesicular release at neuronal synapses

*Published in Guerrier C and Holcman D “Search time for a small ribbon and application to vesicular release at neuronal synapses” SIAM MMS, **13(4)**, pp 1173-1193 (2015) (2015)*

The arrival of a Brownian particle at a narrow cusp located underneath a ball is a model of vesicular release at neuronal synapses, triggered by calcium ions. The asymptotic computation of the arrival time presents several difficulties that can be overcome using conformal mappings and asymptotic analysis of the model equations. Using a regular expansion of the solution of the Laplace equation in the mapped domain, we compute the solution involving both small and large spatial scales. We derive novel asymptotic formulas for Brownian escape through cusps in both two and three dimensions. The range of validity of the asymptotic formulas is challenged by stochastic simulations. Finally, we apply the analysis to estimate the vesicular release probability at pre-synaptic terminals and in particular, we suggest that vesicular organization imposes a severe constraint on calcium channel localization: diffusing calcium ions can trigger vesicular release only in a specific range of positions that we provide.

2.1 Introduction

The search time by a Brownian particle, for a small target hidden inside a narrow cusp, is usually much longer than for a freely accessible target located on a smooth surface. This difference in time is quantified by the mean first passage times [83, 84, 85]. Asymptotic expressions are difficult to obtain due to geometrical difficulties that cannot be resolved by classical methods [203, 85, 114, 154]. This situation is however ubiquitous in cell biology: it can represent the search for an active site located inside a complex protein, or for an ensemble of interacting proteins located between circumvolved membranes. For example, a key step in synaptic transmission between neurons is the release of a vesicle from the pre-synaptic terminal [54, 97, 127,

145, 211]. This event is triggered by calcium ions entering through voltage-gated channels [97]. Although the detailed mechanism of this process remains unclear, a key molecular step is the binding of the diffusing calcium ions to specific proteins such as synaptotagmin, located between the membranes of the docked vesicle and the synaptic terminal. Vesicular release has also been investigated using stochastic numerical simulations [33, 127, 129, 177, 63].

Interestingly, the probability of vesicular release varies over six orders of magnitude for some synapses [106, 169], the exact mechanism of which remains elusive. To investigate the possible mechanism underlying this large range of modulation, we build here a diffusion model to estimate the time for diffusing particles (calcium ions) to find hidden small targets (proteins). We study the effect of several parameters on the search time, such as the initial position of the channels, the size, and the position of the activating molecules. A random particle searching for a small

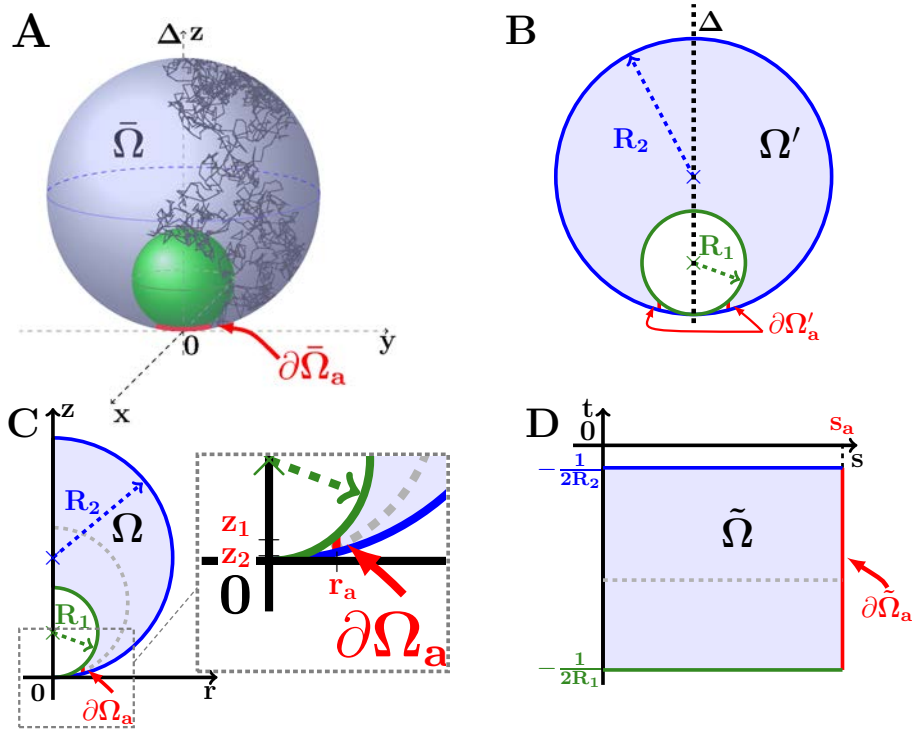


Figure 2.1: **Search in a cusp.** **A:** A Brownian trajectory is reflected on the boundary of two tangent spheres (blue and green) until it finds a small ribbon target (red). The ribbon is a small cylinder that connects the two tangent spheres. **B:** Two-dimensional projection of the ribbon target: the domain Ω' is obtained by projecting the three-dimensional domain $\bar{\Omega}$ in a plane containing the Δ -axis. **C-D:** Conformal mapping of the domain Ω into $\tilde{\Omega}$. The map is $\omega = f(\xi) = 1/\xi$. Circles of radius a centered in $(0, a)$ are mapped into straight lines of ordinate $t = -1/2a$: the gray dashed circle in **C** is transformed into a line in **D**.

target is a Dire Strait Time (DST) problem, as described in [75, 83, 84, 85]. The principle of computing the DST relies on solving a mixed boundary value problem for the Laplace equation with a geometrical cusp at the boundary. The present method combines asymptotic expansion of the solution and conformal mapping to

2.2. Search for a small two-dimensional cusp located between two tangent spheres

resolve the cusp singularity. Once the cusp singularity is de-singularized, we compute the solution by a regular matching asymptotic expansion for the inner (inside the cusp) and outer solution. Using symmetries in dimension three, the analysis can be reduced to two dimensions, allowing again the use of conformal maps. We apply this procedure several times and derive asymptotic expansions for the search time in two and three dimensions. The parameter getting asymptotically smaller here is the size of the small target (size of the binding molecule). One of the most striking results we obtained here is formula (2.39). This formula gives the DST of a Brownian particle to a small ribbon that connects a ball and its tangent plane (FIG. 2.1A):

$$\langle \tau \rangle = \frac{|\bar{\Omega}|}{4\pi D\varepsilon}, \quad (2.1)$$

where $|\bar{\Omega}|$ is the volume of the domain and D is the diffusion coefficient. ε is the height of the ribbon whose surface is $S_{rib} = 2\pi\sqrt{2R}\varepsilon^{3/2}$, where R is the radius of ball. This formula is valid for a general domain, as long as the cusp geometry is preserved.

The manuscript is organized as follows: in section 2.2, we compute the escape time when the target is a narrow absorbing band at a cusp located between a plane and a sphere. We solve the Laplace equation with Dirichlet boundary conditions at the cusp and reflecting conditions otherwise. We use a Möbius transformation to map the domain into a rectangle, and derive formula in dimensions two and three. The range of validity of the asymptotic formulas is investigated using Brownian simulations. In the third and final section, we apply the asymptotic method to estimate the spread of calcium ions near vesicles in the pre-synaptic terminal. We relate the probability of vesicular release to the distance of calcium channels in a model of square lattice vesicle organization. We also estimate the rate of arrival for calcium ions to small protein sites, involved in triggering vesicular release. Finally, we discuss consequences of clustering channels near vesicles. In the appendix, we compute the Brownian escape time when the target is at the end of a three-dimensional cusp in a funnel-shaped domain. The Möbius transformation maps the domain into a banana shape domain. The final asymptotic formula corrects by a factor 2 the previous one, derived in [83].

2.2 Search for a small two-dimensional cusp located between two tangent spheres

A Brownian particle is described by the stochastic equation

$$\dot{\mathbf{X}} = \sqrt{2D}\dot{\mathbf{w}} \quad (2.2)$$

where D is the diffusion coefficient and $\dot{\mathbf{w}}$ is white noise.

The Brownian search for a small target, located between an almost flat line and a circle membrane corresponds to an escape through a narrow cusp in a two dimensional bounded domain (Ω' , FIG. 2.1B). The domain Ω' lies between two tangent

disks of radii R_1 and R_2 ($R_1 \ll R_2$). The target is the two segments of length ε ($\varepsilon \ll R_1$) joining the two disks ($\partial\Omega'_a$ (red) in FIG. 2.1B). The axial symmetry along Δ (FIG. 2.1B) allows to reduce the domain Ω' to the half-domain Ω (FIG. 2.1C). To estimate the escape time in the two-dimensional domain Ω , we solve the boundary value problem

$$\begin{aligned} D\Delta u(\mathbf{x}) &= -1 \text{ for } \mathbf{x} \in \Omega \\ \frac{\partial u}{\partial n}(\mathbf{x}) &= 0 \text{ for } \mathbf{x} \in \partial\Omega \setminus \partial\Omega_a \\ u(\mathbf{x}) &= 0 \text{ for } \mathbf{x} \in \partial\Omega_a, \end{aligned} \quad (2.3)$$

using the conformal mapping

$$f(\xi) = \frac{1}{\xi} = \omega, \quad (2.4)$$

which maps the cusp region into a rectangular domain. The coordinate $\xi = r + iz$ is transformed into $\omega = s + it$ while the domain Ω is mapped into $\tilde{\Omega}$ (FIG. 2.1D). The boundary of Ω is mapped as follows: the green and blue half-circles are mapped onto horizontal lines (same colors in FIG. 2.1C-D) located at $t_1 = -1/(2R_1)$ and $t_2 = -1/(2R_2)$ respectively. The z -axis is mapped onto itself (black). The absorbing boundary is parameterized by

$$\partial\Omega_a = \{(r_a, z) | r_a = \sqrt{2R\varepsilon}(1 + o(1)) \text{ and } z_1 \leq z \leq z_2\}, \quad (2.5)$$

where $R = R_1R_2/(R_2 - R_1)$ and

$$z_1 = \frac{R_2}{R_2 - R_1}\varepsilon(1 + o(1)) \quad (2.6)$$

$$z_2 = \frac{R_1}{R_2 - R_1}\varepsilon(1 + o(1)). \quad (2.7)$$

The points $P_1 = (r_a, z_1)$ and $P_2 = (r_a, z_2)$ are mapped into

$$f(r_a + iz_1) = \frac{1}{\sqrt{2R\varepsilon}}(1 + o(\sqrt{\varepsilon})) - i\frac{1}{2R_1} \quad (2.8)$$

$$f(r_a + iz_2) = \frac{1}{\sqrt{2R\varepsilon}}(1 + o(\sqrt{\varepsilon})) - i\frac{1}{2R_2}. \quad (2.9)$$

Hence, the absorbing boundary is mapped at the first order on a straight vertical line located at

$$s_a = \frac{1}{\sqrt{2R\varepsilon}} = \frac{1}{\sqrt{\varepsilon}}. \quad (2.10)$$

2.2.1 Asymptotic computation of the mean time in two dimensions

To map the boundary value problem eq. (2.3), we set $u(\xi) = v(\omega)$, and we have $\Delta u(\xi) = |f'(\xi)|^2 \Delta v(\omega)$. Because $f'(\xi) = -\frac{1}{\xi^2}$ and $|f'(f^{-1}(\omega))|^2 = |\omega|^4$, equa-

2.2. Search for a small two-dimensional cusp located between two tangent spheres

tion (2.3) is transformed into

$$\begin{aligned} |\omega|^4 \Delta v(\omega) &= -\frac{1}{D} \text{ for } \omega \in \tilde{\Omega} \\ \frac{\partial v}{\partial n}(\omega) &= 0 \text{ for } \omega \in \partial\tilde{\Omega} \setminus \partial\tilde{\Omega}_a \\ v(\omega) &= 0 \text{ for } \omega \in \partial\tilde{\Omega}_a. \end{aligned} \quad (2.11)$$

To determine the solution, we scale the variable $\zeta = \frac{s}{s_a} = s\sqrt{2R\varepsilon}$ and derive an equation for $Y(\zeta, t) = v(\omega)$ for which eq. (2.11) becomes

$$\begin{aligned} \left(\frac{\zeta^2}{\tilde{\varepsilon}} + t^2\right)^2 \left(\tilde{\varepsilon} \frac{\partial^2 Y}{\partial \zeta^2}(\zeta, t) + \frac{\partial^2 Y}{\partial t^2}(\zeta, t)\right) &= -\frac{1}{D} \text{ for } (\zeta, t) \in [0, 1] \times \left[\frac{-1}{2R_2}, \frac{-1}{2R_1}\right] \\ \frac{\partial Y}{\partial t}\left(\zeta, -\frac{1}{2R_1}\right) = \frac{\partial Y}{\partial t}\left(\zeta, -\frac{1}{2R_2}\right) &= \frac{\partial Y}{\partial \zeta}(0, t) = 0 \\ Y(1, t) &= 0. \end{aligned} \quad (2.12)$$

A regular expansion of Y in power of $\tilde{\varepsilon} = 2R\varepsilon$ is

$$Y(\zeta, t) = Y_0(\zeta, t) + \tilde{\varepsilon} Y_1(\zeta, t) + \tilde{\varepsilon}^2 Y_2(\zeta, t) + \dots \quad (2.13)$$

and gives in equation (2.12)

$$\begin{aligned} &\frac{\zeta^4}{\tilde{\varepsilon}^2} \frac{\partial^2 Y_0}{\partial t^2}(\zeta, t) + \frac{1}{\tilde{\varepsilon}} \left(\zeta^4 \frac{\partial^2 Y_1}{\partial t^2}(\zeta, t) + \zeta^4 \frac{\partial^2 Y_0}{\partial \zeta^2}(\zeta, t) + 2\zeta^2 t^2 \frac{\partial^2 Y_0}{\partial t^2}(\zeta, t) \right) \\ &+ \left(\zeta^4 \frac{\partial^2 Y_1}{\partial \zeta^2}(\zeta, t) + t^4 \frac{\partial^2 Y_0}{\partial t^2}(\zeta, t) + \zeta^4 \frac{\partial^2 Y_2}{\partial t^2}(\zeta, t) + 2\zeta^2 t^2 \frac{\partial^2 Y_0}{\partial \zeta^2}(\zeta, t) + 2\zeta^2 t^2 \frac{\partial^2 Y_1}{\partial t^2}(\zeta, t) + \frac{1}{D} \right) \\ &= O(\tilde{\varepsilon}). \end{aligned}$$

The leading order $O(\varepsilon^{-2})$ is

$$\frac{\partial^2 Y_0}{\partial t^2}(\zeta, t) = 0, \quad (2.14)$$

hence using the boundary conditions in eq. (2.13), we obtain that Y_0 is independent of t . The second order term $O(\varepsilon^{-1})$ gives the equation:

$$\zeta^4 \frac{\partial^2 Y_1}{\partial t^2}(\zeta, t) + \zeta^4 \frac{\partial^2 Y_0}{\partial \zeta^2}(\zeta) = 0. \quad (2.15)$$

Integrating this equation over t between $-\frac{1}{2R_1}$ and $-\frac{1}{2R_2}$ and using the boundary condition in (2.13), we obtain:

$$\frac{\partial^2 Y_0}{\partial \zeta^2}(\zeta) = 0, \quad (2.16)$$

and thus, $Y_0(\zeta) = A\zeta + B$, where A and B are two constants. Using the absorbing boundary condition in (2.13), $Y_0(\zeta) = A(\zeta - 1)$ and finally

$$v(s, t) = A \left(1 - s\sqrt{2R\varepsilon}\right). \quad (2.17)$$

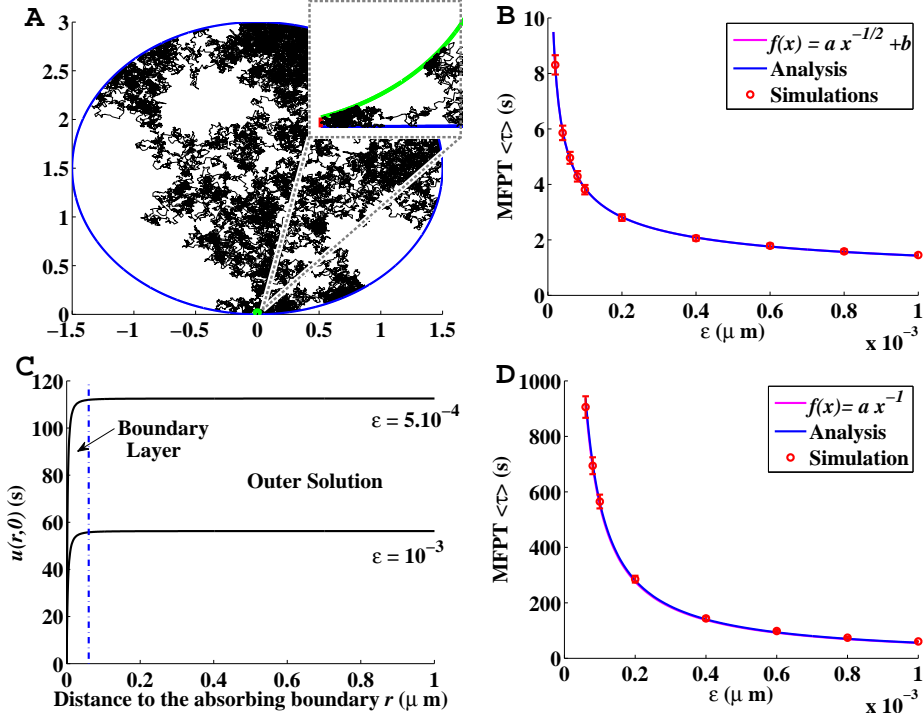


Figure 2.2: **Brownian statistics for the escape time at a narrow cusp.** **A**: Example of Brownian trajectory in Ω' , with parameters $R_1 = 0.02 \mu\text{m}$, $R_2 = 1.5 \mu\text{m}$, $\varepsilon = 0.001 \mu\text{m}$, $D = 20 \mu\text{m}^2 \cdot \text{s}^{-1}$. The square is a magnification of the trajectory near the cusp. **B**: Mean escape time (2000 runs) (red, \pm confident interval 95 %), optimal matlab fit (magenta) and the analytical formula (blue) in two-dimension, for ε between 2.10^{-5} and 1.10^{-3} , (same parameters as in **A**). The fitting coefficients are $a = 35.59 10^{-3}$ and $b = 305.6 10^{-3}$ (Adjusted R-square: 0.9996) compared to the analytical estimation $a = 35.57 10^{-3}$. The term $O(1)$ is $307.3 10^{-3}$. **C**: The solution $u(r,0)$ in the initial three-dimensional domain with $\varepsilon = 0.0005$ (top) and 0.001 (bottom). The parameters are similar to **A**. There are two main regions: the boundary layer and the outer region. **D**: Same as **B** for the three-dimensional domain. The fitting coefficient is $a = 55.24 10^{-3}$ (Adjusted R-square: 0.9992), compared to the analytical estimate $a = 56.24 10^{-3}$.

2.2. Search for a small two-dimensional cusp located between two tangent spheres

To determine the constant A , we use the compatibility condition obtained by integrating (2.3):

$$-\frac{|\Omega|}{D} = \int_{\Omega} \Delta u(\mathbf{x}) d\mathbf{x} = \int_{\partial\Omega_a} \frac{\partial u(\mathbf{y})}{\partial \mathbf{n}} dS_{\mathbf{y}}. \quad (2.18)$$

The normal derivative is

$$\left. \frac{\partial u}{\partial \mathbf{n}} \right|_{\partial\Omega_a} = -\left. \frac{\partial u}{\partial r} \right|_{\partial\Omega_a} = -\left. \frac{\partial s}{\partial r} \frac{\partial v}{\partial s} \right|_{\partial\bar{\Omega}_a} = -\frac{A\sqrt{2R\varepsilon}}{2R\varepsilon} (1 + O(\varepsilon)) = -\frac{A}{\sqrt{2R\varepsilon}} (1 + O(\varepsilon)).$$

Thus with eq. (2.18), we get

$$\frac{|\Omega|}{D} = \int_{\partial\Omega_a} \frac{A}{\sqrt{2R\varepsilon}} dS = \varepsilon \frac{A}{\sqrt{2R\varepsilon}} \quad (2.19)$$

which gives

$$A = \frac{\sqrt{2R}|\Omega|}{D\sqrt{\varepsilon}}, \quad (2.20)$$

and finally,

$$v(s, t) = \frac{\sqrt{2R}|\Omega|}{D\sqrt{\varepsilon}} (1 - s\sqrt{2R\varepsilon}). \quad (2.21)$$

We conclude that the escape time is

$$u(r, z) = \frac{\sqrt{2R}|\Omega|}{D\sqrt{\varepsilon}} \left(1 - \frac{r}{r^2 + z^2} \sqrt{2R\varepsilon} \right), \quad (2.22)$$

where the leading order term is

$$\langle \tau \rangle = \frac{\sqrt{2R}|\Omega|}{D\sqrt{\varepsilon}} (1 + o(1)) = \frac{\sqrt{2R}|\Omega|}{2D\sqrt{\varepsilon}} (1 + o(1)). \quad (2.23)$$

This analytical result is valid in a large range, as shown using Brownian simulations (FIG. 2.2A-B): the analytical curve (blue) is compared to Brownian simulation results (red) and a fitted approximation ($f(x) = \frac{a}{x}$) (magenta).

2.2.2 A three-dimensional escape to a narrow ribbon

In three dimensions, the domain $\bar{\Omega}$ is obtained by rotating Ω' around the axis Δ (FIG. 2.1A-B). We solve eq. (2.3) in domain $\bar{\Omega}$, where the absorbing boundary is the ribbon of height ε , located between the two spheres. In cylindrical coordinates (r, θ, z) , the domain $\bar{\Omega}$ is invariant in θ . Integrating eq. (2.3) according to θ reduces the problem to a two dimensional one in Ω :

$$\begin{aligned} \frac{\partial^2 u}{\partial r^2}(r, z) + \frac{1}{r} \frac{\partial u}{\partial r}(r, z) + \frac{\partial^2 u}{\partial z^2}(r, z) &= -\frac{1}{D} \text{ for } (r, z) \in \Omega \\ \frac{\partial u}{\partial \mathbf{n}}(r, z) &= 0 \text{ for } (r, z) \in \partial\Omega \setminus \partial\Omega_a \\ u(r, z) &= 0 \text{ for } (r, z) \in \partial\Omega_a. \end{aligned} \quad (2.24)$$

The inversion $\omega = f(\xi) = 1/\xi$ sends the coordinate system $\xi = (r, z)$ into $\omega = (s, t)$, where

$$r = \frac{s}{s^2 + t^2}, \quad z = -\frac{t}{s^2 + t^2}, \quad (2.25)$$

and

$$\frac{\partial s}{\partial r}(s, t) = t^2 - s^2 \quad \text{and} \quad \frac{\partial t}{\partial r}(s, t) = 2st. \quad (2.26)$$

In $\tilde{\Omega}$, we set $u(\xi) = v(\omega)$ and eq. (2.24) becomes

$$\begin{aligned} (s^2 + t^2)^2 \Delta v(s, t) &+ \frac{s^2 + t^2}{s} \left(\frac{\partial s}{\partial r} \frac{\partial v}{\partial s}(s, t) + \frac{\partial t}{\partial r} \frac{\partial v}{\partial t}(s, t) \right) \\ &= -\frac{1}{D} \quad \text{for } (s, t) \in \tilde{\Omega} \\ \frac{\partial v}{\partial n}(s, t) &= 0 \quad \text{for } (s, t) \in \partial\tilde{\Omega} \setminus \partial\tilde{\Omega}_a \\ v(s, t) &= 0 \quad \text{for } (s, t) \in \partial\tilde{\Omega}_a. \end{aligned} \quad (2.27)$$

The structure of the solution is similar to the one of section (2.2.1): it is composed of a inner layer near the absorbing boundary $s = s_a$, and an outer solution far away. The scaling variable $\zeta = \frac{s}{s_a}$, $s_a = \frac{1}{\sqrt{2R\varepsilon}} = \frac{1}{\sqrt{\varepsilon}}$, and $Y(\zeta, t) = v(s, t) = v(\frac{\zeta}{\sqrt{2R\varepsilon}}, t)$ can be used in the entire domain. The scaled equation becomes

$$\begin{aligned} &\left(\frac{\zeta^2}{\varepsilon} + t^2 \right)^2 \left(\varepsilon \frac{\partial^2 Y}{\partial \zeta^2}(\zeta, t) + \frac{\partial^2 Y}{\partial t^2}(\zeta, t) \right) \\ &+ \frac{\frac{\zeta^2}{\varepsilon} + t^2}{\zeta} \left((t^2 - \frac{\zeta^2}{\varepsilon}) \varepsilon \frac{\partial Y}{\partial \zeta}(\zeta, t) + 2\zeta t \frac{\partial Y}{\partial t}(\zeta, t) \right) = -\frac{1}{D}. \end{aligned} \quad (2.28)$$

We look for a solution using a regular expansion

$$Y(\zeta, t) = Y_0(\zeta, t) + \varepsilon Y_1(\zeta, t) + \varepsilon^2 Y_2(\zeta, t) + \dots \quad (2.29)$$

which transforms equation (2.28) into

$$\frac{1}{\varepsilon^2} \left[\zeta^4 \frac{\partial^2 Y_0}{\partial t^2} \right] + \frac{1}{\varepsilon} \left[\zeta^4 \frac{\partial^2 Y_1}{\partial t^2} + \zeta^4 \frac{\partial^2 Y_0}{\partial \zeta^2} + 2\zeta^2 t^2 \frac{\partial^2 Y_0}{\partial t^2} - \zeta^3 \frac{\partial Y_0}{\partial \zeta} + 2\zeta^2 t \frac{\partial Y_0}{\partial t} \right] = O(1).$$

The first order in $O(\varepsilon^{-2})$ is

$$\zeta^4 \frac{\partial^2 Y_0}{\partial t^2} = 0, \quad (2.30)$$

and using the boundary conditions in (2.27), we find that Y_0 is independent of t . At order $O(\varepsilon^{-1})$, we get

$$\zeta^4 \frac{\partial^2 Y_1(\zeta, t)}{\partial t^2} + \zeta^4 \frac{\partial^2 Y_0(\zeta)}{\partial \zeta^2} - \zeta^3 \frac{\partial Y_0(\zeta)}{\partial \zeta} = 0. \quad (2.31)$$

2.2. Search for a small two-dimensional cusp located between two tangent spheres

Integrating over t , and using the boundary conditions in (2.27), we obtain

$$\zeta^4 \frac{\partial^2 Y_0}{\partial \zeta^2} - \zeta^3 \frac{\partial Y_0}{\partial \zeta} = 0. \quad (2.32)$$

It follows that $Y_0(\zeta) = A\zeta^2 + B$ where A and B are two constants. Using the absorbing boundary condition in (2.27), we get $Y_0(\zeta) = A(1 - \zeta^2)$. To conclude, the leading order approximation depends on the s -variable only and

$$v(s) = A(1 - 2R\varepsilon s^2). \quad (2.33)$$

To compute the remaining constant A , we compute

$$\begin{aligned} \left. \frac{\partial u}{\partial n} \right|_{\partial \bar{\Omega}_a} &= - \left[- (s^2 - t^2) \frac{\partial v}{\partial r} \right] \Big|_{r=1/\sqrt{2R\varepsilon}} \\ &= \left[\left(\frac{1}{2R\varepsilon} - t^2 \right) \frac{4R\varepsilon A}{\sqrt{2R\varepsilon}} \right] \approx \frac{2A}{\sqrt{2R\varepsilon}} (1 + O(\sqrt{\varepsilon})), \end{aligned}$$

and

$$\int_{\partial \bar{\Omega}_a} \frac{\partial u}{\partial n} dS = 2\pi\sqrt{2R\varepsilon} \int_0^\varepsilon \frac{\partial u}{\partial r} dz = 4\pi A\varepsilon, \quad (2.34)$$

and using the compatibility condition

$$-\frac{|\bar{\Omega}|}{D} = \int_{\bar{\Omega}} \Delta u(\mathbf{x}) d\mathbf{x} = \int_{\partial \bar{\Omega}_a} \frac{\partial u(\mathbf{y})}{\partial \mathbf{n}} dS_{\mathbf{y}}. \quad (2.35)$$

Thus

$$A = -\frac{|\bar{\Omega}|}{4\pi D\varepsilon}, \quad (2.36)$$

and the solution v is

$$v(s) = \frac{|\bar{\Omega}|}{4\pi D\varepsilon} (1 - 2R\varepsilon s^2). \quad (2.37)$$

In the initial variable (FIG. 2.2C):

$$u(r, z) = \frac{|\bar{\Omega}|}{4\pi D\varepsilon} \left(1 - 2R\varepsilon \left(\frac{r}{r^2 + z^2} \right)^2 \right). \quad (2.38)$$

The mean time to the ribbon is obtained by setting $s = 0$ in (2.37):

$$\langle \tau \rangle = \frac{|\bar{\Omega}|}{4\pi D\varepsilon}. \quad (2.39)$$

The range of validity of this formula is examined using Brownian simulations in FIG. 2.2D. The search time to a narrow ribbon is surprisingly different to the one for a funnel cusp ([83], see Appendix), as it does not depend on the curvature at the

cusps and it diverges to infinity with $\frac{1}{\varepsilon}$, as ε tends to zero. This divergence is the same as in the narrow escape for a small hole [83, 84, 85]. We note however that the surface of the ribbon is $S_{rib} = 2\pi\sqrt{2R}\varepsilon^{3/2}$, which increases with a different power law than for a regular circular small hole of radius ε . Formula (2.39) is valid for a general domain, not only the geometry between two spheres, as long as the cusp geometry is preserved. It would be interesting to extend formula (2.39) to higher order cusp

$$z = A \left(\frac{r}{l}\right)^\nu + o(r^\nu) \quad (2.40)$$

where $\nu > 2$ and A, l are two characteristic lengths.

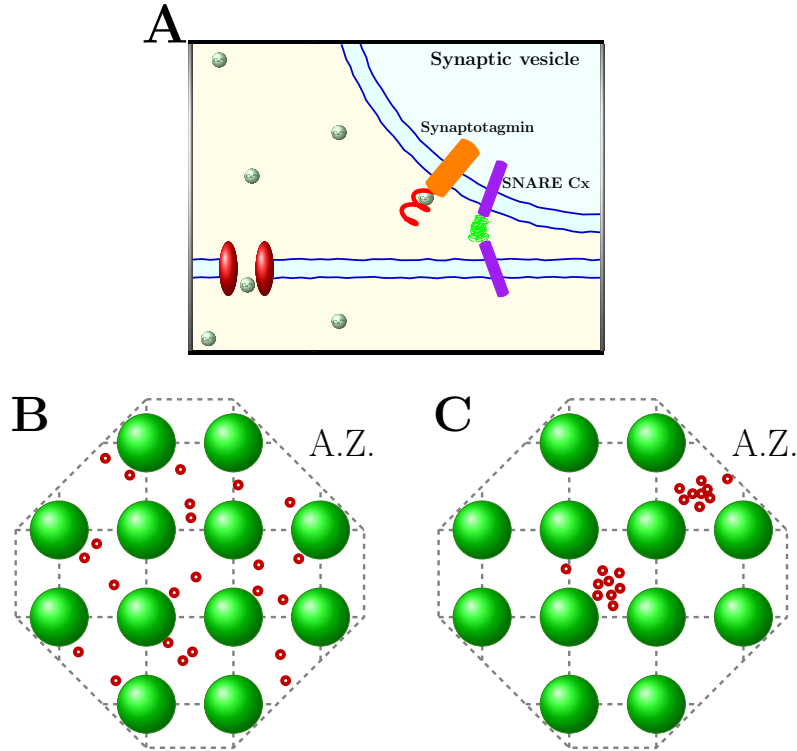


Figure 2.3: **Schematic representation of calcium ions binding to proteins and distribution of vesicles in the Active Zone.** **A:** Calcium ions enter through ionic channels and diffuse to activate key proteins, such as synaptotagmin and SNARE Complex located between the vesicle and synaptic membrane. The binding of several ions is required to activate the SNARE machinery [94]. **B-C: Active Zone organization.** Vesicles (green) are regularly distributed on a square lattice. Calcium channels (red) can be uniformly distributed in the AZ. (**B**) or form clusters (**C**).

2.3 Diffusion to proteins located underneath a pre-synaptic vesicle

We now apply the analytical results derived in the previous sections to estimate the probability that diffusing calcium ions find a small region located underneath a vesicle, when they are initially located at a given distance on the surface membrane (FIG. 2.3). This scenario models a key step in synaptic transmission: when calcium ions are flowing across Voltage-Gated Calcium Channels, in the pre-synaptic terminal, a certain fraction of them make their way underneath a docked vesicle. At such place, they can bind to fundamental molecules or calcium-dependent proteins such as synaptotagmin, a family of proteins (SNARE Complex) located between the vesicle and the pre-synaptic membrane (FIG. 2.3A), leading ultimately to vesicular fusion. Although the exact number of calcium ions needed for this process is small, from 4 to 8, it is still an open question to understand how these ions find such small molecular sites and how the mean time and release probability depend on the local geometry and calcium channel location. Because the distance of the calcium channels to the center of the vesicle can vary, the goal of the present computation is to base the release probability on key parameters of calcium diffusion in the nanodomain between docked vesicles. We shall also explore here how the distribution of vesicles in clusters or uniformly distributed in the active zone (AZ) modulates the release probability.

The model to compute the probability of vesicular release is the following: when several ions hit the narrow ribbon underneath a vesicle, this event triggers the release. As we shall see, this event depends on the relative position of the calcium channels with the vesicles, their organization and the initial number of calcium ions. Indeed, the previous analysis shows that exocytosis cannot be triggered by calcium ions diffusing far away from the vesicles. For example, in a pre-synaptic terminal of volume $1 \mu\text{m}^3$ [208], one diffusing calcium ion located in the pre-synaptic bulk will enter the region underneath the vesicle in approximately 4 sec, as computed from eq. (2.39) with an effective diffusing coefficient that accounts for crowding $D = 20\mu\text{m}^2.\text{s}^{-1}$ [13], and $\varepsilon = 10^{-3}\mu\text{m}$. If the terminal contains 7 docked vesicles, the ion reaches any vesicle in approximately 570 ms. This estimate of 570 ms is two orders of magnitude higher than the time scale of exocytosis, which occurs in less than a millisecond following calcium entry into the pre-synaptic terminal [211]. This dimensional analysis reveals that exocytosis is triggered mainly by calcium ions located in the neighborhood of a vesicle. We conclude that when calcium ions exit the neighborhood of the docked vesicles, they should not contribute anymore to the vesicular release probability.

2.3.1 Splitting probability of a Brownian ion to hit a vesicular ribbon versus entering the pre-synaptic bulk

The splitting probability here is the probability for a Brownian ion to hit the small ribbon below the vesicle before it reaches a distance $2R$ away from the membrane, where it is considered to be lost inside the pre-synaptic bulk. To compute this probability, we shall account for the geometry of the AZ at the pre-synaptic terminal:

it is approximated as a flat three-dimensional domain, containing vesicles regularly distributed on the membrane surface, spaced apart at a distance $2H$ (FIG. 2.3B-C). The activation site for vesicular release is the small two-dimensional ribbon of

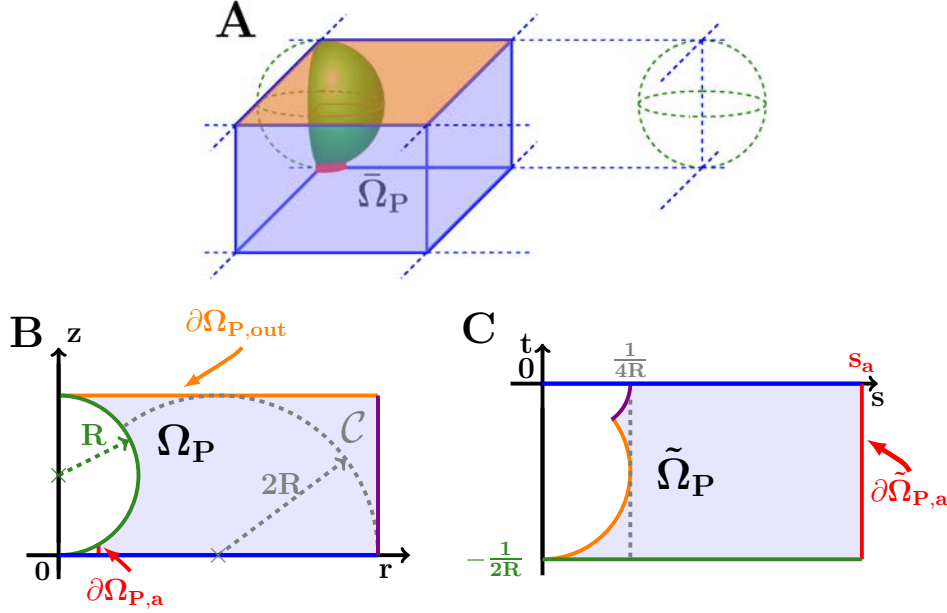


Figure 2.4: **Schematic representation of a thin lattice vesicular domain.** **A:** Modeling the AZ. A flat domain containing spherical obstacles (vesicles) is divided into elementary domains ($\bar{\Omega}_P$). Diffusing particles (calcium ions) are absorbed at the cusp (red) and at the top (orange) where ions are lost in the three-dimensional domain. Ions are reflected in all other boundary parts. **B:** Two-dimensional projection of the elementary domain Ω . Ions are reflected on the purple and blue boundaries and are absorbed on the orange and red regions. **C:** Mapping of the domain Ω_P using $f(\xi) = 1/\xi$. The color code between regions and their images in domains Ω_P and $\tilde{\Omega}_P$ are in correspondence.

height $\varepsilon \ll R$, as already mentioned in section 2.2.2 (FIG. 2.4A red). The AZ is divided into elementary squares $\bar{\Omega}_P$ (see FIG. 2.4A). Ions are absorbed at the cusp (FIG. 2.4A red) and at the upper-part of the domain (FIG. 2.4A orange), and are reflected otherwise. The probability $p_{3D}(\mathbf{x})$ for a Brownian ion starting at position $\mathbf{x} = (x, y, z)$ to reach the ribbon before the upper part of the 3D-domain $\bar{\Omega}_P$ (FIG. 2.4A) satisfies the mixed boundary-value Laplace equation [100, 174, 189]

$$\begin{aligned}
 \Delta p_{3D}(\mathbf{x}) &= 0 \text{ for } \mathbf{x} \in \bar{\Omega}_P & (2.41) \\
 p_{3D}(\mathbf{x}) &= 1 \text{ for } \mathbf{x} \in \partial\bar{\Omega}_{P,a} \\
 p_{3D}(\mathbf{x}) &= 0 \text{ for } \mathbf{x} \in \partial\bar{\Omega}_{P,out} \\
 \frac{\partial p_{3D}}{\partial n}(\mathbf{x}) &= 0 \text{ for } \mathbf{x} \in \partial\bar{\Omega}_P \setminus (\partial\bar{\Omega}_{P,a} \cup \partial\bar{\Omega}_{P,out}).
 \end{aligned}$$

The domain, composed of vesicles centered on a square lattice, is not invariant by rotation around any axis. Nevertheless, the results of the previous sections motivate the restriction of our analysis to the fundamental square domain Ω_P (FIG. 2.4B). In

cylindrical coordinates (r, θ, z) , the three-dimensional problem (2.41) in $\bar{\Omega}_P$ becomes

$$\begin{aligned} \frac{\partial^2 p_{3D}}{\partial r^2}(r, z) + \frac{1}{r} \frac{\partial p_{3D}}{\partial r}(r, z) + \frac{\partial^2 p_{3D}}{\partial z^2}(r, z) &= 0 \text{ for } (r, z) \in \Omega_P \\ p_{3D}(r, z) &= 1 \text{ for } (r, z) \in \partial\Omega_{P,a} \\ p_{3D}(r, z) &= 0 \text{ for } (r, z) \in \partial\Omega_{P,out} \\ \frac{\partial p_{3D}}{\partial n}(r, z) &= 0 \text{ for } (r, z) \in \partial\Omega_P \setminus (\partial\Omega_{P,a} \cup \partial\Omega_{P,out}). \end{aligned} \quad (2.42)$$

We neglect the change in the geometry along the angle θ , which should give a term of order $O(1)$. Using the conformal mapping $f(\zeta) = \frac{1}{\zeta}$, we map the domain Ω_P into $\tilde{\Omega}_P$ (see eq. (2.4), FIG. 2.4C). The mapping $\omega = (s, t) = f(\zeta)$, where $\zeta = r + iz$, transforms horizontal lines $r = \alpha$, $\alpha \in \mathbb{R}$ (resp. vertical lines $z = \beta$, $\beta \in \mathbb{R}$) into circles of radius $\frac{1}{2\alpha}$ and centered at $(s, t) = (\frac{1}{2\alpha}, 0)$ (resp. $\frac{1}{2\beta}$ and $(s, t) = (0, \frac{1}{2\beta})$). In particular, the interval at the cusp ($r = \sqrt{2R\varepsilon}$) is mapped into a portion of a circle of radius $\frac{1}{2\sqrt{2R\varepsilon}}$, centered at $(\frac{1}{2\sqrt{2R\varepsilon}}, 0)$. The first order approximation is a segment $s = s_a = \frac{1}{\sqrt{2R\varepsilon}}$, $t \in [0, -\frac{1}{2R}]$. We set $p_{3D}(r, z) = v_{3D,in}(s, t)$. In the scaling variable $\xi = \frac{s}{s_a}$, the regular expansion of the solution

$$Y_{3D,in}(\xi, t) = v_{3D,in}(s, t) \quad (2.43)$$

is

$$Y_{3D,in}(\xi, t) = Y_{3D,in}^0(\xi, t) + \tilde{\varepsilon} Y_{3D,in}^1(\xi, t) + \dots \quad (2.44)$$

where the small parameter is $\tilde{\varepsilon} = 2R\varepsilon$. This is precisely equation (2.30) and at first order in $O(\varepsilon^{-2})$ with the boundary conditions in (2.42), we obtain that the leading order term Y_0 is independent of t . At order $O(\varepsilon^{-1})$, the equation for $Y_{3D,in}^0$ becomes:

$$\xi^4 \frac{\partial^2 Y_{3D,in}^0}{\partial \xi^2} - \xi^3 \frac{\partial Y_{3D,in}^0}{\partial \xi} = 0, \quad (2.45)$$

and hence $Y_{3D,in}^0(\xi) = A\xi^2 + B$ where A and B are two constants. Thus, the solution $v_{3D,in}$ is

$$v_{3D,in}(s) = As^2 + B. \quad (2.46)$$

We are left with the constants A and B to be determined. We shall compute here the probability $p_{3D}(r, 0)$ where the initial starting point is located on the surface $z = 0$. The splitting probability p_{3D} has the general form

$$p_{3D}(r, z) = A \frac{r^2}{(z^2 + r^2)^2} + B \quad (2.47)$$

and

$$p_{3D}(r, 0) = \frac{A}{r^2} + B. \quad (2.48)$$

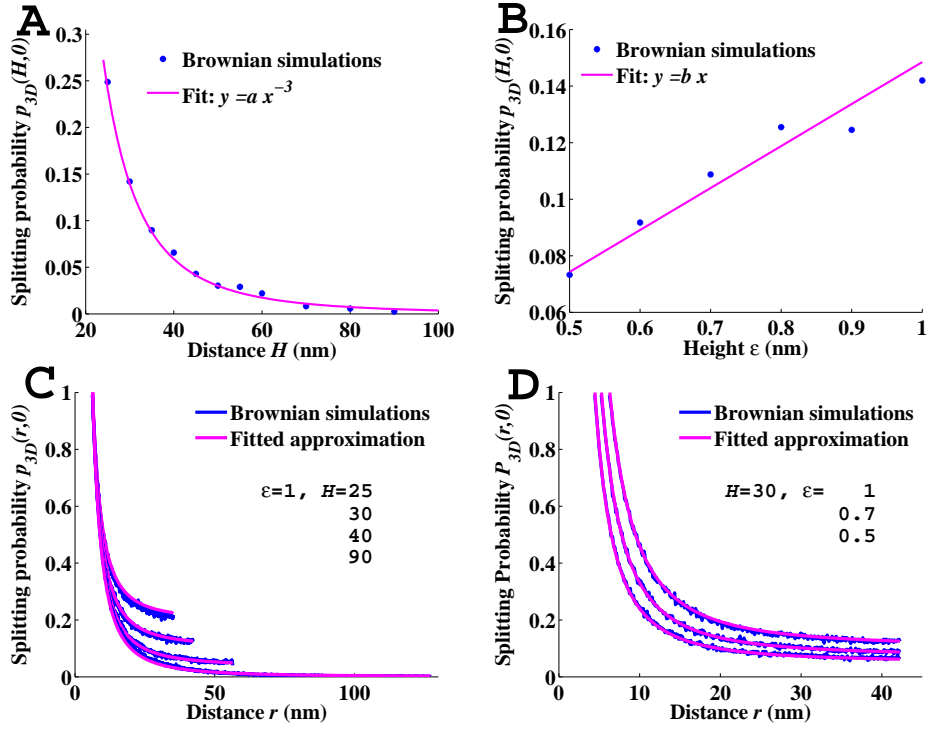


Figure 2.5: **Approximation of the splitting probability $p_{3D}(r, 0)$.** **A-B:** The splitting probability $p_{3D}(H, 0)$ function of the domain size H for R and ϵ fixed (**A**), then for varying ϵ and fixed H and R (**B**). The fitting are obtained using matlab, $a = 3767$ (**A**) and $b = 0.1485$ (**B**). **C-D:** Comparison of the splitting probability computed from Brownian simulations (blue) and the numerical approximation (magenta, eq. (2.54)) (red in FIG. 2.4A). We vary the distance to the absorbing (red) boundary). The radius of a vesicle is $R = 20$ nm, and the diffusion coefficient for calcium is $D = 200 \mu\text{m}^2 \cdot \text{s}^{-1}$. The initial position of the Brownian particle r goes from $\sqrt{2R\epsilon}$ to $\sqrt{2H}$ and H takes the following values (**C**, $H = 25, 30, 40, 90$, $\epsilon = 1$). We also show $p_{3D}(r, 0)$ for different values of ϵ (**D**, $\epsilon = 0.5, 0.7, 1$, $H = 30$). We use 2000 runs per simulations.

We now use the boundary conditions and some approximation to determine these constants A and B . First, the absorbing boundary condition at the cusp in (2.42) gives that

$$p_{3D}(r, 0) = 1 - A \left(1 - \frac{2R\varepsilon}{r^2}\right), \quad (2.49)$$

and the constant A depends on the refined geometry of the domain and the distances H , R and ε .

To determine A , we first assume that the value $p_{3D}(H, 0)$ is known and express the splitting probability as a function of $p_{3D}(H, 0) = p(\varepsilon, R, H)$ in eq. (2.49). We obtain

$$p_{3D}(r, 0) = 1 - \frac{1 - p(\varepsilon, R, H)}{1 - \frac{2R\varepsilon}{H^2}} \left(1 - \frac{2R\varepsilon}{r^2}\right). \quad (2.50)$$

We now determine numerically $p(\varepsilon, R, H)$ when H , R and ε are changing. We start by changing H for fixed values R and ε . We ran stochastic simulations and obtain with a best fit procedure the following interpolation

$$p(\varepsilon, R, H) \approx \frac{a(R, \varepsilon)}{H^3}, \quad (2.51)$$

where the function $a(R, \varepsilon)$ depends on ε and R (see FIG. 2.5A). Similarly, we obtain by varying ε and fixing H and R the following estimation (FIG. 2.5B)

$$p(\varepsilon, R, H) \approx b(R, H)\varepsilon. \quad (2.52)$$

Finally, the dependency in the radius R can be obtained by rescaling the domain. Combining eqs. (2.51-2.52), we propose that

$$p(\varepsilon, R, H) = \alpha \frac{R^2\varepsilon}{H^3}, \quad (2.53)$$

where the constant α is fitted numerically using Matlab. We obtain $\alpha \approx 9.8$. Thus, the splitting probability $p_{3D}(r, 0)$ to reach the absorbing window before the upper part of the thin layer $z = 2R$ is approximated by

$$p_{3D}^{approx}(r, 0) = 1 - \frac{1 - 9.8 \frac{R^2\varepsilon}{H^3}}{1 - \frac{2R\varepsilon}{H^2}} \left(1 - \frac{2R\varepsilon}{r^2}\right). \quad (2.54)$$

The range of validity of this formula is investigated in FIG. 2.5C-D, showing the nice agreement between the asymptotic formula and Brownian simulations for different values of H and ε .

2.4 Discussion: estimation of the vesicular release probability

In this final section, we apply the result obtained in the section 2.3.1 about the splitting probability, to estimate the variability of the vesicular release process. Indeed, we can now compute the probability

$$p_{act}(r, N) = \mathbb{P}(T \text{ ions have reached the synaptotagmin} | N \text{ ions, distance } r) \quad (2.55)$$

that a finite number T of calcium ions (we consider $T = 3, 4$ and 5 ions) bind a molecule such as synaptotagmin, when N calcium ions have entered through a channel. The synaptotagmin molecules are positioned between a vesicle and the synaptic membrane and calcium channels are at a distance r from the center of the closest vesicle.

If we neglect the dynamics of calcium ion unbinding events, the probability $p_{act}(r, N)$ is thus the one to find at least T ions inside the ribbon. Because the probability to find exactly k ions out of N follows the Binomial distribution $\mathcal{B}(N, p_{3D}(r))$, we obtain that

$$\begin{aligned} p_{act}(r, N) &= \sum_{k \geq T} \binom{N}{k} p_{3D}(r)^k (1 - p_{3D}(r))^{N-k} \\ &= 1 - \sum_{k=0}^{T-1} \binom{N}{k} p_{3D}(r)^k (1 - p_{3D}(r))^{N-k}. \end{aligned} \quad (2.56)$$

Using approximation eq. (2.54), we obtain an explicit expression for the probability of activation $p_{act}(r, N)$ after a single channel opens. The probability p_{act} depends on the channel locations, decreasing from one to almost zero in only a few nanometers (FIG. 2.6A-B). This result can explain the large variability in the release probability as calcium channel position can vary over time.

Moreover, the organization of vesicles in the AZ determines the release probability. Indeed, when vesicles are sparsely distributed (FIG. 2.6A, $H = 100$ nm) and 100 ions have entered, then to obtain a 80% release probability ($p_{act} = 0.8$), the distance between the vesicle and the channels must be smaller than 24 nm, which has to be compared to the 20 nm radius of the vesicle. This result shows that the co-localization of channels with a vesicle is a key feature determining a high release probability. However, for high vesicular crowding (FIG. 2.6B, described by choosing the distance $H = 35$ nm) and 100 ions have entered, then the probability p_{act} is higher than 0.9, regardless of the initial position of the channels, suggesting that vesicles are certainly released. We predict that a high crowding of vesicles should be associated with a high release probability.

Channels can be organized in cluster or uniformly distributed and this is also a major determinant governing release probability. Indeed, channels clustering in our model is accounted for by an increase in the number of entering ions. When vesicles are sparsely distributed, the 24 nm distance required to obtain a release probability $p_{act} = 0.8$ when 100 ions are entering through one channel, is increased to 61 nm for 500 ions. This effect results from the local geometry of the ribbon underneath the vesicle. When the number of ions is low, this maximal distance to guarantee

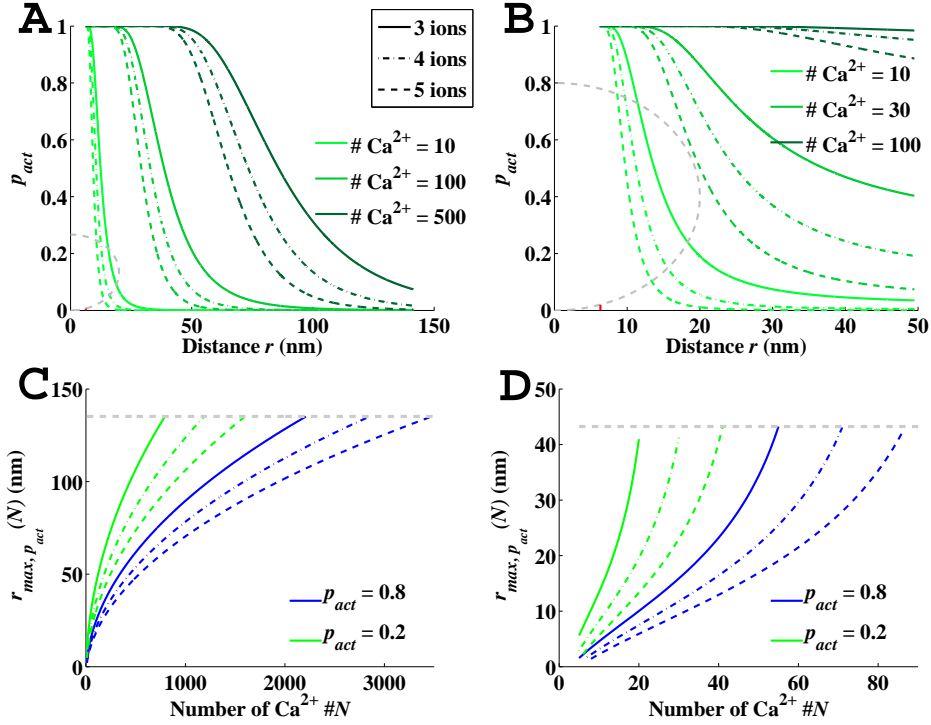


Figure 2.6: **Consequences on the release probability of calcium channel location and vesicular crowding at the AZ.** **A-B:** Probability to find three, four or five calcium ions (full, dashed and dotted lines respectively) underneath a vesicle, in the case of sparse vesicular distribution: $H = 100$ nm, **A**; and in the case of crowding of vesicles at the AZ: $H = 35$ nm, **B**. The relation depends on the initial number of calcium ions. The diameter of the pre-synaptic vesicles is fixed at $R=40$ nm (grey dashed circle), the diffusion coefficient for free calcium ions is $D_{Ca} = 200\mu m^2 s^{-1}$. The height of the absorbing boundary is $\varepsilon = 1nm$ (red dashed line). **C-D:** Maximal channels distance $r_{max, p_{act}}(N)$ to activate the vesicle with a probability $p_{act} \geq 0.8$ (blue) and 0.2 (green), when there are N initial ions, for $H = 100$ nm **C** and $H = 35$ nm **D**. We fix the threshold to 3, 4 or 5 calcium ions. The gray dashed line represents the maximal distance to the vesicle in the elementary domain: $\sqrt{2}H$.

$p_{act} = 0.8$ does not vary much when the activation threshold T increases from 3 to 5; however, for 500 ions, this distance changes significantly over 15 nm.

To better understand how the maximal distance $r_{\max,p_{act}}(N)$ between channels and vesicles varied with the number N of entering ions, for a fixed probability p_{act} , we plotted $r_{\max,p_{act}}(N)$ in FIG. 2.6C-D. For a sparse distribution of vesicles, characterized by the distance $H = 100\text{nm}$, a vesicle is activated with a probability $p_{act} = 0.8$ (resp. $p_{act} = 0.2$), when 1200 ions are entering at a distance 100 nm (resp. 450 ions), and 340 ions at a distance 50 nm (resp. 125 ions). This result has to be compared to the 200 - 500 nm diameter of the AZ [187]. Consequently, a sparse distribution of vesicles at the AZ requires a high number of entering ions in order to trigger fusion, which can be achieved when channels are clustered. However, when channels are co-localized with vesicles, the activation probability p_{act} is significantly increased: indeed 450 ions are necessary for activation for $p_{act} = 0.2$ at a distance 100 nm. When the probability increases to 0.8, the distance reduces to 58 nm. Thus, a synapse with high release probability requires a nanometer precision of the channel location. However, this high requirement can be compensated by increasing the number of initial ions: with 2000 ions, the maximum distance is relaxed to 140 nm. On the contrary, in a pre-synaptic terminal crowded at its surface with vesicles (characterized by $H = 35\text{ nm}$), very few initial ions are needed for an efficient release. Indeed, 50 ions are enough to activate a vesicle with probability 0.8, wherever the channels are located in AZ (FIG. 2.6D). The number of calcium ions estimated for reliable release could be affected by calcium buffers located within the nanometer layer of the AZ, but not in the bulk as discussed above.

2.5 Conclusion

To conclude, the present asymptotic analysis of the model equations and their corresponding stochastic simulations provide a robust tool to study diffusion in cellular nanodomains and in particular in the pre-synaptic terminal of neuronal synapses. We reported here that channel positioning, the number of entering ions, and the organization of the AZ are key factors governing the search by diffusing ions to relevant proteins that trigger vesicular release. Channel clustering provides a way to increase the initial number of calcium ions at a specific location. According to the present results, we found that vesicles located near channel clusters will be reliably activated at distances of tens of nanometers. We speculate that releasing a sequence of vesicles at the same location might be an unrealistic scenario due to relocalization of the channels following vesicular fusion [169, 170]. The present approach complements previous numerical studies by specifically addressing the role of the three-dimensional geometry between a vesicle and the synaptic membrane for diffusing calcium ions to trigger vesicular release [33, 127, 129].

Finally, we reported here that a uniform distribution of calcium channels is associated with a low release probability. For vesicles positioned near a small amount of calcium channels, a train of stimulations will most likely activates several vesicles. Thus changing the AZ organization, or the colocalization of calcium channels with respect to vesicles, can modify the synaptic response. After several stimulations this redistribution of channels can influence short-term synaptic plasticity,

the mechanism of which could be further investigated using the present modeling approach.

2.6 Appendix A : Revisiting the Dire Strait Search in a three-dimensional cusp located at the end of a funnel

In this appendix, we compute the time for a Brownian particle to escape through a narrow cusp located at the end of a funnel in a three dimensional bounded domain ($\bar{\Sigma}_R$, FIG. 2.7A). The mean first passage time (MFPT) $\tilde{u}(\mathbf{x})$ starting at position \mathbf{x} is solution of

$$\begin{aligned} \mathcal{D}\Delta\tilde{u}(\mathbf{x}) &= -1 \text{ for } \mathbf{x} \in \bar{\Sigma}_R \\ \frac{\partial\tilde{u}}{\partial n}(\mathbf{x}) &= 0 \text{ for } \mathbf{x} \in \partial\bar{\Sigma}_R \setminus \partial\bar{\Sigma}_{R,a} \\ \tilde{u}(\mathbf{x}) &= 0 \text{ for } \mathbf{x} \in \partial\bar{\Sigma}_{R,a}, \end{aligned} \quad (2.57)$$

where \mathcal{D} is the diffusion coefficient and $\partial\bar{\Sigma}_R$ (resp. $\partial\bar{\Sigma}_{R,a}$) is the boundary (resp. the absorbing part of the boundary). We compute asymptotically the solution $u(\mathbf{x})$

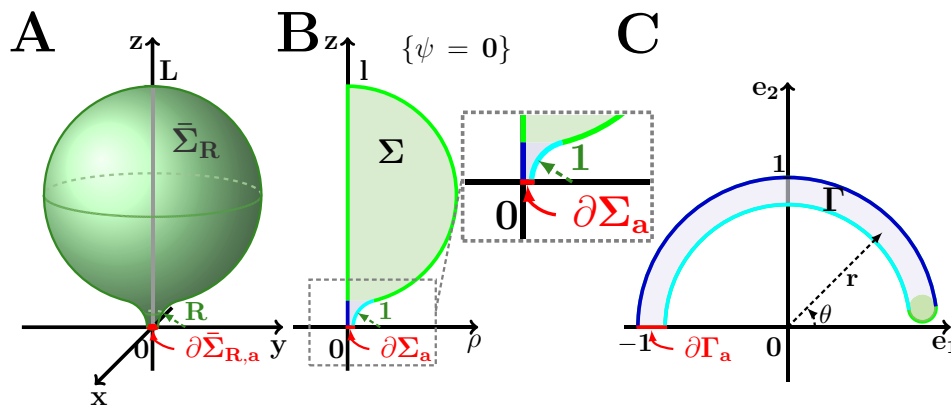


Figure 2.7: **Domain with a funnel-shaped cusp.** **A:** Initial domain $\bar{\Sigma}_R$ consists of two geometrical features: a large domain or a ball and a small narrow cusp. R is the radius of curvature at the cusp. **B:** Σ is the projection of the three-dimensional domain $\bar{\Sigma}_1$, in the plane $\psi = 0$ (cylindrical coordinates). **C:** The two-dimensional projection Σ is mapped using a Möbius transformation (the boundary parts with a given color is mapped with the one of the same color in the image domain).

for problem (2.57), using the conformal mapping method. The geometry of the domain $\bar{\Sigma}_R$ is the following: it contains a small absorbing window $\partial\bar{\Sigma}_{R,a}$ of diameter \mathcal{E} located at the end of the funnel connected smoothly to a three dimensional ball. The domain $\bar{\Sigma}_R$ can be as large as wanted. The radius of curvature R at the boundary shapes the funnel, as shown in FIG. 2.7A. The symmetric cusp can be parametrized in the cylindrical coordinates (ρ, ψ, z) (ρ is the distance to the z -axis)

by

$$\rho(z) = \frac{1}{2R}z^2 + \frac{\mathcal{E}}{2}, \quad (2.58)$$

for z small. In dimensionless variables $\mathbf{x}' = R\mathbf{x}$ and $\tilde{u}(\mathbf{x}') = u(\mathbf{x})$, the equation is written as

$$\begin{aligned} D\Delta u(\mathbf{x}) &= -1 \text{ for } \mathbf{x} \in \bar{\Sigma}_1 \\ \frac{\partial u}{\partial n}(\mathbf{x}) &= 0 \text{ for } \mathbf{x} \in \partial\bar{\Sigma}_1 \setminus \partial\bar{\Sigma}_{1,a} \\ u(\mathbf{x}) &= 0 \text{ for } \mathbf{x} \in \partial\bar{\Sigma}_{1,a}. \end{aligned} \quad (2.59)$$

The domain $\bar{\Sigma}_R$ is mapped on the its image $\bar{\Sigma}_1$, $|\bar{\Sigma}_R| = R^3|\bar{\Sigma}_1|$, $\mathcal{E} = R\varepsilon, L = Rl$, and $\mathcal{D} = R^2D$. Due to the rotational invariance, in cylindrical coordinates (ρ, ψ, z) , the solution of the two-dimensional problem in the domain $\{\psi = 0\}$ (see FIG. 2.7B) satisfies

$$\begin{aligned} \frac{\partial^2 u}{\partial \rho^2}(\rho, z) + \frac{1}{\rho} \frac{\partial u}{\partial \rho}(\rho, z) + \frac{\partial^2 u}{\partial z^2}(\rho, z) &= -\frac{1}{D} \text{ for } (\rho, z) \in \Sigma \\ \frac{\partial u}{\partial n}(\rho, z) &= 0 \text{ for } (\rho, z) \in \partial\Sigma \setminus \partial\Sigma_a \\ u(\rho, z) &= 0 \text{ for } (\rho, z) \in \partial\Sigma_a. \end{aligned} \quad (2.60)$$

2.6.1 Mapping the cusp domain with a Möbius transformation into a narrow Banana

The key step to the asymptotic computation is the Möbius transformation that maps domain $\bar{\Sigma}_1$ into a narrow domain, where the mapped equation reduces to a single variable:

$$f(\xi) = \frac{\xi - \alpha}{\xi - \beta}, \quad (2.61)$$

where $\xi = \rho + iz$ is the variable in the original domain, that maps the domain Σ into two concentric circles. The pair (α, β) lies symmetric on the real axis $Re(z) = 0$. We obtain their values using the conditions $\alpha = -\beta$ and $(1 + \varepsilon/2 - \alpha)(1 + \varepsilon/2 - \beta) = 1$. Finally, we obtain

$$\alpha_\varepsilon = \sqrt{\varepsilon(1 + \varepsilon/4)} = \sqrt{\varepsilon}(1 + \frac{1}{8}\varepsilon + o(\varepsilon)), \quad (2.62)$$

$$f(\xi) = \frac{\xi - \alpha_\varepsilon}{\xi + \alpha_\varepsilon}. \quad (2.63)$$

The domain Σ (FIG. 2.7B) is mapped into Γ (FIG. 2.7C), and the boundary parts $\partial\Sigma_a$ is mapped on the segment $\partial\Gamma_a = [-1; -1 + \sqrt{\varepsilon}]$ of length $\sqrt{\varepsilon}$. The cusp is mapped on the narrow hot-dog shaped domain, and the other external part of the domain is mapped on the small green region (FIG. 2.7C), concentrated at an angle

2.6. Appendix A : Revisiting the Dire Strait Search in a three-dimensional cusp located at the end of a funnel

θ of order $\sqrt{\varepsilon}$. To map eq. (2.60) into to the new domain, we use $\omega = re^{i\theta} = f(\xi)$ and $u(\xi) = v_\varepsilon(\omega)$. The conformal map changes the Laplace equation into

$$\Delta u(\xi) = |f'(\xi)|^2 \Delta v(\omega) \quad (2.64)$$

$$f'(\xi) = \frac{2\alpha_\varepsilon}{(\xi + \alpha_\varepsilon)^2} = \frac{(1 - \omega)^2}{2\alpha_\varepsilon}. \quad (2.65)$$

The first order derivative is

$$\begin{aligned} \frac{\partial u}{\partial \rho} &= \frac{\partial v_\varepsilon}{\partial r} \frac{\partial r}{\partial \rho} + \frac{\partial v_\varepsilon}{\partial \theta} \frac{\partial \theta}{\partial \rho} \\ &= \left(\frac{1 - r^2}{2\alpha_\varepsilon} \cos(\theta) + \frac{r}{\alpha_\varepsilon} (r \cos(\theta) - 1) \right) \frac{\partial v_\varepsilon}{\partial r} + \frac{r^2 - 1}{2\alpha_\varepsilon r} \sin(\theta) \frac{\partial v_\varepsilon}{\partial \theta}, \end{aligned} \quad (2.66)$$

and the variable ρ is now expressed by

$$\rho = \alpha_\varepsilon \operatorname{Re} \left(\frac{\omega + 1}{1 - \omega} \right) = \alpha_\varepsilon \frac{1 - |\omega|^2}{|1 - \omega|^2} = \alpha_\varepsilon \frac{r^2 - 1}{2r \cos(\theta) - 1 - r^2}. \quad (2.67)$$

Equation (2.60) is mapped into

$$\begin{aligned} \frac{|1 - \omega|^4}{4\alpha_\varepsilon^2} \Delta v_\varepsilon + \frac{|1 - \omega|^2}{\alpha_\varepsilon(1 - |\omega|^2)} \left[\frac{\partial v_\varepsilon}{\partial r} \frac{\partial r}{\partial \rho} + \frac{\partial v_\varepsilon}{\partial \theta} \frac{\partial \theta}{\partial \rho} \right] &= -\frac{1}{D} \text{ for } (r, \theta) \in \Gamma \\ \frac{\partial v_\varepsilon}{\partial n}(r, \theta) &= 0 \text{ for } (r, \theta) \in \partial\Gamma \setminus \partial\Gamma_a \\ v_\varepsilon(r, \theta) &= 0 \text{ for } (r, \theta) \in \partial\Gamma_a. \end{aligned} \quad (2.68)$$

To solve asymptotically equation (2.68) in Γ , we neglect the variation in the r-

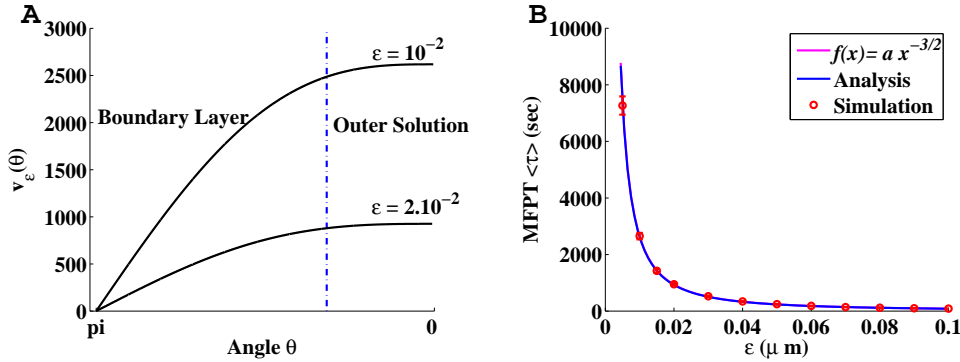


Figure 2.8: **Profile of the solution v_ε for escape in the three dimensional funnel-shaped cusp** **A**: Solution v_ε in the mapped domain for $\varepsilon = 10^{-2}$ (top) and $2 \cdot 10^{-2}$ (bottom), with $R = 1$, $D = 0.2$ and $|\bar{\Sigma}_1| = \frac{4}{3}\pi 5^3$. There are two regions: the boundary layer and the outer region. **B**: Analytical formula (Blue) for the DST (eq. (2.76)) versus Brownian simulations (red). We used 2000 runs for values of ε in the range 0.01 to 0.1. The parameters are described in **A**. The optimal fit using Matlab (Magenta) gives $a = 2650$ is comparable with the estimation from the analytical formula $a = 2618$.

variable because $r = 1 + O(\sqrt{\varepsilon})$ and thus $v_\varepsilon(r, \theta) \approx v_\varepsilon(\theta)$ with absorbing boundary condition at π ($v_\varepsilon(\pi) = 0$) and reflection inside the upper part ($v'_\varepsilon(c\sqrt{\varepsilon}) = 0$), where the constant $c = O(1)$. Equation (2.68) reduces to:

$$v''_\varepsilon(\theta) + \frac{\sin(\theta)}{\cos(\theta) - 1} v'_\varepsilon(\theta) = -\frac{\alpha_\varepsilon^2}{D(\cos(\theta) - 1)^2}, \quad (2.69)$$

the general solutions of which has the form

$$v_\varepsilon(\theta) = A(\sin(\theta) - \theta) + B + \frac{\alpha_\varepsilon^2}{15D} \left[2 \ln(1 - \cos(\theta)) - 2 \cos(\theta) + \frac{3}{\cos(\theta) - 1} \right] \quad (2.70)$$

where the two constants A and B are found from the boundary conditions. From $v_\varepsilon(\pi) = 0$, we get

$$\begin{aligned} v_\varepsilon(\theta) &= A(\sin(\theta) + \pi - \theta) \\ &+ \frac{\alpha_\varepsilon^2}{15D} \left[2 \ln \left(\frac{1 - \cos(\theta)}{2} \right) - 2(1 + \cos(\theta)) + \frac{3}{\cos(\theta) - 1} + \frac{3}{2} \right]. \end{aligned} \quad (2.71)$$

To estimate the other constant A , we use the compatibility condition [83] obtained by integrating equation (2.59) over the initial domain

$$-\frac{|\bar{\Sigma}_1|}{D} = \int_{\bar{\Sigma}_1} \Delta u(\mathbf{x}) d\mathbf{x} = \int_{\partial\bar{\Sigma}_{a,1}} \frac{\partial u}{\partial \mathbf{n}}(\mathbf{y}) dS_{\mathbf{y}}. \quad (2.72)$$

Using expression (2.71) for the solution v_ε , we get

$$\begin{aligned} \frac{\partial u}{\partial \mathbf{n}} \Big|_{\partial\bar{\Sigma}_{a,1}} &= -\frac{\partial u}{\partial z} \Big|_{\partial\bar{\Sigma}_{a,1}} = -\frac{\partial u}{\partial z} \Big|_{\partial\Sigma_a} = -\left[\frac{r \cos(\theta) - 1}{\alpha_\varepsilon} + \frac{(1 - r^2) \cos(\theta)}{2\alpha_\varepsilon r} \right] \frac{\partial v_\varepsilon}{\partial \theta} \Big|_{\theta=\pi, r \in [-1; -1+\sqrt{\varepsilon}]} \\ &= \frac{2}{\alpha_\varepsilon} (1 + O(\sqrt{\varepsilon})) \frac{\partial v_\varepsilon}{\partial \theta} \Big|_{\theta=\pi, r \in [-1; -1+\sqrt{\varepsilon}]} = -\frac{4A}{\alpha_\varepsilon} (1 + O(\sqrt{\varepsilon})). \end{aligned}$$

Thus,

$$\int_{\partial\bar{\Sigma}_{a,1}} \frac{\partial u}{\partial \mathbf{n}}(\rho, z) dS = -2\pi \frac{4A}{\alpha_\varepsilon} \int_0^{\varepsilon/2} \rho d\rho = -2\pi \frac{4A}{\alpha_\varepsilon} \frac{\varepsilon^2}{8} = -\frac{A\pi\varepsilon^2}{\alpha_\varepsilon} = -A\pi\varepsilon\sqrt{\varepsilon}(1 + O(\sqrt{\varepsilon})).$$

Using the compatibility condition (2.72), we get

$$A_\varepsilon = \frac{|\bar{\Sigma}_1|}{D\pi\varepsilon\sqrt{\varepsilon}} \quad (2.73)$$

and

$$\begin{aligned} v_\varepsilon(\theta) &= \frac{|\bar{\Sigma}_1|}{D\pi\varepsilon\sqrt{\varepsilon}} (\sin(\theta) + \pi - \theta) \\ &+ \frac{\alpha_\varepsilon^2}{15D} \left[2 \ln \left(\frac{1 - \cos(\theta)}{2} \right) - 2(1 + \cos(\theta)) + \frac{3}{\cos(\theta) - 1} + \frac{3}{2} \right]. \end{aligned} \quad (2.74)$$

The solution and the extension of the boundary layer [6] are represented in FIG. 2.8A. The mean first passage time $\langle \tau \rangle$ from the domain is computed for trajectories starting outside the cusp, located in the mapped domain by the starting angle $\theta = c\sqrt{\varepsilon}$:

$$\langle \tau \rangle = \frac{|\bar{\Sigma}_1|}{D\varepsilon\sqrt{\varepsilon}} + O(1). \quad (2.75)$$

In dimensional units, we obtain

$$\langle \tau \rangle = \frac{|\bar{\Sigma}_R|\sqrt{R}}{\mathcal{D}\mathcal{E}\sqrt{\mathcal{E}}} + O(1), \quad (2.76)$$

where R is the curvature at the cusp, \mathcal{D} the diffusion coefficient and $|\bar{\Sigma}_R|$ the total volume of the domain. This formula corrects by a factor 2 the asymptotic expansion for the Dire Strait Time derived in [83, 84, 85, 86]. The asymptotic formula (2.76) seems to be valid in a large range of the absorbing radius \mathcal{E} as shown in FIG. 2.8B, where the analytical formula is directly compared to Brownian simulations.

2.7 Appendix B: Simulating the NET in two and three dimension.

We present in this appendix a method to realize numerical Brownian simulations in two and three dimensions, in confined geometries.

2.7.1 Simulating Brownian trajectory using Euler scheme in confined domains.

The trajectory of a Brownian particle with a diffusion coefficient D can be represented by the solution of the stochastic differential equation:

$$\dot{\mathbf{X}}(t) = \sqrt{2D}\dot{\mathbf{w}}(t) \text{ for } t > 0, \quad (2.77)$$

$$\mathbf{X}(0) = x_0 \quad (2.78)$$

where $\dot{\mathbf{w}}(t)$ is white noise. To discretize such equation for $0 \leq t \leq T$, we consider the lattice $t_k = t_0 + k\Delta t$ with $\Delta t = \frac{T}{N}$. According to Ito's definition of the stochastic integral, the solution $\mathbf{X}(t)$ is the limit as $\Delta t \rightarrow 0$ of the solution of the Euler scheme [183]:

$$X^N(t + \Delta t) = X^N(t) + \sqrt{2D\Delta t}\xi(t), \quad (2.79)$$

where $\xi(t)$ are independent standard Gaussian variables $\mathcal{N}(0, 1)$ for each t on the lattice.

To perform simulations in dimension 2 and so on, one can simply consider the Euler Scheme for the discretized vector $\mathbf{X} = (X_1(t), X_2(t))$ on the numerical mesh:

$$X_1^N(t + \Delta t) = X_1^N(t) + \sqrt{2D\Delta t}\xi_1(t) \quad (2.80)$$

$$X_2^N(t + \Delta t) = X_2^N(t) + \sqrt{2D\Delta t}\xi_2(t), \quad (2.81)$$

where $\xi_j(t)$ are independent standard Gaussian variables $\mathcal{N}(0, 1)$ for each t on the lattice and each $j \in \{1, 2\}$.

In the case of Brownian particles evolving in confined domains, we have to consider the behavior of the particles at boundaries that can be either reflecting or absorbing. To simulate a reflecting boundary, we consider the classical Snell-Descartes reflection principle [173]. Hence, a trajectory that hits the boundary is reflected according to the tangent plane to the boundary at the hitting point. To simulate an absorbing boundary, we simply truncate the trajectory at the first time it hits the absorbing part of the boundary [173].

When simulating rare events such as the DST, one should be particularly careful in the choice of the time step Δt . Indeed, in the simulations the very long first passage times are usually very sensitive to Δt . We propose now a method to choose such time step, when the Brownian particle has to reach a small target.

2.7.2 Choosing the optimal time step Δt

When a Brownian particle has to reach a small target of size a , the time step of the simulation is limited by a . Indeed to insure a correct Brownian simulation and that the discretized trajectory does not jump over the binding site, the time step Δt of the simulations should be restricted by the target size. A criteria is that the mean square displacement should be less than a fraction of the target size a :

$$\langle |\mathbf{X}(t + \Delta t) - \mathbf{X}(t)|^2 \rangle = 2dD\Delta t \leq \alpha^2 a^2, \quad (2.82)$$

where d is the dimension of the Brownian motion. In dimension 2, for $\alpha = 0.4$, $D_{Ca} = 200 \mu m^2 s^{-1}$ and $a = 0.001 \mu m$, $\Delta t = 10^{-10} ms$ which would lead to simulation time of several weeks to estimate the NET. Hence, imposing such a small Δt decreases drastically the efficiency of the simulations. It is possible to circumvent partially this difficulty by using an adaptive time step and creating an artificial larger hole, outside which the simulation can be much faster. In a disk of radius R , the strategy is the following (Fig. 2.9): away from the small target, the time step can be chosen such that the corresponding mean square displacement between two steps is smaller than $\Delta x_{\max} = \alpha R$, which gives $\Delta t_{\max} \leq \frac{\alpha^2 R^2}{4D}$. This time step Δt_{\max} is chosen outside a ball centered in the hole, and of radius $r_{\max} \geq R + 5\Delta x_{\max}$ (Fig. 2.9). Close to the hole, the mean square displacement should be $\Delta x_{\min} = \alpha a$, and thus $\Delta t_{\min} \leq \frac{\alpha^2 a^2}{4D}$, inside a ball of radius $r_{\min} \geq a + 5\Delta x_{\min}$ centered in the hole (Fig. 2.9). In the annulus $A(r_{\min}, r_{\max})$ between the balls of radii r_{\min} and r_{\max} , a linear interpolation of the mean square displacement can be chosen

$$\Delta x = v\Delta x_{\min} + (1 - v)\Delta x_{\max}, \quad v \in [0, 1]. \quad (2.83)$$

The annulus $A(r_{\min}, r_{\max})$ is thus partitioned into sub-domains obtained by intersecting balls of different radii.

The convergence of the simulations can then be checked by comparing the results of the arrival time for smaller time steps when an asymptotic value has been reached.

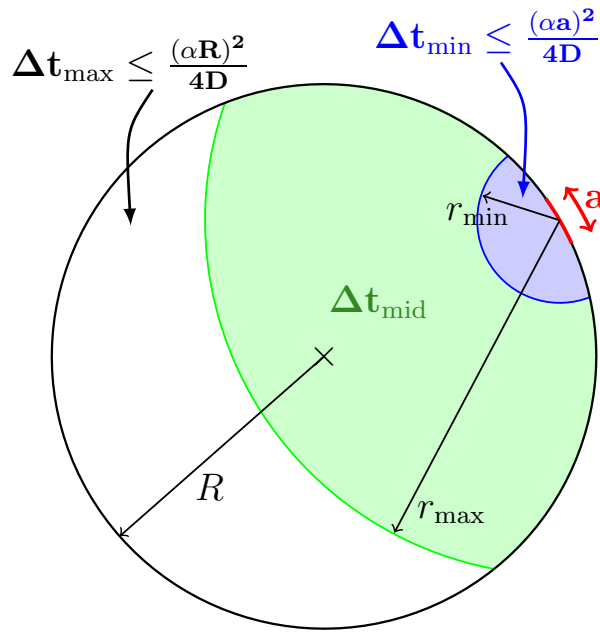


Figure 2.9: **Strategy to choose the adaptive time step for a two-dimensional disk.** Far from the target ($r > r_{\max}$), the time step Δt_{\max} depends on the radius of the disk. Close to the target ($r < r_{\min}$), the time step depends on the radius of the hole. The evolution of the mean square displacement between r_{\min} and r_{\max} is linear. The threshold r_{\min} and r_{\max} can be chosen considering that more than 99 % of a Gaussian function belongs to an interval of size ten times the variance.

Part II

Coarse-grained multiscale simulations of molecular dynamics

Chapter 3

Multi-scale methods and simulations of Brownian particles reaching small targets to compute the time distribution of vesicular release at neuronal synapses

The difficulties of simulating diffusion processes at a molecular level in cell microdomains are due to the multiple scales involving nano- to micrometers. Indeed, few to many particles have to be simulated and simultaneously tracked while exploring large portions of the cellular space, but also while binding small targets such as buffers or active sites. All these different spatial scales create rare events, due to the long time for finding a small target, which is the bottleneck in long simulations. Naive stochastic simulations involving many Brownian particles are computationally greedy and inefficient, and solving the associated partial differential equations is difficult due to the time dependent boundary conditions and the very heterogeneous geometrical constraints. The PDEs approach is also limited by the change of regimes from continuum to discrete, when a few particles are involved. We present here two reduced modeling approaches that allow fast computing of diffusing fluxes in microdomains. The first approach is based on new Markov-Mass action law equations, where a Markov chain is coupled to continuous differential equations. The second is based on the narrow escape and Poissonian rate approximation to coarse-grain simulations. The main application concerns diffusion in synapses where we compute the arrival time of calcium to small targets and predict the distribution of vesicular release following a single stimulation.

3.1 Introduction

A key procedure in computing statistical quantities and predicting cellular responses from molecular events, is to derive models and to design associated stochastic simulations of many Brownian particles. Those particles usually interact through binding events, and through the activation of specific sites. The challenges are several: in

principle long time simulations are expected because stochastic particles have to find small targets in a heterogeneous geometry containing large bulk, narrow passages and hidden sites. Moreover, the physical description of the particles motion involves many coupled stochastic equations in such geometry, leading to costly, long and inefficient numerical simulations. However, solving this ensemble of stochastic equations provides fundamental insights into the cellular processes, that are usually not yet resolved in live cell microscopy.

Past examples include hybrid simulations involving the connection between discrete and continuous events in simplified geometries [42, 56, 58]. This approach avoids to simulate a large number of particles in an infinite space. The difficulty is to code the appearance and disappearance of particles, which consists in computing at each simulation step the probability density function in the neighborhood (in the continuum) of an artificial boundary between the two regions.

We present here two reduced approaches based on the principle of replacing a system of PDE by a Markov chain coupled to a system of differential equations, and a molecular stochastic simulation by a Poissonian rate model. The first approach consists in a reduced model of molecular binding where we replace a complex system of coupled diffusion-reaction equations, too complicated to be resolved because it involves small targets and time dependent boundary conditions, by a Mass-action law system coupled to a Markov chain. This model accounts for the transition from the continuous to the discrete level, where a small and finite number of particles are necessary to activate a small target site and thus triggers a cellular event, a process that represents a change of scale. The second method we shall present coarse-grains traditional Brownian trajectories simulation into Gillespie's simulations, using rates that are estimated asymptotically by the narrow escape theory (NET) [85, 70]. Indeed, the arrival rate of a Brownian particle to a small target is well approximated by a Poissonian distribution.

We apply these two approaches to compute the distribution of the release time of a vesicle in the pre-synaptic terminal of a neuronal cell. This process called vesicular release, involves tracking ions binding at small targets positioned underneath a vesicle, when hundreds of ions are initially entering the synaptic domain following the propagation of an action potential [98]. For the past 20 years, a large modeling effort to understand vesicular release led to available Monte Carlo algorithms [104, 57] that allow to track individual particles and to simulate reaction-diffusion of discrete molecules in complex spatial environments [134]. Calcium-induced vesicular release was studied using MCell [3] and recently it was shown that the stochastic opening kinetics of the VGCCs are the main contributor to the variability observed in the release probability [134]. An other mathematical modeling study [204] predicts that a certain type of calcium channel (Ca(V)2.2) can create calcium nanodomains, that can activate a calcium-fusion sensor located on the proximal face of synaptic vesicles.

The paper is organized as follows: first, we present our model for the dynamic of calcium concentration in the pre-synaptic terminal. We describe the reaction-diffusion model and its limitations that prevented us to use it. This part is followed by our two reduced models. The first one is a Markov model coupled to a system of mass action law equations, and the second is stochastic, based on rate equations. We compare the results given by the two models that are in good agreement. Finally,

consequences for neuronal synaptic transmission are discussed.

3.2 Multi-scale model of diffusing ions in pre-synaptic terminal

Although multi-scale modeling of diffusing particle is generic in cell biology, we focus here on a specific example to build coarse-grained models. This example is the dynamic of calcium ions in the pre-synaptic terminal of neuronal cells.

3.2.1 Modeling calcium dynamic in the pre-synaptic terminal

The pre-synaptic terminal of a neuron contains vesicles that are released following an action potential, but the exact pathway and underlying molecular mechanisms are still under investigation. The molecular processes involved in vesicular release start after an action potential has triggered the opening of voltage-gated calcium channels (VGCCs), followed by calcium flow into the pre-synaptic domain. When several ions have succeeded by diffusion to find small molecular targets (synaptotagmin and many others) underneath a vesicle, a complex molecular machinery is activated leading to vesicular fusion with the cell membrane and neurotransmitters release [186]. Calcium ions can also bind and unbind to buffer molecules located in the bulk of the pre-synaptic terminal. Finally, they can be extruded through small pumps located on the surface of the domain or can exit at the end of the terminal, although this process is not completely documented. The success of the process where calcium ions find the target molecules by diffusion, depends also on the relative position between vesicles and channels and on their organization on the surface [106, 169, 103].

We model the pre-synaptic terminal geometry as a sphere (head) smoothly connected to a short cylinder (neck) (Fig. 3.1A). Vesicles are located in a region called the Active Zone (AZ), a small surface of the domain boundary that contains also VGCCs. VGCCs can be uniformly distributed on the AZ, or can form clusters. Calcium ions enter through VGCCs, and although they are charged, they are modeled as Brownian particles. The terminal also contains calcium buffer molecules and pumps, modeled as spherical binding sites located respectively inside the head and at the boundary. All ions, called also here particles, exit the domain when they are extruded through pumps or when they reach the end of the neck. Upon hitting a pump, a particle is absorbed during an extrusion time τ_{pump} , during which the pump is deactivated [88]. To trigger vesicular fusion, we assume that four to six calcium ions need to find the small target located at the junction between the vesicle, modeled as a sphere, and the surface membrane. This molecular target is represented by a small ribbon of height ε , located underneath the vesicle, which defines a geometrical cusp (Fig. 3.1B). After vesicular fusion, calcium ions previously bound to the target are released into the terminal.

The central question that motivates this analysis and the stochastic simulations is the following: how to compute the release probability of a vesicle and the distribution

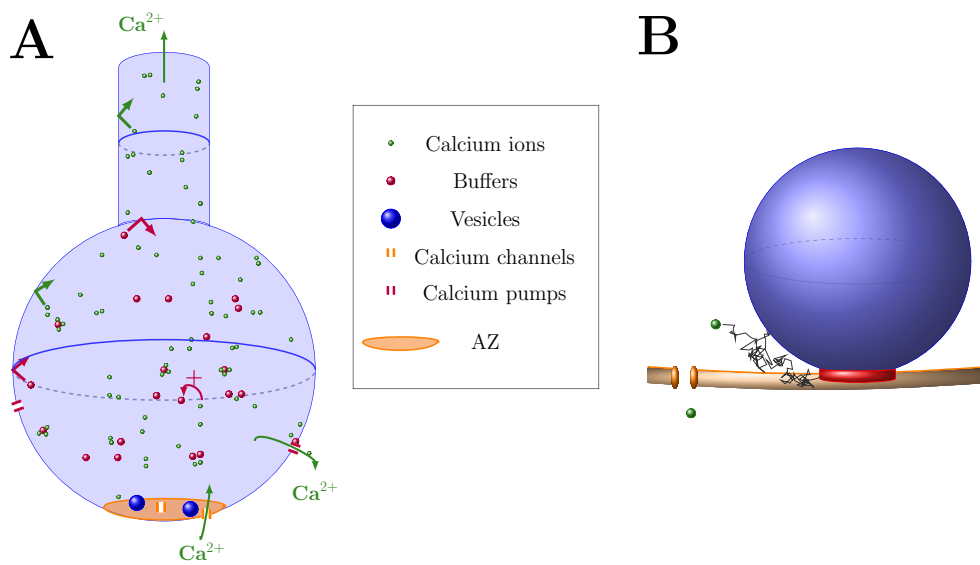


Figure 3.1: **Schematic representation of the pre-synaptic terminal.** **A:** The terminal is modeled as a sphere (head) connected to a cylinder (thin neck). Calcium ions are Brownian particles (green spheres) that enter through calcium channels located at the AZ (orange). They are reflected everywhere on the boundary except at the pumps (purple) and at the upper part of the cylinder where they are absorbed. They can be extruded through pumps and bind buffers (purple spheres) or the small targets underneath the vesicles (blue). **B:** Magnification of a docked vesicle at the AZ. Calcium ions (green spheres) enter through calcium channels (orange). They can bind the small ribbon target (red) located underneath a vesicle (blue).

of release events following an AP? And how does it depend on key parameters such as the relative distribution of channels and vesicles, the buffer concentration, or the minimal number T of bound particles (ions) necessary to trigger fusion? We start by a general description of the reaction-diffusion process, followed by some coarse-grained approximation that allow to perform realistic computations and simulations.

3.2.2 Reaction-diffusion equations for calcium in pre-synaptic terminal

The continuum description for the number of particles is based on a reaction-diffusion system of equations developed in [78, 80]. The density of particles (calcium ions) $M(\mathbf{x}, t)$ can be computed from the Fokker-Planck equation [171]. We partition the boundary of the domain Ω into two parts: one containing the pumps and the bottom of the neck $\partial\Omega_a(t)$ which absorb particles, while the remaining surface of the domain $\partial\Omega_r(t)$ reflect ions. The surface representing the AZ is denoted S_{AZ} (Fig. 3.1A). At the AZ, the vesicles are represented by spheres tangent to S_{AZ} , and the target molecules are represented by a small ribbon located near the tangential point (see section 3.2.1 and Fig. 3.1B).

We introduce the variables $B^{(j)}(\mathbf{x}, t)$, ($j \in \{0, 1\}$), that represent the density of buffers at point \mathbf{x} containing j bound particles at time t . The buffers are modeled as Brownian particles with a diffusion coefficient D_B . The total density of buffers at point \mathbf{x} at time t is

$$B_{tot}(\mathbf{x}, t) = B^{(0)}(\mathbf{x}, t) + B^{(1)}(\mathbf{x}, t). \quad (3.1)$$

The total number of buffers in the pre-synaptic domain is $B_{tot} = \int_{\Omega} B_{tot}(\mathbf{x}, t) d\mathbf{x}$, which is fixed. We assume that the forward and backward reaction rates, k_0 and k_{-1} , are constant and independent of the densities. The other variables to be introduced are the density of targets $S^{(j)}(\mathbf{x}, t)$, ($0 \leq j \leq T$) with j bound particles, where T is the number of bound particles necessary for activation. The targets are fixed in the domain, and hence the total density of targets at point \mathbf{x} is

$$S_0(\mathbf{x}) = \sum_j S^{(j)}(\mathbf{x}, t). \quad (3.2)$$

We shall neglect the unbinding from the targets, and assume that the forward reaction rate k_S is constant. A more detailed model taking into account cooperativity at the buffer binding sites, and the number of already bound particles at a target is presented in Appendix 3.7.

The reaction-diffusion equations for the density of free particles, $M(\mathbf{x}, t)$, of

buffers $B^{(j)}(\mathbf{x}, t)$ and of active targets $S^{(j)}(\mathbf{x}, t)$ are given by (see [78] for a derivation)

$$\begin{aligned}
 \frac{\partial M(\mathbf{x}, t)}{\partial t} &= -\nabla \cdot \mathbf{J}_M(\mathbf{x}, t) - k_0 M(\mathbf{x}, t) B^{(0)}(\mathbf{x}, t) + k_{-1} B^{(1)}(\mathbf{x}, t) \\
 &\quad - k_S M(\mathbf{x}, t) \sum_{j=0}^{T-1} S^{(j)}(\mathbf{x}, t) + T k_S M(\mathbf{x}, t) S^{(T-1)}(\mathbf{x}, t) \\
 \frac{\partial B^{(0)}(\mathbf{x}, t)}{\partial t} &= -\nabla \cdot \mathbf{J}_{B^{(0)}}(\mathbf{x}, t) - k_0 M(\mathbf{x}, t) B^{(0)}(\mathbf{x}, t) + k_{-1} B^{(1)}(\mathbf{x}, t) \quad (3.3) \\
 \frac{\partial B^{(1)}(\mathbf{x}, t)}{\partial t} &= -\nabla \cdot \mathbf{J}_{B^{(1)}}(\mathbf{x}, t) - k_{-1} B^{(0)}(\mathbf{x}, t) + k_0 M(\mathbf{x}, t) B^{(1)}(\mathbf{x}, t) \\
 \frac{\partial S^{(0)}(\mathbf{x}, t)}{\partial t} &= -k_S M(\mathbf{x}, t) S^{(0)}(\mathbf{x}, t), \\
 \frac{\partial S^{(i)}(\mathbf{x}, t)}{\partial t} &= k_S M(\mathbf{x}, t) [S^{(j-1)}(\mathbf{x}, t) - S^{(i)}(\mathbf{x}, t)], \quad i = 1..T-1 \\
 \frac{\partial S^{(T)}(\mathbf{x}, t)}{\partial t} &= k_S M(\mathbf{x}, t) S^{(T-1)}(\mathbf{x}, t),
 \end{aligned}$$

where the fluxes are defined by

$$\mathbf{J}_X(\mathbf{x}, t) = -D \nabla X(\mathbf{x}, t), \quad \text{for } X \in \{M, B^{(0)}, B^{(1)}\}. \quad (3.4)$$

The initial conditions are

$$B^{(0)}(\mathbf{x}, 0) = B_{tot}(\mathbf{x}), \quad B^{(1)}(\mathbf{x}, 0) = 0. \quad (3.5)$$

$$S^{(0)}(\mathbf{x}, 0) = S_0(\mathbf{x}), \quad S^{(j)}(\mathbf{x}, 0) = 0 \quad \text{for } 1 \leq j \leq T. \quad (3.6)$$

A target is activated by the binding of T particles. The system of equations 3.3 is a reaction-diffusion model of the transient calcium chemical-reaction in Ω . The initial and boundary conditions for $M(\mathbf{x}, t)$ are the initial reactant density, absorption at the absorbing boundary, and fluxes at the reflecting boundary:

$$\begin{aligned}
 M(\mathbf{x}, 0) &= c_0(\mathbf{x}) \quad \text{for } \mathbf{x} \in \Omega \\
 M(\mathbf{x}, t) &= 0 \quad \text{for } \mathbf{x} \in \partial\Omega_a(t) \\
 \mathbf{J}_M(\mathbf{x}, t) \cdot \boldsymbol{\nu}(\mathbf{x}) &= 0 \quad \text{for } \mathbf{x} \in \partial\Omega_r(t) \setminus S_{AZ} \\
 \mathbf{J}_M(\mathbf{x}, t) \cdot \boldsymbol{\nu}(\mathbf{x}) &= \frac{J_{tot}(t)}{S_{AZ}} \quad \text{for } \mathbf{x} \in S_{AZ}.
 \end{aligned} \quad (3.7)$$

$J_{tot}(t)$ is the flux of particles entering through the channels. A description of the flux of particles entering through one channel, $J(t)$, is given in subsection 3.4.1. Using this description, and in the case of l_V channels present at the AZ, the flux of particles entering becomes $J_{tot}(t) = l_V J(t)$. The initial boundary conditions for $B^{(0)}(\mathbf{x}, t)$ and $B^{(1)}(\mathbf{x}, t)$ are reflecting on all the boundary $\partial\Omega$. The geometric effect of target distribution is expressed in $S_0(\mathbf{x})$. The particular shape of the targets is quite delicate to account for, as they are small ribbons located at a cusp-like geometry (Fig. 3.1B). There are no moving internal boundaries, because the support of $S^{(j)}(\mathbf{x}, t)$ at all times is that of $S_0(\mathbf{x})$.

Finally, the number of activated vesicles is given by

$$N_{act}(t) = \int_{\Omega} S^{(T)}(\mathbf{x}, t) d\mathbf{x}. \quad (3.8)$$

In summary, this ensemble of reaction-diffusion equations describes the entrance of ions in a pre-synaptic terminal. This model already makes the approximation that pumps are replaced by fully absorbing holes, and doesn't allow to study the effect of calcium channels organization at the AZ. Moreover, there are several difficulties with this system of equation: first the analysis for the transient regime is not easy, second the location of the target in cusp leads to analytical and numerical difficulties. Thus, instead of analyzing or trying to simulate this difficult set of equations, we shall propose two alternatives and reduced models. The first is based on a new Markov-Mass action coupled system of equations, and the second is numerical based on coarse-graining diffusion to narrow target by Poissonian rates [84].

3.3 Markov-Mass action model for bridging the discrete-continuum levels

Brownian particles and small targets can be described by a coarse-grained model where particles are described by differential equations (continuum) for their number, while the binding to the targets is described by a Markov chain. We first describe our modeling of the AZ organization, followed by the Markov and the mass action equations, used later on to compute the vesicular release probability.

3.3.1 Model of target site organization at the AZ

The model starts when the Brownian particles enter the domain Ω through open channels located at points P_{ch} at the AZ. The inward flux through one channel at time t is $J(t)$ (an example of calcium influx is presented in section 3.4.1). Following the entrance, there are two fate for the particles. They either hit the small target sites underneath a sphere (vesicle) or they reach the bulk where they are lost in the undifferentiated state of many particles. These possibilities can precisely be computed from the splitting probability p_s that a particle hits a small target before entering the bulk [70]. We shall now describe our model for the AZ organization (Fig. 3.2).

We consider that there are N_{Dock} spheres (vesicles) of radius r_{ves} positioned on a square lattice (Fig. 3.2A-B) of length $2H$. The surface S_{AZ} of the AZ is

$$S_{AZ} = 4H^2 N_{Dock}. \quad (3.9)$$

When $H \geq H_c$ ($H_c = 0.07 \mu m$), the spheres are sparsely distributed, and for $H \leq H_{cc}$ ($H_{cc} = 0.03 \mu m$), we consider that we are in dense distributed regime. The target sites are small cylinders between the bottom of the sphere and the plane (red in Fig. 3.1B and 3.2A). We subdivide the AZ into squares S_Q of length $2H$ surrounding each sphere. To characterize the splitting probability p_s that a particle reaches any target on the AZ before reaching the bulk, we define a region called

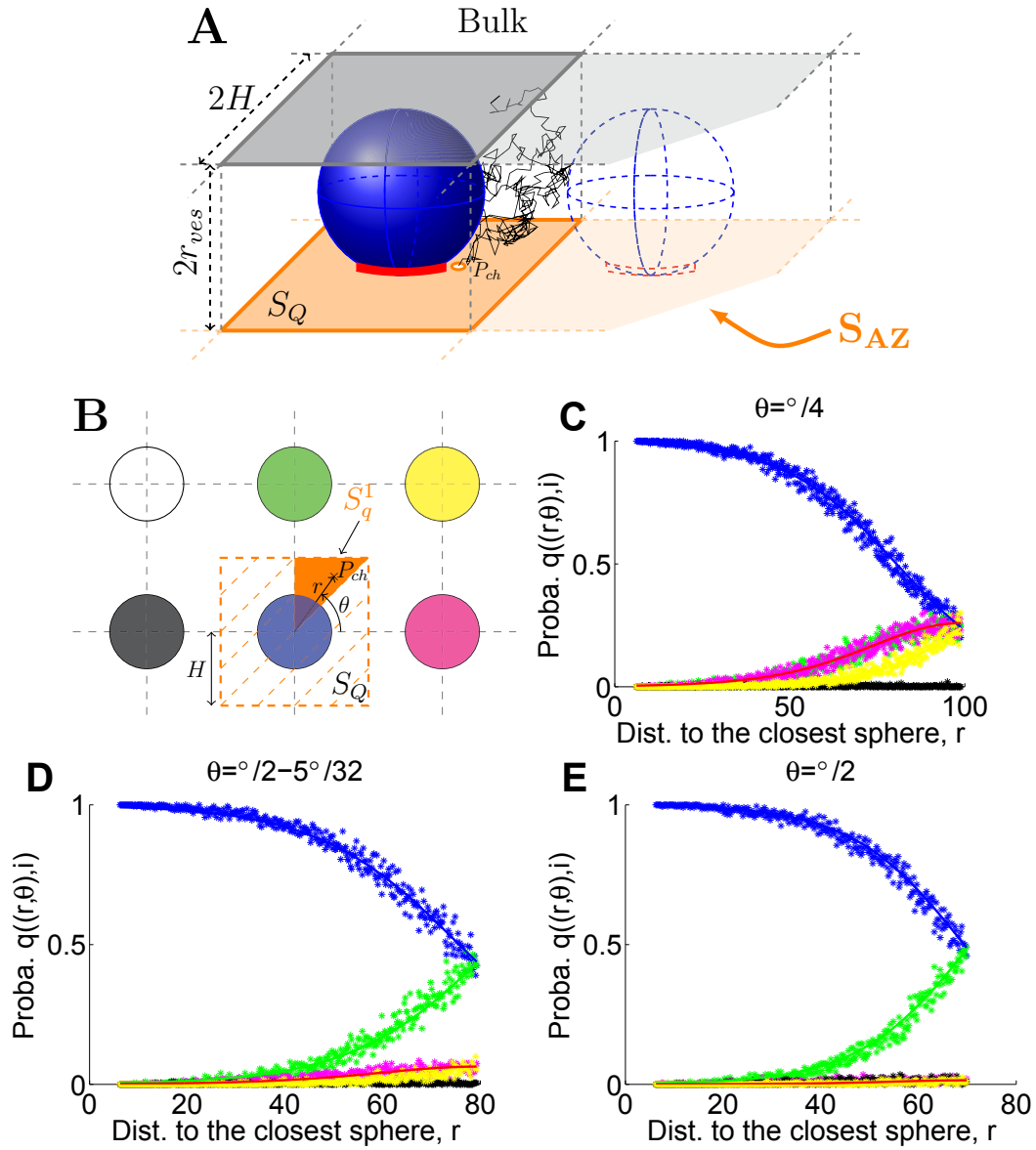


Figure 3.2: **Organization of the Active Zone (AZ).** The AZ is divided into elementary squares S_Q , where a vesicle (a sphere) is docked (**A**). The boundary layer around a sphere is the volume define as the rectangular cuboid around the sphere with lower face S_Q (orange square in **A**), height $2r_{ves}$ and upper face tangent to the sphere (gray square in **A**). The bulk is defined as the volume above the boundary layer, which is the complement of the bounadry layers of all the spheres. Brownian particles (calcium ions) enter through channels located at point P_{ch} (**A**), and escape the boundary layer through the gray surface. Each square S_Q can be subdivided into triangular subunits S_q^i (**B**), where we compute numerically the probability that a particle reaches the closest target (**C-E**, blue), the second closest (green or magenta), and so on. The length is $H = H_c$ and we use different values for the angle θ . The colors in **B** and **C-E** correspond.

boundary layer near each sphere, defined as a rectangular cuboid with face S_Q and height $2r_{ves}$, that engulf the spheres (Fig. 3.2A). The bulk is defined as the complement of the boundary layer above the AZ, which is the ensemble of boundary layers of all the spheres. After a Brownian particle enters through a channel located at point P_{ch} on the AZ, it can either reach a target site or leave the boundary layer around the spheres, through the face opposite to the AZ (gray in Fig. 3.2A). The splitting probability that a particle reaches any target before leaving the boundary layer, considering an infinite lattice full of spheres was computed in [70]:

$$p_s(P_{ch}) = 1 - \frac{1 - A \frac{r_{ves}^2 \varepsilon}{H^3}}{1 - \frac{2r_{ves} \varepsilon}{H^2}} \left(1 - \frac{2r_{ves} \varepsilon}{r(P_{ch})^2} \right), \quad (3.10)$$

where $A = 9.8$ and $r(P_{ch})$ is the distance to the closest target site. To determine the specific target that a particle will bind, we subdivide each square S_Q near a sphere into 8 sub-triangles $(S_q^i)_{i=1\dots 8}$ (Fig. 3.2B). Using symmetry we restrict our analysis to triangle S_q^1 . For an initial point $P_{ch} \in S_q^1$ (Fig. 3.2B), we estimate numerically the probability $q(P_{ch}, i_1)$ that the entering particle bind to the closest target i_1 , (blue in Fig. 3.2A), to the second closest i_2 , $q(P_{ch}, i_2)$ (green or magenta) and so on, as the distance $r(P_{ch})$ increases. We recall that the normalization identity is

$$\sum_{i=1}^{N_{Dock}} q(P_{ch}, i) = 1. \quad (3.11)$$

To compute numerically the distribution $q(P_{ch}, i)$, we decompose the triangle S_q^1 in uniform blocks parameterized in polar coordinates $(r_k, \theta_k)_k$, run 200 simulations for each k and fit the results using a routine procedure in Matlab (Fig. 3.2, the color code in **B** and **C-E** are the same). We neglect the probability to bind to the 5th-closest target and farther. This numerical result allows to compute the probability $q(P_{ch}, i)$ to reach specifically the target site i , when starting from point P_{ch} .

Finally, the fraction of particles entering through a channel positioned at P_{ch} , that reaches a target i , is $p_s(P_{ch})q(P_{ch}, i)$. Hence, the flux fraction coming from channel l located at \mathbf{x}^l and arriving to target i , $J^i(\mathbf{x}^l, t) = J(t)p_s(\mathbf{x}^l)q(\mathbf{x}^l, i)$, depends on the channel position \mathbf{x}^l and the target i .

3.3.2 A Markov chain to describe target activation

We shall now describe the Markov equations governing the target activation at the AZ. For a stationary channel distribution $f(\mathbf{x})$, the mean flux of particles originating from a channel that will arrive to a target is the average over the distribution

$$J^i(t) = \langle J^i(\mathbf{x}, t) \rangle_{\mathbf{x}} = \int_{S_{AZ}} J(t)p_s(\mathbf{x})q(\mathbf{x}, i)f(\mathbf{x})d\mathbf{x}. \quad (3.12)$$

When there are N_{Dock} independent targets sites and l_V channels located at positions $\vec{\mathbf{x}} = (\mathbf{x}^1, \dots, \mathbf{x}^{l_V})$, then for each target site i , the probability $Pr^i\{k, t, \vec{\mathbf{x}}\}$ that k particles are bound at time t can be computed from a Markov chain that we shall

describe now. In this model, once a particle (ion) binds to a target, it cannot unbind. Thus the transition probability from the state where there are $k - 1$ bounds to the state k during t and $t + \Delta t$ is due to the flux of particles originating from the bulk plus the one from open channels. In that case,

$$\begin{aligned} Pr^i\{k, t + \Delta t, \vec{\mathbf{x}}\} &= Pr^i\{k - 1, t, \vec{\mathbf{x}}\} \left(\sum_{l=1}^{l_V} J^i(\mathbf{x}^l, t) + k_S N_f(t) \right) \Delta t \\ &+ Pr^i\{k, t, \vec{\mathbf{x}}\} \left(1 - \left(\sum_{l=1}^{l_V} J^i(\mathbf{x}^l, t) + k_S N_f(t) \right) \Delta t \right), \end{aligned}$$

where k_S is the rate of arrival from the bulk and $N_f(t)$ the number of free particles in the bulk at time t .

A target is activated when there are exactly T -bound particles. In the limit Δt goes to zero, we obtain for each target $1 \leq i \leq N_{Dock}$ the Markov chain for the probabilities

$$\begin{aligned} p_k^i(t, \vec{\mathbf{x}}) &= Pr^i\{k, t, \vec{\mathbf{x}}\}, \\ \frac{dp_0^i(t, \vec{\mathbf{x}})}{dt} &= - \left(\sum_{l=1}^{l_V} J^i(\mathbf{x}^l, t) + k_S N_f(t) \right) p_0^i(t, \vec{\mathbf{x}}) \\ \frac{dp_k^i(t, \vec{\mathbf{x}})}{dt} &= \left(\sum_{l=1}^{l_V} J^i(\mathbf{x}^l, t) + k_S N_f(t) \right) (p_{k-1}^i(t, \vec{\mathbf{x}}) - p_k^i(t, \vec{\mathbf{x}})) \\ \frac{dp_T^i(t, \vec{\mathbf{x}})}{dt} &= \left(\sum_{l=1}^{l_V} J^i(\mathbf{x}^l, t) + k_S N_f(t) \right) p_{T-1}^i(t, \vec{\mathbf{x}}), \end{aligned} \quad (3.13)$$

where the last equation for p_T^i describes the absorbing state for $k = T$. The initial conditions at time $t = 0$ are

$$\forall i \in [1, N_{Dock}], p_k^i(0, \vec{\mathbf{x}}) = \delta_{k=0}. \quad (3.14)$$

Finally, the normalization condition is

$$\forall i \in [1, N_{Dock}], \sum_{k=0}^T p_k^i(t, \vec{\mathbf{x}}) = 1. \quad (3.15)$$

The time τ_T^i to the threshold T at target i is the first time that T particles are located at the target and it is also the last binding time of a particle when $T - 1$ particles are already at the site. In the context of vesicular release, τ_T^i is the time when the vesicle is released. The distribution of release time for the target i is given by

$$Pr\{\tau_T^i < t | \vec{\mathbf{x}}\} = p_T^i(t, \vec{\mathbf{x}}), \quad (3.16)$$

hence the probability density function $f_{\tau_T^i, \vec{\mathbf{x}}}$ of the release times is given by

$$f_{\tau_T^i, \vec{\mathbf{x}}}(t) = \frac{dp_T^i(t, \vec{\mathbf{x}})}{dt} = \left(\sum_{l=1}^{l_V} J^i(\mathbf{x}^l, t) + k_S N_f(t) \right) p_{T-1}^i(t, \vec{\mathbf{x}}) \quad (3.17)$$

and the mean release time is

$$\bar{\tau}_T^i = \int_0^\infty t f_{\tau_T^i, \vec{\mathbf{x}}}(t) dt. \quad (3.18)$$

3.3.3 The Mass action equations for the ion in the bulk

The dynamics of particles in the bulk is described by the differential equations for the number of free $N_f(t)$ and bound particles $N_b(t)$. Binding (resp. unbinding) occurs with a rate k_0 (resp. k_{-1} , section 3.2.2). The total number of buffer sites B_{tot} is fixed, but at time t , the number of available sites is $B_f(t) = B_{tot} - N_b(t)$. To model the extrusion of particles through pumps, the leaving through the neck and the binding to the target sites, we use that the arrival time of a Brownian particle to a small target is well approximated by a Poissonian process [175], which allows to replace the diffusion equation 3.3 by simple ordinary differential equations. Thus, particles are extruded by N_p pumps located on the surface of the domain Ω with a rate constant k_p , leave the domain with a rate k_a , and bind to target sites with a rate k_S (Table 3.1). Thoses rates can be estimated using the NET theory ([70, 85, 84] and section 3.4.2).

To derive the equations, we note that the total number of free target sites is given by, for each target i :

$$\sum_{k=0}^{T-1} p_k^i(t, \vec{\mathbf{x}}) = 1 - p_T^i(t, \vec{\mathbf{x}}). \quad (3.19)$$

Thus, the total number of free sites are

$$N_{Dock} - \sum_{i=1}^{N_{Dock}} p_T^i(t, \vec{\mathbf{x}}). \quad (3.20)$$

The influx of ions entering the bulk is $(l_V - \sum_{l=1}^{l_V} p_s(\mathbf{x}^l)) J(t)$.

In summary, the number of free particles in the bulk N_f , and the number of buffered ions N_b satisfies the mass-action equations:

$$\begin{aligned} \frac{dN_f}{dt} &= k_{-1}N_b - k_0(B_{tot} - N_b)N_f(t) + \left(l_V - \sum_{l=1}^{l_V} p_s(\mathbf{x}^l) \right) J(t) \\ &\quad - \left(k_p N_p + k_a + k_S \left(N_{Dock} - \sum_{i=1}^{N_{Dock}} p_T^i(t, \vec{\mathbf{x}}) \right) \right) N_f(t) \\ &\quad + T \sum_{i=1}^{N_{Dock}} \left(\sum_{l=1}^{l_V} J^i(\mathbf{x}^l, t) + k_S N_f(t) \right) p_{T-1}^i(t, \vec{\mathbf{x}}) \\ \frac{dN_b}{dt} &= -k_{-1}N_b + k_0(B_{tot} - N_b)N_f. \end{aligned} \quad (3.21)$$

The first two terms in the first equations are the classical unbinding and binding of calcium ions to buffers. The third terms represents the fraction of ions coming from the channels directly to the bulk. The fourth term corresponds to calcium

ions that are leaving the bulk by being extruded by pumps, by reaching the end of the neck and due to the binding at the target sites. Finally the last term account for the release of bound ions into the bulk following a release event. Indeed, after a release event, the T bound particles are released into the bulk, leading to an increase of N_f of T particles (eq. 3.17). The second equation is the classical mass action law for the number of bound buffers. The ensemble of equations 3.13-3.21 with the probability $p_T^i(t, \vec{\mathbf{x}})$ constitutes the Markov-Mass action description for the vesicular release based on calcium molecular dynamics.

3.3.4 Solving the coupled Markov equations

To solve equations 3.13 for each target site i , and for a specific channel distribution $\vec{\mathbf{x}}$, we rename the flux of particles by

$$g^i(t, \vec{\mathbf{x}}) = \sum_{l=1}^{l_V} p_s(\mathbf{x}^l) q(\mathbf{x}^l, i) J(t) + k_S N_f(t). \quad (3.22)$$

We solve the equations by a direct integration between t_0 and t , starting from the probability $p_0^i(t)$:

$$p_0^i(t) = A_0 \exp\left(-\int_{t_0}^t g^i(u, \vec{\mathbf{x}}) du\right). \quad (3.23)$$

The general solution for $k \in [0, T-1]$ is:

$$p_k^i(t, \vec{\mathbf{x}}) = \sum_{j=0}^k \frac{A_j}{(k-j)!} \left(\int_{t_0}^t g^i(u, \vec{\mathbf{x}}) du\right)^{k-j} \exp\left(-\int_{t_0}^t g^i(u, \vec{\mathbf{x}}) du\right), \quad (3.24)$$

and for the final step:

$$p_T^i(t, \vec{\mathbf{x}}) = A_T - \exp\left(-\int_{t_0}^t g^i(u, \vec{\mathbf{x}}) du\right) \sum_{j=0}^{T-1} \sum_{k=0}^{T-1-j} \frac{A_j}{k!} \left(\int_{t_0}^t g^i(u, \vec{\mathbf{x}}) du\right)^k, \quad (3.25)$$

where $(A_k)_{k \in [0, T]}$ are constants. Using the initial conditions 3.14, we get:

$$A_k = \delta_{k0} \quad (3.26)$$

for $k \in [0, T-1]$, and

$$A_T = 1, \quad (3.27)$$

which gives:

$$p_k^i(t, \vec{\mathbf{x}}) = \frac{1}{k!} \left(\int_{t_0}^t g^i(u, \vec{\mathbf{x}}) du\right)^k \exp\left(-\int_{t_0}^t g^i(u, \vec{\mathbf{x}}) du\right), \quad (3.28)$$

and

$$p_T^i(t, \vec{\mathbf{x}}) = 1 - \exp\left(-\int_{t_0}^t g^i(u, \vec{\mathbf{x}}) du\right) \sum_{k=0}^{T-1} \frac{1}{k!} \left(\int_{t_0}^t g^i(u, \vec{\mathbf{x}}) du\right)^k \quad (3.29)$$

$$= \exp\left(-\int_{t_0}^t g^i(u, \vec{\mathbf{x}}) du\right) \sum_{k \geq T} \frac{1}{k!} \left(\int_{t_0}^t g^i(u, \vec{\mathbf{x}}) du\right)^k. \quad (3.30)$$

The probability that k particles are bound at time t averaged over the distribution of channels is given for $k \in [0, T - 1]$:

$$\begin{aligned} p_k^i(t) &= \langle p_k^i(t, \vec{\mathbf{x}}) \rangle_{\vec{\mathbf{x}}} \\ &= \int_{S_{AZ}^{l_V}} \frac{1}{k!} \left(\int_{t_0}^t g^i(u, \vec{\mathbf{x}}) du \right)^k \exp \left(- \int_{t_0}^t g^i(u, \vec{\mathbf{x}}) du \right) f(\vec{\mathbf{x}}) d\mathbf{x}^1 \dots d\mathbf{x}^{l_V}, \end{aligned} \quad (3.31)$$

where $S_{AZ}^{l_V}$ is the product of l_V copies of the AZ. For $k = T$:

$$\begin{aligned} p_T^i(t) &= \langle p_T^i(t, \vec{\mathbf{x}}) \rangle_{\vec{\mathbf{x}}} \\ &= \int_{S_{AZ}^{l_V}} \exp \left(- \int_{t_0}^t g^i(u, \vec{\mathbf{x}}) du \right) \sum_{k \geq T} \frac{1}{k!} \left(\int_{t_0}^t g^i(u, \vec{\mathbf{x}}) du \right)^k f(\vec{\mathbf{x}}) d\mathbf{x}^1 \dots d\mathbf{x}^{l_V}, \end{aligned} \quad (3.32)$$

where $f(\vec{\mathbf{x}})$ is the probability density function of channels repartition. We shall simulate these equation and compare the result to a stochastic simulation approach that we describe now.

3.4 Exhaustive Brownian simulations of ions

An alternative approach for analyzing calcium dynamics with a finite number of targets and a large amount of buffers is to perform classical Brownian simulations, where we follow in time all single trajectories and binding events. However, this approach is quite greedy and inefficient. We now describe the main steps of such algorithm and our approach to coarse-grain it into a much faster numerical method based on Poissonian rates, where the narrow escape methodology [84] is used to obtain an expression for the mean arrival time to a target hidden in a cusp [70]. Long stochastic simulations are now replaced by a Gillespie algorithm.

3.4.1 Stochastic simulations

Ion trajectories are modeled as independent Brownian particles, with a diffusion coefficient D , when they are not bound to buffers:

$$\dot{\mathbf{X}}_k = \sqrt{2D} \dot{\mathbf{w}}_k, \text{ for } k = 1..N, \quad (3.33)$$

where \mathbf{w}_k are i.i.d Brownian motions of variance 1 and mean zero. The Euler's scheme $X(t + \Delta t) = X(t) + \sqrt{2D\Delta t} \xi$ where ξ is Gaussian, is used for simulations.

Geometry of the domain

The pre-synaptic terminal of neuron is approximated by a bulbous head, connected to the axon by a thin neck (Fig. 3.1). We represent the head as a sphere of radius R , continued by a cylinder of radius r_{neck} and height l_{neck} representing the neck (see Table 3.2 for the empirical values). Calcium ions are Brownian particles entering the terminal through channels located at the AZ and diffuse within the domain. The AZ is represented by a surface S_{AZ} , where vesicles are docked. The organization of the AZ was previously described in section 3.3.1.

Boundary conditions

The boundary $\partial\Omega$ contains a reflective $\partial\Omega_r$ and absorbing $\partial\Omega_a$ part. Diffusing particles are reflected at $\partial\Omega_r$ according to the classical Snell-Descartes reflection principle. The absorbing part of the boundary $\partial\Omega_a$ is composed of the end of the neck, and of the pumps, modeled by spheres of radius r_{pump} uniformly distributed along $\partial\Omega$ (Fig. 3.1). Upon hitting a pump, a particle is absorbed during a mean time τ_{pump} . During this extrusion time, the boundary becomes reflective [88], and hence the boundaries $\partial\Omega_a$ and $\partial\Omega_r$ are time-dependent.

Binding to buffers

Because the Smoluchowski's limit of the Langevin equation does not account for the velocity, when a particle is bound to a buffer represented by a potential well (see description in [88] and [78]), we place the ion at the buffer position during an exponential waiting time, the rate of which is the backward rate (reciprocal of the mean time to escape the energy barrier of the well). The buffer binding site is a sphere of radius r_{buff} . The buffers are distributed uniformly within the terminal, and can diffuse with a diffusion coefficient D_B . The binding of an ion on a buffer site occurs when the Brownian particle hits the small sphere $\partial B(r_{buff})$. For each bound ion, the probability to unbind is computed from the backward binding rate of calcium on the buffer, k_{-1} , and it is given by

$$P(\tau_{ub} \in [t, t + \Delta t]) \approx k_{-1}\Delta t. \quad (3.34)$$

After a particle unbinds, it is positioned outside the boundary layer of the binding site, about few (such as 3) radii away from the site [88, 78], and resumes its stochastic motion.

Activating the small targets

Activation of a vesicle is modeled here by the cumulative binding of particles to the target site. The target site is a narrow cylinder joining the plane and a tangent sphere representing the vesicle (Fig. 3.1B). When a particle hits the target, it increments the number of bound particles. When T particles are bound, we assume that the vesicle is released (vesicular fusion).

Influx of ions

The initial influx of ions through the voltage-gated calcium channels is driven in a neuronal cell by an AP [73, 178]. Using a simplified Hodgkin-Huxley model for calcium current, the membrane depolarization following an action potential (AP) is modeled using an applied current I_{app} . The equations are classical and summarized

below.

$$\begin{aligned}
 C \frac{dV}{dt} &= -I_{Na}(V, n) - I_K(V, n) - I_L(V) - I_{Ca}(V, m, h) + I_{app} \quad (3.35) \\
 \frac{dx}{dt} &= 0.1\alpha_x(1-x) - \beta_x x, \quad \text{for } x = n, m, h, \\
 V(0) &= V_0 \\
 n(0) &= n_0 \\
 m(0) &= m_0 \\
 h(0) &= h_0,
 \end{aligned}$$

where

$$\begin{aligned}
 I_{Na} &= g_{Na} p^3 (0.89 - 1.1n)(V - E_{Na}) \\
 I_K &= g_K n^4 (V - E_K) \\
 I_{Ca} &= g_{Ca} m^3 h (V_m - E_{Ca}) \\
 I_L &= g_L (V - E_L) \\
 p &= \frac{\alpha_p}{\alpha_p + \beta_p} \\
 \alpha_k &= \frac{1}{\tau_k} \frac{\theta_k - V_m}{e^{\frac{\theta_k - V_m}{\tau_k}} - 1}, \quad \beta_k = \eta_k e^{-\frac{V_m + 65}{\sigma_k}}, \quad \text{for } k = n, m, h, p.
 \end{aligned}$$

The initial values V_0, n_0, m_0, h_0 are the equilibrium solutions of the ODE and the different parameters are summarized in Table 3.3. The result of this classical routine is to generate a transient $I_{Ca}(t)$. The arriving of an AP is modeled by applying a current $I_{app} = 50$ mV during 1 ms that depolarizes the membrane potential V . This depolarization creates sodium, potassium, calcium and leak currents that shape the AP. The corresponding calcium current (Fig. 3.3) lasts 2.75 ms, with a maximal

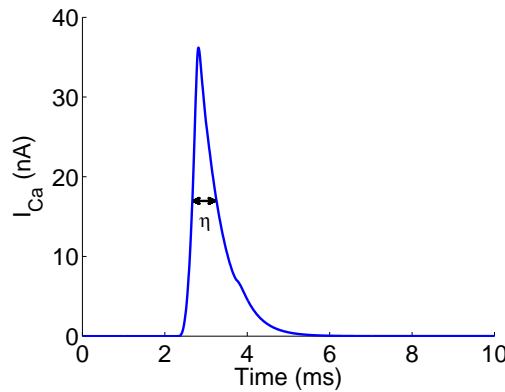


Figure 3.3: **Total calcium flux entering the domain through one channel.** The calcium current is generated using eq. 3.35, with parameters described in Table 3.3. The full width at half maximum η is 580 μ s. 80 ions enter into the domain.

value of $I_{Ca, \max} = 36.2$ nA, and a full-width at half maximum $\eta = 580$ μ s. The total charge is $Q = 0.025$ fC. This current corresponds to the entry of 80 calcium ions injected in the domain.

3.4.2 Coarse-grained stochastic dynamics with Poissonian rates

Instead of running a Brownian simulations, we shall now coarse-grain the model using rates that we shall describe now. Indeed, the arrival time of a Brownian particle to a small target is well approximated by a Poissonian process [175], the rate of which is computed from the NET for the cases at hand [70, 85, 84]. The coarse-graining consists in replacing the Brownian simulations by a rate process. Instead of following each stochastic trajectories, we disregard the motion of ions in the bulk. Indeed, the main goal of these simulations is to track rare events of binding to small targets (SNARE-binding sites of radii 1 nm for a synaptic domain), which is well approximated by an exponential law of mean the NET. We can thus replace the motion of particles by rates processes. We now present the Poissonian rates used in the simulations.

Rates of Arrival to small buffers and of escape from the domain

The arrival rate of a Brownian particle to small binding sites that are uniformly distributed over the domain Ω is Poissonian [175, 81]. The buffer are positioned at independent sites, modeled by small spheres. The mean first arrival time $\bar{\tau}_B$ of a Brownian particle to a small spherical target of radius r in the domain Ω , with diffusion coefficients D for the particle and D_B for the buffer, is given by [173]

$$\bar{\tau}_B = \frac{|\Omega|}{4\pi(D + D_B)r}. \quad (3.36)$$

The binding times are exponentially distributed with a rate equal to the reciprocal of the binding time

$$k_0 = 1/\bar{\tau}_B. \quad (3.37)$$

When there are N_f independent Brownian particles, the rate constant for the first binding event is

$$\lambda(N_f) = k_0 N_f. \quad (3.38)$$

The conditional probability that a binding event occurs between time t and $t + \Delta t$, when there are N_f particles is $\mathbb{P}(t \leq T_b < t + \Delta t | N_f) = \lambda(N_f)\Delta t$. The arrival probability during Δt at each buffer site available $N_b(t)$ is $k_0 N_f(t)\Delta t$, when there are exactly $N_f(t)$ free particles. The release rate to a binding site is also Poissonian with probability $k_{-1}\Delta t$ (see section 3.2.2).

The number of particles (ions) is not fixed, but decays in time due to the escape occurring either at some part of the domain (the end of the neck) or at the pumps, summarized into the boundary $\partial\Omega_a(t)$. Assuming that $|\partial\Omega_a(t)| \ll |\partial\Omega|$, then the NET ensures that the escape at the end of the neck is Poissonian, which is the reciprocal of the mean escape time [82], given by

$$\bar{\tau}_a = \frac{|\Omega_h|}{4Dr_{neck}} + \frac{l_{neck}|\Omega_h|}{D\pi r_{neck}^2} + \frac{l_{neck}^2}{2D}, \quad (3.39)$$

where D is the particles diffusion coefficient and the geometry of the domain is described in Fig. 3.1 and consists of a head, of volume $|\Omega_h|$ and a cylindrical neck with parameters r_{neck} and l_{neck} . The entire domain is $\Omega = \Omega_h \cup \Omega_{neck}$. When there are $N_f(t)$ particles in Ω at time t , the probability $p_a(t)$ that a particle leaves through the neck between t and $t + \Delta t$ is

$$p_a(t, \Delta t) = \frac{N_f(t)}{\tau_a} \Delta t. \quad (3.40)$$

We do not model at this stage the dynamics of the N_p pumps, that occupy a small fraction of the boundary, there are modeled as pure absorbers and thus the extrusion rate is Poissonian with a mean time

$$\bar{\tau}_{pump} = \frac{|\Omega_h|}{4Dr_{pump}}. \quad (3.41)$$

where r_{pump} is the radius of a pump. The probability $p_{pump}(t)$ that a particle arrives between time t and $t + \Delta t$ is

$$p_{pump}(t, \Delta t) = \frac{N_f(t)}{\tau_{pump}} \Delta t. \quad (3.42)$$

However, when a particle binds to a pump, it is extruded for a deterministic time τ_{pump} during which no other particle can be trapped. To finish, we note that crowding by obstacles in the pre-synaptic terminal of a neuron is taken into account by reducing the effective diffusion coefficient. Calcium diffusion coefficient is $D_{Ca,f} = 200 \mu\text{m}^2\text{s}^{-1}$ [121], but the effective diffusion coefficient can be reduced to $D_{Ca,c} = 20 \mu\text{m}^2 \text{s}^{-1}$ in dendrites to account for crowding and obstacles [13]. The NET presented here are computed using $D = D_{Ca,c}$ (Table 3.1).

Rates of arrival to the target site

The fraction of particles entering through a channel positioned at \mathbf{x} , that reaches a target i , is $p_s(\mathbf{x})q(\mathbf{x}, i)$ (section 3.3.1). We approximate the conditional mean time to exit the boundary layer before reaching any of the target (see section 3.3.1) by the escape time from a band of width $2r_{ves}$:

$$\bar{\tau} = \frac{(2r_{ves})^2}{2D_{Ca,f}} \quad (3.43)$$

where $D_{Ca,f}$ is the diffusion coefficient for particle moving inside the boundary layer of the AZ. Using the parameter of Tables 3.1 and 3.2 ([121, 208]), we obtain $\bar{\tau} \approx 4 \cdot 10^{-3}$ ms. To estimate the conditional binding time $\bar{\tau}_b$ with respect to the distance r , we generated stochastic Brownian numerical simulations in an infinite checkerboard with $H = 90$ nm. We find from our numerical approximation that the time $\bar{\tau}_b$ is linear with respect to the distance r to the closest vesicle, and thus

$$\bar{\tau}_b = p_1 r + p_2, \quad (3.44)$$

where $p_1 = 7.34 \cdot 10^{-2} \text{ ms } \mu\text{m}^{-1}$ and $p_2 = 2.1 \cdot 10^{-4} \text{ ms}$ (fitted using Matlab).

Finally, because ions present in the bulk and hence located outside the boundary layer of the vesicle can also bind to the targets, with a Poissonian rate, we use the narrow escape theory [70] to get an estimate

$$\langle \tau_{Target} \rangle = \frac{|\Omega_h|}{4\pi D_{Ca,c} \varepsilon}, \quad (3.45)$$

where $|\Omega_h|$ is the volume of the head and ε is the height of the ribbon defining the target sites. Finally, the probability $p_{Target}(t)$ to bind a target from the bulk, between t and $t + \Delta t$ is

$$p_{Target}(t) = \frac{N_f(t)}{\tau_{Target}} \Delta t. \quad (3.46)$$

The ensemble of rate formula described in this section will be used now in fast stochastic simulations to compute the time course of calcium dynamics in the pre-synaptic terminal and to estimate vesicular release.

3.4.3 Stochastic simulations with the Poissonian rate and the Markov-Mass action law models

We compare the numerical results obtained from the stochastic model based on rate equations (section 3.4.2), and from the Markov-Mass action model which gives a system of ODE coupled to a Markov chain (section 3.3), in the case of a uniform distribution of the channels on the Active Zone.

Using the Poissonian rates described above for the stochastic model (section 3.4.2), we use a Gillespie's type algorithm to simulate the response to a single influx of particles $l_V J(t)$ (Fig. 3.4). The influx from a single channel $J(t)$ is described in section 3.4.1. We investigate the influence of the number of buffer sites in the bulk (Fig. 3.4), and observe that the mean number of activated sites decreases to reach a plateau.

3.4.4 Computing the distribution of release times for a uniform channel distribution

Using the two methods described above about coarse-graining stochastic equations into rate simulations and deriving a Markov-Mass action system, we now compute the probability distribution of the release time for target i , τ_T^i , when channels are uniformly distributed (eq. 3.16).

Using the rate simulation approach, we compute the empirical distribution of vesicular release time $\tau_T^{i,k}(\mathbf{x})$ for the k^{th} -realization when a channel is located at position \mathbf{x} and use the convergence of the empirical sum to the expectation, as an estimator

$$\bar{\tau}_T^i(\mathbf{x}) = \lim_{N \rightarrow \infty} \frac{1}{N} \sum_{k=1}^N \tau_T^{i,k}(\mathbf{x}), \quad (3.47)$$

We find that the distribution of release time $\tau_T^i(\mathbf{x})$ is bimodal (Fig. 3.4D): the first peak corresponds to the vesicular release by ions that are coming directly from the

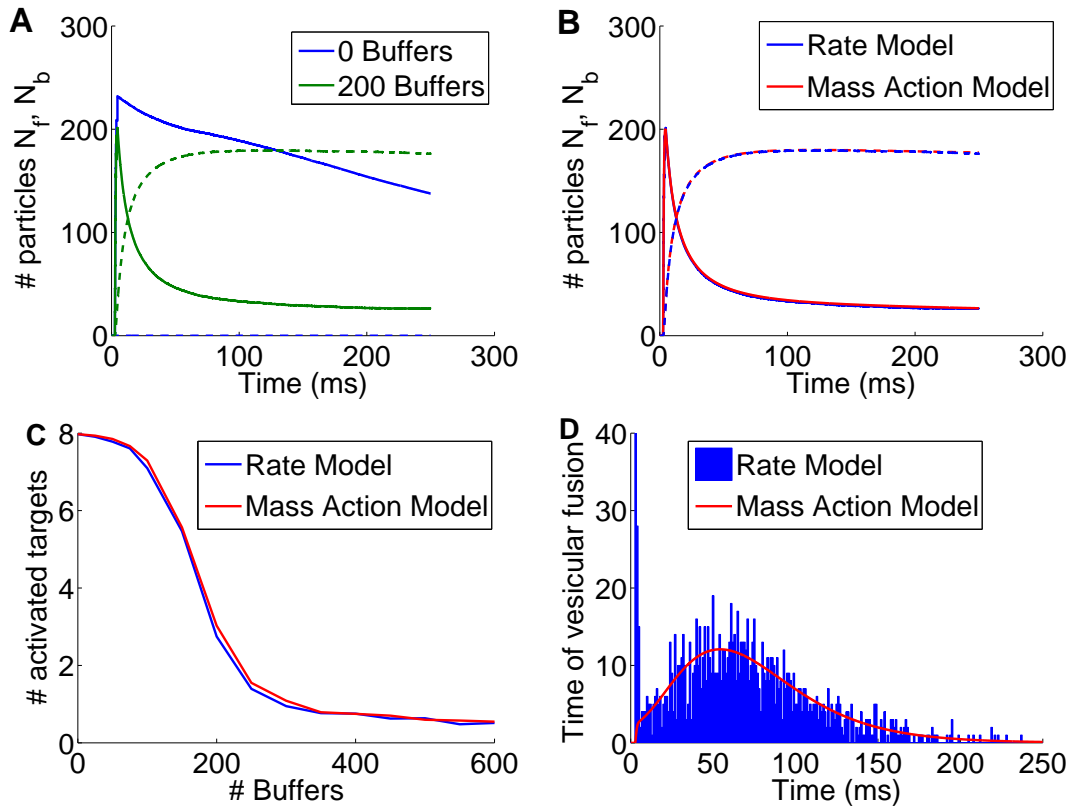


Figure 3.4: **Calcium time course in the pre-synaptic terminal and vesicular release activation.** Channels are uniformly distributed. **A:** Number of free (continuous) and buffered (dotted) ions for 0 (blue) and 150 (green) buffer sites. The curves represent the mean over 150 simulations obtained using the rate model. **B:** Comparison between the stochastic rate model (blue) and Markov-Mass action chain (red). The curves represent the number of free (continuous) and buffered (dotted) ions when there are 200 buffers. They are averaged over 150 simulations for both models. **C:** Mean number of activated targets with respect to the number of buffers, for the stochastic (blue) and the Markov-Mass action (red) models. **D:** Histogram of vesicular release time for the stochastic (blue), and the Markov-Mass action model (red) when there are no buffer sites.

channel influx, while the second peak is due to release from the random arrival of ions located in the bulk to the vesicular target sites, until $T - 1$ sites per vesicle are occupied. This large distribution follows the entrance of ions from channels activated by an AP, so that vesicles are already occupied by some ions.

To compute the fraction of particles reaching a target, we recall that the flux of particles reaching a target i and coming from the opening of a channel is given in eq. 3.12 by

$$J^i(t) = \langle J^i(\mathbf{x}, t) \rangle_{\mathbf{x}} = \int_{S_{AZ}} J(t) p_s(\mathbf{x}) q(\mathbf{x}, i) f(\mathbf{x}) d\mathbf{x} \quad (3.48)$$

$$= J(t) \int_{S_{AZ}} p_s(\mathbf{x}) q(\mathbf{x}, i) f(\mathbf{x}) d\mathbf{x}, \quad (3.49)$$

where we average over the position of channels in the AZ. To further determine the flux to the target sites, we need to account for the relative distribution of channels with respect to vesicle. The AZ is divided into elementary squares where vesicles are centered at the lattice points (section 3.3.1, Fig. 3.2A-B). Due to symmetry, we subdivide each square S_Q^i into elementary triangles $(S_{q_j^i})_{j=1..8}$ (Fig. 3.2B). Hence the surfaces are related by $|S_{AZ}| = N_{Dock} |S_Q^1| = 8N_{Dock} |S_{q_1^1}|$, and for a uniform distribution of channels

$$f(\mathbf{x}) = \frac{1}{|S_{AZ}|} \mathbb{1}_{S_{AZ}}. \quad (3.50)$$

We assume that for a given channel location, the closest target receives all the particles, i.e. $\forall \mathbf{x}, i, q(\mathbf{x}, i) = 1$ if i is the closest target to \mathbf{x} , and 0 otherwise. Hence, the fraction of particles reaching a target i does not depend anymore on the target i , and is given by

$$F_{ions} = \int_{S_{AZ}} p_s(\mathbf{x}) q(\mathbf{x}, i) f(\mathbf{x}) d\mathbf{x} = \frac{1}{|S_{AZ}|} \sum_j \int_{S_Q^j} p_s(\mathbf{x}) q(\mathbf{x}, i) d\mathbf{x} \quad (3.51)$$

$$= \frac{1}{|S_{AZ}|} \int_{S_Q^i} p_s(\mathbf{x}) d\mathbf{x} \quad (3.52)$$

$$= \frac{1}{N_{Dock} |S_{q_1^1}|} \int_{S_{q_1^1}} p_s(\mathbf{x}) d\mathbf{x}. \quad (3.53)$$

Using the expression for the splitting probability (eq. 3.10), we find that the leading order term in ε for the fraction F_{ions} of particles reaching a target, when there is only one channel is

$$F_{ions} = \frac{r_{ves}\varepsilon}{N_{Dock}H^2} \left[\pi \ln \left(\frac{2H}{\sqrt{2r_{ves}\varepsilon}} \right) + \left(\frac{Ar_{ves}}{H} - 2(K+1) \right) \right] + O(\varepsilon^2 \ln(\varepsilon)), \quad (3.54)$$

where $K = \sum_{n \geq 0} \frac{(-1)^n}{(2n+1)^2} \approx 0.9160$ (see Appendix 3.8 for a detailed computation). When there are l_V channels uniformly distributed, the mean fraction is simply $l_V F_{ions}$.

The results for various values of l_V , for channels uniformly distributed on a lattice with $N_{Dock} = 8$ targets [208], are presented in Table 3.4. The linear relation between

the number of channels and the fraction of particles reaching the targets under vesicles indicates that the channel organization (clustered or uniformly distributed) has no influence on the number of particles (ions) reaching the targets. Indeed, for l_V channels and n particles entering through a single channel, in the case of a uniform distribution of channels, the mean number of particles that reach the targets is $nl_V F_{ions}$. When the l_V channels are organized in p clusters uniformly distributed, containing each $(l_{V,i})_{i=1..p}$ channels, then the mean number of particles reaching the targets is the sum

$$\sum_{i=1}^p nl_{V,i} F_{ions} = nl_V F_{ions}. \quad (3.55)$$

3.4.5 Computing the distribution of release times for a uniform channel distribution

We compute the probability that k ions are bound to the target proteins underneath a vesicle at time t , averaged over the distribution of channels. We consider that the closest target receives all ions. The probability of having a vesicle with an empty target site is exactly the zero order probability of the Markov chain (see eq. 3.23), thus

$$\begin{aligned} p_0^i(t) &= \int_{S_{AZ}^{l_V}} \exp \left(- \int_{t_0}^t \sum_{l=1}^{l_V} p_s(\mathbf{x}^l) q(\mathbf{x}^l, i) J(u) + k_S N_f(u) du \right) f(\vec{\mathbf{x}}) d\mathbf{x}^1 \dots d\mathbf{x}^{l_V} \\ &= \frac{1}{|S_{AZ}|^{l_V}} \exp \left(-k_S \int_{t_0}^t N_f(u) \right) \left[\int_{S_{AZ}} \exp \left(-p_s(\mathbf{x}) q(\mathbf{x}, i) \int_{t_0}^t J(u) du \right) d\mathbf{x} \right]^{l_V} \\ &= \frac{1}{|S_{AZ}|^{l_V}} \exp \left(-k_S \int_{t_0}^t N_f(u) \right) \left[|S_{AZ} \setminus S_Q^i| + 8 \int_{S_{q_1}^1} \exp \left(-p_s(\mathbf{x}) \int_{t_0}^t J(u) du \right) d\mathbf{x} \right]^{l_V} \end{aligned} \quad (3.56)$$

where $S_{AZ}^{l_V}$ is the product of l_V copies of the AZ. Similarly, for $k = 1..T-1$ (eq. 3.33):

$$\begin{aligned} p_k^i(t) &= \frac{1}{k! |S_{AZ}|^{l_V}} \exp \left(-k_S \int_{t_0}^t N_f(u) \right) \int_{S_{AZ}^{l_V}} \left(\sum_{l=1}^{l_V} p_s(\mathbf{x}^l) q(\mathbf{x}^l, i) \int_{t_0}^t J(u) du + k_S \int_{t_0}^t N_f(u) du \right)^k \\ &\quad \times \exp \left(- \sum_{l=1}^{l_V} p_s(\mathbf{x}^l) q(\mathbf{x}^l, i) \int_{t_0}^t J(u) du \right) d\mathbf{x}^1 \dots d\mathbf{x}^{l_V}. \end{aligned} \quad (3.57)$$

For each target i , using the partition of S_{AZ} into S_Q^i and $S_{AZ} \setminus S_Q^i$. We get,

$$\begin{aligned} p_k^i(t) &= \frac{1}{k! |S_{AZ}|^{l_V}} \exp \left(-k_S \int_{t_0}^t N_f(u) \right) \sum_{j=1}^{l_V} \binom{l_V}{j} |S_{AZ} \setminus S_Q^i|^{l_V-j} \times \\ &\quad \int_{S_Q^i} \left(\sum_{l=1}^j p_s(\mathbf{x}^l) \int_{t_0}^t J(u) du + k_S \int_{t_0}^t N_f(u) du \right)^k \exp \left(- \sum_{l=1}^j p_s(\mathbf{x}^l) \int_{t_0}^t J(u) du \right) d\mathbf{x}^1 \dots d\mathbf{x}^j. \end{aligned} \quad (3.58)$$

Finally, the mean activation probability, $p_T^i(t)$ is given by:

$$p_T^i(t) = 1 - \sum_{k=0}^{T-1} p_k^i(t). \quad (3.59)$$

Because these probabilities p_k^i are independent of i , the probability that k particles are bound at time t to any target is $p_k(t) = p_k^1(t)$ for $k = 0..T$.

We now compare the analytical expression of the probabilities with the stochastic simulations (150 runs), for 10 different values of the number of buffers (from 0 to 600) and for an activation threshold $T = 5$. The values of l_V are (3, 12, 24), while we keep the total number of ions entering the domain fixed. We compare the analytical probabilities 3.58 and the stochastic simulations at time $t_1 = 5.3ms$, just after the last entry of ions from a channel. We notice in the stochastic simulations that the probabilities $p_k(t_1)$ do not depend much on the number of buffers, as the number of ions arriving from the bulk between $t = 0$ and $t = t_1$ (averaged over all runs) is very small 0.88 ± 0.12 . We thus neglect the flux from the bulk $k_S N_f(t)$ in the total flux to the target in the analytical expression. Thus, the probabilities that k particles are bound at time t_1 are well approximated from relation 3.56, leading to

$$p_0(t_1) = \frac{1}{|S_{AZ}|^{l_V}} \left[|S_{AZ} \setminus S_Q^i| + 8 \int_{S_{q_1}^1} \exp(-p_s(\mathbf{x})Q) d\mathbf{x} \right]^{l_V} \quad (3.60)$$

and for $k = 1..T - 1$ (eq. 3.33) by

$$p_k(t_1) = \frac{1}{k! |S_{AZ}|^{l_V}} \sum_{j=1}^{l_V} \binom{l_V}{j} |S_{AZ} \setminus S_Q^1|^{l_V-j} \times \int_{S_Q^{1..j}} \left(\sum_{l=1}^j p_s(\mathbf{x}^l)Q \right)^k \exp \left(- \sum_{l=1}^j p_s(\mathbf{x}^l)Q \right) d\mathbf{x}^1 \dots d\mathbf{x}^j, \quad (3.61)$$

where $Q = \int_0^{t_1} J(u)du$ is the total charge entering through one channel (section 3.4.1).

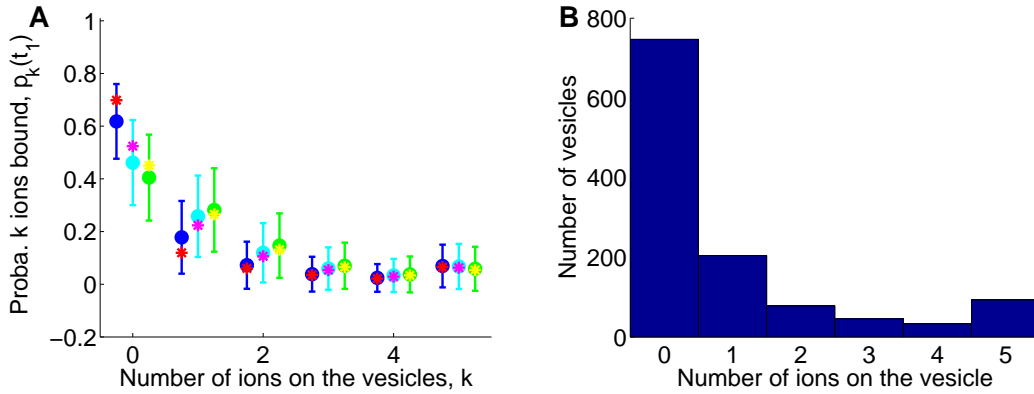


Figure 3.5: **Distribution of ions on target sites after the transient injection of calcium ion.** **A:** Comparing the stochastic simulation of the rate model (error bars) and the analytical results from the Markov-Mass action model (stars), for $l_V = 3$ (red and blue), $l_V = 12$ (magenta and cyan) and $l_V = 24$ (yellow and green). **B:** Histogram of the number of ions on the vesicles at the end of the short transient regime ($t = 5.3$ ms) for the stochastic simulations, with 200 buffer sites and the parameters in Tables 3.1 and 3.2 (150 runs). The total number of vesicles in the histogram is 1200. Note that $n=5$ corresponds to the sum of fused vesicles.

We have estimated these integrals numerically and obtained a good agreement while comparing them with numerical simulations (Fig. 3.5A). Finally Fig. 3.5B show the distribution of vesicle containing 0,1,2,3,4 ions and the cumulative distribution of those that have fused ($T=5$).

3.5 Discussion and Conclusion

We presented two models and computational approaches to analyze the coupling of Brownian ions from a continuum ensemble with a discrete ensemble of events described by a set of Markov equations. The first model couples mass action law to a Markov chain and the second uses the Narrow Escape Theory to coarse-grain Brownian simulations into a Gillespie's approach combined with Poissonian rates (Fig. 3.4).

These two approaches can be used for any large ensemble of particles, where they interact in the continuum but can also trigger the activation of a sub-system, monitored by the accumulation of few particles to a given threshold. In addition, both procedures allow running fast simulations with precise analytical descriptions. In a biological context, these computing procedures reflect the change of scale from the molecular to the cellular level.

To illustrate the applicability of these two methods, we focused on the distribution of vesicular release at synapses from calcium dynamics. Both approaches converge to the conclusion that there are two regimes for vesicular release: one at short time scale (less than 10 ms) following the direct opening of the calcium channels where a large fraction of vesicles are released, while in the second period, the distribution is strongly depend on the interaction with buffer molecules and can last hundreds of milliseconds. The emergence of these two phases can also explain asynchronous quantal release reported in [168], without introducing any additional time constant at a molecular level [134].

The present approach can be generalized to describe short-term plasticity at a molecular level, see also [103, 150]. It might also be possible to include calcium channel motion as recently observed [170].

3.6 Tables

Table 3.1: Biophysical parameters used in simulations. Extracted from literature for the Parallel fiber to Purkinje cell synapse, and estimated from the model (section 3.4.2).

Parameter	Description	Value
D	Calcium diffusion coefficient	$200 \mu m^2 s^{-1}$ [121]
$D_{Ca,c}$	Calcium diffusion coefficient + crowding	$20 \mu m^2 s^{-1}$ [88]
D_B	Buffer diffusion coefficient	$20 \mu m^2 s^{-1}$ see [129]
k_{-1}	Buffer unbinding constant	500 ms
τ_{Buff}	Buffer mean binding time	1.8 sec (computed from the model)
$k_0 = \frac{1}{\tau_{Buff}}$	Rate of binding to buffers	0.56 sec^{-1}
τ_{Target}	Mean time to bind to a ribbon target	3.6 sec (computed from the model)
$k_S = \frac{1}{\tau_{Target}}$	Rate of binding to targets	0.28 sec^{-1}
τ_a	Mean time to leave through the neck	0.659 sec (computed from the model)
$k_a = \frac{1}{\tau_a}$	Rate of leaving through the neck	1.52 sec^{-1}
τ_{pump}	Mean time to bind to a pump	11.3 sec (computed from the model)
$k_p = \frac{1}{\tau_{pump}}$	Rate of binding to pumps	0.089 sec^{-1}
$\tau_{In,pump}$	Inactivation time of a pump	9 ms [88]

Table 3.2: Geometrical parameters used in simulations. Extracted from literature for the Parallel fiber to Purkinje cell synapse.

Parameter	Description	Value
R	Radius of the pre-synaptic terminal	$0.6 \mu m$ [209]
N_{Buff}	Buffer quantity/type	[0-700]
r_{Buff}	Radius of the buffers binding site	$0.001 \mu m$ [88]
r_{ves}	Radius of the vesicle	$0.02 \mu m$ [208]
ε	Height of the ribbon target	$0.001 \mu m$
r_{neck}	Radius of the pre-synaptic neck	$0.1 \mu m$ [208]
l_{neck}	Length of the pre-synaptic neck	$0.15 \mu m$ [208]
S_{AZ}	Surface of the AZ	$0.13 \mu m^2$ [208]
N_{Dock}	Mean/maximal number of Docked vesicles	8 [208]
N_{Pump}	Quantity of pumps	10
r_{pump}	Radius of the pumps binding site	$0.001 \mu m$ [88]
l_V	Quantity of calcium channels	[3-24]
# Ca	# Ca entered after 1 AP	[10-80], estimated from [129, 139]

Table 3.3: Hodgkin-Huxley

Parameter	Description	Value
C	Capacitance	$1 \mu\text{F.cm}^{-2}$
g_{Na}	Conductance of Na^{2+} -current	120 mS.cm^{-2}
E_{Na}	Equilibrium potential of Na^{2+} -current	50 mV
τ_m	Parameter for m	10 ms
θ_m	Parameter for m	-40 mV
η_m	Parameter for m	4
σ_m	Parameter for m	18
g_K	Conductance of K^+ -current	36 mS.cm^{-2}
E_K	Equilibrium potential of K^+ -current	-77 mV
g_L	Conductance of leak current	0.3 mS.cm^{-2}
E_L	Equilibrium potential of leak current	-54.4 mV
τ_n	Parameter for n	10 ms
θ_n	Parameter for n	-55 mV
η_n	Parameter for n	0.125
σ_n	Parameter for n	80
g_{Ca}	Conductance of Ca^{2+} -current	$14.5 \cdot 10^{(-9)} \text{ mS.cm}^{-2}$
E_{Ca}	Equilibrium potential of Ca^{2+} -current	140 mV
τ_m	Parameter for m	ms
θ_m	Parameter for m	mV
η_m	Parameter for m	
σ_m	Parameter for m	
τ_h	Parameter for h	ms
θ_h	Parameter for h	mV
η_h	Parameter for h	
σ_h	Parameter for h	
V_0	Initial value for V	-65.0974
n_0	Initial value for n	0.3162
m_0	Initial value for m	$4.5649 \cdot 10^{-45}$
h_0	Initial value for h	1

Table 3.4: Fraction of particles reaching a target for different channel number l_V

l_V	Simulated mean \pm std	Theoretical value $l_V F$
3	0.0158 ± 0.0043	0.0160
12	0.0628 ± 0.0090	0.0642
24	0.1264 ± 0.0135	0.1283

3.7 Appendix A: A refined model of diffusing ions in the pre-synaptic terminal

We present in this appendix a refinement of the models detailed in sections 3.2.2 and 3.3. We consider that the ribbon is now divided into N_s target sites, which allows to take into account the availability of each site at a target. We also consider that buffers has $N_{b,s}$ binding sites that express cooperativity, as for example when considering the binding of calcium ions on calmodulin. We first present the corresponding system of partial differential equations, and then the corresponding reduced Markov-Mass action law equations.

3.7.1 PDEs description

As for the previous model equations, the density of particle $M(\mathbf{x}, t)$ satisfies the Fokker-Planck equation [171], and the boundary of the domain Ω is partitioned into two parts, $\partial\Omega_a(t)$ (absorbing) and $\partial\Omega_r(t)$ (reflecting). S_{AZ} represents the AZ.

We introduce the variables $B^{(j)}(\mathbf{x}, t)$, ($0 \leq j \leq N_{b,s}$), that represent the number of buffer in a volume about \mathbf{x} that contains j bound particles at time t . The number of occupied binding sites on these proteins is $jB^{(j)}(\mathbf{x}, t)$ and the number of free binding sites is $(N_{b,s} - j)B^{(j)}(\mathbf{x}, t)$. Obviously, at all times the mass conservation is

$$\sum_{j=0}^{N_{b,s}} \int_{\Omega} B^{(j)}(\mathbf{x}, t) = B_{tot},$$

where B_{tot} is the total number of proteins in the domain, which is fixed. We consider the forward reaction rates for the binding of one particle on an available site, when j particles are already bound, k_j , ($0 \leq j \leq N_{b,s} - 1$) and the backward reaction rates for the unbinding of one of the j bound particles, $k_{-(j)}$, ($1 \leq j \leq N_{b,s}$). We assume that those rates are independent of the densities. We will further consider a forward binding rate when j particles are already bound, \tilde{k}_j , that already include the number of available sites. k_j and \tilde{k}_j can be connected through the relation $\tilde{k}_j = (N_{b,s} - j)k_j$. In the same way, we will consider the backward binding rates $(\tilde{k}_{-(j)})_j$ that include the number of already bound particles, $\tilde{k}_{-(j)} = jk_{-(j)}$.

The density of target $S^{(j)}(\mathbf{x}, t)$ ($0 \leq j \leq T$) with j bound particles was introduced in section 3.2.2. We consider that the target is divided into N_s different sites, which allows to take into account the site occupancy at each target. We assume that the sites are identical and independent, and that the binding constant to a site is k_{sn} . The threshold for target activation is T .

The reaction-diffusion equations for the number of free particles, $M(\mathbf{x}, t)$, the

buffer $B^{(j)}(\mathbf{x}, t)$ and the active targets $S^{(j)}(\mathbf{x}, t)$ are

$$\begin{aligned}
\frac{\partial M(\mathbf{x}, t)}{\partial t} &= -\nabla \cdot \mathbf{J}_M(\mathbf{x}, t) - M(\mathbf{x}, t) \sum_{j=0}^{N_{bs}-1} \tilde{k}_j B^{(j)}(\mathbf{x}, t) + \sum_{j=1}^{N_{bs}} \tilde{k}_{-(j)} B^{(j)}(\mathbf{x}, t) \\
&\quad - M(\mathbf{x}, t) \sum_{j=0}^{T-1} k_{sn}(N_s - j) S^{(j)}(\mathbf{x}, t) + T M(\mathbf{x}, t) k_{sn}(N_s - T + 1) S^{(T-1)} \\
\frac{\partial B^{(0)}(\mathbf{x}, t)}{\partial t} &= -\nabla \cdot \mathbf{J}_{B^{(0)}}(\mathbf{x}, t) + \tilde{k}_{-(1)} B^{(1)}(\mathbf{x}, t) - M(\mathbf{x}, t) \tilde{k}_0 B^{(0)}(\mathbf{x}, t) \\
\frac{\partial B^{(j)}(\mathbf{x}, t)}{\partial t} &= -\nabla \cdot \mathbf{J}_{B^{(j)}}(\mathbf{x}, t) + \tilde{k}_{-(j+1)} B^{(j+1)}(\mathbf{x}, t) - \tilde{k}_{-(j)} B^{(j)}(\mathbf{x}, t) \\
&\quad + M(\mathbf{x}, t) (\tilde{k}_{j-1} B^{(j-1)}(\mathbf{x}, t) - \tilde{k}_j B^{(j)}(\mathbf{x}, t)), \quad j = 1..N_{bs} \\
\frac{\partial B^{(N_{bs})}(\mathbf{x}, t)}{\partial t} &= -\nabla \cdot \mathbf{J}_{B^{(N_{bs})}}(\mathbf{x}, t) - \tilde{k}_{-(N_{bs})} B^{(N_{bs})}(\mathbf{x}, t) + M(\mathbf{x}, t) \tilde{k}_{N_{bs}-1} B^{(N_{bs}-1)}(\mathbf{x}, t) \\
\frac{\partial S^{(0)}(\mathbf{x}, t)}{\partial t} &= -M(\mathbf{x}, t) k_{sn} N_s S^{(0)}(\mathbf{x}, t) \\
\frac{\partial S^{(i)}(\mathbf{x}, t)}{\partial t} &= M(\mathbf{x}, t) k_{sn} (N_s - i + 1) S^{(i-1)}(\mathbf{x}, t) - M(\mathbf{x}, t) k_{sn} (N_s - i) S^{(i)}(\mathbf{x}, t), \quad i = 1..T - 1 \\
\frac{\partial S^{(T)}(\mathbf{x}, t)}{\partial t} &= M(\mathbf{x}, t) k_{sn} (N_s - T + 1) S^{(T-1)}(\mathbf{x}, t)
\end{aligned} \tag{3.62}$$

where the fluxes are defined by

$$\mathbf{J}_X(\mathbf{x}, t) = -D \nabla X(\mathbf{x}, t), \quad \text{for } X \in \{M, (B^{(j)})_j\}. \tag{3.63}$$

The initial conditions are

$$B^{(0)}(\mathbf{x}, 0) = B_{tot}(\mathbf{x}), \quad B^{(j)}(\mathbf{x}, 0) = 0 \quad \text{for } 1 \leq j \leq N_{bs}. \tag{3.64}$$

$$S^{(0)}(\mathbf{x}, 0) = S_0(\mathbf{x}), \quad S^{(j)}(\mathbf{x}, 0) = 0 \quad \text{for } 1 \leq j \leq T. \tag{3.65}$$

The initial and boundary conditions for $M(\mathbf{x}, t)$ are as in section 3.2.2 the initial reactant density, absorption at the absorbing boundary, and flux given by the motion of the reflective boundary:

$$\begin{aligned}
M(\mathbf{x}, 0) &= c_0(\mathbf{x}) \quad \text{for } \mathbf{x} \in \Omega(t) \\
M(\mathbf{x}, t) &= 0 \quad \text{for } \mathbf{x} \in \partial\Omega_a
\end{aligned} \tag{3.66}$$

$$\begin{aligned}
\mathbf{J}_M(\mathbf{x}, t) \cdot \boldsymbol{\nu}(\mathbf{x}) &= 0 \quad \text{for } \mathbf{x} \in \partial\Omega_r \setminus S_{AZ} \\
\mathbf{J}_M(\mathbf{x}, t) \cdot \boldsymbol{\nu}(\mathbf{x}) &= \frac{J_{tot}(t)}{S_{AZ}} \quad \text{for } \mathbf{x} \in S_{AZ}
\end{aligned} \tag{3.67}$$

$J_{tot}(t)$ is the flux of particles entering through the channels. The initial boundary conditions for $(B^{(j)})_j$ are reflective on $\partial\Omega$.

3.7.2 Markov-Mass action model

We now derive the Markov equation for each target and the mass action equations for the number of free particles in the bulk, considering that the ribbon is divided

into N_s target sites that are identical and independent, and that buffers have $N_{b,s}$ binding sites that express cooperativity.

Equations for the Markov chain

As for the previous model (section 3.3), we consider l_V channels, located at positions $\vec{\mathbf{x}} = (\mathbf{x}^1, \dots, \mathbf{x}^{l_V})$. For each target site i , the probability $Pr^i\{k, t, \vec{\mathbf{x}}\}$ that k particles are bound at time t can be computed from a Markov chain. We assume here that once a particle is bound to the target, it cannot be released. The binding rate from the bulk is k_{sn} , and the target is activated when there are exactly T -bound particles. We consider the flux of particles arriving to a site located at target i , entered at point \mathbf{x}^l when k sites are occupied at i : $J^i(\mathbf{x}^l, t, k)$. As all the sites at a target are independent, we have $J^i(\mathbf{x}^l, t, k) = (N_s - k)J^i(\mathbf{x}^l, t)$, where $J^i(\mathbf{x}^l, t)$ represents the flux of particle arriving at one site.

We obtain for each target $1 \leq i \leq N_{Dock}$ the Markov chain, with $p_k^i(t, \vec{\mathbf{x}}) = Pr^i\{k, t, \vec{\mathbf{x}}\}$,

$$\begin{aligned} \frac{dp_0^i(t, \vec{\mathbf{x}})}{dt} &= -N_s \left(\sum_{l=1}^{l_V} J^i(\mathbf{x}^l, t) + k_{sn}N_f(t) \right) p_0^i(t) \\ \frac{dp_k^i(t, \vec{\mathbf{x}})}{dt} &= (N_s - k + 1) \left(\sum_{l=1}^{l_V} J^i(\mathbf{x}^l, t) + k_{sn}N_f(t) \right) p_{k-1}^i(t) \\ &\quad - (N_s - k) \left(\sum_{l=1}^{l_V} J^i(\mathbf{x}^l, t) + k_{sn}N_f(t) \right) p_k^i(t) \\ \frac{dp_T^i(t, \vec{\mathbf{x}})}{dt} &= (N_s - T + 1) \left(\sum_{l=1}^{l_V} J^i(\mathbf{x}^l, t) + k_{sn}N_f(t) \right) p_{T-1}^i(t), \end{aligned} \quad (3.68)$$

where the last equation for p_T^i describes the absorbing state for $k = T$. The initial conditions at time $t = 0$ are:

$$p_k^i(0) = \delta_{k0}. \quad (3.69)$$

Finally, the normalization is

$$\forall i \in [1, N_s], \sum_0^T p_k^i(t) = 1. \quad (3.70)$$

Mass action equations in the bulk

We describe the dynamic in the bulk using differential equations for the number of free particles $N_f(t)$ and the number of buffer proteins with j particles bound $B_j(t)$, $0 \leq j \leq N_{b,s}$. The number of bound particles $N_b(t)$ is then:

$$N_b(t) = \sum_{j=1}^{N_{b,s}} jB_j(t). \quad (3.71)$$

To derive the system of equation for N_f and $(B_j)_j$, we note that the number of free sites at target i , $S_f^i(t)$ is given by

$$\begin{aligned} S_f^i(t) &= \sum_{k=0}^{T-1} (N_s - k) p_k^i(t, \vec{\mathbf{x}}) \\ &= N_s(1 - p_T^i(t, \vec{\mathbf{x}})) - \mathbb{E}^i(t, \vec{\mathbf{x}}), \end{aligned} \quad (3.72)$$

where $\mathbb{E}^i(t, \vec{\mathbf{x}}) = \sum_{k=0}^{T-1} k p_k^i(t, \vec{\mathbf{x}})$ is the expectation of the number of occupied sites at target i .

The influx of ions entering the bulk J_{bulk} is given by:

$$\begin{aligned} J_{bulk}(t) &= J_{tot}(t) - \sum_{l=1}^{l_V} \sum_{i=1}^{N_{Dock}} \sum_{k=0}^T J^i(\mathbf{x}^l, t, N_s - k) p_k^i(t, \vec{\mathbf{x}}) \\ &= J_{tot}(t) - \sum_{l=1}^{l_V} \sum_{i=1}^{N_{Dock}} J^i(\mathbf{x}^l, t) S_f^i(t). \end{aligned} \quad (3.73)$$

The release of bound ions into the bulk following a release event is, as in section 3.3,

$$T \sum_{i=1}^{N_{Dock}} \frac{dp_T^i(t, \vec{\mathbf{x}})}{dt}. \quad (3.74)$$

The mass action equations in the bulk, for the number of free particles N_f and the number of buffers with j bound particles B_j , $j = 0..N_{b,s}$ is:

$$\begin{aligned} \frac{dN_f}{dt} &= \sum_{j=1}^{N_{b,s}} \tilde{k}_{-(j)} B_j(t) - \sum_{j=0}^{N_{b,s}-1} \tilde{k}_j B_j N_f(t) + J_{bulk}(t) \\ &\quad - \left(k_p N_p + k_a + k_{sn} \sum_{i=1}^{N_{Dock}} S_f^i(t) \right) N_f(t) \\ &\quad + T \sum_{i=1}^{N_{Dock}} \frac{dp_T^i(t, \vec{\mathbf{x}})}{dt} \end{aligned} \quad (3.75)$$

$$\begin{aligned} \frac{dB_0(t)}{dt} &= \tilde{k}_{-(1)} B_1 - N_f \tilde{k}_0 B_0 \\ \frac{dB_j(t)}{dt} &= -\tilde{k}_{-(j)} B_j + \tilde{k}_{-(j+1)} B_{j+1} - N_f \tilde{k}_j B_j + N_f \tilde{k}_{j-1} B_{j-1}, \quad j = 1..N_{b,s} - 1 \\ B_{N_{b,s}} &= B_{tot} - \sum_{j=0}^{N_{b,s}-1} B_j. \end{aligned}$$

Solving the Markov equations

We solve the system of equations 3.68 for each target i . The flux of particles in the boundary layer reaching one site is $g^i(t) = \left(\sum_{k=1}^{l_V} J^i(\mathbf{x}^l, t) + k_{sn} N_f(t) \right)$. We can solve by mathematical induction the equations between t_0 and t , starting from $p_0^i(t)$:

$$p_0^i(t) = A_0 \exp \left(-N_s \int_{t_0}^t g^i(u) du \right). \quad (3.76)$$

3.8. Appendix B: Detailed computation of the mean fraction of particles reaching any target, F_{ions} presented in section 3.4.4

The solution $p_k^i(t)$, for $k \in [0, T - 1]$ is:

$$p_k^i(t) = \sum_{j=0}^k (-1)^{j+k} A_j \frac{\prod_{l=j}^{k-1} (N_s - l)}{(k-j)!} \exp\left(- (N_s - j) \int_{t_0}^t g^i(u) du\right), \quad (3.77)$$

and for $p_T^i(t)$:

$$p_T^i(t) = A_T + \sum_{j=0}^{T-1} (-1)^{j+T} A_j \frac{\prod_{l=j+1}^{T-1} (N_s - l)}{(T-1-j)!} \exp\left(- (N_s - j) \int_{t_0}^t g^i(u) du\right), \quad (3.78)$$

where $(A_k)_{k \in [0, T]}$ are the integration constants. Using the initial conditions 3.69, we get:

$$A_k = \frac{\prod_{l=0}^{k-1} (N_s - l)}{k!} \quad (3.79)$$

for $k \in [0, T - 1]$, and

$$A_T = \frac{\prod_{l=0}^{T-1} (N_s - l)}{(T-1)!} \sum_{j=0}^{T-1} \binom{T-1}{j} \frac{(-1)^{j+T-1}}{N_s - j}. \quad (3.80)$$

3.8 Appendix B: Detailed computation of the mean fraction of particles reaching any target, F_{ions} presented in section 3.4.4

In this appendix section, we present the detailed computation of F_{ions} , the mean fraction of particles reaching any target in the case of a uniform distribution of channels. We remind that we do the approximation that the closest target receives all the particles, i.e. $\forall \mathbf{x}, i, q(\mathbf{x}, i) = 1$ if i is the target closest to \mathbf{x} , and 0 otherwise. The AZ is divided into elementary squares, $S_{AZ} = \cup_Q S_Q$ (Fig. 3.2A), and $|S_{AZ}| = 8N_{Dock}|S_q^1|$. For a uniform distribution of channels, $f(\mathbf{x}) = \frac{1}{|S_{AZ}|} \mathbf{1}_{S_{AZ}}$ and hence the mean fraction of particles reaching a target is:

$$\begin{aligned} \int_{S_{AZ}} p_s(\mathbf{x}) q(\mathbf{x}, i) f(\mathbf{x}) d\mathbf{x} &= \frac{1}{|S_{AZ}|} \sum_j \int_{\Omega_p^j} p_s(\mathbf{x}) q(\mathbf{x}, i) d\mathbf{x} \\ &= \frac{1}{|S_{AZ}|} \int_{S_Q} p_s(\mathbf{x}) d\mathbf{x} \\ &= \frac{1}{N_{Dock}|S_q^1|} \int_{S_q^1} p_s(\mathbf{x}) d\mathbf{x} \end{aligned}$$

We compute the leading order term in ε of the previous integral. In polar coordinates (r, θ) we get

$$\begin{aligned}
& \frac{1}{|S_q^1|} \int_{S_q^1} p_s(\mathbf{x}) d\mathbf{x} \\
&= \frac{2}{H^2} \int_0^{\pi/4} \int_{\sqrt{2r_{ves}\varepsilon}}^{H/\cos(\theta)} \left(1 - \frac{1 - 9.8 \frac{r_{ves}^2 \varepsilon}{H^3}}{1 - \frac{2r_{ves}\varepsilon}{H^2}} \left(1 - \frac{2r_{ves}\varepsilon}{r^2} \right) \right) r dr d\theta \\
&= \left[\frac{2r_{ves}\varepsilon}{H^4} \left(9.8 \frac{r_{ves}}{H} - 2 \right) + O(\varepsilon^2) \right] \left(\frac{H^2}{2} + O(\varepsilon) \right) \\
&\quad + \frac{2}{H^2} \left[2r_{ves}\varepsilon + \frac{(2r_{ves}\varepsilon)^2}{2H^2} \left(2 - 9.8 \frac{r_{ves}}{H} \right) + O(\varepsilon^3) \right] \int_0^{\pi/4} \int_{\sqrt{2r_{ves}\varepsilon}}^{H/\cos(\theta)} \frac{1}{r} dr d\theta \\
&= \left[\frac{r_{ves}\varepsilon}{H^2} \left(9.8 \frac{r_{ves}}{H} - 2 \right) + O(\varepsilon^2) \right] \\
&\quad + \frac{2}{H^2} \left[2r_{ves}\varepsilon + \frac{(r_{ves}\varepsilon)^2}{H^2} \left(2 - 9.8 \frac{r_{ves}}{H} \right) + O(\varepsilon^3) \right] \int_0^{\pi/4} \ln \left(\frac{H}{\cos(\theta)} \right) - \ln(\sqrt{2r_{ves}\varepsilon}) d\theta \\
&= \left[\frac{r_{ves}\varepsilon}{H^2} \left(9.8 \frac{r_{ves}}{H} - 2 \right) + O(\varepsilon^2) \right] \\
&\quad + \frac{2}{H^2} \left[2r_{ves}\varepsilon + \frac{(r_{ves}\varepsilon)^2}{H^2} \left(2 - 9.8 \frac{r_{ves}}{H} \right) + O(\varepsilon^3) \right] \left[\frac{\pi}{4} \ln \left(\frac{H}{\sqrt{2r_{ves}\varepsilon}} \right) - \frac{K}{2} + \frac{\pi \ln(2)}{4} \right] \\
&= \left[\frac{r_{ves}\varepsilon}{H^2} \left(9.8 \frac{r_{ves}}{H} - 2 \right) + O(\varepsilon^2) \right] \\
&\quad + \frac{2}{H^2} \left[2r_{ves}\varepsilon + \frac{(r_{ves}\varepsilon)^2}{H^2} \left(2 - 9.8 \frac{r_{ves}}{H} \right) + O(\varepsilon^3) \right] \left[\frac{\pi}{4} \ln \left(\frac{H}{\sqrt{2r_{ves}\varepsilon}} \right) - \frac{K}{2} + \frac{\pi \ln(2)}{4} \right] \\
&= \frac{\pi r_{ves}\varepsilon}{H^2} \ln \left(\frac{2H}{\sqrt{2r_{ves}\varepsilon}} \right) + \frac{r_{ves}\varepsilon}{H^2} \left(\frac{9.8r_{ves}}{H} - 2(K+1) \right) + O(\varepsilon \ln(\varepsilon)),
\end{aligned}$$

where $K = \sum_{n \geq 0} \frac{(-1)^n}{(2n+1)^2} \approx 0.915$ is the Catalan constant. We finally obtain the mean fraction F_{ions} of particles reaching any target, when there are l_V channels:

$$F_{ions} = \frac{l_V r_{ves} \varepsilon}{N_{Dock} H^2} \left[\pi \ln \left(\frac{2H}{\sqrt{2r_{ves}\varepsilon}} \right) + \left(\frac{9.8r_{ves}}{H} - 2(K+1) \right) \right] + O(\varepsilon \ln(\varepsilon)). \quad (3.81)$$

Part III

Modeling bursting oscillations in
neuronal networks for the genesis
of pre-Bötzinger Complex rhythms

Chapter 4

Robust network oscillations during mammalian respiratory rhythm generation driven by synaptic dynamics

*Published in Guerrier C, Hayes JA, Fortin G and Holcman D “Robust network oscillations during mammalian respiratory rhythm generation driven by synaptic dynamics. ” Proc. Natl. Acad. Sci. **112(31)**, pp 9728-33 (2015)*

How might synaptic dynamics generate synchronous oscillations in neuronal networks? We address this question in the preBötzinger Complex (preBötC), a brainstem neural network that paces robust, yet labile, inspiration in mammals. The preBötC is composed of a few hundred neurons that alternate bursting activity with silent periods, but the mechanism underlying this vital rhythm remains elusive. Using a computational approach to model a randomly connected neuronal network that relies on short-term synaptic facilitation (SF) and depression (SD), we show that synaptic fluctuations can initiate population activities through recurrent excitation. We also show that a two-step SD process allows activity in the network to synchronize (bursts) and generate a population refractory period (silence). The model was validated against an array of experimental conditions, which recapitulate several processes the preBötC may experience. Consistent with the modeling assumptions, we reveal, by electrophysiological recordings, that SF/SD can occur at preBötC synapses on timescales that influence rhythmic population activity. We conclude that nondeterministic neuronal spiking and dynamic synaptic strengths in a randomly connected network are sufficient to give rise to regular respiratory-like rhythmic network activity and lability, which may play an important role in generating the rhythm for breathing and other coordinated motor activities in mammals.

Significance Statement

The mechanism underlying mammalian respiratory rhythm generation in the preBötzinger Complex is still under debate. Here, we developed a simulation model to show that a synaptic depression/facilitation mechanism sufficient for neurons

to generate network rhythms, without the need for intrinsically rhythmic neurons. Simulations of the model under several normal or pathological conditions the living system experiences, together with critical electrophysiological experiments, converge to show that randomly connected neuronal networks with synaptic dynamics underlie rhythmic activity. This study provides a generally applicable mechanism for other central pattern generator systems that are less well understood.

4.1 Introduction

Central pattern generators (CPGs) are neuronal circuits that generate coordinated activity in the absence of sensory input [67]. One such mammalian CPG, the preBöttinger complex (preBötC), gives rise to the eupneic respiratory rhythm [184, 53]. Located in the medulla, the preBötC preserves a spontaneous respiratory-like rhythm when isolated in transverse slices, but the precise nature of the cellular and synaptic mechanisms underlying rhythmogenesis remains elusive [53, 143, 140, 110, 132]. An early hypothesis was that the neuronal activity is driven by intrinsically bursting pacemaker neurons synchronized via excitatory synaptic connections [184, 110, 23, 24]. However, electrophysiological and modeling studies [132, 160, 46, 164] now suggest the rhythm emerges through stochastic activation of intrinsic currents conveyed by recurrent synaptic connections, without the need for pacemaker neurons [53, 143, 46, 25, 111]. In either case, excitatory synapses are required for rhythm generation; the possibility that synaptic properties also underlie periodic burst initiation and termination is yet to be demonstrated.

Synaptic transmission relies on the release of vesicles, which can be modulated at the presynaptic terminal. Synaptic depression (SD), based on vesicular release, consists of decaying release probability after sustained activity, which subsequently decreases excitability within the underlying connected network. Conversely, synaptic facilitation (SF) enhances vesicular release probability and promotes neuronal synchronization. These synaptic dynamics are critical for short-term synaptic plasticity, and here they are explored in the context of preBötC rhythm generation.

We first consider a randomly connected network where each neuron is modeled using a generalized Hodgkin-Huxley system of equations, and exhibits spontaneous spiking activity based on a random process, but the neurons do not have intrinsic bursting mechanisms. These neurons are sparsely connected within a realistically sized network by excitatory synapses. The distinction of this model, from previous preBötC models, is that synapses express SF and SD that is implemented using two separate pools of vesicles, and creates dynamic synapses. The first pool is the readily releasable pool (RRP) and the other is the recycling pool (RP) [161] modeled with mass-action kinetics. Synaptic dynamics has been repeatedly used to describe changes in spike rates in neural network populations [49] and emergence of gamma oscillations [16]. Furthermore network connectivity can also participate to define bursting or the oscillation frequency in neural networks [196, 45].

We show here that random networks connected with these synaptic properties, with random spiking, are sufficient for periodic bursting and examine a variety of

experimental scenarios testing this model. The present model shows that an ensemble of excitatory neurons driven by synaptic dynamics can generate population-wide rhythmic activity and behaves in a manner similar to the preBötC under different conditions observed *in vitro*. Finally, we show experimentally that excitatory inputs to preBötC neurons often exhibit dynamically changing excitatory postsynaptic currents (EPSCs) supporting the modeled concept that SF/SD occurs on a timescale relevant to influence respiratory periods.

4.2 Results

4.2.1 Robust rhythmic activity generated in the model network.

To investigate whether rhythmic activity can emerge from randomly connected neurons with dynamic synapses, we simulated the membrane potential (V) in 400 neurons (*Materials and Methods*), comparable to the number of preBötC rhythm-generating neurons [72]. For each neuron, the key active properties are the RP and RRP for synaptic vesicles (Fig. 4.1A), whereas neuronal spikes are governed by Hodgkin-Huxley equations and driven by random membrane noise. The network has a structure where the neurons were laid on a 2D grid with a Gaussian distance-based connection probability with respect to each neurons neighbors [151] and is within the bounds of previous experimental observations [160, 25, 51]. The average number of output connections per neuron was 3.7, and the mean total number of connections was 7.5 (Fig. 4.1B, and *SI Appendix*, Fig. 3.S1A, $s = 0.9$, Eq. 4.2), which represents a neuron-to-neuron connection probability of about 2%. The connection probability required to obtain rhythmicity, with these cellular parameters, is in the range 1.2-2.5% (*Discussion* and *SI Appendix*, Fig. 3.S2).

In the absence of any external input, we found that local spontaneous spiking can generate rhythmic activity among the population (Fig. 4.1C, S1B), and like in experimental studies [25], the model reproduced the cycle-to-cycle variability both in the identity of the neurons leading successive population bursts (Movie S1) and the timing jitter of individual neuronal spike patterns across cycles. The bursts lasted on average 708 ± 140 ms and were followed by silent periods lasting on average 5.1 ± 1.2 sec (*SI Appendix*, Fig. 3.S1C and D), which is in the range observed for inspiratory cycles *in vitro* [53] (*SI Appendix*, Fig. 3.S3).

To further characterize bursting in this model, we illustrate the four principal state variables of a neuron with respect to time (Fig. 4.1D-E): its voltage V , its facilitation variable x , and the normalized depression-related variables Y_{free} and Y_{dock} . The fraction of vesicles in the RP (Y_{free}) is quite stable, oscillating between 80% and 98% of its maximum value, while the fraction of docked vesicles in the RRP (Y_{dock}) fluctuates between 20% and 100% of its filled state. Thus the RRP alternates between an empty and full state, where the mean maximum number of vesicles is 4.5. When the percentage of vesicles in the RRP (Y_{dock}) reaches its minimal value, the bursting period ends, leading to a decrease in the facilitation variable (x) that relaxes back to equilibrium (Fig. 4.1E). On the contrary, x increases exponentially

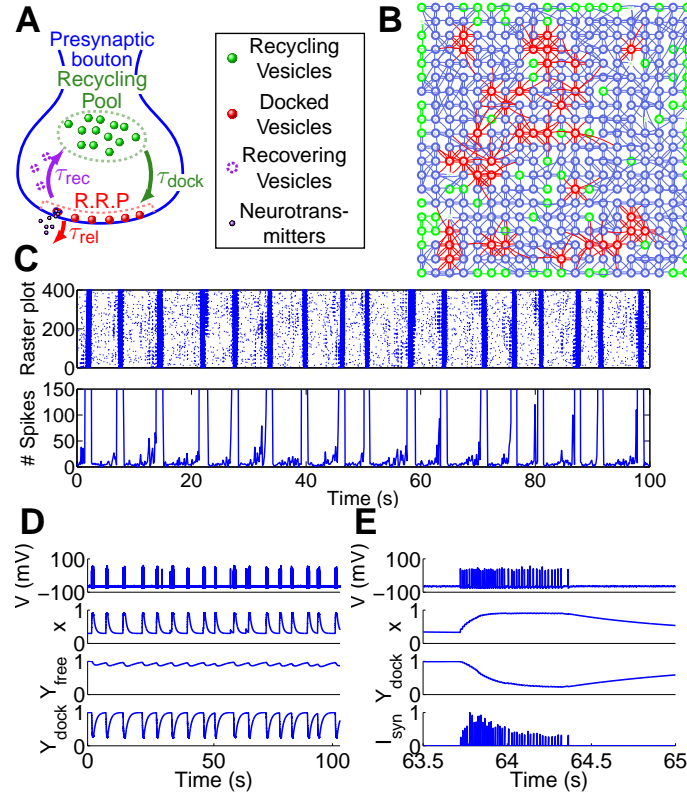


Figure 4.1: **The preBötzinger complex model and resulting network activity.** **A:** Schematic representation of the presynaptic bouton: vesicles are divided into two pools: diffusing (green) and docked at the active zone (AZ, red) with recovering ones (purple). After fusion, vesicles recover and enter the recycling pool. **B:** Example of a neuronal network (400 neurons) where neurons are located on a square lattice. The connections can be higher than 10 (red), between 5 and 10 (blue), or less than 5 (green). Neurons with no input or output are marked by green crosses, with no circles around. **C:** Upper) Raster plot for spiking neurons generated in Fig. 4.1B. During 100 s, the synchronous rhythmic patterns alternate between active and silent periods. Lower) Time-dependent plot of the number of spikes in the network, computed in time windows of 100 ms. The y axis is zoomed to observe the preburst increase in the number of spikes. **D:** Time-dependent plot of the voltage V , the facilitation variable x , and the scaled variables $Y_{\text{free}} = \frac{y_{\text{free}}}{y_{\text{max}}}$, $Y_{\text{dock}} = \frac{y_{\text{dock}}}{y_{\text{max}}}$ for a single neuron chosen randomly from the network (the mean bursting duration is 777 ± 98 ms, and the mean interburst interval is 5.2 ± 1.0 s). **E:** Magnification of V , x , Y_{dock} and I_{syn} for the neuron in Fig. 4.1D, during 1.5 s (same simulation as C and D).

when each population burst begins (Movie S2), which, associated with the decrease in Y_{dock} is reflected by a transient increase and subsequent decrease in the amplitude of synaptic currents during the bursts (I_{syn} , Fig. 4.1E). Each neuron within the network that reaches its minimum $y_{\text{dock}}^{\text{min}}$ enters a refractory state that shuts down its synaptic transmission (*SI Appendix*, Fig. 3.S1E and F). This minimum value leads to burst termination across the population because recurrent excitation ceases. As synapses recover, a subsequent burst can begin when several connected neurons spike in a short time interval to facilitate postsynaptic neuronal activation. This nonlinearly promotes spiking activity to spread through neighboring neurons and invade the entire network (Movie S2 and S3). These features were characteristic of additional networks with similar topologies and each network resulted in similar cycle periods (CPs), burst durations (BDs) and interburst intervals (IBIs) of 5.5 ± 1 s, 694 ± 138 ms, and 4.8 ± 1 s, respectively ($n = 10$ networks), which is in the range observed *in vitro*. Additionally, the CP and BD can be altered by changing synaptic parameters (*SI Appendix*, Figs. 3.S4 and 3.S5), and the spiking frequency during a burst (normally up to 60 Hz) can be modified by changing the HH-model parameters (*SI Appendix*, Fig. 3.S6). Altogether, this suggests that a large range of *in vitro* and *in vivo* data can be accounted for by this model.

4.2.2 Rhythmic activity depends on the number and strength of connected neurons.

With some neurodegenerative diseases, brainstem neurons die and are not replenished [68]. Similar conditions in rats cause sleep apneas that could lead to death without intervention [128]. To investigate the role of network size in our model, we randomly removed neurons as shown in Fig. 4.2A. When 12.5% of the network neurons were removed (50 neurons, *SI Appendix*, Fig. 3.S7), the network activity was not perturbed. When 25% (100 neurons) of the network was removed, the rhythm started to be affected, whereas bursts became erratic when this fraction reached 31% (125 neurons, Fig. 4.2Aa-b), and disappeared when more than 44% of neurons were removed (≥ 175 neurons, *SI Appendix*, Fig. 3.S7). Lesioning 175 neurons resulted in a CV of ~ 1 indicating a very unstable rhythm, and lesions beyond that eliminated all spontaneous bursts. Normalizing the number of lesioned neurons to the total required for complete rhythm cessation resulted in exponential increases in the CPs and variability (Fig. 4.2Ac), comparable to those obtained in previous physiological *in vitro* experiments [72, 52]. The proportion of lesioned neurons required to stop bursting is nevertheless higher than observed experimentally *in vitro* (*Discussion* and *SI Appendix*, *SI Appendix*, Fig. 3.S7E). The BD (about 670 ms) was not statistically changed by reduction of the network size by 50, 100, and 125 neurons, whereas the CP increased from 5.5 ± 1.1 s to 7.1 ± 2.2 s to 10.2 ± 5.3 s to 15.5 ± 13.3 s, respectively. If CP depends on the number of neurons within the population, it could be because each lesioned cell creates holes in the network that put at risk the spread of activity within the population (Movies S4 and S5). In addition, these lesions also effectively decrease the number of inputs to each remaining neuron and thus the strength of inputs to each of them.

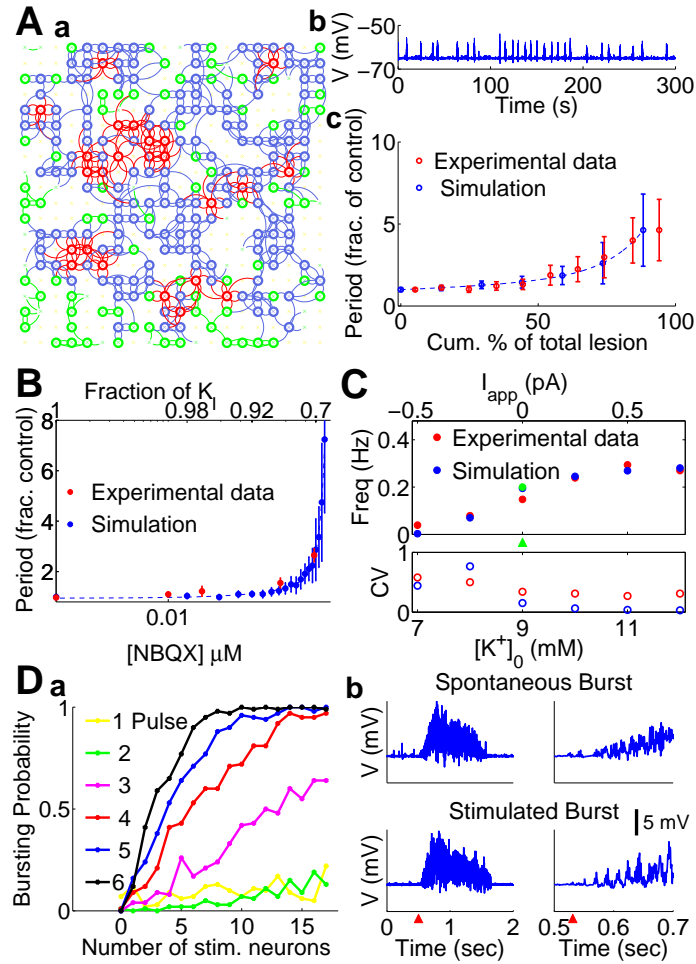


Figure 4.2: **Modeled characteristics of burst induction comply with physiology.** **A:** Effect of deleting random neurons on the network rhythm. a) 125 neurons (31% of the network) have been removed. b) Corresponding mean membrane potential over the whole lesioned network. c) Comparison between simulated (blue) and experimental lesions (red, extracted from [72]) of increasing numbers of preBötC neurons (see also *SI Appendix*, Fig. 3.S7). **B:** Consequences of gradually decreasing synaptic strength. Comparison between simulations (blue) and experimental results (red, extracted from [136]). The initial synaptic strength, controlled via K_I in the model and via [NBQX] in the experimental protocol, is gradually decreased (see also *SI Appendix*, Fig. 3.S8). **C:** Hyperpolarizing and depolarizing the network from its resting state (green arrowhead) leads, respectively, to slower more variable and accelerated more regular rhythms in simulated (blue) and experimental conditions (red, extracted from [142]), see also *SI Appendix*, Fig. 3.S9. **D:** Response of the network to increasing stimulations. a) Probability of stimulus evoked population bursts as a function of the number of randomly stimulated neurons ($n=1-17$) and the number of stimuli per train ($n=1-6$ pulses). b) Left: Mean V over the whole network for spontaneous and stimulated bursts ($n=9$ neurons, 6 pulses at 60 Hz, starting at $t=550$ ms, red arrowhead). Right: Magnification of the burst induction. The vertical calibration bar applies to all burst, each having a baseline potential of -65 mV.

To test the role of unitary synaptic strength, in contrast to the spread of excitatory transmission through the network, we simulated a decrease in the maximum synaptic transmission from 100% to 65%, to mimic pharmacological blockade of AMPA receptors, until population burst cessation with the full 400 neuron network (Fig. 4.2B and *SI Appendix*, Fig. 3.S8). The results were similar to experimental conditions [136] and were notably similar to Fig. 4.2Ac with respect to the exponential divergence of cycle period as well. The latter point further suggests that the net strength of connections between neurons are of principal importance for burst induction, and thereby, rhythm generation.

4.2.3 Depolarizing neurons increases the rhythm frequency.

The preBötC is the target of many neuromodulators, the balance of which can affect the tonic excitability of the network [34]. To investigate how tonic changes in V affect bursting, we modulated the neuronal excitability by adding an applied current (I_{app}) to the current balance equation of the entire network. Positive I_{app} is equivalent to increasing extracellular $[K^+]$. After hyperpolarization ($I_{\text{app}} = -0.5$ pA), the IBI and variability in rhythm increases drastically (Fig. 4.2C and *SI Appendix*, Fig. 3.S9), while depolarizing the network ($I_{\text{app}} = 0.75$ pA) decreased the CP and variability in rhythm. At higher depolarization, the frequency of bursting reaches a plateau principally constrained by the refractoriness in the model ($CP_{\text{plateau}} = 3.5 \pm 0.1$ s, $BD_{\text{plateau}} = 560 \pm 227$ ms compared to control values $I_{\text{app}} = 0$ pA: $CP = 5.1 \pm 0.8$ s, $BD = 660 \pm 161$ ms). These values are comparable to the ones reported in physiological experiments [142] for $CP = 5.7 \pm 0.5$ s and $CP_{\text{plateau}} = 3.5 \pm 0.2$ s, with no notable decreases in BD and spike frequency. In the case of hyperpolarization, we detected very few bursts after 1500 s, corresponding to $CP = 240.6 \pm 185.7$ s, which is comparable to the long CP (143.2 ± 3.9 s) reported in [142]. We conclude that changing the tonic excitability in our model has drastic consequences on CP owing to changes in IBI but not BD, in agreement with previous experimental data.

At hyperpolarized potentials we also observed, during the IBI or immediately preceding bursts, patterns of activity reminiscent of burstlets, described in the preBötC as rhythmic bouts of low-rate spiking (*SI Appendix*, Fig. 3.S10) [95]. These patterns did not involve SF/SD like in full-network bursts (*SI Appendix*, Fig. 3.S11). They rested on tens of spiking neurons but cannot properly be considered burstlets, as the latter involve $\sim 90\%$ of preBötC neurons. Rather, these simulated patterns constitute low amplitude events that may seed burstlets and pre-inspiratory activity [95].

4.2.4 Few active neurons are sufficient to trigger population bursts.

Another important feature of the preBötC network is its rapid responsiveness to phasic inputs from central or peripheral (reflex) origins, [137, 147, 185]. Therefore, we sought to evaluate the minimal number of concurrently active neurons necessary

for initiating a preBötC network response. To do so, we depolarized a variable number of randomly chosen neurons with graded trains of stimulation (1-6 stim/train, 50 μ s, 60 Hz). We quantified the probability of evoked bursts for the respective conditions (Fig. 4.2D, *SI Appendix* section 2.8). When 17 neurons (4.25% of the network), were stimulated with a single stimulus, or with a two-stimulus train, it was possible to induce a burst with a low probability $\leq 15\%$. However, using trains of five to six stimuli, the probability was higher than 80% and in these cases, decreasing the number of stimulated neurons revealed that 5-10 neurons were sufficient to induce network bursts. The early phase of the evoked burst, manifesting the propagation of excitatory synaptic inputs in the network (Movie S3), was similar to that of spontaneously occurring bursts (Fig. 4.2Db), in agreement with the group-pacemaker hypothesis [46, 164, 159] and burstlet-dependent generation of bursts [95]. Finally, these results are in keeping with the recent physiological demonstration in slice preparations that targeting four to nine preBötC neurons with glutamate uncaging was sufficient to induce ectopic endogenous-like bursts [96].

4.2.5 Short-term synaptic plasticity in the preBötC inspiratory rhythm generator.

To support the possibility that SD, and also SF, may be occurring *in vitro* on time-scales that could impact normal respiratory rhythms, we recorded synaptic responses in inspiratory preBötC neurons in slice preparations (Fig. 4.3A) evoked by electrical stimulation of preBötC commissural axons [48] (Fig. 4.3B). The experiments were performed in the presence of picrotoxin and strychnine (5 μ M) suppressing GABAergic and glycinergic synaptic currents known to be dispensable for rhythm generation [160, 20, 92] to best reproduce the predominant glutamatergic synaptic transmission of the model. We concurrently reduced the extracellular $[K^+]$ from 8 to 3 mM to minimize spontaneous population activity after identifying recorded inspiratory neurons (Fig. 4.3C), and these recordings did not exhibit unclamped spikes (*SI Appendix*, Fig. 3.S12). For electrical stimulation we used trains (2- to 5-s duration) of repetitive (10-30 Hz) stimuli. The intensity of stimulation was set so that at low frequency (1/9 s) the stimulus resulted in about 50% EPSC failures.

At 20 and 30 Hz, stimulation frequently resulted in population recruitment even in our suppressed excitability. In three of seven preBötC neurons stimulated at 10 Hz, the amplitude of evoked EPSCs (eEPSCs) varied according to their timing during the stimulus trains. Typically in these cells, the amplitude of successive eEPSCs in the train showed a rapid waxing phase followed by a slow waning phase so that eEPSCs increased amplitude over the first few stimuli of the train and declined thereafter during the train, resulting in the reoccurrence of transmission failures at the end of subsequent trains (Fig. 4.3D). We quantified failures of transmission during the trains of stimuli and observed that failures mirrored changes in EPSC amplitudes (black histograms Fig. 4.3E and F), suggesting that the two phenomena might be tied through a similar mechanism like the availability of vesicles at the synapse as modeled here. The other four cells did not show any discernible modulation in eEPSC amplitude during the train (Fig. 4.3E gray). In these four cells,

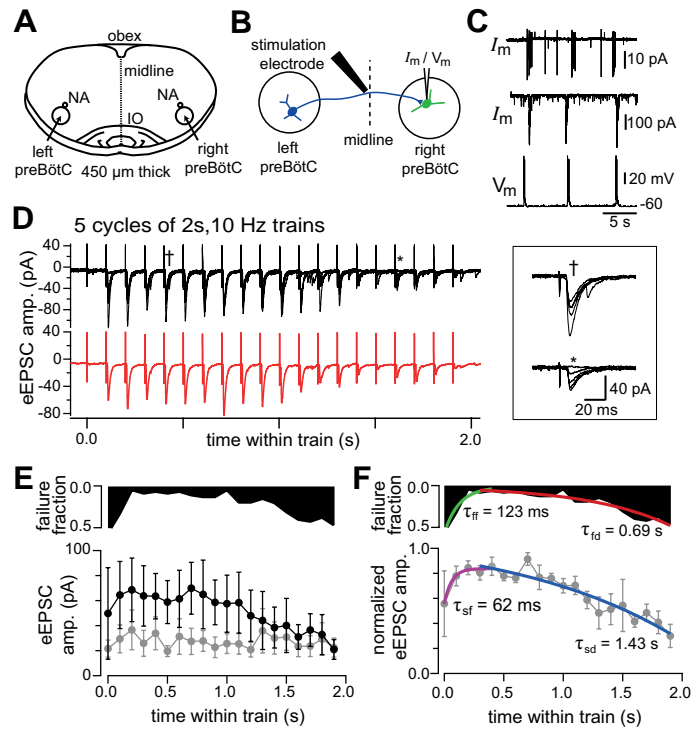


Figure 4.3: **Experimental support for rapid accommodation of synaptic strength.** **A:** A transverse preBötC slice depicting key features of the *in vitro* preparation (IO: inferior olive, NA: subcompact nucleus ambiguus, obex: caudal termination of the IVth ventricle). **B:** The experimental strategy (see text for details). **C:** Top) On-cell voltage clamp recording, Middle) whole-cell voltage-clamp recording, and Bottom) current-clamp recording. **D:** Upper) Five cycles of train stimuli from the cell recorded in **C**, and Lower) The mean of the 5 cycles. Inset) Details showing the eEPSCs overlaid at the indicated places within the trains. **E:** solid-black histogram) Fraction of trials that failed to produce eEPSCs. Lower) eEPSC amplitudes (black: N=3 neurons, n=5-16 trials; gray: N=4 neurons, n=4-10 trials). **F:** Same data as **E** normalized to the peak within each neuron's mean train (gray) with exponential fit overlays to the rising components (green/magenta) and the falling components (red/blue) of the normalized data. The command potential for all voltage-clamp recordings was -60 mV.

the slope of the time-dependent change of eEPSC amplitude during the train was significantly different from that of the aforementioned ones (-1.2 ± 0.9 pA/s, $n=4$ vs -20.1 ± 8.3 pA/s, $n=3$, t-test: $p=0.043$). These stationary cells may belong to the $\sim 50\%$ fraction of nonrhythmogenic inhibitory neurons within the preBötC [50] and were not considered further.

For the recordings that exhibited dynamic synapses (Fig. 4.3E, black), normalizing their eEPSC amplitudes with respect to the maximal eEPSC of each neuron's mean train revealed a more consistent trend among the data than the raw data may have initially suggested (Fig. 4.3F [gray], $N=3$, $n=5-16$ trials), with exponential fits to their rising and falling components. The rising exponential suggests the presence of short-term SF, (as illustrated by x in Fig. 4.1E) and the falling exponential consistent with short-term SD (an amalgamation of x and Y_{dock} , Fig. 4.1E). These electrophysiological data match the predicted model dynamics of I_{syn} in Fig. 4.1E and would suggest that, together with the rest of the favorable modeling tests performed here recapitulating experimental results [72, 136, 142, 96], the modeling approach we exercised is applicable to the respiratory rhythm-generating network *in vitro*.

4.3 Discussion

4.3.1 Can bursting oscillations be generated in neuronal networks without any intrinsically rhythmic neurons?

We found that a neuronal network based on Gaussian-distributed sparse synaptic connections can generate an endogenous rhythm initiated by neuronal noise. A key feature of the network is the SF and SD dynamics. Here, SD was based on a two-pool model where vesicles of one pool interact with the RRP and is a refinement of the classical SD model [199].

Pacemaker neurons can generate an intrinsic oscillation based on their biophysical properties such as persistent sodium current (I_{NaP}). For I_{NaP} , this current slowly inactivates to hyperpolarize and terminate bursts, whereas subsequent deinactivation causes the next depolarization and burst [23, 165, 193], which sustains rhythmic activity under certain parameter regimes. A calcium-activated nonspecific cation current (I_{CAN}), ubiquitous in preBötC neurons [46, 149], can also give rise to intrinsic bursting activity [193, 192] and may contribute to SF in preBötC neurons by enhancing excitatory postsynaptic potentials (EPSPs) [149]. However, electrophysiological recordings [143, 46, 47, 148] revealed that endogenous rhythmic activity was not driven by pacemaker neurons, as inhibiting them does not suppress population bursting or change the frequency. This result led to the conclusion that bursting oscillations could be generated by other mechanisms, such as the group-pacemaker hypothesis [140, 132, 46, 159], where respiratory rhythm is thought to emerge from the dynamics of synaptic input impinging on inspiratory neurons and those interactions with intrinsic cellular properties.

Modeling approaches [164, 39] have shown that the cooperation of I_{CAN} , activated by synaptic activity, coupled with activity-dependent outward currents, can

generate periods of bursting separated by quiescent phases. These quiescent periods can also be achieved by transient inactivation of an I_{NaP} similar to the one observed in pacemaker neurons, which is equivalent to activating an outward current. However, that model requires intrinsic regular spiking to activate I_{CAN} and initiate the bursts even when the system is driven by synaptic noise, and I_{CAN} -mediated SF and depolarization-block dependent SD alone are not sufficient for regular bursting.

Here, we modeled a neuronal network that contains sparse connections and is based on SF with a two-pool state for SD. Burst initiation relies on spontaneous spiking of a small number of neurons that recruit the entire network by recurrent excitation among neurons. The increase in SF in our model promotes the recurrent excitation, similar to the I_{CAN} evoked by intrinsic activity in ref [164], and observed in electrophysiological recordings *in vitro* [148, 141]. To propagate to the entire network, nearly synchronous firing must first occur in several neurons. This synchronization may be caused by synaptic inputs coincidentally converging onto small groups of preBötC neurons or, in recurrently connected neurons, in a stochastic manner, from the relief of the refractory period during the interburst interval. After a few hundred milliseconds, the first part of SD takes over and stops each neuron from transmitting synaptic activity. Population spiking subsequently terminates. Finally, the second part of the SD, characterized by the entry of neurons in a refractory period to let synapses recover to equilibrium, prevents neurons from firing back immediately. This behavior is in agreement with previous studies [96, 113]. The next cycle starts after the neuronal refractory periods end and when noise-driven spontaneous spiking occurs at several neurons. The end of the refractory period and the beginning of the next burst (*SI Appendix*, Fig. 3.S1E) principally depend on four factors: the rate of SF τ_f (see x in Fig. 4.1E), the effective degree of network connectivity (Fig. 4.2A, *SI Appendix*, Figs. 3.S2 and 3.S7), the maximal synaptic strength K_I (Fig. 4.2B-S8), and the amount of spontaneous spiking (Fig. 4.2C-D-S9). Changing any one of these factors affects the bursting frequency and regularity.

To conclude, our modeling confirms the group pacemaker hypothesis [46], where eupneic respiratory rhythm is attributed to the cooperative interactions between inspiratory neurons. The present results show that periodic inspiratory bursts can emerge from recurrent neuronal connections and synaptic dynamics, without the need of any underlying neuronal rhythm driven by pacemaker neurons or a subpopulation of oscillatory firing neurons. Synaptic dynamics are thus a plausible mechanism of preBötC rhythmogenesis, even if other nonsynaptic mechanisms might be involved to fully reproduce the range of respiratory behaviors.

4.3.2 Local network structure and dynamics.

Network connectivity within the preBötC could influence the dynamics of population activity [176]. Other preBötC-related studies have used all-to-all coupling [24] or various degrees of sparse networks [25, 52] including small-world topology [132]. In this study, we modeled a realistic-sized preBötC network using random connections between neurons with a distribution law that decays exponentially with the distance between neurons (Fig. 4.1B, S2B). This decay has been used in several

models such as the visual cortex (figure 5 from ref [2]) or the auditory cortex [131]. Connectivity between preBötC neurons could be as high as 13% when recorded in local proximity ($< \sim 60 \mu\text{m}$) [160] whereas it could be as low as 1% as determined from multielectrode array experiments [25]. Additionally, experiments with organotypic slices suggest that a preBötC-like network could be organized into loosely connected clusters, i.e., a small-world network [51].

Our choice of connectivity is broadly consistent with the three previous experimental results [160, 25, 51] when the pair-to-pair coupling decays fast at large distances. The decay of neuronal connectivity with the distance between neurons prevents the emergence of nonhomogeneous connectivity in the network. Indeed, in the classical Erdős-Rényi preBötC network model, increasing the coupling probability leads to the occurrence of higher connected neurons, as studied in ref. [176]. The connectivity map used in ref. [25] for a low coupling probability is nevertheless very similar to the one used in our model. Varying the Gaussian distribution (parameter s in Eq. 4.2, *SI Appendix*, Fig. 3.S2) shows that the rhythm is preserved only for s in the range 0.8-1. With $s \leq 0.8$ the IBI has large variability, and when $s \geq 1$ waves of APs at low frequency can emerge in the network (*SI Appendix*, Fig. 3.S2F and Movie S6 and S7).

4.3.3 Role of synaptic depression in burst termination.

Synaptic depression is described classically as the depletion of vesicles following activation [186]. Here we had to account for the depletion of both the RRP and the RP so that vesicles can arrive with the proper dynamics, which is not contained in the classical coarse-grained depression model where the rate of synaptic depression depends on the resource's availability [199]. In the classical depression model, presynaptic stimulation through a spike train produces a regime of stationary EPSPs postsynaptically after a few spikes, which does not result in burst termination due to full depletion of available vesicles. The two-pool model where vesicles can either be in the RRP or RP compartments resolves this difficulty: the arrival of a presynaptic AP triggers fusion of vesicles from the RRP, and the postsynaptic current is proportional to the amount of fused vesicles. Bursting termination in the preBötC is still unknown and might be due to several different processes such as synaptic depression, voltage-dependent/ion-activated outward currents [113], or, as postulated in previous models, due to the deactivation of inward currents [23], or a combination. In our model, burst termination is based on short-term SD, where the ready-to-fuse vesicles are lacking. Indeed, they are released in the high firing rate bursting that lasts several hundreds of milliseconds and take up to seconds to recover, consistent with respiratory refractory periods observed experimentally *in vitro* [96]. Our approach shows that bursting oscillations can be generated in an ensemble of neurons connected by synapses, driven by depression/facilitation dynamics, without the need for any underlying endogenously rhythmic pacemaker neurons. In addition, the IBI is controlled by recurrent excitations arising from the network's spontaneous activity. This phenomenon may be quite generic and could explain oscillations in other neuronal networks, where the mechanism remains un-

clear, such as the circuits for chewing, swallowing, whisking, locomotion or, indeed, any coordinated ensembles of repetitively synchronous neuronal activities.

4.4 Materials and Methods

4.4.1 Electrophysiology.

All animal studies were done in accordance with the guidelines issued by the European Community and have been approved by the research ethics committee in charge (Comité d'éthique pour l'expérimentation animale) and the French Ministry of Research.

Swiss mice (P0-P4) were anesthetized and dissected in artificial cerebrospinal fluid (ACSF) containing (in mM): 132.5 NaCl, 8 KCl, 0.58 Na₂HPO₄, 8.5 NaHCO₃, 30 D-glucose, 1.26 CaCl₂, 1.15 MgCl₂. Hindbrains were quickly removed and embedded within a 4% agarose block and glued to the pedestal of a Leica microtome. Transverse slices were cut from the medulla (450 μ m thick) where the rostral surface was 400-500 μ m caudal to the caudal end of the facial nucleus in line with the calibrated atlas of ref. [163]. Slices were then placed into a recording chamber and held down by a platinum grid with nylon fibers. The slices were perfused with 30-31 °C extracellular ACSF for at least 30 min before patch recording commenced. Picrotoxin (5 μ M) and strychnine (5 μ M) were bath-applied to block GABA_A and glycinergic synaptic currents. Evoked EPSCs (eEPSCs) were identified by patch-recording preBötC respiratory neurons and electrically stimulating the midline of the slice just dorsal to the midline aspect of the inferior olive (Fig. 4.3A and B) using an ISO-Flex stimulation isolation unit (A.M.P.I.). The 8 mM [K⁺] was exchanged with 3 mM [K⁺] ACSF to suppress spontaneous population activity once a recorded neuron was identified. For voltage-clamp recordings, we used a command potential of -60 mV and recordings with unclamped spikes were discarded. Further details are given in the *SI Appendix, Materials and Methods*.

4.4.2 Mathematical Modeling.

Neuronal network modeling. We model a neuronal network consisting of 20 x 20 (i.e. 400) connected neurons organized on a square lattice and account for synaptic dynamic and voltage properties. To model the membrane potential of each neuron, we use a simplified Hodgkin-Huxley model, where we consider the changes in Na⁺, K⁺ and leak channels. The associated currents are I_{Na} , I_K and I_L . The resting potential of each neuron is at a mean of -65.1 mV, distributed randomly according to a Gaussian distribution with variance 0.2. To account for spontaneous fluctuations of the membrane potential, we add a Gaussian noise source term \dot{W} to the potential with a variance σ . The general equation for one neuron is

$$C\dot{V} = -I_{Na} - I_K - I_L + \sum_j I_{syn,j} + \sigma\dot{W}. \quad (4.1)$$

The synaptic current for each neuron is $\sum_j I_{syn,j}$, which is the sum of the postsynaptic currents over all connected neurons (*SI Appendix*). These currents are computed for each synapse from the short-term facilitation and depression properties, modeled by two pools of vesicles (*SI Appendix*). These two pools generate two different time scales for the synaptic depression. The model we adopted for the facilitation dynamics is, however, classical, as developed in ref. [198]. Synaptic depression results from the depletion of the RRP, where synaptic vesicles are gathered at the membrane before fusion. We also account for the other pool of recycling vesicles (RP) that are diffusing.

Computing the synaptic current. To compute the synaptic current between two connected neurons, we use the synaptic model described above (*SI Appendix*). The postsynaptic current $I(t)$, due to an action potential generated in the presynaptic neuron, is proportional to the amount of released vesicles.

Construction of the network connectivity. The connectivity map for the network is implemented between every neuron. They are distributed on a square lattice (Fig. 4.1B) and connected randomly according to the probability distribution

$$\mathbf{P}(i \rightarrow j) = \exp(-d(i, j)^2 / (2s^2)) \quad (4.2)$$

for neuron i and j , where $d(i, j)$ is the Euclidian distance between neurons i and j normalized by the minimal distance between two neurons.

Acknowledgments We thank C.A. Del Negro and C.S. Poon for critical reading of the manuscript. This work was supported by CNRS, grants from the Agence Nationale de la Recherche ANR-32-BSV5-0011-02 and from the Fondation pour la Recherche Médicale DEQ20130326472 to GF. DH thanks Labex MemoLife and the Fondation pour la Recherche Médicale FDT20140931147 for support.

Supplementary Information

C. Guerrier¹, J.A. Hayes², G. Fortin², D. Holcman¹

This SI is divided into 3 parts. In the first part, we complement the experimental procedure, providing details about short-term depression analysis in the preBötzing Complex, and we provide specific information about the modeling aspect. We describe the dynamics of the membrane potential, synaptic facilitation and the two step synaptic depression model. We further describe synaptic connections between neurons. In the second part, we present additional simulations. The third part describes the legends for the movies mentioned in the main text.

4.5 Complement on the Material and Methods

4.5.1 Experimental procedure

Swiss mice (P0-P4) were anesthetized and dissected in artificial cerebrospinal fluid (ACSF) containing (in mM): 132.5 NaCl, 8 KCl, 0.58 Na₂HPO₄, 8.5 NaHCO₃, 30 D-glucose, 1.26 CaCl₂, 1.15 MgCl₂. Hindbrains were quickly removed and embedded within a 4% agarose block and glued to the pedestal of a Leica microtome. Transverse slices were cut from the medulla (450 μ m thick) where the rostral surface was 400-500 μ m caudal to the caudal end of the facial nucleus in line with the calibrated atlas of [163]. Slices were then placed into a recording chamber and held down by a platinum grid with nylon fibers. The slices were perfused with 30 – 31 °C extracellular ACSF for at least 30 min before patch recording commenced.

Tissue was visualized using a Nikon Eclipse upright microscope in IR-DIC configuration using a water-immersible 40x objective and a CoolSnap HQ2 camera (Photometrics, AZ) controlled by Micro-Manager [40]. Whole-cell patch recordings were performed with a MultiClamp 700B, digitized by a 1440a Digidata, and controlled by pClamp 10 (Molecular Devices, CA). The intracellular patch solution contained (in mM): 123 K-gluconate, 21 KCl, 0.5 EGTA, 10 HEPES, 3 MgCl₂. Picrotoxin (5 μ M) and strychnine (5 μ M) were bath-applied to block GABA_A and glycinergic synaptic currents.

Evoked excitatory postsynaptic currents (eEPSCs) were identified by patch-recording preBötC respiratory neurons and electrically stimulating the midline of the slice just dorsal to the midline aspect of the inferior olive (Fig. 3A-B) using an ISO-Flex stimulation isolation unit (A.M.P.I., Israel). Once a respiratory neuron was identified, the bath [K⁺] was dropped to 3 mM to reduce spontaneous respiratory activity. Low-intensity electrical pulses were applied for 100 μ s duration approximately every 9 s and the intensity increased until >50% of the pulses resulted in eEPSCs observed in the voltage-clamp recording. After that, we switched to gap-free recording and periodically stimulated trains of variable length and frequency to

¹Group of Applied Mathematics and Computational Biology, Ecole Normale Supérieure, 46 rue d'Ulm 75005 Paris, France.

²Université Paris-Saclay, Université Paris-Sud, CNRS, UMR 9197, Institut des Neurosciences Paris-Saclay, F-91190, Gif-sur-Yvette, France.

investigate the postsynaptic response. The eEPSCs were identified and quantified offline using *PhysImage* software (<http://physimage.sourceforge.net/>).

4.5.2 Hodgkin-Huxley Model of the membrane potential

To model the membrane potential of each neuron, we used a simplified Hodgkin-Huxley model, where we considered the changes in Na^+ , K^+ and leak channels. We further added the synaptic currents generated from connected neurons. The resting potential of each neuron was at a mean of -65.1 mV, distributed randomly according to a Gaussian distribution with variance 0.2. To account for the spontaneous fluctuations of the membrane potential, we added a Gaussian noise source term to the potential with a variance σ . The equations are

$$C\dot{V} = I_{app} - I_{Na} - I_K - I_L + \sum_j I_{syn,j} + \sigma\dot{W} \quad (4.3)$$

$$\dot{n} = \alpha_n(1 - n) - \beta_n n \quad (4.4)$$

where

$$\begin{aligned} I_{Na} &= g_{Na} m_\infty^3 h (V - E_{Na}) \\ I_K &= g_K n^4 (V - E_K) \\ I_L &= g_L (V - E_L) \\ m_\infty &= \frac{\alpha_m}{\alpha_m + \beta_m} \\ \alpha_k &= \frac{1}{\tau_k} \frac{\theta_k - V}{e^{\frac{\theta_k - V}{\tau_k}} - 1} \text{ for } k = n, m \\ \beta_k &= \eta_k e^{-\frac{V + 65}{\sigma_k}} \end{aligned}$$

The variables m and n represent the opening of the Na^+ and K^+ channels respectively. We used the following approximation for the closing of the Na^+ channel $h = (0.89 - 1.1n)$. The synaptic current $\sum_j I_{syn,j}$ integrates the sum over all connecting neurons that we shall describe next. The term \dot{W} in eq. 4.3 represents the derivative of standard white noise. Indeed, in the discretized form, $W(t + \Delta t) - W(t) = \sqrt{\Delta t} Z$ where Z is a Gaussian variable of mean 0 and variance 1.

4.5.3 Model of the synaptic dynamics

To characterize the synaptic dynamics, we built a two pool model that accounted for two different time scales of depression. Indeed, synaptic depression results from the depletion of the readily releasable pool (RRP) (Fig. 1A), where synaptic vesicles are gathered at the membrane before fusion. We also accounted for the other pool of recycling vesicles (recycling pool, RP) that are diffusing. Finally after fusion, vesicles

are not participating in any of the two previous pools. This state is described as recovering. In the present model, we considered that the total amount of vesicles at a synapse is constant. Thus the fraction y_{free} (resp. y_{dock}) of vesicles in the RP (resp. RRP), with the fraction of recovering vesicles y_{rec} satisfies the conservation equation

$$y_{\text{free}} + y_{\text{dock}} + y_{\text{rec}} = 1. \quad (4.5)$$

Finally, the synaptic facilitation variable x reflects all possible mechanisms that enhance vesicular release, and thus is associated with an increase in the release probability [198]. It is given by

$$\dot{x} = \frac{X - x}{\tau_f} + k(1 - x)H(V - T), \quad (4.6)$$

where τ_f is the facilitation rate, X its value at equilibrium, and H is the Heaviside function. The facilitation x increases due to the term $k(1 - x)$ during an Action Potential (AP), when the membrane potential V is above a threshold T ($H(V - T) = 1$), and relaxes back to equilibrium when V is below T ($H(V - T) = 0$).

We shall now present the mass action equations that describe the vesicular exchanges between different pools. The amount of vesicles in the RP depends on the arrival of vesicles from the recovering state, given by the flux $\Phi_{\rightarrow\text{RP}} = \frac{y_{\text{rec}}}{\tau_{\text{rec}}}$, where τ_{rec} is the delivery time. The outward flux of vesicles is proportional with the rate constant τ_{dock} to the fraction of available sites ($y_{\text{dock}}^{\text{max}} - y_{\text{dock}}$) at RRP, where $y_{\text{dock}}^{\text{max}}$ is the maximal number of sites in the RRP, and to the fraction of available vesicles in the RP. Finally, the outward $\Phi_{\rightarrow\text{RRP}}$ is generated in the absence of an AP by the intrinsic turn over, when the membrane potential is below a threshold T . However, when the membrane potential is above the threshold T , $\Phi_{\rightarrow\text{RRP}}$ depends on the facilitation variable x and we finally get

$$\Phi_{\rightarrow\text{RRP}} = \frac{1}{\tau_{\text{dock}}} (y_{\text{dock}}^{\text{max}} - y_{\text{dock}}) y_{\text{free}} \left[1 + \frac{x - X}{X} H(V - T) \right]. \quad (4.7)$$

Finally,

$$\begin{aligned} \dot{y}_{\text{free}} &= \Phi_{\rightarrow\text{RP}} - \Phi_{\rightarrow\text{RRP}} \\ &= \frac{y_{\text{rec}}}{\tau_{\text{rec}}} - \frac{1}{\tau_{\text{dock}}} (y_{\text{dock}}^{\text{max}} - y_{\text{dock}}) y_{\text{free}} \left[1 + \frac{x - X}{X} H(V - T) \right]. \end{aligned} \quad (4.8)$$

The equation for the fraction y_{dock} of vesicles in the RRP is given by the balances of inward vesicles arriving from the RP, $\Phi_{\rightarrow\text{RRP}}$ (eq. 4.7), and on the flux of released vesicles $\Phi_{\text{RRP}\rightarrow}$, which vanishes in the absence of an AP. Following a stimulation, it is proportional to the fraction y_{dock} of vesicles in the RRP and to the facilitation variable x with a rate τ_{rel} :

$$\Phi_{\text{RRP}\rightarrow} = \frac{1}{\tau_{\text{rel}}} y_{\text{dock}} \left(\frac{x - X}{X} \right) H(V - T). \quad (4.9)$$

Balancing the fluxes $\Phi_{\rightarrow\text{RRP}} - \Phi_{\text{RRP}\rightarrow}$ leads to

$$\begin{aligned} \dot{y}_{\text{dock}} = & \frac{1}{\tau_{\text{dock}}} (y_{\text{dock}}^{\text{max}} - y_{\text{dock}}) y_{\text{free}} \left[1 + \frac{x - X}{X} H(V - T) \right] \\ & - \frac{1}{\tau_{\text{rel}}} y_{\text{dock}} \frac{x - X}{X} H(V - T). \end{aligned} \quad (4.10)$$

Finally, changes in the amount of recovering vesicles y_{rec} is equal to the difference of the fluxes $\Phi_{\rightarrow\text{RRP}}$ and $\Phi_{\rightarrow\text{RP}}$, which leads to

$$\dot{y}_{\text{rec}} = \Phi_{\text{RRP}\rightarrow} - \Phi_{\rightarrow\text{RP}} = \frac{1}{\tau_{\text{rel}}} y_{\text{dock}} \frac{x - X}{X} H(V - T) - \frac{y_{\text{rec}}}{\tau_{\text{rec}}}. \quad (4.11)$$

In summary, using the conservation equation 4.5, we obtain the following system of equations

$$\begin{aligned} \dot{x} &= \frac{X - x}{\tau_f} + k(1 - x)H(V - T) \\ \dot{y}_{\text{free}} &= \frac{1 - y_{\text{free}} - y_{\text{dock}}}{\tau_{\text{rec}}} - \frac{1}{\tau_{\text{dock}}} (y_{\text{dock}}^{\text{max}} - y_{\text{dock}}) y_{\text{free}} \left[1 + \frac{x - X}{X} H(V - T) \right] \\ \dot{y}_{\text{dock}} &= \frac{1}{\tau_{\text{dock}}} (y_{\text{dock}}^{\text{max}} - y_{\text{dock}}) y_{\text{free}} \left[1 + \frac{x - X}{X} H(V - T) \right] \\ & - \frac{1}{\tau_{\text{rel}}} y_{\text{dock}} \frac{x - X}{X} H(V - T). \end{aligned} \quad (4.12)$$

4.5.4 Computing the synaptic current I_{syn}

To compute the synaptic current between two connected neurons, we used the synaptic model described above. The postsynaptic current $i(t)$, due to an action potential generated in the presynaptic neuron is proportional to the amount of released vesicles ($y_{\text{dock}}(t) - y_{\text{dock}}(t_0)$), where t_0 is the time of the presynaptic AP. It is set to zero when the RRP is empty.

To account for the inherent discrepancy between the continuous description of the fraction of vesicles in the RRP and the actual discrete number, we imposed an empty RRP when the variable y_{dock} was below $y_{\text{dock}}^{\text{min}} = 0.04$. This minimal value for y_{dock} corresponds to a total of around twenty-five vesicles in the synapse and to a mean maximal number of vesicles in the RRP of 4.5. The threshold $y_{\text{dock}}^{\text{min}}$ was chosen by plotting the variable y_{dock} during a protocol where the membrane potential V was constantly stimulated at 60 Hz for 2 seconds, which reflects the mean spike frequency during bursting. The variable y_{dock} decreased abruptly during the first 500 ms, and then slowed down before reaching an asymptotic regime. From these considerations, we chose the value of threshold $y_{\text{dock}}^{\text{min}}$ in the intermediate regime, before y_{dock} enters its asymptotic regime (Fig. 3.S1F, the red line shows the asymptotic regime, when the tangent of $y_{\text{dock}}(t)$ is equal to the limit value of the one at infinity, computed by a numerical fit).

After a bursting event, we implemented a refractory period (RefP) reflecting that in order for the synapse to recover and for a vesicle to be released, several vesicles need to accumulate at the active zone. This refractory period is monitored using

the facilitation variable x , and ends when it reaches the value $x_{\text{RefP}} = 0.31$, close to its equilibrium value $X = 0.3$ (eq. 4.6).

Finally, when a presynaptic AP arrived at a time t_0 , which does not fall into the refractory period window, the synaptic current is

$$i_{t_0}(t) = K_I(y_{\text{dock}}(t) - y_{\text{dock}}(t_0))H(V - T)H(y_{\text{dock}} - y_{\text{dock}}^{\min}), \quad (4.13)$$

where K_I is a constant, which converts the proportion of fused vesicles during an AP, into a postsynaptic current. For spikes arriving at times t_k , the synaptic current is for $t \in [t_k, t_{k+1}]$,

$$I_{\text{syn}}(t) = \begin{cases} 0 & \text{during a refractory period} \\ i_{t_k}(t - \tau_{\text{del}}), & \text{else} \end{cases} \quad (4.14)$$

where $\tau_{\text{del}} = 1$ ms is a delay.

4.5.5 Constructing the network connectivity

We present now the connectivity map for the network that we implemented between neurons. Neurons were distributed on a square lattice (Fig. 1B) and were connected randomly according to the probability distribution

$$\mathbf{P}(i \rightarrow j) = \exp(-d(i, j)^2/(2s^2)) \quad (4.15)$$

for neuron i and j and the parameter s , that is specified later on, and where $d(i, j)$ is the Euclidian distance between neurons i and j normalized by the minimal distance between two neurons. For $s = 0.9$, the mean number of output connections per neurons was around 3.7, and the mean total number of connections was around 7.5.

As presented in Fig. 3.S2, the probability to connect directly to one of the 8 proximal neighbors was around 0.3, whilst for the second square it dropped to 0.1. More than 99 % of the network (around 396 neurons out of 400) were part of the network. Thus only few neurons were completely isolated.

4.5.6 Summary of the network dynamics

For a neuronal network consisting of 20 x 20 (i.e. 400) neurons organized on a square lattice, we modeled the synaptic properties and voltage as previously described. We studied various network configurations (for various s) and also studied the effect of changing the size. However, during each simulation, the connections will be kept fixed. In summary, each neuron is then described by four differential equations (one for the action potential and three for the synaptic dynamics, Fig. 3.S1, Movies

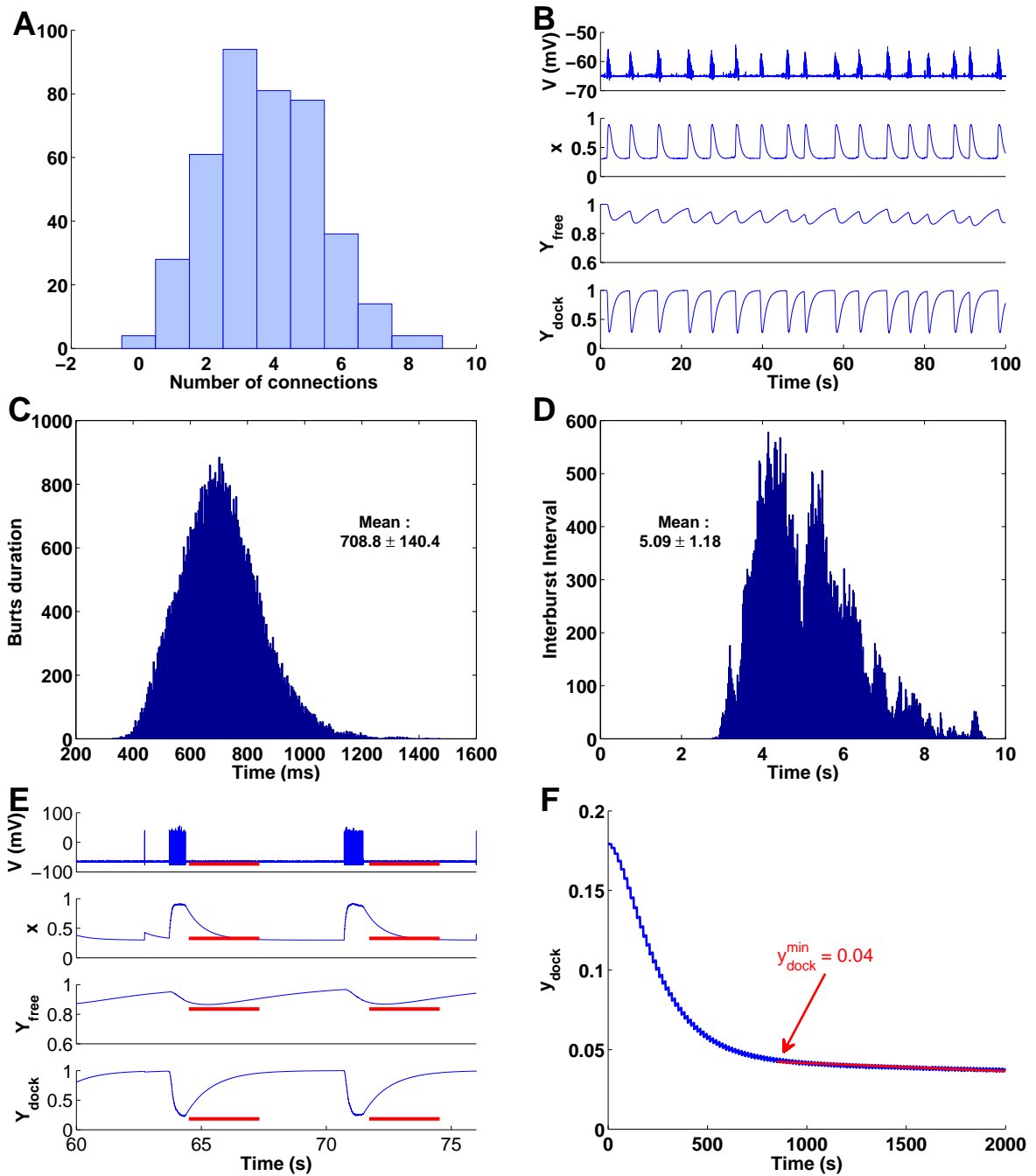


Figure 3.S1: **Histogram of the number of output connections per neuron, and network rhythmic activity with 400 neurons.** **A:** Histogram of the number of output connections per neuron associated to Fig. 1B. Here, the mean number of output connections is 3.75. **B:** Mean voltage V , depression and facilitation average over the network. **C:** Bursting duration histogram (average over one network monitored during 900 sec): the mean burst duration is 708 ± 140 ms. **D:** Interburst interval histogram (mean : 5.1 ± 1.2 sec). The histogram of the interburst interval displays two different peaks at $T=4.3$ sec and $T=5.4$ sec, which shows that the rhythm is multimodal. **E:** Zoom on the voltage V , the facilitation variable x and the two scaled depression variable $Y_{\text{free}} = y_{\text{free}}/y_{\text{free}}^{\text{max}}$ and $Y_{\text{dock}} = y_{\text{dock}}/y_{\text{dock}}^{\text{max}}$ for a single neuron during sixteen seconds. The red bars represent the refractory period coming after a burst. **F:** Dynamics of the depression variable y_{dock} during a 60 Hz stimulation lasting two seconds. The red line shows the asymptotic regime.

S1-S2-S3)

$$\begin{aligned}
 C\dot{V}_i &= -I_{Na} - I_K - I_L + \sum_{j \text{ connected to } i} I_{syn,j} + \sigma\dot{W} \\
 \dot{x}_i &= \frac{X - x_i}{\tau_f} + k(1 - x_i)H(V - T) \\
 \dot{y}_{free,i} &= \frac{1 - y_{free,i} - y_{dock,i}}{\tau_{rec}} - \frac{1}{\tau_{dock}} (y_{dock}^{\max} - y_{dock,i}) y_{free,i} \left[1 + \frac{x_i - X}{X} H(V - T) \right] \\
 \dot{y}_{dock,i} &= \frac{1}{\tau_{dock}} (y_{dock}^{\max} - y_{dock,i}) y_{free,i} \left[1 + \frac{x_i - X}{X} H(V - T) \right] \\
 &\quad - \frac{1}{\tau_{rel}} y_{dock,i} \frac{x_i - X}{X} H(V - T),
 \end{aligned} \tag{4.16}$$

where $i = 1..400$. All the simulations are performed in MATLAB (Mathworks, MA), using the RK4-ode solver with a step time $\Delta t = 0.05$ ms, and with the set of parameters described in Table 4.1. Results are expressed as mean \pm S.E.M. MATLAB code for this model is accessible on the authors' website (<http://www.bionewmetrics.org>).

4.6 Complementary simulations

4.6.1 Decreasing the network connectivity gradually suppresses the endogenous rhythm.

To study the influence of scaling synaptic connections, we decreased the value of the connectivity parameter s from 0.9 (initial network) to 0.7, (connection probability, eq. 4.15 and Fig. 3.S2A), while keeping the neuronal resting membrane potentials at the same values. We first investigated how the connecting probability was decreased for increased distances between neurons (Fig. 3.S2B). Each block represents the probability to connect neighboring neurons: the first four closest are on bar 1 and so on (details on Fig. 3.S2B). In summary, as long as $s \geq 0.85$ (mean number of output connections $M_{CN} = 3.2$) the network dynamics is not much affected (Fig. 3.S2C-D-E). However, lowering s below 0.75 leads to $M_{CN} = 2.3$, the bursting pattern remains, but the interburst intervals show a large variability, lasting in some cases 25 sec instead of 5 sec. For $s < 0.7$, ($M_{CN} = 1.9$), the rhythm disappears, the network can generate bursts between silent periods that can last more than 100 seconds. This result is confirmed by the power spectrum analysis (Fig. 3.S2D). We conclude here that a minimal network connectivity is required to induce periodic bursting patterns.

The neuronal connectivity characterized here by the variable s is the key parameter governing the network rhythm. We could discern three different regimes depending on the value of s : for $s < 0.8$, the network expresses irregular bursting patterns, due to a high variability in the interburst interval duration. In that case, the mean number of connections per neurons (M_{CN}) is below 3. This small amount of connections prevents the propagation of Action Potentials (APs) within the network, preventing the recruitment of neurons required for burst induction (Movie

S6). When the connectivity parameter s is in the range $0.8 - 1$, M_{CN} varies approximately between 3 and 5. The network expresses regular bursting patterns, and APs propagate quickly within the whole network (Movie S3). Finally, when the parameter $s > 1$, the $M_{CN} > 5$, and network bursts cannot terminate (Fig. 3.S2F). Interestingly, during these periods, the RRP never empties (Fig. 3.S2F). This results from the low spiking frequency (around 20 Hz) during bursting, which permits a steady-state refilling of vesicles. This low frequency results from the high efficient propagation of AP in the network, as illustrated in Movie S7. Indeed, an AP can generate a wave of APs that crosses the entire network very quickly, followed by another wave of depolarization, which prevents the recurrent excitation observed in Movie S3. Thus a high connectivity between neurons leads to waves of APs in the networks, as studied in [18].

4.6.2 Histograms of the interburst interval for four different network realizations.

Neuronal network dynamics can also be characterized by the interburst interval. Indeed, different network realizations with identical synaptic and electrophysiological parameters lead to different interburst interval distributions, while the mean is identical (Fig. 3.S3).

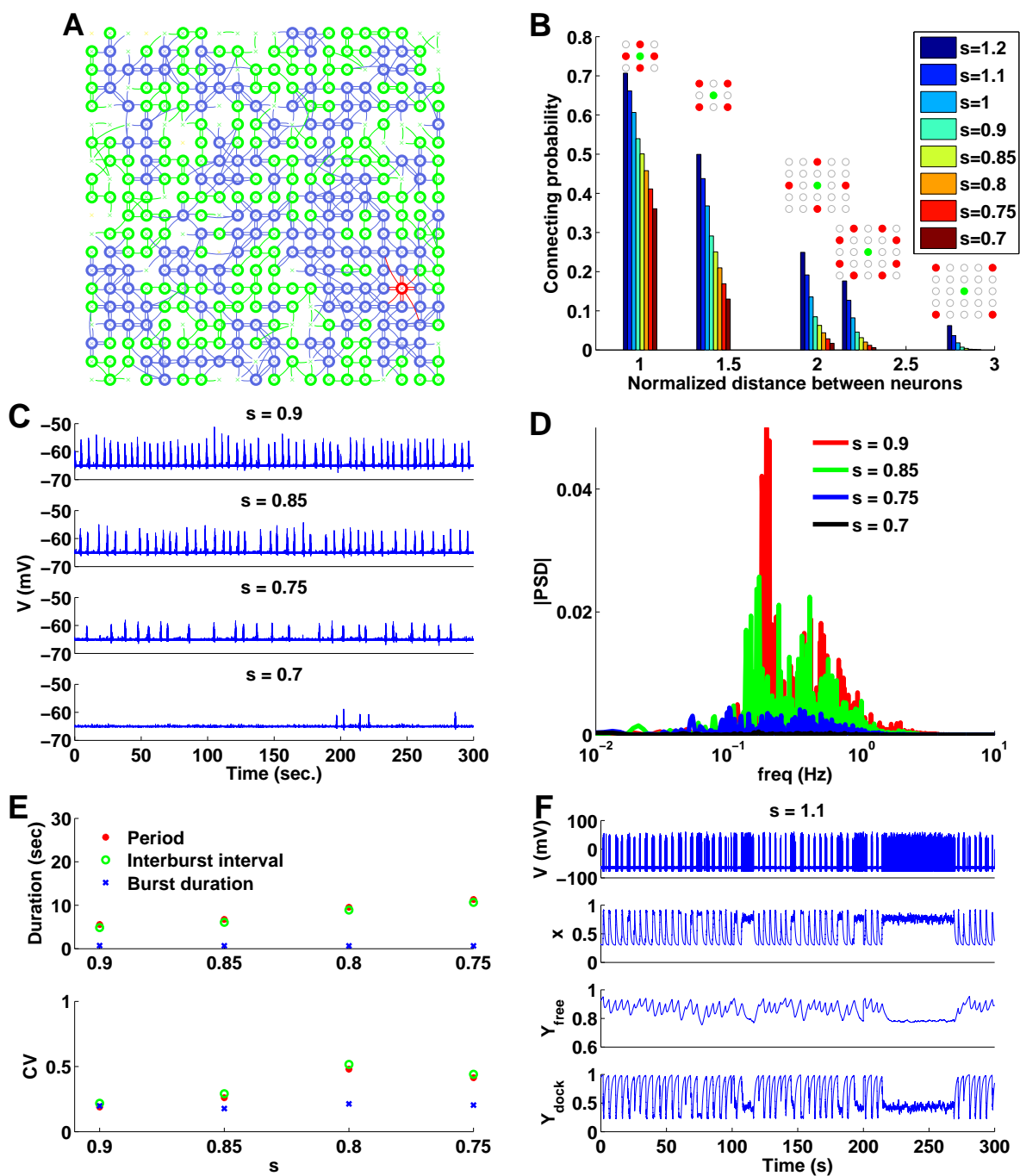


Figure 3.S2: **Effect of connectivity on the network rhythm** **A**: Example of a network (400 neurons) connected with parameter $s = 0.75$ (Materials and Methods). **B**: Empirical distribution of neuronal connections. **C**: Mean membrane potential for networks generated with $s = 0.9, 0.85, 0.75$ and 0.7 , where the mean number of output connections per neuron (M_{CN}) is 3.8, 3.2, 2.3 and 1.9 respectively. **D**: Power spectrum of the mean membrane potential computed for the entire network. **E**: Mean and CV of the burst duration, interburst interval and the period as a function of s . **F**: Time dependent plot of the voltage and the scaled variables Y_{free} , Y_{dock} and x for a single neuron chosen randomly from the network in the case of a very high network connectivity, when $s = 1.1$ ($M_{CN} = 6$).

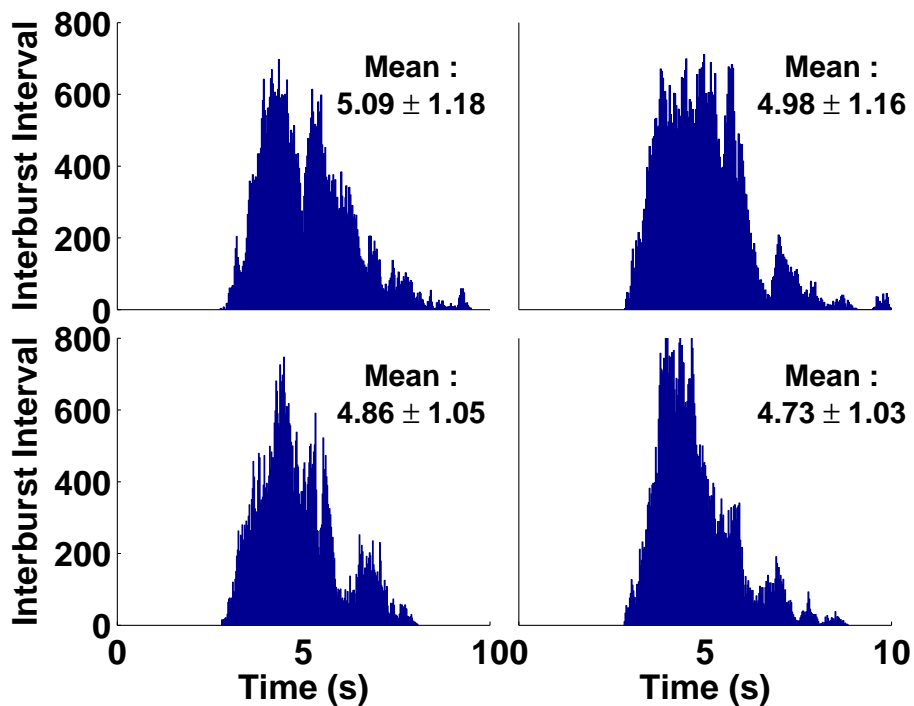


Figure 3.S3: Histograms of the interburst interval for four different network realizations, generated with identical synaptic and electrophysiological parameters (400 neurons). The networks have different neuronal organization. The histograms show several peaks, at different times: top-left) $T_{\text{peaks}}=4.3$ and 5.4 sec. top-right) $T_{\text{peaks}}=3.8, 4.5, 4.9$ and 5.7 sec. bottom-left) $T_{\text{peaks}}=4.3, 5.2$ and 5.6 sec. bottom-right) $T_{\text{peaks}}=4.0$ and 4.4 sec.

4.6.3 Influence of the synaptic properties on the network.

To explore the parameter space in our model, we studied the influence of four key synaptic parameters on the network rhythm: the facilitation time constant τ_f , the vesicular fusion time τ_{rel} , the docking time τ_{dock} and the recovery time τ_{rec} (the synaptic dynamics is summarized in the system of eqs. 4.12 and the associated parameters are reported in Table 4.1). Using a neuronal network containing 400 neurons, we ran simulations similar to Fig. 1D and the results are shown in Fig. 3.S4. We eval-

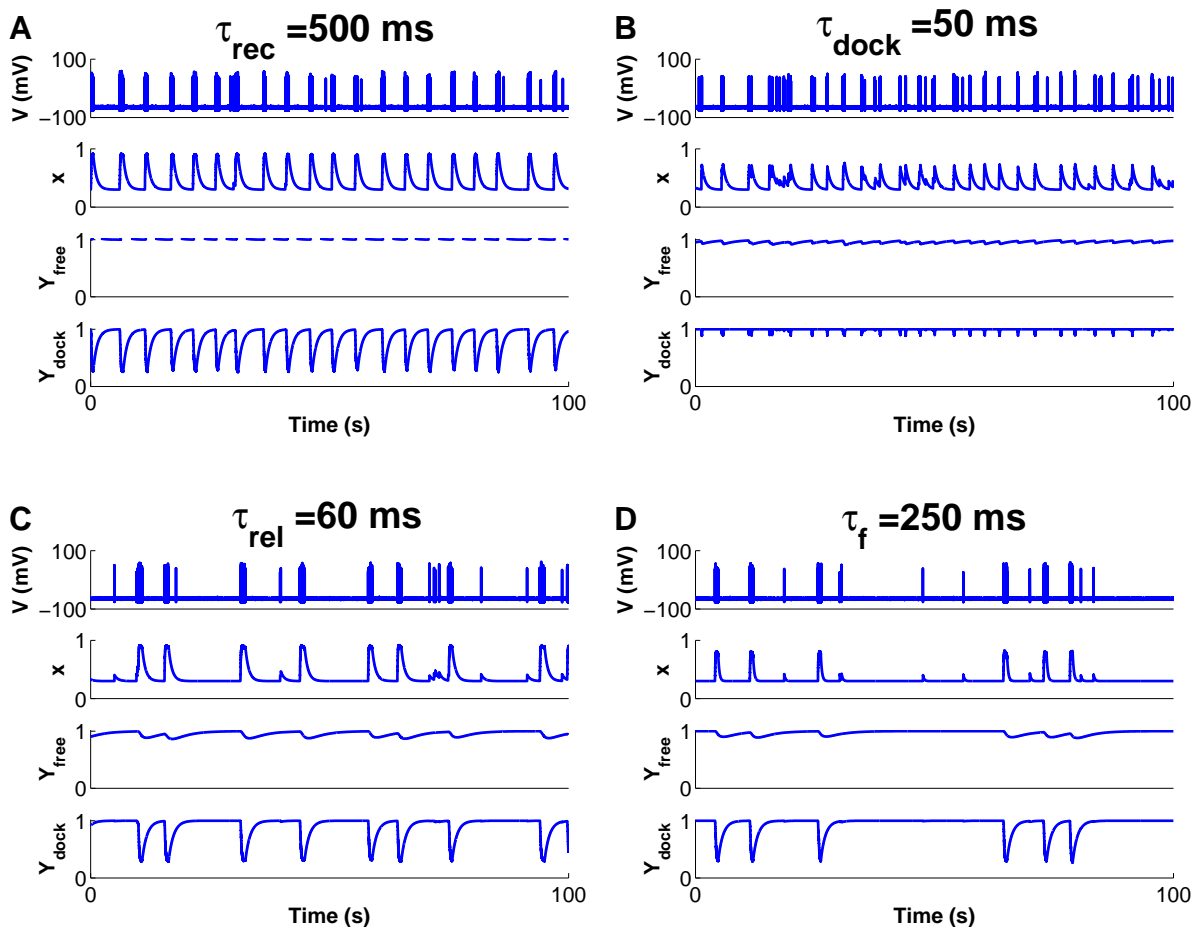


Figure 3.S4: **Responses of the network and mean synaptic properties.** We have shown below the neuronal response, the graph for x (facilitation), Y_{free} (depression 1), Y_{dock} (depression 2). We changed the parameter written on top of each sub-figure. The rest of the parameters are the ones in Table 1.

uated how the rhythm was altered when changing the four parameters (time scales) described above and ran simulations for 100 sec, and varied the different time scales (one at a time) while fixing the others. The results are shown in figure Fig. 3.S5.

The time constant for vesicular recovery τ_{rec} has almost no influence on the cycle period and the burst duration (Fig. 3.S5A). The influence of the time scale for switching from the RP to RRP (τ_{dock}) is also almost negligible, but decreasing τ_{dock} to a value of 50 ms leads to a network desynchronization (Fig. 3.S4B and Fig. 3.S5B) and disruption of the rhythm.

Increasing the time constant for the vesicular depletion in the RRP (τ_{rel}) from

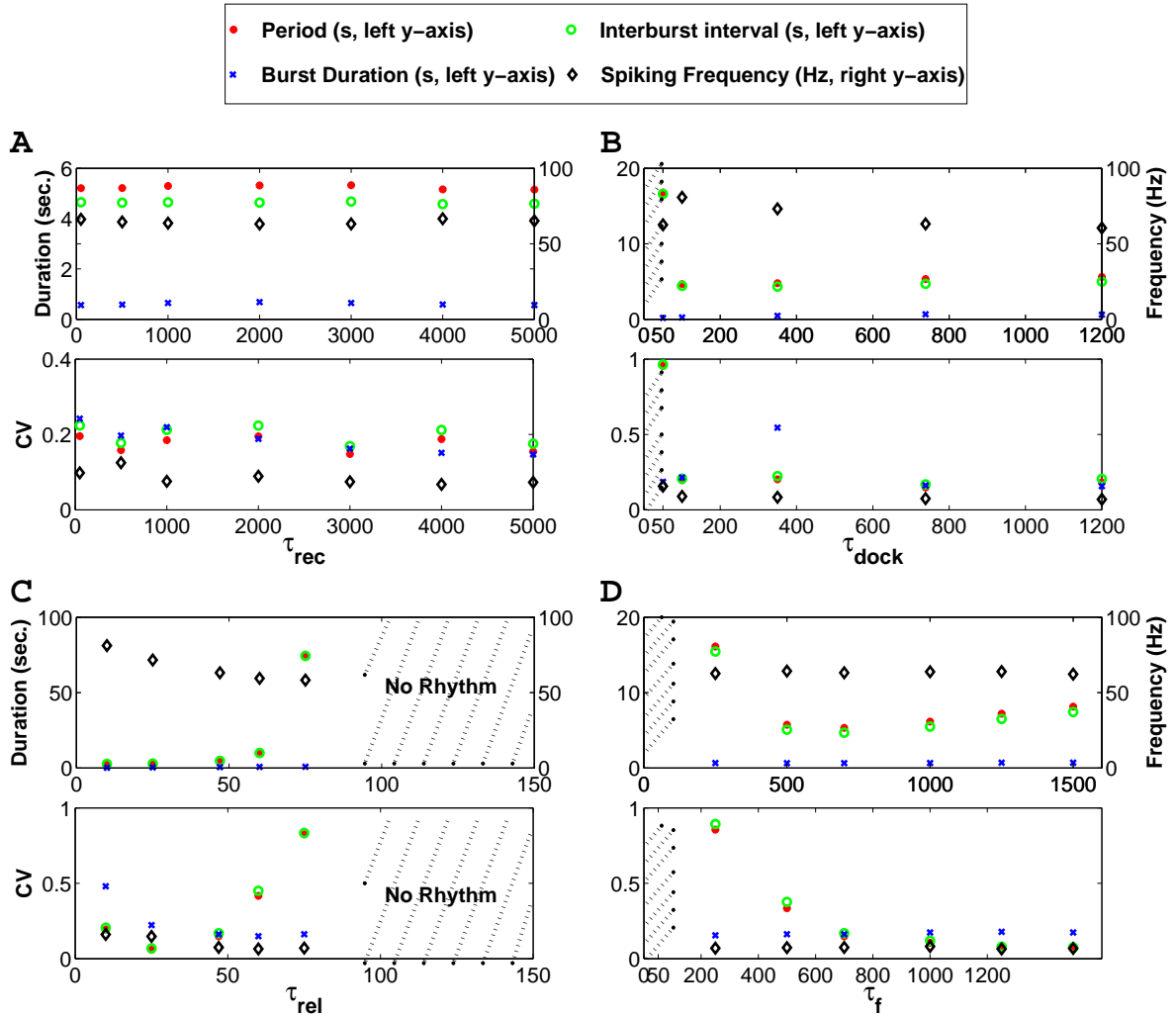


Figure 3.S5: **Synaptic dynamics at the network level:** Mean and CV of the burst duration, the interburst interval, the cycle period (left y-axis, sec), and the spiking frequency during bursts (right y-axis, Hz) as a function of τ_{rec} (**A**), τ_{dock} (**B**), τ_{rel} (**C**) and τ_f (**D**). All the other parameters are the same as described in Table 1, except y_{dock}^{\min} (eq.10 of SI), which is computed for each value of τ_x . The network is the same for each simulation.

10 ms to 60 ms widely increases the cycle periods from 2.9 ± 0.6 sec to 10.7 ± 0.1 sec, and also the burst duration from 200 ± 100 ms to 772 ± 115 ms. In addition, past the value $\tau_{\text{rel}} = 75$ ms, the rhythm is unstable, with cycle periods of 75.1 ± 61.9 sec, and burst duration of 851 ± 138 ms (Fig. 3.S4C).

Finally, by increasing the time constant for the facilitation variable (τ_f), the cycle period increases linearly. More interestingly, decreasing τ_f from 700 ms to 250 ms widely increases the cycle period and variability from 5.3 ± 0.8 sec to 16.1 ± 13.8 sec respectively. This increase is due to the difficulty in recruiting neighboring neurons, as the facilitation variable $x(t)$ drops to its steady state too quickly. However, the burst duration is stable, changing from 650 ± 100 ms to 666 ± 100 ms.

Technically, when we modified these four time constants, the dynamics of Y_{dock} ($Y_{\text{dock}} = \frac{Y_{\text{dock}}}{y_{\text{dock}}^{\text{max}}}$) are changed and we had to modify the value of $y_{\text{dock}}^{\text{min}}$ accordingly. Indeed, the value of $y_{\text{dock}}^{\text{min}}$ is chosen to represent the value of Y_{dock} that accounts for the emptiness of the RRP. This parameter is key in the transformation from the continuous model and the discrete number of vesicles (*SI Appendix*, section “Computing the synaptic current”). To choose $y_{\text{dock}}^{\text{min}}$ for the previous set of parameters (Table 4.1), we applied a 60 Hz stimulation protocol to a single neuron, and chose for termination of release the first time for which the derivative of $Y_{\text{dock}}(t)$ is equal to the limit value of the tangent at infinity, computed by a numerical fit. We applied the same procedure for each of the four time-related parameters. We then ran simulations for each value during 300 sec while keeping the same neuronal network. For $\tau_f = 50$ ms, 100 ms, 250 ms and $\tau_{\text{rel}} = 75$ ms, 100 ms, the cycle period was above 10 sec, and we ran longer simulations for about 1500 sec to obtain enough cycles.

4.6.4 Modification of the spiking frequency during a burst.

The mean spiking frequency during bursts is around 60 Hz, and is stable under the different conditions we imposed to the model. This frequency was not fixed, but emerged as a result of the simulations with the parameters of the model described in Table 1. To determine which parameters could control this frequency, we decreased the re-polarization constants α_n and β_n in equation 4.4, that govern potassium dynamics in the HH model. This results in slowing down the dynamic of the variable n , which increases the refractory period of the AP. It also reduces the minimal current I_{app} needed to induce an AP. To compare the dynamics of the model for different values of α_n and β_n , we also modify the amplitude of the voltage noise σ and the synaptic strength K_I : when parameters α_n and β_n are scaled by a factor 0.35 in eq. 4.4, the AP-threshold in the HH dynamic reduces from -21.6 mV to -28.4 mV. After we further reduce the amplitude of the noise σ eq. 4.3 from 0.4 to 0.2, and the synaptic strength K_I (eq. 4.13) from 2666 to 2250, we simulated the bursting activity of the network and the results are presented in Fig. 3.S6, which affect the network dynamics as follows:

- the spiking frequency is decreased during a burst, from 59 Hz to 34.8 ± 10 Hz,
- the mean number of spikes within a burst is decreased from 42 to 10.4,
- the burst duration is decreased from 694 ± 138 ms to 315 ± 225 ms,
- the cycle period has decreased from 5.5 ± 1 sec to 3.4 ± 1.7 sec.

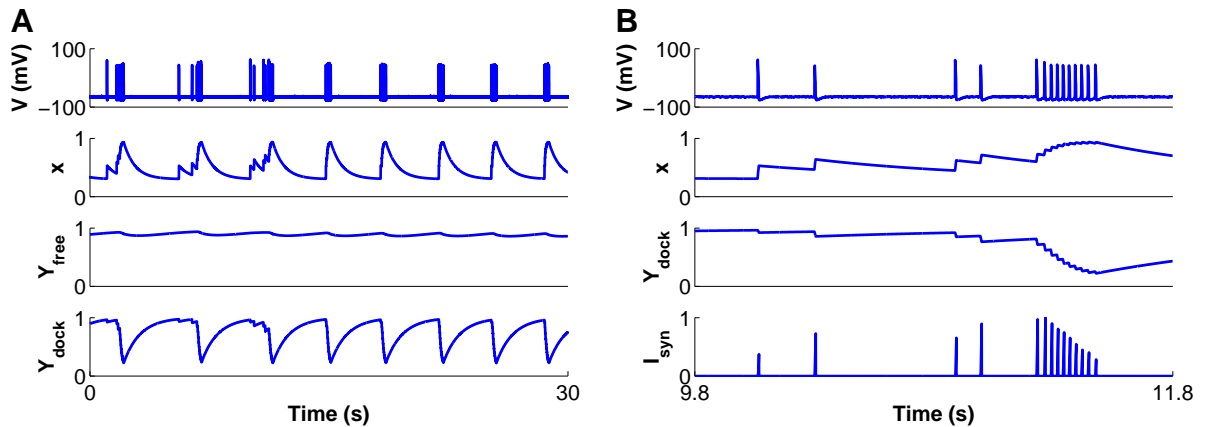


Figure 3.S6: **Burst Spiking Frequency** **A**: Time dependent plot of the voltage V , the facilitation variable x , and the scaled variables Y_{free} , Y_{dock} for a single neuron chosen randomly from the network for a scaling of variables α_n and β_n of 0.35, with parameter $\sigma = 0.2$ and $K_I = 2252$ (the mean bursting duration is 315 ± 225 ms, and the mean cycle period is 3.4 ± 1.7 s). **B**: Magnification of V , x , Y_{dock} and I_{syn} for the neuron of Fig. 3.S6A, during 1.5 s

4.6.5 Effect of deleting random neurons on the network activity.

We randomly suppressed different neurons (from 25 to 200 in a network of 400 neurons) by removing their connections with the rest of the network. We ran, for each number of removed neurons, three simulations for 100 sec. and for different random network realizations. We found that the rhythm was not changed by adding more simulations. However the rhythm period kept increasing when deleting more neurons. When at least 125 neurons are suppressed, the rhythm period exceeds 15 seconds, and thus we increased the time window of simulation to 300 seconds to observe many cycles. When removing 175 neurons, the number of bursts decreased drastically, leading to quiet periods lasting more than 300 seconds, and to rhythm disruption.

We compare in Fig. 3.S7 the rhythm period obtained by suppressing an increasing number of neurons in the simulations, with lesioning by cumulative single-cell laser ablation (Fig. 5c in [72]). Interestingly, we could fit both the experimental and simulation data with a single exponential curve (Fig. 3.S7A), although we found that a double exponential is a better approximation (dashed curve in Fig. 3.S7A). The goodness of fit as measured by the summed square of residuals (SSE) = 0.002. To compare the bursting period, we first normalized by the one obtained in the absence of any neuronal removal. Since the number of removed neurons to rhythm disruption was not known, we used our numerical simulations to estimate this number. We found that the rhythm was completely abolished between 150 and 175 neurons removed, and fixed 160 for a complete rhythm disruption (Fig. 3.S7A). We represent the average time-dependent voltage changes over the neuronal population (Fig. 3.S7B) and the associated power spectrum density (PSD) absolute value (Fig. 3.S7C).

When no neurons are removed, (Fig. 3.S7C, red, x-axis is in logarithmic scale) the absolute value of the PSD presents a main peak around $f_0 = 0.2$ Hz (fundamental frequency), followed by several peaks at different frequencies that are integer multiples of f_0 and represents the harmonics. This analysis shows that our system is almost periodic, with a mean frequency around 0.2 Hz. When 50 neurons are removed (12.5 % of the network), the network activity is not seriously damaged; with 100 neurons (25 % of the network), the rhythm starts to be affected and it disappears by removing 175 neurons and more. The mean burst duration (interburst intervals, periods) are plotted in Fig. 3.S7D. Interestingly, during neuronal lesioning, the burst duration remains quite stable, with a mean spike frequency around 58.1 ± 2 Hz during burst.

The fraction of lesioned neurons leading to burst termination in our model is around 40%, whereas in [72], the estimated value coming from experiments was between 15 and 20 %, showing that our model is too robust. This robustness could result from the mean-field modeling used for the synaptic dynamics, which does not account for synaptic failures. To test this hypothesis, we modified this aspect of the model, by introducing a release probability parameter P_{rel} in the system of eqs. 4.12

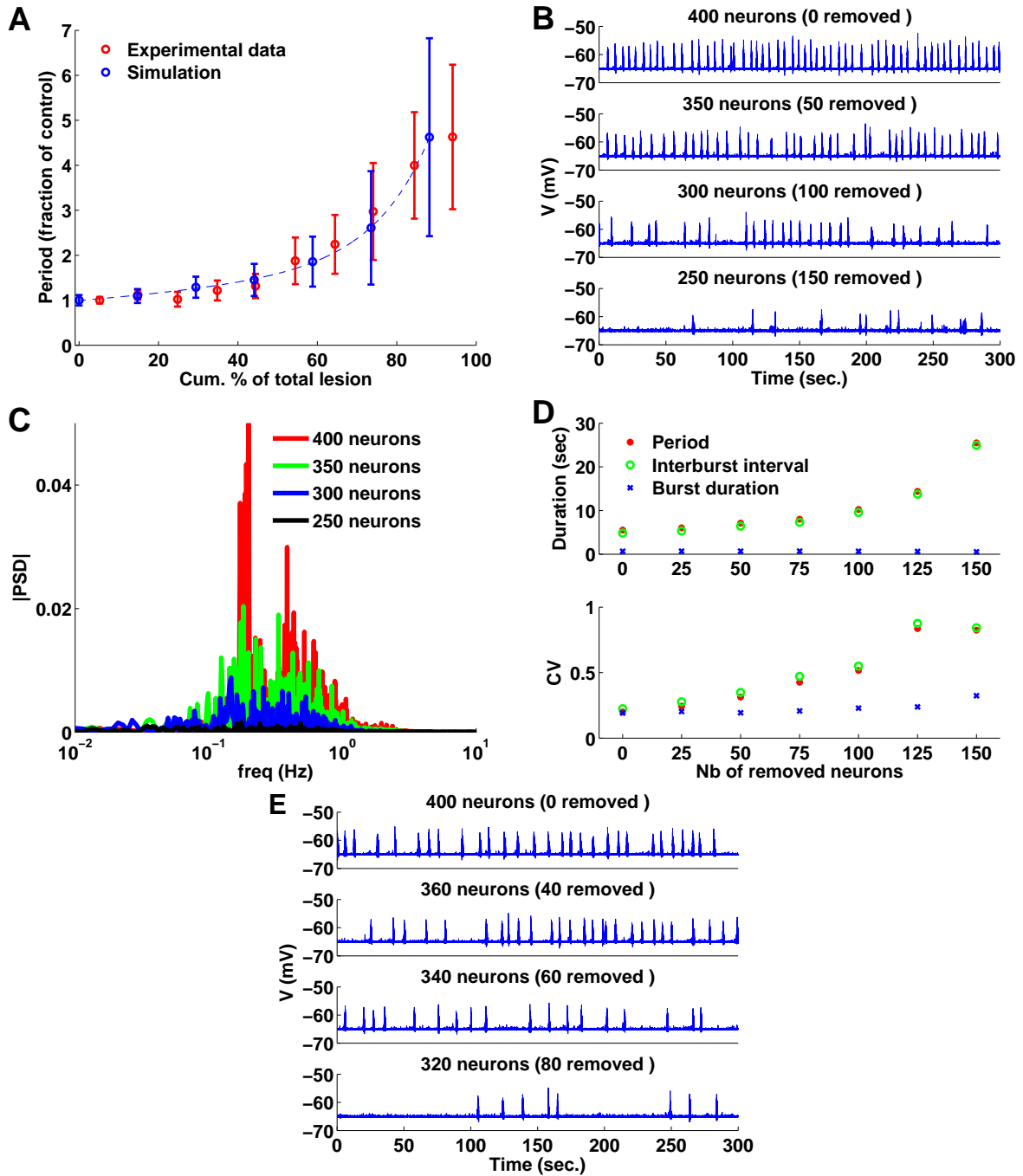


Figure 3.S7: **Effect of deleting random neurons on the network activity.** **A:** Comparison between simulations (blue) and experimental results (red, extracted from [72]). **B:** Mean membrane potential when 0, 50, 100, and 125 neurons are removed, corresponding to 400, 350, 300 and 275 remaining neurons. **C:** Power spectrum associated with **B** (logarithmic scale). **D:** Mean and CV of the burst duration, interburst interval and rhythm period for several removed neurons. **E:** Mean membrane potential when 0, 40, 60, 80 neurons are removed in a network of 400 neurons, with a release probability $P_{rel}=0.8$.

governing vesicular release:

$$\begin{aligned}
 \dot{x} &= \frac{X - x}{\tau_f} + k(1 - x)H(V - T) \\
 \dot{y}_{\text{free}} &= \frac{1 - y_{\text{free}} - y_{\text{dock}}}{\tau_{\text{rec}}} - \frac{1}{\tau_{\text{dock}}} (y_{\text{dock}}^{\text{max}} - y_{\text{dock}}) y_{\text{free}} \left[1 + \frac{x - X}{X} H(V - T) \right] \\
 \dot{y}_{\text{dock}} &= \frac{1}{\tau_{\text{dock}}} (y_{\text{dock}}^{\text{max}} - y_{\text{dock}}) y_{\text{free}} \left[1 + \frac{x - X}{X} H(V - T) \right] \\
 &\quad - \frac{1}{\tau_{\text{rel}}} y_{\text{dock}} \frac{x - X}{X} H(V - T) H(r - P_{\text{rel}}),
 \end{aligned} \tag{4.17}$$

where r is a uniform random variable on $[0, 1]$. We used a value of this parameter $P_{\text{rel}}=0.8$. We simulated the network and we found the following changes: the cycle period is increased from 5.0 ± 1 to 9.8 ± 4.1 sec. When removing 80 neurons, we observe very few bursts with IBIs lasting more than 80 sec, and a clear disruption of the rhythm (Fig. 3.S7E). We conclude that by introducing a stochastic release, our model can now replicate the disruption of the rhythm with a similar robustness as in lesioning experiments.

4.6.6 Consequences of gradually decreasing the synaptic strength.

To study the consequences of decreasing the synaptic strength, we decreased parameter K_I in the model, which has an effect equivalent to applying [NBQX], an antagonist of AMPARs that mediate synaptic transmission and underlie respiratory drive in the preBötzinger Complex [136]. We implemented the numerical procedure as follows: we chose a network with randomly connected neurons and ran simulations over 300 seconds while decreasing values of K_I , from 100% $K_I = 2666$ to 60% $K_I = 1600$ in steps of 2%. For values lower than 70%, we ran simulations for 900 seconds to account for a sufficient amount of periods. We observed a step increase in the rhythm period, with no major changes in burst duration (Fig. 3.S8). The rhythm started to be highly irregular at 68%, with interburst intervals lasting more than 100 seconds, and disappeared around 60%. The curve is well-fitted by a double exponential (dashed curve in Fig. 3.S8A, SSE = 0.94). To compare with experimental data extracted from [136], we considered that the control conditions in simulations (100% control) corresponds to $0.001 \mu\text{M}$ [NBQX]. We then scaled the abscissa of the simulation plot so that the two curves best match (Fig. 3.S8A).

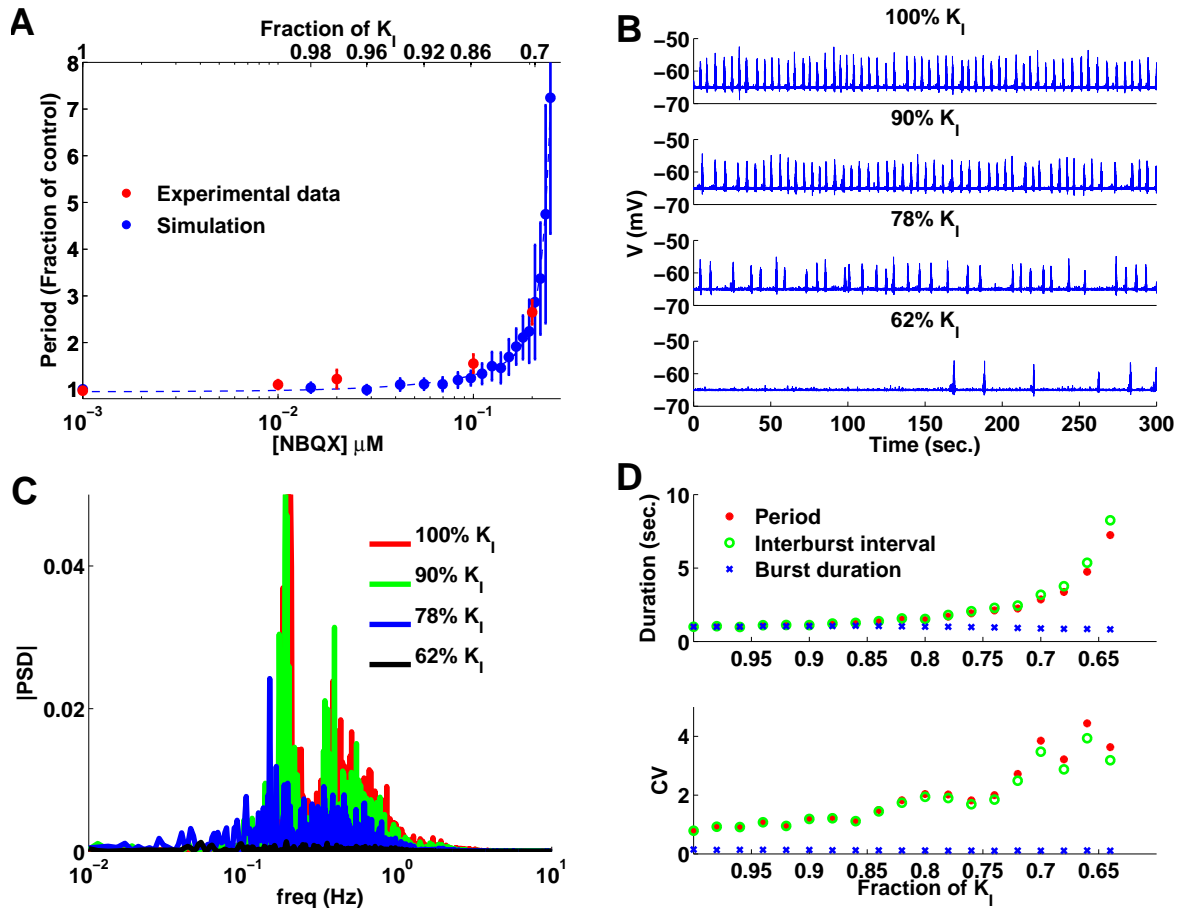


Figure 3.S8: **Consequences of gradually decreasing synaptic strength, comparison with experimental data.** **A:** Comparison between simulations (blue) and experimental results (red, extracted from [136]). Results are presented as mean \pm S.E.M. **B:** Mean potential over all the network for different values of the fraction of the initial synaptic strength, controlled via K_I . **C:** Power spectrum of the mean membrane potential computed for several fractions of K_I . **D:** Mean and CV of the burst duration, interburst interval, and rhythm period for several fractions of K_I .

4.6.7 Depolarizing neurons increases the rhythm frequency.

Changing (depolarizing and hyperpolarizing) the membrane potential affects bursting: to depolarize (hyperpolarize) neurons, we added (or subtracted) a current I_{app} to their current balance equation (Fig. 3.S9). This current is equivalent to increasing the extracellular potassium concentration $[K^+]$ and the probability of ectopic spikes. To compare experimental and simulation data, we scaled the abscissa and superimposed the two curves, where 9 mM $[K^+]$ corresponds to control conditions ($I = 0$, no additional current).

At 9 mM $[K^+]$, the correspondence between preBötC and XIIIn activity is known to be almost one-to-one [142], whereas at 6 mM and 3 mM $[K^+]$, Kam et al [95] observed burstlets in the preBötC activity that do not show up in XIIIn activity. Burstlets are characterized by smaller amplitude than preBötC bursts. In our model, for $I_{app} = -0.25$ pA and $I_{app} = -0.5$ pA, we observe periods of times during the inter-burst interval where several neurons are spiking together but no population-wide activity is generated (red line in Fig. 3.S10A).

This effect recalls the pre-inspiratory patterns observed in control conditions ($I_{app} = 0$ pA, green line in Fig. 3.S10A): before each spike, a small group of tens of neurons, that differs from one burst to another, spike together, and recruit the entire network for a bursting event (Movie S3). Those neurons could represent the pre-inspiratory neurons observed experimentally. We postulate that after hyperpolarization of the network ($I_{app} = -0.25$ pA), those groups of neurons fail to recruit the entire network; likely because of the hyperpolarization that makes recruitment more difficult. These patterns, formed by small groups of tens of spiking neurons that do not trigger a burst, show similarities with the burstlets observed experimentally [95]. Nevertheless, burstlet activity observed in [95] is widespread in the preBötC and not restricted to a small number of neurons like in our model.

To investigate how hyperpolarization of the network modifies the rhythm's dynamics, we plotted Poincaré maps of the cycle periods when $I_{app} = -0.25$ pA over 1000 sec (Fig. 3.S10B, nine runs). We observed a wide, quasi-periodic distribution comparable to the experimental results observed in ([95], Figure 1D), which was different from the single cluster expected when the system is regularly periodic ($I_{app} = 0$ pA, Fig. 3.S10C). We conclude that hyperpolarization of the network modifies the rhythm's dynamics and an almost periodic regime appears as revealed by the Poincaré maps.

To clarify the mechanism of these low amplitude events (red in Fig. 3.S10A) in our study, we now show using numerical simulations (Fig. 3.S11) that contrary to the burst activity, which extends through the neuronal network, during these events, the synaptic properties (depression and facilitation) are not involved, preventing the recruitment of the network.

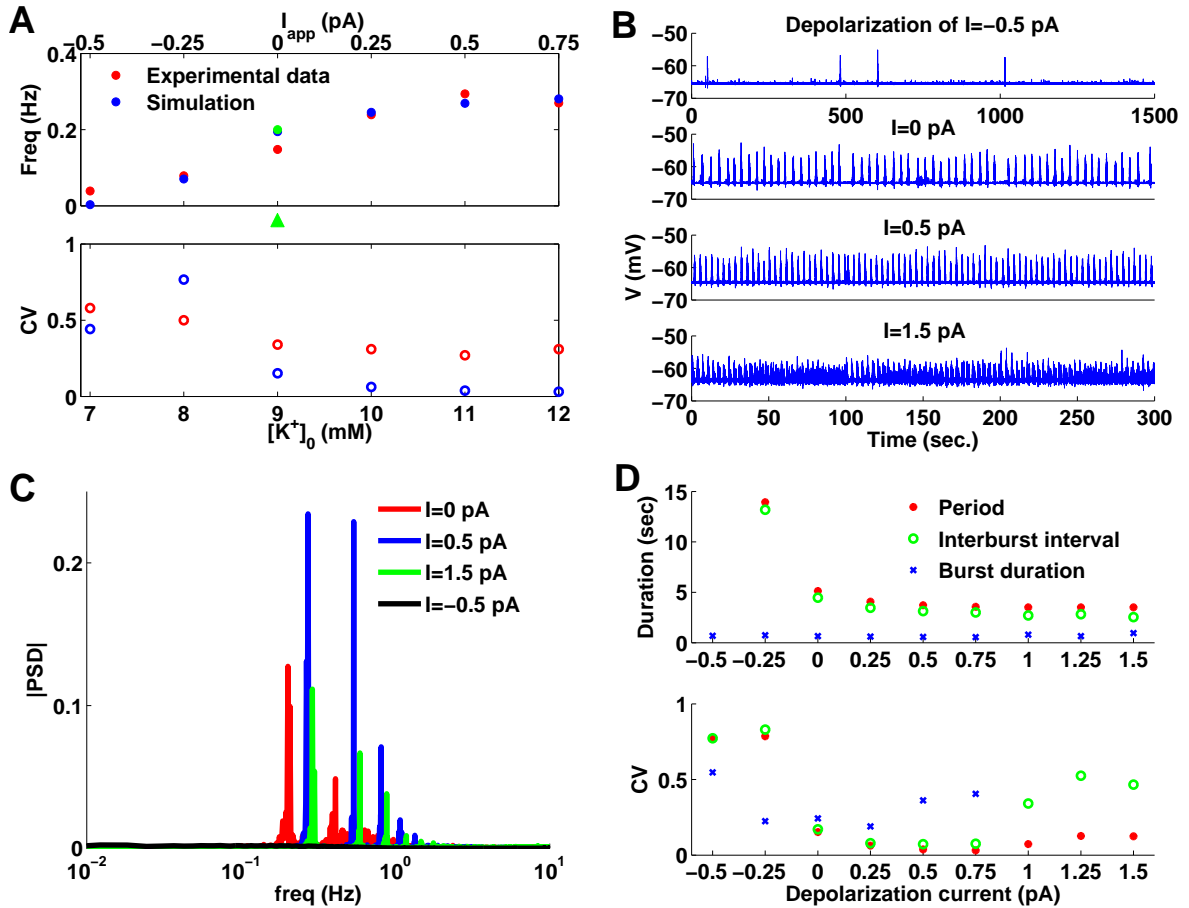


Figure 3.S9: **Consequence of a global neuronal depolarization on the network rhythm.** **A:** Comparison between experimental results published in [142] (red) and simulations (blue). The experimental results are obtained by moving the extra-cellular potassium concentration from 3 mM to 12 mM. To compare with the simulations, we scaled the abscissa and superimposed the two curves, taking into account that 9 mM corresponds to control conditions. The green circle represents the mean frequency in control conditions (at 9 mM $[K^+]$, green arrowhead), which differs during the experimental protocol. **B:** Mean potential over all the network for different values of I . **C:** Power spectrum associated with **C**. **D:** Mean and CV of the burst duration, interburst duration and rhythm period for several values of the applied current I_{app} .

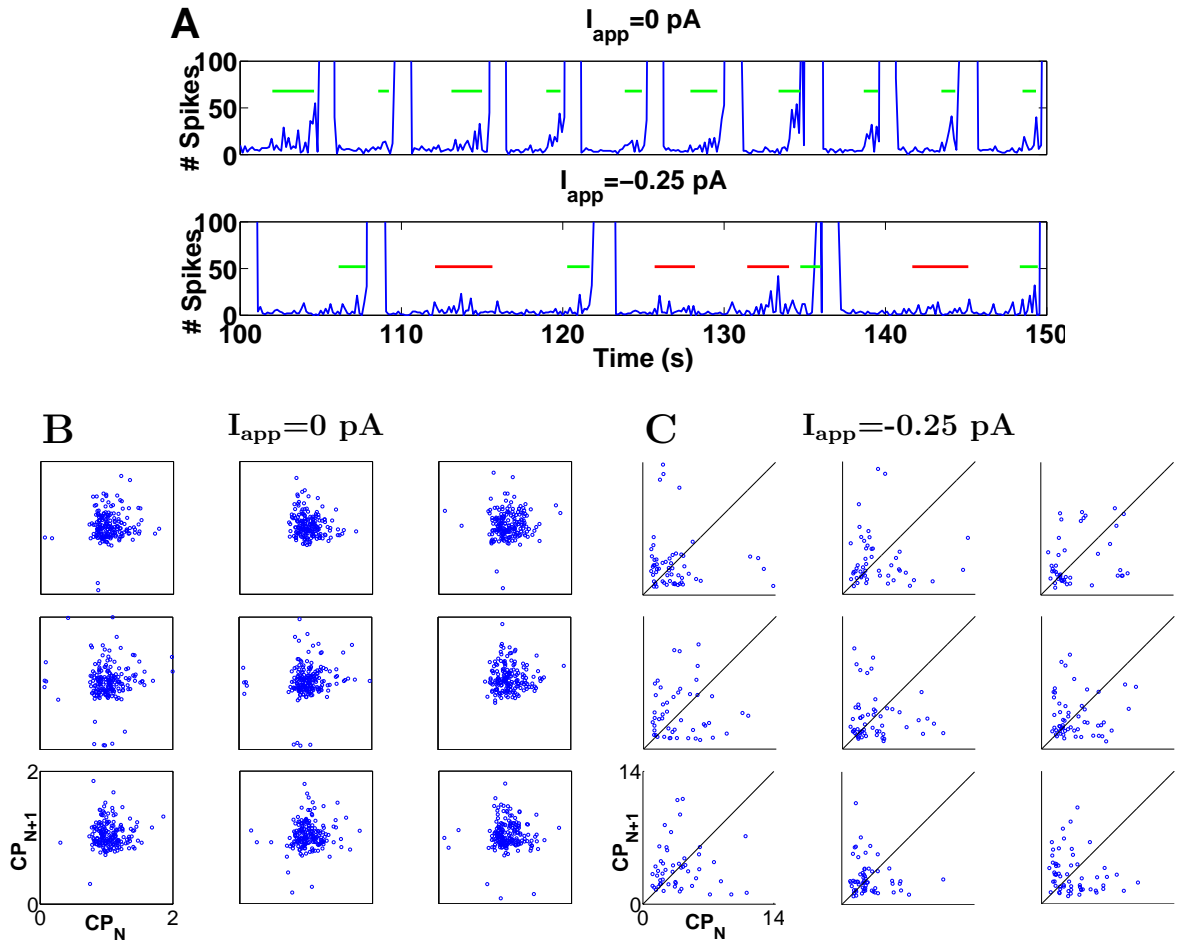


Figure 3.S10: **Network-wide hyperpolarization** **A**: Time dependent plot of the number of spikes in the network when no current is applied ($I_{app} = 0$ pA, top), and when the network is hyperpolarized ($I_{app} = -0.25$ pA, bottom). Note the increasing spiking activity preceding the burst (green bars) in both plots. The red bars show periods when several neurons are spiking together but fail to recruit the network, which show similarities (but see text) with the burstlets observed experimentally. **B-C**: Poincaré maps of the cycle periods of one random neuron when $I_{app} = 0$ pA (**B**) and $I_{app} = -0.25$ pA (**C**). The network is recorded over 1000 sec (nine runs), cycle periods are normalized by the mean period when $I_{app} = 0$ pA, equal to 5.0 sec. Notice the difference in the axes range in **B** and **C**.

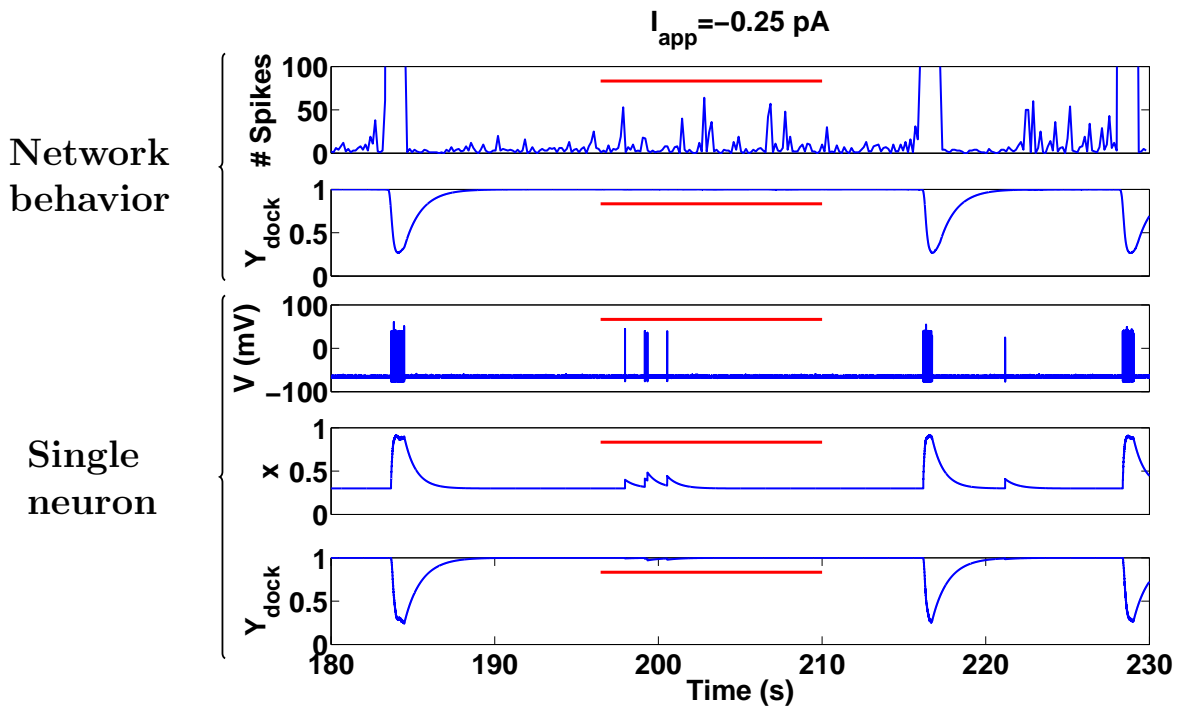


Figure 3.S11: **Low amplitude events and synaptic properties.** Low amplitude events are observed when the network is hyperpolarized by $I_{app}=-0.25$ pA. Time dependent plot of the number of spikes in the network (first), the mean depression over the network $Y_{dock} = y_{dock}/y_{dock}^{max}$ (second graph), the potential of a single neuron (third graph), the facilitation (fourth) and the depression variable Y_{dock} of a single neuron (last). Low amplitude activity events involving few neurons (red lines) cannot trigger a burst. During low amplitude events the depression and facilitation variables are not activated. Thus the synaptic properties are not involved in their termination, in contrast to bursts.

4.6.8 Minimal number of stimulations for burst induction.

To determine the minimal number of neurons necessary for inducing a network burst (Fig. 2D), we depolarized an increasing number of randomly chosen neurons. In practice, within the HH-model, we generated trains from 1 to 6 events consisting of 100 mV-depolarization during 0.05 ms with an interval separation of 17 ms between the train (at 60 Hz). This 60 Hz-frequency corresponds to the endogenous spiking dynamics. We started running the network at time $t = 0$ while we generated the stimulation at time $t=550$ ms, where steady state is achieved. We then monitored for 2 seconds the activity. A burst was detected when 80% of the neurons were spiking one second after initiation. We could then estimate the probability of bursting for different numbers of pulses and stimulated neurons.

4.6.9 Inspiratory drive currents.

Experimentally, respiratory preBötC neurons receive a volley of inward synaptic currents that typically last for hundreds of milliseconds, peak at more than 100 pA, occur at periodic intervals, and are referred to as inspiratory drive currents (Fig. 3.S12).

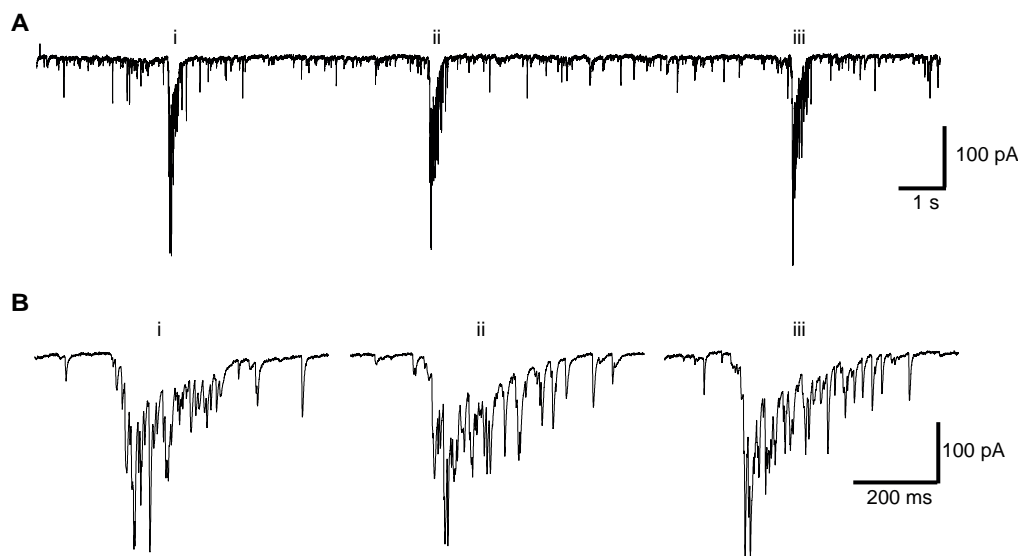


Figure 3.S12: **Inspiratory drive currents in an experimentally-recorded pre-BötC neuron** **A**: Inspiratory drive currents in voltage-clamp configuration. The command voltage was -60 mV, and this is an expanded view of the trace displayed in the middle of Fig. 3C. **B**: Individual bursts (i., ii., iii.) are shown at a faster timescale.

4.7 Movie

Seven movies are provided as supplementary information. In each movie, the network is organized in a square lattice ($20 \times 20 = 400$ neurons), where each square of the grid is the voltage V or the facilitation parameter x (Video S2) of a neuron, and the right color bar encodes the amplitude of the variable. The plot at the bottom of the movie is the average V over all the neuronal network. The time-dependent color represents the progression in the movie. Each movie lasts 60 seconds with 25 frames per second. Gray squares represent neurons isolated from the network (no input nor output connections).

4.7.1 Movie S1:

Time evolution of the membrane potential V in the network population during sixty seconds (real time). Bursting events are generated in the entire network.

4.7.2 Movie S2:

Time evolution of the facilitation variable x in the network population during 20 seconds (slowed down 3 times). Each of the three bursts begins from a random location in the network. Bursts are initiated when several neighboring neurons start firing together. This movie confirms that neurons triggering bursts are not the same from one burst to another. This proves that the burst is generated by random neurons and confirm the absence of any pacemaker.

4.7.3 Movie S3:

This movie shows how the rhythm propagates within the network. We present the time evolution of the voltage V during one burst lasting 1.5 seconds (slowed down 40 times).

4.7.4 Movie S4:

This movie shows the time evolution of the voltage V , after 125 neurons have been removed from the network, over 60 seconds (real time). Isolated neurons with no connections (in gray) make the propagation of bursts within the network more difficult.

4.7.5 Movie S5:

This movie shows a burst in the neuron network S4 (the voltage V) during 1.5 seconds, and slowed down 40 times.

4.7.6 Movie S6:

Time evolution of the voltage V for a network with a small degree of connectivity, generated with a parameter $s = 0.75$, monitored during 1.5 seconds and slowed down

40 times. We observe the propagation of action potentials during a single burst.

4.7.7 Movie S7:

This movie shows the time evolution of the voltage V for a network with a higher degree of connectivity, generated with a parameter $s = 1.1$ (compare to $s = 0.9$ in movies S1-S5), during 1.5 seconds and slowed down 40 times. We note that however, the bursting period lasts for tens of seconds or more as indicated in Fig. 3.S2F. The results presented in this movie predicts that increasing the connectivity could result in wave propagation. These results should be seen as a possible prediction of neuronal connection changes.

Tables

Table 4.1: Parameters of synaptic transmission

Parameter	Description	Value
x	Facilitation variable	
y_{dock}	First depression variable	
y_{free}	Second depression variable	
X	Equilibrium value of x	0.3
x_{RefP}	Threshold for refractory period	0.31
$y_{\text{free}}^{\text{max}}$	Maximum value of y_{free}	0.82
$y_{\text{dock}}^{\text{max}}$	Maximum value of y_{dock}	0.18
$y_{\text{dock}}^{\text{min}}$	Minimum value of y_{dock}	0.04
k	Facilitation parameter	0.08
τ_f	Facilitation time constant	700 ms
τ_{dock}	First time constant for y_{dock}	738 ms
τ_{rel}	Second time constant for y_{dock}	47 ms
τ_{rec}	Time constant for the recovery	3000 ms
τ_{del}	Delay of the synaptic response	1 ms
K_I	Synaptic strength	2666
s	Connectivity	0.9
σ	Amplitude of voltage noise	$0.89 \text{ (pA.cm}^{-2}\text{)}^2 \cdot \text{ms}^{-1}$
T	Action Potential threshold	-58 mV

Table 4.2: Hodgkin-Huxley

Parameter	Description	Value
C	Capacitance	$1 \mu\text{F}.\text{cm}^{-2}$
g_{Na}	Conductance of Na^{2+} -current	$120 \text{ mS}.\text{cm}^{-2}$
V_{Na}	Equilibrium potential of Na^{2+} -current	50 mV
τ_m	Parameter for m	10 ms
θ_m	Parameter for m	-40 mV
η_m	Parameter for m	4
σ_m	Parameter for m	18
g_K	Conductance of K^+ -current	$36 \text{ mS}.\text{cm}^{-2}$
V_K	Equilibrium potential of K^+ -current	-77 mV
g_L	Conductance of leak current	$0.3 \text{ mS}.\text{cm}^{-2}$
V_L	Equilibrium potential of leak current	-54.4 mV
τ_n	Parameter for n	100 ms
θ_n	Parameter for n	-55 mV
η_n	Parameter for n	0.125
σ_n	Parameter for n	80

Conclusion

In this thesis, I have studied neuronal structures at different scales through mathematical analysis and modeling. The main tools I used are partial differential equations, elliptic equations, asymptotic analysis, stochastic processes and numerical simulations. In the first part, I presented a method to compute the leading order term of the mean first passage time to a narrow opening located between two tangent spheres (DST). I used this idealized geometry to build a model of the Active Zone at neuronal pre-synaptic terminals, to investigate the influence of channels and vesicular organization on the release probability. In the second part, I combined my previous result on the DST and my model of the Active Zone, to build a more general model of the pre-synaptic terminal. I used that the mean first passage time to a small target is Poissonian, to coarse-grain the classical PDE description of diffusive processes into a system of ODE based on Poissonian rate equations. This approach allows also to realize fast stochastic simulations by replacing the naive Brownian simulations with Gillespie's algorithm. Finally, I presented in the last part a model and numerical simulations for the pre-Bötzinger Complex, the neuronal network that paces inspiration in mammals. This model shows how synaptic properties at the neuronal level, such as facilitation and depression, can trigger the emergence of oscillations at the network level. The model was benchmarked against several experimental studies, and our prediction that pre-Bötzinger Complex neurons express depression at time scales influencing respiratory rhythm was confirmed by experimental measurements.

The analytical results for the DST computed in the first part of the thesis reveal the role of the local geometrical structure for diffusion processes at a molecular level. A further analytical development will be to add a drift term, to account for hydrodynamical flows or active transport of proteins in the corresponding microdomains. In the case of the domain with a funnel-shaped cusp, an interesting future work will be to compute the leading order term of the mean first passage time when the local description of the cusp takes the form $y = Ax^\nu$, $\nu \neq 2$. This small modification of the geometry cannot be solved using the mapping function for $\nu = 2$. Indeed, while using this mapping function, increasing ν creates a cusp in the mapped region. One can also notice that increasing ν modifies the original domain, creating a geometry that looks like the problem of a sphere connected to a cylinder, studied in [83]. A new mapping function must be found here, that will have to account for this transition between two different geometries.

The model of the Active Zone I developed using the DST analysis shows that channel positioning, the number of entering ions and vesicular organization are cru-

cial parameters governing vesicular release at the pre-synaptic terminal. Hence, changing the Active Zone organization modifies the synaptic response. The relative simplicity of this model could be criticized. In that, a possible development of the model will be to add calcium channels motion at the Active Zone, as suggested by recent experimental measurements.

The modeling approach developed in the second part of the thesis allows to analyze the coupling between many Brownian particles evolving in a domain, which is usually modeled using a continuum ensemble, with the activation of a process by few Brownian particles, more likely to be represented by discrete events. The combination of a system of ODE developed using rate theory with a set of Markov equations, allows running fast simulations with precise analytical descriptions. From a biological point of view, this procedure reflects the change of scale from the cellular to the molecular level.

In the context of vesicular release at the pre-synaptic terminal, our modeling approach allows to investigate the role of various parameters on the release probability. However, to predict some properties at a given synapse, this requires to have access to several biophysical properties, sometimes hardly obtained from experiments, such as the number of buffers, their type of motion, the number of ions entering through one calcium channel, and so on. This comes with the fact that the aim of our study is to propose coherent models for phenomena that are hardly accessible through experimental measurements. An example is the relative distances between channels and vesicles that take place at sub-micrometers dimensions, which imposes to infer them from functional measurements.

A further development of the model will be to study paired-pulse facilitation, and to understand if and how it is due to calcium accumulation in the terminal. Indeed, the hypothesis that residual calcium concentration could be responsible for paired-pulse facilitation [158] seems in opposition to our results concerning the small influence of the number of calcium ions present in the bulk on vesicular release probability.

Ultimately, this modeling approach can be extended to other activation processes in neuronal microdomains, such as the Calcium/calmoduline-dependent protein kinase II (CaMKII) activation in dendritic spines. Indeed, these proteins are thought to play a key role in learning and memory formation in glutamatergic synapses, because of their role in long-term potentiation induction, and also because of their persistent activation after LTP induction. Activation of CaMKII is made through calcium and calmoduline, a calcium buffer highly concentrated in spines. After persistent stimulation, CaMKII has the particular property to autophosphorylate, which permit the kinase to stay active for very long times, even after calcium concentration went back to its resting level. However, this autonomous activity is not induced by a single pre-synaptic action potential, which activates CaMKII only for a short time. The mechanism that permits this switch between two states of activation at two different time scales is still unclear today [121]. A modeling approach as presented in part 2 will solve the change of scale from the molecular to the cellular level, and allow to study the switching between the two different time scales.

Finally, in the last part of the thesis, we study in the context of the pre-Bötzinger Complex network, the change of scale from the neuronal to the network level. Indeed, our modeling approach shows that bursting oscillations can emerge in an ensemble of neurons, due to the synaptic activity of individual neurons. This phenomenon may be quite generic and could explain oscillations in other neuronal networks where the mechanism remains unclear, such as for example the circuits for chewing, swallowing, whisking or locomotion.

The main limitation of this model relies on the lack of biophysical data at the synaptic level, and concerning the connectivity between neurons. Recent experimental studies have started to look at the synaptic properties of the pre-Bötzinger Complex neurons, and further experimental results will allow to refine the model [112].

In order to do a mathematical analysis of the model, which contains 2000 coupled ordinary differential equations, a future work will be to derive a system of mean-field equations. A key challenge for this derivation will be to understand how to take into account the spatial aspect in the recruitments between neurons, which is crucial in our model to obtain a periodic rhythm.

To summarize, our approach to study the change of scale from the molecular to the network level can be used in many biological processes that include diffusion in microdomains. It allows to propose hypotheses on phenomenon not accessible yet through direct experimental measurements. These predictions should then be refined using an experimental approach, and so on. This move back and forth between experiments and modeling provides a very powerful tool to break into the extremely complex challenges biological science faces today.

Appendix & Bibliography

Appendix A

Calcium dynamics in neuronal microdomains: modeling, stochastic simulations and data analysis

Published in Guerrier C, Korkotian E and Holcman D “Calcium Dynamics in Neuronal Microdomains: Modeling, Stochastic Simulations and Data Analysis” In Jaeger D. jung R (eds.) Encyclopedia of Computational Neuroscience, pp 1-37 (2014) Springer New York Heidelberg Dordrecht London

Calcium is ubiquitous in neuronal microdomains, but its regulation still remains unclear due to the different time scales involved. This multiscale process is generated by the local cell geometry, the exchanger and channel rates that define calcium residence time. This time is indeed crucial in several regulatory mechanisms such as synaptic plasticity, receptor trafficking, spine morphology, long range calcium spread, and many others. We describe here mathematical modeling and numerical simulations that have been used to obtain quantitative and qualitative results about calcium time course from live cell imaging and electrophysiological recordings. Computational approaches allow studying calcium integration from short to long time scales, which remains today a challenging problem to solve. We review recent progress over the past years in modeling, analysis and simulations of calcium dynamics in neuronal microdomains as well as the associated applications in extracting information from live cell imaging.

A.1 Definition

Calcium is a key but ubiquitous messenger in cell physiology. Yet, direct electrophysiological or light imaging measurements are limited by the intrinsic small nano- to micro- meter space where chemical reactions occur and also by the small number of molecules. Thus any fluorescence dye molecule added to measure the number of calcium ions can severely perturb the endogenous chemical reactions. Over the years, an alternative approach based on modeling, mathematical analysis and numerical

simulations has demonstrated that it can be used to obtain precise quantitative results about the order of magnitude, rate constants, the role of the cell geometry and flux regulation across scales from channels to the cell level.

The aim of this chapter is to present physical models of calcium ions from the molecular description to the concentration level, to present the mathematical tools used to analyze the model equations. From such analysis, asymptotic formulas can be obtained, which are usually valid for a certain range of parameters. However these formulas allow exploring at low cost the parameter space. The methods to analyze these equations are part of classical analysis of partial differential equations and stochastic processes, which will not be reviewed here, see [171, 172]. We shall present several models related to diffusion, where formulas can be derived and we shall specify how these formulas are used to extract parameters from experimental measurements. But in general models are far too complicated to lead to equations that can be analyzed and, most of the time, numerical simulations have to be built. Building rational simulations requires discretizing the physical equations and bridging the gap between the limits of the equations and the physical description that they account for. We will present here several stochastic simulations, their rules, limitations and tricks that have been developed over the years. As we shall see here, any bottleneck in the equation can lead to heavy simulations running for days. In that case, coarse-graining is a key step to reduce the complexity of the equation so that some analysis can be obtained and can be used to check in some limit the validity of the simulations.

All together physical modeling, mathematical analysis, numerical simulation and their application to the statistical analysis of experimental data form an ensemble of approaches that are used today to better understand molecular interaction in nano- to microdomains. But the most striking convergence of these methods is to derive physiological laws from their first physical principles. We shall present 1) stochastic modeling of calcium ions and their trajectories, 2) modeling of local interactions with discussion of the rate constants, 3) derivation of asymptotic formulas for the residence of calcium in microdomains and dendritic spines, 4) modeling and simulation of diffusion in a crowded three dimensional dendrite, 5) modeling calcium in spines, 6) modeling the CaM activation pathway, and 7) a coarse grained model based on Markov chain to estimate the probability that the number of calcium ions bound to key molecule is reached. Finally, we shall discuss how these simulations can be used to study physiological processes such as transient calcium ions in a dendritic spine, long term potentiation induction or what limits the spread of calcium following synaptic stimulations.

A.2 Detailed Description

A.2.1 Neuronal microdomains

Neurons can be decomposed into several keys microdomains involved in specific functions: dendrites integrate electrical signals, whereas dendritic spines are microcompartments receiving the postsynaptic terminal of excitatory synapses (Fig. A.1). The pre-synaptic terminal is also a key compartment that controls calcium

in relation to vesicular release. Dendrites further decompose into distal and apical dendrites which seem to have different electrophysiological properties that can be correlated with a difference in the structure. The soma and the axon are also separate compartments. We show in Fig. A.1 different distinct compartments. Finally, it was found that aspiny neurons can confine calcium for a time scale comparable to dendritic spine [64]. Can organelles such as vesicles or endoplasmic reticulum control calcium concentration?

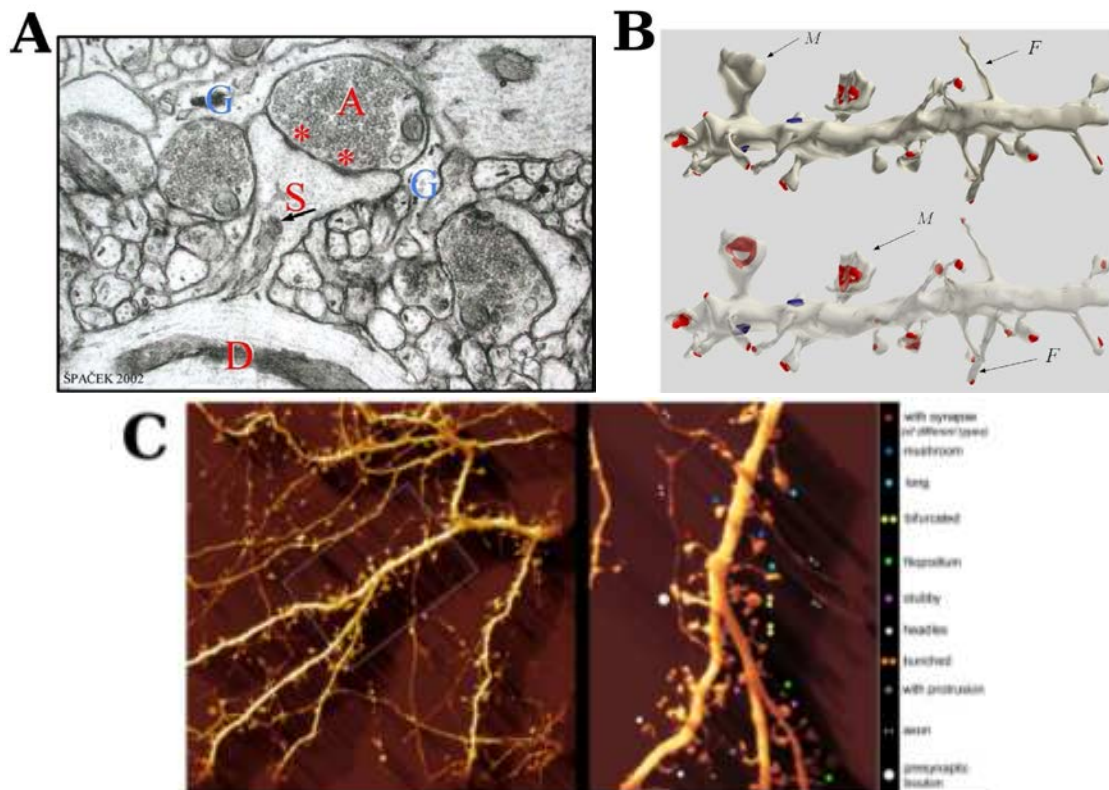


Figure A.1: **Neuronal microdomains.** **A:** Electron microscopy of a synapse. The Postsynaptic terminal is located on a dendritic spine (S) branched in the dendrite (D). Around the axon (A) are located the Glial cells (G). **B:** Three-dimensional EM reconstruction of two dendrites from the hippocampus. The PSDs of excitatory synapses are marked in red and of inhibitory synapses in blue. Filopodia (marked F) and mushroom spines (marked M) are clearly seen. **C:** All possible types of dendritic spines using as example a 3D reconstructed hippocampal dendrite, 3 weeks old in primary culture.

A.2.2 Diffusion in neuronal microdomains: stochastic modeling

We start with a Brownian description of calcium ions. Indeed motion due to thermal fluctuations is the main driving force for the motion of particles such as ions or

molecules. Calcium motion has been well approximated as diffusion, which confirms that the ionic charge is screened. This is not the case for calcium influx through channels, where the nanometer space restriction is a dominant factor for the interaction between the channel charges and the ion [5, 41]. In cells, long distances are overcome mostly by the diffusion process. For example free calcium ions diffuse in dendritic spines or any neuronal microdomain in the dendrite or the axons [108]. At the molecular level, diffusion of ions is described by a random walk. When an ion meets any plasma membrane, it is reflected, or translocated inside an organelle at pumps or exchangers. The transition from one region to another can be modeled by specifying absorbing conditions in specific boundary regions, such as the fictive separation between a dendrite and a spine.

Description of calcium stochastic trajectories

A calcium ion trajectory is described by the Smoluchowski's limit in the large damping approximation of the Langevin equation. The position x at time t satisfies the stochastic equation

$$\gamma [\dot{x} - V(x, t)] + F(x) = \sqrt{2\varepsilon\gamma}w, \quad (\text{A.1})$$

Here $\varepsilon = k_B T/m$, where T is the temperature and k_B the Boltzmann constant, $\gamma = 6\pi a\eta$ is the dynamical viscosity, where η is the viscosity coefficient per unit mass and a is the radius of the ion. w is a random white noise modeling the thermal fluctuations, and the electrostatic force is

$$F(x) = -ze\nabla_x U_0(x),$$

where U_0 is the potential created by the site where the proteins are located. In a first approximation, each protein creates a localized parabolic potential, where the depth can be calibrated by using the backward binding rate and the radius by using the forward binding rate [109]. The frictional drag force, $-\gamma [\dot{x} - V(x, t)]$, is proportional to the relative velocity of the ion and the cytoplasmic fluid. The field of fluid $V(x, t)$ induced by calcium ions will be discussed below.

The Langevin equations

We shall here explain the physical consideration behind the reduction to equation A.1. For a dendritic spine containing N ions of different species (e.g., Ca^{++} , Na^+ , Cl^- , and so on), $\mathbf{x}_i(t)$ is the displacement vector of the i -th ion, m_i is its mass, and z_i is its valence. $\tilde{\mathbf{x}} = (\mathbf{x}_1, \mathbf{x}_2, \dots, \mathbf{x}_N)$ is the coordinate of the N ions in configuration space. We consider a given flow field $\mathbf{V}(\mathbf{x}, t)$ (see description below) and that ions interact with a fixed potential of the charges on the proteins, $U_0(\mathbf{x})$, and with the variable potential of all other ions. The variable potential consists of both the electrostatic ion-ion interaction potential, $U_{\text{ii}}(\tilde{\mathbf{x}})$, and the potential of Lennard-Jones-type repulsions, $U_{\text{LJ}}(\tilde{\mathbf{x}})$ (that represents the finite size of the ions). The force per unit mass on the i -th ion is

$$\mathbf{F}_i(\tilde{\mathbf{x}}) = -z_i e \nabla_{\mathbf{x}_i} [U_0(\mathbf{x}_i) + U_{\text{ii}}(\tilde{\mathbf{x}})] - \nabla_{\mathbf{x}_i} U_{\text{LJ}}(\tilde{\mathbf{x}}).$$

The dynamics of the i -th ion is given by the Langevin equation

$$\ddot{\mathbf{x}}_i + \gamma_i [\dot{\mathbf{x}}_i - \mathbf{V}(\mathbf{x}_i, t)] + \mathbf{F}_i(\tilde{\mathbf{x}}) = \sqrt{2\epsilon_i\gamma_i} \dot{\mathbf{w}}_i, \quad (\text{A.2})$$

where $\epsilon_i = k_B T / m_i$, T is the temperature, $\gamma_i = 6\pi a_i \eta_i$ is the dynamical viscosity, η_i is the viscosity coefficient per unit mass, and a_i is the radius of the ion. The frictional drag force, $-\gamma [\dot{\mathbf{x}}_i - \mathbf{V}(\mathbf{x}_i, t)]$, is proportional to the relative velocity of the ion and the cytoplasmic fluid. The accelerations $\dot{\mathbf{w}}_i$ represent the thermal fluctuations of the fluid. The relation between the velocity diffusion constant and the friction coefficient,

$$D_i = \frac{k_B T}{m_i \gamma_i},$$

is Einstein's fluctuation-dissipation principle [171]. In the Smoluchowski limit of large damping [171] the Langevin equation (A.2) reduces to

$$\gamma_i [\dot{\mathbf{x}}_i - \mathbf{V}(\mathbf{x}_i, t)] + \mathbf{F}_i(\tilde{\mathbf{x}}) = \sqrt{2\epsilon_i\gamma_i} \dot{\mathbf{w}}_i, \quad (\text{A.3})$$

When neglecting the ion-ion interactions, we set $U_{\text{LJ}}(\tilde{\mathbf{x}}) = U_{\text{ii}}(\tilde{\mathbf{x}}) = 0$, so that eq.(A.3) becomes

$$\gamma_i [\dot{\mathbf{x}}_i - \mathbf{V}(\mathbf{x}_i, t)] + \mathbf{F}(\mathbf{x}_i) = \sqrt{2\epsilon_i\gamma_i} \dot{\mathbf{w}}_i, \quad (\text{A.4})$$

where

$$\mathbf{F}(\mathbf{x}_i) = -z_i e \nabla_{\mathbf{x}_i} U_0(\mathbf{x}_i).$$

Since we are interested in tracing only one species in the spine, namely, the concentration of calcium, we assume that $\gamma_i = \gamma_{\text{Ca}^{++}}$, $m_i = m_{\text{Ca}^{++}}$, $z_i = z = 2$. Under these assumptions, equations (A.4) are independent and identical, so that their transition probability densities are identical. We denote the transition probability density function (pdf) of each ion by $p(\mathbf{x}, t | \mathbf{x}_0, t_0)$ so that the calcium concentration is

$$c(\mathbf{x}, t) = \int_{\Omega_t} p(\mathbf{x}, t | \mathbf{x}_0, t_0) c_0(\mathbf{x}_0) d\mathbf{x}_0,$$

where $c_0(\mathbf{x}_0)$ is the initial calcium density.

Specification of the hydrodynamical flow

The flow of the incompressible cytoplasmic fluid in spines is generated by the local contraction of actin-myosin complexes saturated by calcium ions. We assume that the flow field is derived from a potential $\phi(\mathbf{x}, t)$ (see, e.g., [117]),

$$\mathbf{V}(\mathbf{x}, t) = \nabla \phi(\mathbf{x}, t). \quad (\text{A.5})$$

The incompressibility condition, $\nabla \cdot \mathbf{V}(\mathbf{x}, t) = 0$, reduces to the Laplace equation in the head $\Omega_H(t)$ of the spine at time t . The surface of the head, $\Sigma(t)$, is partitioned into the surface $\Sigma_H(t)$ of the spine head, that does include the surface common with the neck, and the cap $\Sigma_N(t)$ of the surface of the head inside the neck, $\Sigma(t) = \Sigma_H(t) \cup \Sigma_N(t)$. The Laplace equation in $\Omega_H(t)$ is

$$\Delta_{\mathbf{y}} \phi(\mathbf{y}, t) = 0 \quad \text{for } \mathbf{y} \in \Omega_H(t), t > 0, \quad (\text{A.6})$$

with the boundary conditions

$$\left. \frac{\partial \phi(\mathbf{y}, t)}{\partial n} \right|_{\mathbf{y} \in \Sigma_H(t)} = -V(t), \quad \left. \frac{\partial \phi(\mathbf{y}, t)}{\partial n} \right|_{\mathbf{y} \in \Sigma_N(t)} = F(V(t)), \quad (\text{A.7})$$

where $V(t)$ is the average velocity induced by the deformation of the head (see eq.(A.8) below) [78], due to the sum of all the local contractions, and $F(V(t))$ is the induced field velocity at the top of the neck $\Sigma_N(t)$: for a volume displaced per unit time equal to $4\pi R^2(t)V(t)$ in dimension 3 and $2\pi R(t)V(t)$, where $R(t)$ is the instantaneous radius of the head, then $\dot{R}(t) = -V(t)$. The flux through Σ_N is $|\Sigma_N|v(t)$, hence

$$v(t) = F(V(t)) = \begin{cases} \frac{4\pi R^2(t)V(t)}{|\Sigma_N|} & \text{in dimension 3} \\ \frac{2\pi R(t)V(t)}{|\Sigma_N|} & \text{in dimension 2} \end{cases},$$

when the field is due to the contraction of myosin after 4 calcium ions are bound. The total number of sites bound to 4 calcium is $S^{(4)}(t)$ and can be obtained by solving a system of reaction-diffusion equations [78]. Finally the velocity at the boundary is given by

$$V(t) = v_Q S^{(4)}(t), \quad (\text{A.8})$$

where v_Q is a constant velocity. The quantities $V(t)$ and $F(V(t))$ are stochastic processes, that are proportional to the number of saturated proteins at any given time t . The flow field can be expressed explicitly in terms of the functions $V(t)$ and $F(V(t))$ by Green's function for the Neumann problem for Poisson's equation in a sphere (or a disk) through Stokes' formula. Green's function $G(\mathbf{x}, \mathbf{y}, t)$ is the solution (defined up to a constant) of the equation

$$\begin{aligned} -\Delta_{\mathbf{y}} G(\mathbf{x}, \mathbf{y}, t) &= \delta(\mathbf{x} - \mathbf{y}) - \frac{1}{|\Omega_t|} \quad \text{for } \mathbf{x}, \mathbf{y} \in \Omega_H(t) \\ \frac{\partial G(\mathbf{x}, \mathbf{y}, t)}{\partial \nu(\mathbf{y})} &= 0 \quad \text{for } \mathbf{x} \in \Omega_H(t), \mathbf{y} \in \Sigma(t). \end{aligned} \quad (\text{A.9})$$

Multiplying equation (A.6) by $G(\mathbf{x}, \mathbf{y}, t)$ and equation (A.9) by $\phi(\mathbf{y}, t)$ and integrating with respect to \mathbf{y} over the domain, using Stokes' theorem and the boundary

condition (A.7), we get

$$\begin{aligned}
\phi(\mathbf{x}, t) &= \int_{\mathbf{y} \in \Sigma(t)} \frac{\partial \phi(\mathbf{y}, t)}{\partial n} G(\mathbf{x}, \mathbf{y}, t) dS_{\mathbf{y}} - \int_{\mathbf{y} \in \Sigma(t)} \frac{\partial G(\mathbf{x}, \mathbf{y}, t)}{\partial n} \phi(\mathbf{y}, t) dS_{\mathbf{y}} \\
&\quad + \frac{1}{V_H} \int_{\Omega_H(t)} \phi(\mathbf{y}, t) d\mathbf{y} \\
&= \int_{\mathbf{y} \in \Sigma(t)} \frac{\partial \phi(\mathbf{y}, t)}{\partial n} G(\mathbf{x}, \mathbf{y}, t) dS_{\mathbf{y}} + \frac{1}{V_H} \int_{\Omega_H(t)} \phi(\mathbf{y}, t) d\mathbf{y} \\
&= - \int_{\Sigma_H(t)} V(t) G(\mathbf{x}, \mathbf{y}, t) dS_{\mathbf{y}} + \int_{\Sigma_N(t)} F(V(t)) G(\mathbf{x}, \mathbf{y}, t) dS_{\mathbf{y}} \\
&\quad + \frac{1}{V_H} \int_{\Omega_H(t)} \phi(\mathbf{y}, t) d\mathbf{y} \\
&= -V(t) \int_{\Sigma_H(t)} G(\mathbf{x}, \mathbf{y}, t) dS_{\mathbf{y}} + F(V(t)) \int_{\Sigma_N(t)} G(\mathbf{x}, \mathbf{y}, t) dS_{\mathbf{y}} \\
&\quad + \frac{1}{V_H} \int_{\Omega_H(t)} \phi(\mathbf{y}, t) d\mathbf{y}.
\end{aligned}$$

The flow field is given by

$$\nabla \phi(\mathbf{x}, t) = -V(t) \int_{\Sigma_H} \nabla_{\mathbf{x}} G(\mathbf{x}, \mathbf{y}) dS_{\mathbf{y}} + F(V(t)) \int_{\Sigma_N} \nabla_{\mathbf{x}} G(\mathbf{x}, \mathbf{y}) dS_{\mathbf{y}}.$$

In the neck, due to the symmetries and the uniform initial conditions, we simplify the flow field by assuming its velocity is parallel to the axis of the neck. It is given by

$$\nabla \phi(\mathbf{x}, t) = \mathbf{V}(\mathbf{x}, t) = F(V(t)) \mathbf{k},$$

where \mathbf{k} is a unit vector along the axis of the neck. We note that according to (A.8), as the number of saturated proteins increases the hydrodynamical flow begins to dominate the diffusion. In [78, 88], we connected the strength of flow field to the number of bound myosin molecules induced by calcium. This results in nonlinear coupled partial differential equations, that can be solve numerically by stochastic simulations.

Rate constants and molecular dynamics

We shall now recall how to model chemical reactions, described by the backward and the forward binding rate, which are usually obtained in aqueous solution, where diffusion is not limited by space. In confined micro-domains where the number of ions involved can be small, the binding rates have to be reinterpreted.

Backward binding rate The mean time that two molecules react chemically is modeled as the mean time the first molecule stays imprisoned in the potential well of the second. The random time interval between the binding and the reappearance

of the binding molecule into the free state is exponentially distributed with a rate constant equal to the backward binding reaction. The exponentially distributed waiting time for the backward reaction is based on Kramers' theory of activated barrier crossing, as described in [126]. Thus for transient chemical reactions, each molecule reacting with a calcium ion has two consequences: first, the molecule can become activated and second, the time course of calcium is delayed. The unbinding events are modeled as Poissonian processes. Fixing a scale Δt , the probability to unbind is $k_b \Delta t$ (take a uniform variable and check whether it is above or below $k_b \Delta t$).

Forward binding rate The forward binding rate K_{for} corresponds to the flux of particles to the binding sites. Contrary to the backward binding rate, this rate does not contain local properties only, but includes the effect of the global geometry of the domain, where the chemical reaction occurs. Such a rate has been computed at equilibrium by Smoluchowski and can be converted as the effective radius R_a of a ball that mimics the binding site and so that the average probability that an ion meets such ball is equal to the forward rate. The radius is calibrated according to the formula

$$K_{\text{for}} = 2\pi R_a D [Ca^{2+}], \quad (\text{A.10})$$

where $[Ca^{2+}]$ is the initial calcium concentration and D the diffusion constant. This calibration can also be used to estimate the effective radius of a binding molecule in a transient state, calibrated for the initial concentration condition. When the binding sites are located on the boundary, the narrow escape formula should be used [84].

A.2.3 Modeling the interaction of calcium ion with surface or receptors

We shall now specify the interaction conditions between a calcium ion and a receptor or a membrane, the model at a molecular and population level, and the physical laws that can be derived from elementary physical principles.

Absorption

Absorption at surface $\partial\Omega$ is the process by which a particle is removed after it hits $\partial\Omega$, which can be an artificial interface such as the one between a spine and the dendrite, or an effective one such as a channel. Indeed, during a simulation, when an ion hits such a surface, it disappears. In general, absorption on a surface is modeled by killing the trajectories when it encounters or passes over the surface $\partial\Omega$. Thus the probability density function to make a transition from $\mathbf{x} \in \partial\Omega$ to any point \mathbf{y} during time t is zero: $p(\mathbf{y}, t | \mathbf{x}) = 0$.

Partial absorption

Partial absorption accounts for a probability that a particle arriving at a surface is reflected with a probability p or absorbed with probability $1 - p$. This condition can

be calibrated to describe the interaction between the moving particle and the binding site of a receptor. This condition is formulated at a molecular level for stochastic simulations, or with a probability density function to describe the macroscopic level. This condition is called also radiation or reactive or Robin boundary conditions and has been widely used to describe diffusion in a biological cell with chemical reactions on its surface [1, 4, 10, 42, 135, 116, 191, 212].

Schematic description

The overdamped Langevin equation can be written as a stochastic equation

$$\dot{x} = a(x, t) + \sqrt{2\sigma(x, t)} \dot{w}. \quad (\text{A.11})$$

The process $x(t)$ defined by equation (A.11) with partially absorbing boundaries can be defined as the limit of Markovian jump processes generated by the Euler scheme

$$x_{\Delta t}(t + \Delta t) = x_{\Delta t}(t) + a(x_{\Delta t}(t), t)\Delta t + \sqrt{2\sigma(x_{\Delta t}(t), t)} \Delta w(t, \Delta t) \quad \text{for } t \geq s \quad (\text{A.12})$$

$$x_{\Delta t}(s) = x \quad (\text{A.13})$$

in the interval $x > 0$, for $0 \leq t - s \leq T$, with $\Delta t = T/N$, $t - s = iT/N$ ($i = 0, 1, \dots, N$), where for each t the random variables $\Delta w(t, \Delta t)$ are normally distributed and independent with zero mean and variance Δt . In dimension one, with boundary at 0, the boundary behavior for the simulated trajectories that cross the boundary, identified by $x_{\Delta t}(t) + a(x_{\Delta t}(t), t)\Delta t + \sqrt{2\sigma(x_{\Delta t}(t), t)} \Delta w < 0$, is described by

$$x_{\Delta t}(t + \Delta t) = \begin{cases} -(x_{\Delta t}(t) + a(x_{\Delta t}(t), t)\Delta t + \sqrt{2\sigma(x_{\Delta t}(t), t)} \Delta w) & \text{w.p. } 1 - P\sqrt{\Delta t} \\ \text{terminate trajectory otherwise.} & \end{cases} \quad (\text{A.14})$$

Thus the exiting trajectory is normally reflected w.p.

$$R = 1 - P\sqrt{\Delta t} \quad (\text{A.15})$$

and is otherwise terminated (absorbed). The scaling of the termination probability with $\sqrt{\Delta t}$ reflects the fact that the discrete unidirectional diffusion current at any point, including the boundary, is $O(1/\sqrt{\Delta t})$ [182]. This means that the number of discrete trajectories hitting or crossing the boundary in any finite time interval increases as $1/\sqrt{\Delta t}$.

Partial reflecting condition in dimension larger than 2

The scheme (A.14) is generalized to diffusion with drift and anisotropic constant diffusion matrix $\sigma(t)$ in the half space, $x_1 > 0$, with partial oblique reflection. The

Robin boundary condition is recovered if and only if trajectories are reflected in the direction of the unit vector

$$\mathbf{v} = \frac{\boldsymbol{\sigma}\mathbf{n}}{\|\boldsymbol{\sigma}\mathbf{n}\|}, \quad (\text{A.16})$$

where \mathbf{n} is the unit normal to the boundary. The radiation parameter $\kappa(\mathbf{x}, t)$ in the d -dimensional Robin boundary condition and the absorption parameter $P(\mathbf{x})$ are related by

$$\kappa(\mathbf{x}, t) = rP(\mathbf{x})\sqrt{\sigma_n(t)}, \quad x_1 = 0, \quad (\text{A.17})$$

with $r = 1/\sqrt{\pi}$ and $\sigma_n(t) = \mathbf{n}^T \boldsymbol{\sigma}(t) \mathbf{n}$. The relation (A.17) can also be adapted for curved boundaries and applied to the tangent plane at each point of the boundary. Indeed this is due to the fact that a smooth local mapping of the domain to a half space with an orthogonal system of coordinates preserves the constant isotropic diffusion matrix, though the drift changes according to Itô's formula. In this case the vector \mathbf{v} coincides with the normal \mathbf{n} .

The reflection law and the relation are new for diffusion in higher-dimensions. The constant r for the Euler scheme is not the same as that for other schemes, e.g., for a discrete random walk with radiation boundaries, $r = 1/\sqrt{2}$. The reflection can be constructed explicitly. Indeed, the d -dimensional stochastic dynamic is

$$\dot{\mathbf{x}} = \mathbf{a}(\mathbf{x}, t) + \sqrt{2}\mathbf{B}(t) \dot{\mathbf{w}} \quad (\text{A.18})$$

in the half space

$$\Omega = \{\mathbf{x} = (x_1, x_2, \dots, x_d) \in \mathbb{R}^d : x_1 > 0\}$$

where \mathbf{w} is a vector of d independent Brownian motions and when we assume that the diffusion tensor $\boldsymbol{\sigma}(t) = \mathbf{B}(t)\mathbf{B}^T(t)$ is uniformly positive definite for all $t \geq s$. We use henceforward the abbreviation $\boldsymbol{\sigma}(t) = \boldsymbol{\sigma}$. The radiation condition (A.35) becomes

$$-\mathbf{J}(\mathbf{y}, t | \mathbf{x}, s) \cdot \mathbf{n} = \kappa(\mathbf{y}, t)p(\mathbf{y}, t | \mathbf{x}, s), \quad \text{for } \mathbf{y} \in \partial\Omega, \mathbf{x} \in \Omega, \quad (\text{A.19})$$

where the components of the flux vector $\mathbf{J}(\mathbf{y}, t | \mathbf{x}, s)$ are defined by

$$J^k(\mathbf{y}, t | \mathbf{x}, s) = -[a^k(\mathbf{y}, t)p(\mathbf{y}, t | \mathbf{x}, s)] + \sum_{j=1}^d \frac{\partial}{\partial y_j} [\sigma^{j,k}p(\mathbf{y}, t | \mathbf{x}, s)]. \quad (\text{A.20})$$

The Fokker-Plank equation for the pdf of $\mathbf{x}(t)$ can be written as

$$\frac{\partial p(\mathbf{y}, t | \mathbf{x}, s)}{\partial t} = -\nabla_{\mathbf{y}} \cdot \mathbf{J}(\mathbf{y}, t | \mathbf{x}, s) \quad \text{for all } \mathbf{y}, \mathbf{x} \in \Omega. \quad (\text{A.21})$$

If $\mathbf{x} \in \Omega$, but

$$\mathbf{x}' = \mathbf{x} + \mathbf{A}(\mathbf{x}, t)\Delta t + \sqrt{2}\mathbf{B}(t) \Delta \mathbf{w}(t, \Delta t) \notin \Omega,$$

the Euler scheme for (A.18) with oblique reflection in $\partial\Omega$ reflects the point \mathbf{x}' obliquely in the constant direction of \mathbf{v} to a point $\mathbf{x}'' \in \Omega$, as described below. First, we denote by \mathbf{x}'_B the normal projection of a point \mathbf{x}' on $\partial\Omega$, that is,

$\mathbf{x}'_B = \mathbf{x}' - (\mathbf{x}' \cdot \mathbf{n})\mathbf{n}$. Then we write the Euler scheme for (A.18) with partially reflecting boundary as

$$\mathbf{x}(t + \Delta t) = \begin{cases} \mathbf{x}' & \text{for } \mathbf{x}' \in \Omega \\ \mathbf{x}'' & \text{w.p. } 1 - P(\mathbf{x}'_B)\sqrt{\Delta t}, \text{ if } \mathbf{x}' \notin \Omega, \\ \text{terminate trajectory w.p. } P(\mathbf{x}'_B)\sqrt{\Delta t}, & \text{if } \mathbf{x}' \notin \Omega. \end{cases} \quad (\text{A.22})$$

The value of the termination probability $P(\mathbf{x}'_B)\sqrt{\Delta t}$, that varies continuously in the boundary, is evaluated at the normal projection of the point \mathbf{x}' on the boundary. The oblique reflection in the direction of the unit vector \mathbf{v} ($v_1 \neq 0$) is defined by

$$\mathbf{x}'' = \mathbf{x}' - \frac{2x'_1}{v_1}\mathbf{v}. \quad (\text{A.23})$$

Note that $x''_1 = -x'_1$ guarantees that the reflected point of a crossing trajectory is inside the domain Ω . The fact that the normal components of \mathbf{x}'' and \mathbf{x}' are of equal lengths makes the high-dimensional boundary layer analysis similar to that in one dimension. Normal reflection corresponds to $\mathbf{v} = \mathbf{n} = (1, 0, \dots, 0)$. We note that for a point $\mathbf{y} \in \Omega$, we can write $\Pr\{\mathbf{x}'' = \mathbf{y}\} = \Pr\{\mathbf{x}' = \mathbf{y}'\}$, where

$$\mathbf{y} = \mathbf{y}' - \frac{2\mathbf{y}' \cdot \mathbf{n}}{v_1}\mathbf{v} \quad (\text{A.24})$$

is the oblique reflection of \mathbf{y}' (see fig. A.2). If the scheme described above is not used, a paradox can arise [182]: while the pdf of the solution of (A.12), (A.13) converges to the solution of the FPE (A.32) and the initial condition (A.34), it does not satisfy the boundary condition (A.35), leading to a boundary layer, due to the diffusion approximations in the Markovian jump process.

Generic modeling of calcium ions at pumps or exchangers

Partial absorbing boundary condition can be used to model the behavior of calcium ion near a channel or a pump. However cooperativity should be implemented for each case at hand. For example, after entering inside an exchanger, an ion takes a certain time to exit: this is modeled by changing a partial reflecting boundary condition to a reflecting one as long as the ion is inside the exchanger.

Some pumps can work with several ions. As the intrinsic biophysical mechanism of permeability is not necessarily understood, there is no consensus for a universal coarse-graining scheme of ion extrusion. If two ions are required, we propose that once the first ion enters the channel, it cannot move before another has hit the binding area. If the second ion enters while the first one is not returned (after an exponential waiting time), then the first one can be extruded. During that time, no other ions can enter the channel.

Modeling calcium influx from channels: NMDA Receptors, AMPA Receptors and VSCC.

We shall now present examples of three classical channels such as NMDA, AMPAR (GluR2-calcium permeable) and Voltage Sensitive Calcium Channel (VSCC) for

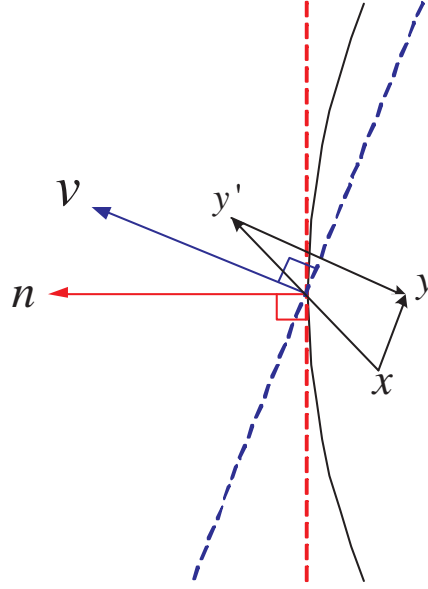


Figure A.2: **Reflection scheme.** A simulated trajectory can get from \mathbf{x} to \mathbf{y} in a single time step Δt in two different ways: (i) directly from \mathbf{x} to \mathbf{y} , without crossing the boundary, and (ii) by crossing the boundary from \mathbf{x} to \mathbf{y}' and reflection in the oblique direction \mathbf{v} with probability $1 - P(\mathbf{y}'_B)\sqrt{\Delta t}$ to \mathbf{y} . The reflection law (A.22)-(A.24) satisfies $y'_1 = -y_1$.

simulating the flux of calcium inside neuronal cells. The flow of ions through open channels has been studied using Langevin equation [41, 162]. The fluxes of ions can be implemented numerically as follow.

Calcium influx through NMDAR Calcium influx through NMDA-channels can be approximated by (p. 99 [105])

$$I_N(t) = g_N \frac{e^{-t/\tau_{N,1}} - e^{-t/\tau_{N,2}}}{1 + 0.33[Mg^{2+}]e^{-0.06V_m}} (V_m - E_N). \quad (\text{A.25})$$

where the conductance is $g_N = 0.16$ nS, the Nernst potential $E_N = 0$, V_m is the membrane potential. When the potential V_m is fixed and the fraction of current carried by calcium ions is 15%, we can simulate such a flux by injecting particles at random times such that the instantaneous rate is the one obtained from relation (A.25). Indeed, the entrance is a Poissonian process with a time dependent rate $\lambda(t + \Delta t) = \frac{I_{Ca}(t)\Delta t}{2e}$. The number of entering ions is $N(t)\Delta t = \frac{I_{Ca}(t)\Delta t}{2e}$, where $I_{Ca}(t)\Delta t = \int_t^{t+\Delta t} I_N(s)ds$. An example of stochastic calcium ion entry is presented in Fig. A.4 (discretized at a time step $\Delta t = 0.1$ ms). In some dendritic spine models [88, 78], the entrance dynamics is neglected and ions are initially placed at channels, located at the top of the dendritic spine head. Typically, the total charge is $Q_N = \int_0^\infty I(s)ds$, thus the fraction of calcium is $Q_{Ca} = 0.15 Q_N$ Coulomb. The number of calcium ions entering is $N_{N,Ca} = \frac{Q_{Ca}}{2e}$, where the e is the electron charge. Using parameters of table A.1, we obtain that $Q_N = 6.38pC$ and thus there are

about $N_{N,Ca} = 3000$ ions entering in average inside a single NMDA receptor (for a fixed mean voltage $V_m = -65.1$ mV).

Calcium influx through AMPAR The stochastic arrival of ions entering through an AMPAR is computed exactly with the same method as for NMDA, except that the mean flux is given by

$$I_A = g_A \frac{t}{\tau_A} e^{-t/\tau_A} (V_m - E_A), \quad (\text{A.26})$$

where $g_A = 0.3$ nS, and the Nernst potential $E_A = 0$ mV. The fraction of AMPAR current carried by calcium ions is 1.4%, thus we find that the total charge is $Q_A = 11.51$ fC, leading to approximatively 500 ions.

Influx through VSCC Calcium influx through VSCC requires computing the changes in the membrane potential depolarization. One possibility is to use the simplified Hodgkin-Huxley model [73]. The voltage change follows the dynamics

$$\begin{aligned} C \frac{dV}{dt} &= -I_{Na}(V, n) - I_K(V, n) - I_L(V) - I_{Ca}(V, m, h) - \gamma I_N - \eta I_A \\ \frac{dx}{dt} &= 0.1 \alpha_x (1 - x) - \beta_x x, \quad \text{for } x = n, m, h. \end{aligned}$$

where the currents are

$$\begin{aligned} I_{Na} &= g_{Na} p^3 (0.89 - 1.1n) (V - E_{Na}) \\ I_K &= g_K n^4 (V - E_K) \\ I_{Ca} &= g_{Ca} m^3 h (V_m - E_{Ca}) \\ I_L &= g_L (V - E_L) \end{aligned}$$

with parameters

$$p = \frac{\alpha_p}{\alpha_p + \beta_p}, \quad \alpha_k = \frac{1}{\tau_k} \frac{\theta_k - V_m}{e^{\frac{\theta_k - V_m}{\tau_k}} - 1}, \quad \beta_k = \eta_k e^{-\frac{V_m + 65}{\sigma_k}}, \quad \text{for } k = n, m, h, p.$$

where γ and η are summarized in Table A.1. The total charge becomes $Q_V = 0.6$ fC, which leads approximatively to 2000 ions entering through VSCC.

A.2.4 Stochastic simulation of calcium in a dendritic spine

The major benefit of stochastic simulations is to access the total number of biochemical bonds induced by calcium ions on specific molecules and to quantify the amount of structural changes occurring at the spine level. There are many other consequences such as computing the hydrodynamics component that changes the nature of the ion trajectories, or to distinguish the periods of calcium dynamics. Novel coarse-grained equations are derived in [78].

Space exploration

The geometric characteristics of ionic trajectories with the hydrodynamic flow are distributed differently from pure diffusion [78] (see Fig.A.3). Not only the nature of the movement is different but the hydrodynamic flow causes the ions to drift in the direction of the neck and consequently the time they spend in the spine head is reduced. As a consequence, the probability of a trajectory to leave through a pump located in the head decreases. Similarly, the probability to return to the head from the spine neck is reduced if it has to diffuse upstream, against the hydrodynamic drag force. Thus the ionic trajectory stays inside the spine a shorter time in the presence of the hydrodynamic flow, as compared to the time without it. As discussed in [88], the total number of bound molecules can change as much as 30 percent with and without the flow.

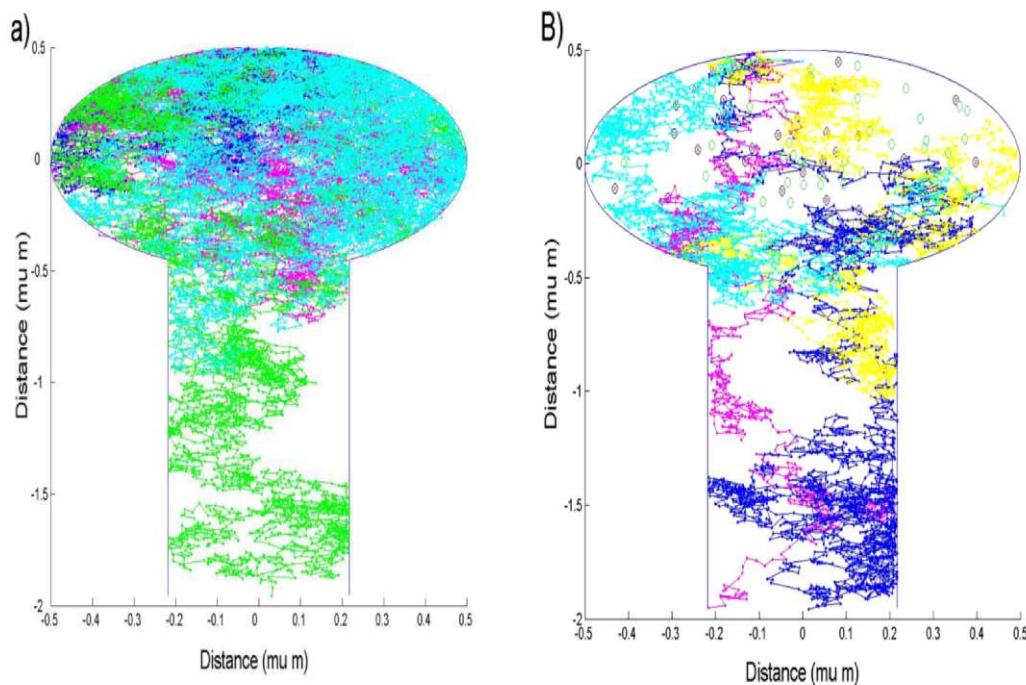


Figure A.3: **The filling of space by 5 random trajectories in the spine with no drift (a), and with drift (b).** Each color corresponds to a trajectory. Proteins are uniformly distributed in the spine head, and are represented by circles and crossed circles, respectively. A trajectory starts at the top of the spine head where channels are located and continues until it is terminated at the dendritic shaft or at an active pump. The parameters for the simulation are $\delta_1 = 0.02\mu\text{m}$, $\delta_2 = 0.01\mu\text{m}$, $K_{\text{back}}^{\text{AM}} = 10^4\text{s}^{-1}$, $K_{\text{back}}^{\text{cal}} = 2.10^3\text{s}^{-1}$, $R = 0.5\mu\text{m}$, $d/2 = 0.21794\mu\text{m}$, $l = 1.5\mu\text{m}$, $N_{\text{pumps}} = 10$.

Two stages of calcium concentration decay

Two very distinct decay rates of the fast extrusion periods have been reported in [124, 167]. The second decay period is identified as purely driven by random movement and the time constant equals the first eigenvalue of the Laplacian on the spine

domain, with the adequate boundary conditions. It was shown that the first period corresponds to a fast calcium extrusion, measured in [124] with an exponential decay rate $\lambda = 0.14s^{-1}$ and is due to the diffusion of saturated buffers, binding kinetics of endogenous buffers, diffusion of buffers, buffered calcium diffusion across the spine neck, and the effect of the pumps. The first period dynamics is defined by the fast binding to calcium stores [124, 167]. On the other hand, in the simulation resulting from the model [88], based on fast spine motility, the first time period has an exponential decay rate, constant $\lambda_t = 0.16s^{-1}$ derived in [78]. The decay seems to be a consequence of the dynamics created by the push effect, since stores were neglected. Further studies that include large numbers of buffers should reveal the precise contribution of buffers to the calcium fast decay rate, as compared to the rate imposed by the spine contraction.

Multiscale modeling of connecting a continuum bath with single molecular dynamics There are various interesting multiscale modeling approaches where the goal is to connect a discrete description of brownian particles with a continuum [58, 56]. The conservation of fluxes at the connecting interface generates boundary layer behavior that needs to be specifically studied.

Recipe for a successful stochastic simulation

- **Choosing a time step for a simulation.** The time step of a simulation is critical: when it is too small, the simulation takes forever, while if it is too large, then binding to buffers of a certain size a are missed. For a time step Δt and a diffusion coefficient D , a Brownian particle moving in three dimensions jumps to a distance $\Delta x^2 = 6D\Delta t$. Thus the constraint $|\Delta x| = a/4$ provides an estimate for the time step. In general the size of the smallest target defines the condition for the time step Δt . In most cases, where target sites are fixed, it is more interesting to refine the time step when a particle enters its neighborhood.
- **Positioning a particle that has unbound.** In the Smoluchowski's limit equation (where there is no dynamic for the velocity), the coarse graining of a potential well is usually done by freezing the position of the particle at the binding position during an exponential waiting time, the rate of which is the backward rate (reciprocal of the mean time to escape the well). After the particle unbinding, where should the particle be positioned? Certainly not at the absorbing boundary defining the well, otherwise the particle is immediately absorbed, unless the boundary condition is changed from absorbing to reflecting during a certain refractory time. Another possibility is to position the particle outside the boundary layer of the binding site: a small distance away from the site (3 to 4 radii away). This is possible if the sites are not surrounded by other absorbing sites. Inside a structure that contains a high concentration of binding sites, a different simulation approach is needed: either to derive a homogenized equation or the dynamics in the wells should not be coarse-grained.

- **Partial absorption.** When there are many absorbing sites located at close proximity, nonlinear effects should be taken into account. It is possible to derive homogenized boundary conditions: see for detail [190].
- **Coarse-graining a simulation with the narrow escape rate.** Instead of running a full Brownian simulation where the position of each calcium ion and calmodulin molecule is computed with Euler's scheme, it is possible to coarse-grain it into a rate model based on the narrow escape theory [85, 84]. The gain of this procedure is to avoid lengthy simulation imposed by the smallest length. In a Brownian simulation, due to the small calmodulin binding site of radius $R_{CaM} = 2$ nm, in order to ensure that the process does not jump over the site, the MSD-formula leads to a time step of 10^{-6} ms (with $D_{Ca} = 200 \mu\text{m}^2 \text{ms}^{-1}$), which would lead to days of simulations. To circumvent this difficulty, it is possible to compute directly the rate of arrival of calcium ions to one of the free calmodulin binding sites. The mean first binding time $\bar{\tau}_B$ of a Brownian particle diffusing with diffusion coefficient D_1 in a spherical domain Ω , to a small spherical target (radius r) diffusing with coefficient D_2 is $\bar{\tau}_B = \frac{|\Omega|}{4\pi(D_1+D_2)r}$. Due to the small size r , the binding times are exponentially distributed with a mean $\lambda_1 = 1/\bar{\tau}_B$. For N independent calcium ions diffusing within Ω , the first binding time T_b to a calmodulin site is distributed with rate

$$\lambda(N) = \lambda_1 N \tag{A.27}$$

Thus, the probability that a binding event occurs between time t and $t + \Delta t$ is $\mathbb{P}(t \leq T_b < t + \Delta t) = \lambda(N)\Delta t$. An application consists in replacing the Brownian movement of calcium ions in a spine head by the binding rate $\lambda(N)\Delta t$ at each calmodulin site. We thus need to compute at each time step the number N of free calcium in the spine.

Furthermore, calcium ions can escape a dendritic spine head Ω_{head} through small pumps. To model this calcium escape, we use a similar method as described above where we approximate the binding of calcium to a pump by using the mean first passage time of a diffusing ion to a small target located on the boundary. When there are N calcium ions, the first binding time is

$$\mu(N) = \frac{4R_{pump}D_{Ca}N}{|\Omega|_{head}}. \tag{A.28}$$

It is also possible to account for the competition with escaping through the spine neck using the narrow escape formula for a spine (equation A.45). This procedure accelerates the simulations and gives excellent results (fig. A.5).

In Figs. A.4-A.5, we present a simulation of calcium entry in a dendritic spine binding to calmodulin, [69].

A.2.5 Diffusion laws in microdomains with small openings

Synaptic input creates calcium transients in single dendritic spines and dendrites (Fig. A.6). We shall now present the modeling approach used to study calcium transients.

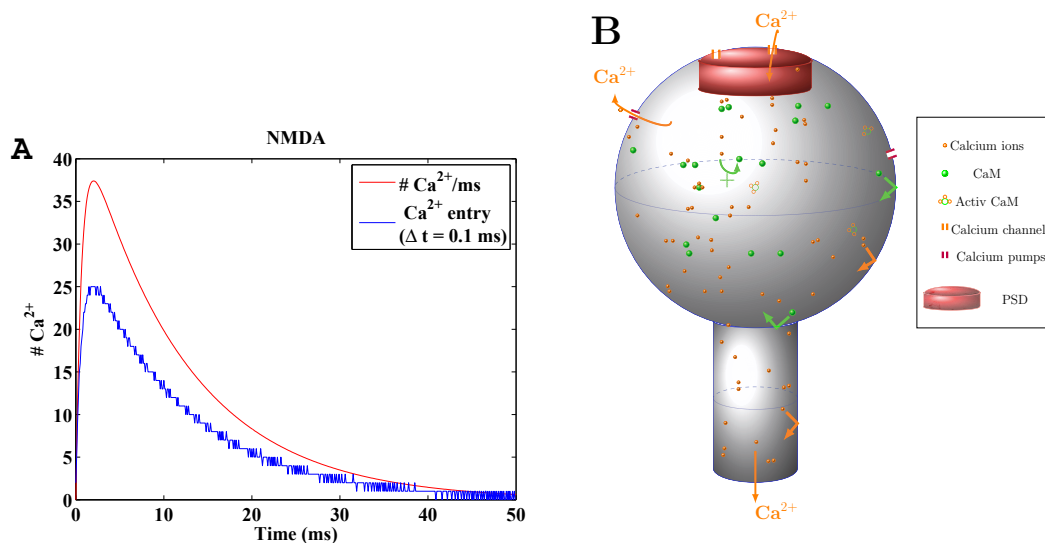


Figure A.4: **Calcium entry and dynamics** **A**: Time course of calcium entry inside a spine through a NMDA receptor. **B**: Schematic representation of the Calcium and calmodulin (CaM) pathway inside a dendritic spines. [69].

Probability density function of an ion

The stochastic nature of the calcium motion requires a probabilistic approach. Indeed, the location of an ion is not certain and the probability $p(x, t)$ to find an ion at time t at a position x satisfies the standard Fokker-Planck or diffusion equation

$$\frac{\partial p}{\partial t}(x, t) = D\Delta p(x, t), \quad (\text{A.29})$$

where Δ is the Laplacian operator and D is the diffusion constant in the cytoplasm. The solution of equation A.29 requires specifying initial and boundary conditions, and allows the entire characterization of a transient regime or the steady state distribution of a single ion. For a general domain, the solution cannot be derived analytically but it is possible to obtain long and short time asymptotic estimations. As we shall see, these expressions provide the dependency with respect to many geometrical parameters. When necessary, numerical simulations are used to obtain the missing information. They are usually tedious to obtain and require careful discretization of the domain, especially when small and large scales are present. For many independent calcium ions, the concentration $c(x, t)$ is given by $c(x, t) = Np(x, t)$, where N is the initial number of ions. Ignoring at this stage the effect of any chemical reaction, the microdomain geometry Ω is the main determinant of the characteristic time scale involved in diffusion. When the boundary decomposes into two parts, $\partial\Omega_a$ the absorbing part, made of key fast binding elements and $\partial\Omega_r$ the reflective part, then it is usually a critical aspect to quantify the mean time $\mathbb{E}(\tau)$

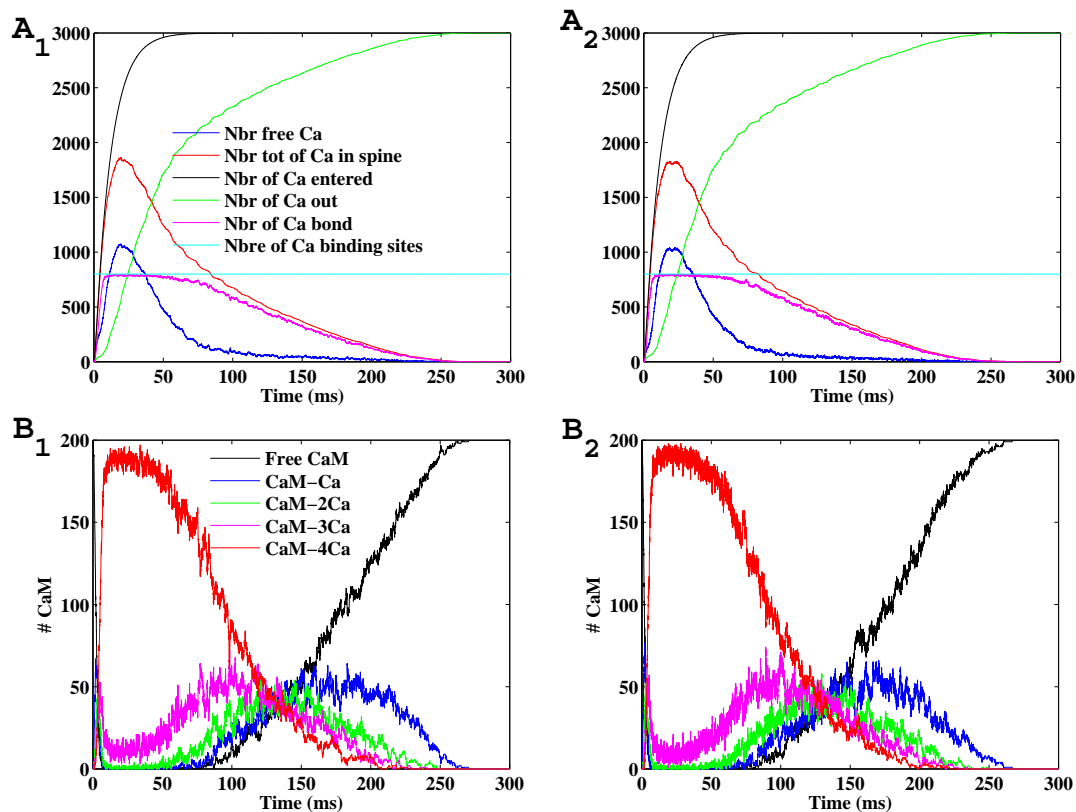


Figure A.5: **Calcium dynamics: comparing a Brownian simulation with a coarse-grained rate model for the binding to calmodulin.** **A₁** and **A₂** : Time course of calcium for 3000 ions entering a dendritic spine through NMDA receptors containing 200 calmodulin. The Brownian time step is $\Delta t = 3 \cdot 10^{-6}$ ms (**A₁**). For the rate model, $\Delta t = 10^{-4}$ ms (**A₂**). Ions diffuse freely in the synapse (dark blue), can be bound to calmodulin (magenta) or can leave the spine (green). The curves are compared with the total number of ions (black) and the total amount of calcium in the spine (free plus bound) (in red). **B₁** and **B₂** : Activation of calmodulin during the Brownian simulation (**B₁**) and the rate model (**B₂**). A calmodulin molecule can be bound to zero, one, two, three or four calcium bound (black, dark blue, green, magenta and red respectively).

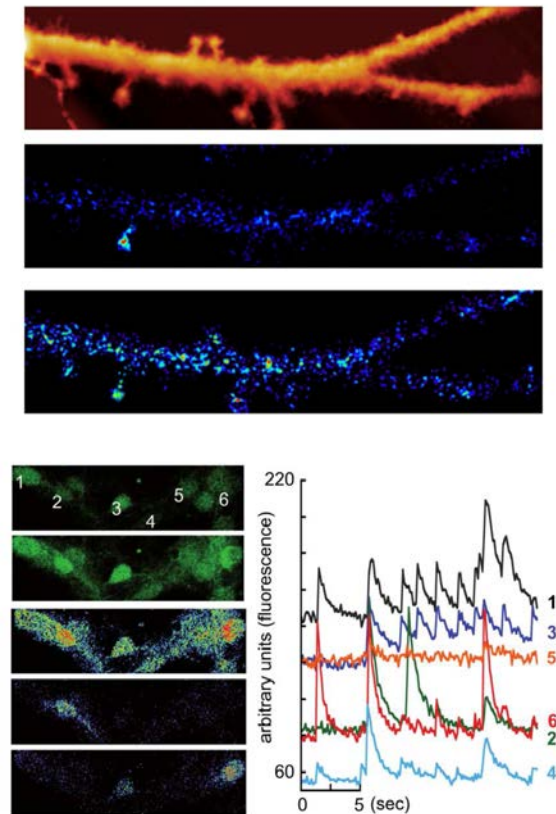


Figure A.6: **Upper: Isolated calcium transients in a single dendritic spine.** Synaptic activity generates a transient calcium change in a spine and a whole dendritic segment, triggered by a back propagating action potential. **Lower:** Spontaneous calcium activity in neurons. Synchronized and not synchronized activity as well as small (probably EPSPs), larger (probably single spike) and very large events (burst of several spikes). The decay phase of calcium is approximated by exponentials or sum of exponentials

for an ion to reach $\partial\Omega_a$. The boundary conditions are

$$\begin{aligned}\frac{\partial p(x, t)}{\partial n} &= 0 \text{ on } \partial\Omega_r, \\ c(x, t) &= 0 \text{ on } \partial\Omega_a,\end{aligned}$$

The general solution of the diffusion equation can be formally expanded as

$$c(\mathbf{x}, t) = \sum_{k=1}^{\infty} c_k u_k(\mathbf{x}) \exp(-\lambda_k t) \quad (\text{A.30})$$

where $\lambda_k > 0$ are the eigenvalues, u_k , $k = 1..$ the eigenfunctions and c_k are constant. The general explicit computation of the solution of diffusion equations can be found in [26, 31]. Although expression (A.30) justifies fitting a sum of exponentials to experimental data, connecting the eigenvalues with the precise geometry is in general very difficult, except in a few cases where the geometry contains a narrow passage or small hole. This is the case for a dendritic spine or a narrow domain in dendrites. When $|\partial\Omega_a| \ll |\partial\Omega_r|$, the reciprocal of the mean time to escape a domain $\mathbb{E}(\tau)$ is the first eigenvalue [175]. Indeed, $\frac{1}{\lambda_0}$ is usually very large, so that there is a large gap with the rest of the eigenvalue $\lambda_0 \ll \lambda_1, ..$ and thus the solution A.30 can be further approximated by a single exponential for a time $t \gg \frac{1}{\lambda_1}$,

$$c(\mathbf{x}, t) \approx c_0 \exp(-\lambda_0 t). \quad (\text{A.31})$$

We conclude that for domains with narrow neck, the arrival of diffusing particles to the small domain is almost Poissonian. This is a consequence of the geometry.

Transition probability density function with partial reflecting boundary condition

The transition probability density function (pdf) of the limit process A.11, $p(y, t | x, s) = \Pr\{x(t) = y | x(s) = x\}$, is the solution of the FPE

$$\frac{\partial p(y, t | x, s)}{\partial t} = -\frac{\partial[a(y, t)p(y, t | x, s)]}{\partial y} + \frac{\partial^2[\sigma(y, t)p(y, t | x, s)]}{\partial y^2}, \quad (\text{A.32})$$

or equivalently,

$$\frac{\partial p(y, t | x, s)}{\partial t} = -\frac{\partial J(y, t | x, s)}{\partial y} \quad \text{for all } y, x > 0,$$

where

$$J(y, t | x, s) = a(y, t)p(y, t | x, s) - \frac{\partial[\sigma(y, t)p(y, t | x, s)]}{\partial y}, \quad (\text{A.33})$$

is the flux. The initial condition is

$$p(y, t | x, s) \rightarrow \delta(y - x) \quad \text{as } t \downarrow s \quad (\text{A.34})$$

and the radiation boundary condition is

$$-J(0, t | x, s) = \kappa p(0, t | x, s), \quad (\text{A.35})$$

where κ is a constant related to the constant c and to the values of the coefficients at the boundary. The no flux and Dirichlet boundary conditions are recovered if $c = 0$ or $c = \infty$, respectively. The relation between the reactive ‘‘constant’’ $\kappa(t)$ and the absorption parameter P for the dynamics (A.11) on the positive axis with drift and with a variable diffusion coefficient is

$$\kappa(t) = rP\sqrt{\sigma(0, t)}, \quad r = \frac{1}{\sqrt{\pi}}. \quad (\text{A.36})$$

The relation (A.36) is true for diffusion with variable coefficients. The value $r = 1/\sqrt{\pi}$ is different than values obtained for other schemes, e.g., than the value $r = 1/\sqrt{2}$, predicted by the discrete random walk theory of radiation boundaries [29]. Values of r for other schemes are given in [42].

Exit diffusion rate from dendritic spines

We summarize in this section the approach used to derive asymptotic formulas for the rate of diffusional exit from spines. A dendritic spine with a narrow neck has very degenerate geometry [A.1], but the exit time of a diffusing particle which is the reciprocal of the first eigenvalue, can be directly measured from fluorescence imaging. We shall now recall the main formula for the exit rate that was obtained in the context of the narrow escape (NET) and dire strait (DST) theory [85].

A free Brownian particle moves in a bounded domain $D \subset \mathbb{R}^d$ ($d = 2, 3$), whose boundary $\partial\Omega$ is sufficiently smooth (the analysis in higher dimensions is similar to that for $d = 3$). The Brownian trajectory $\mathbf{x}(t)$ is reflected at the boundary, except for a small hole $\partial\Omega_a$, where it is absorbed, as shown in Fig. A.7. The reflecting part of the boundary is $\partial\Omega_r = \partial\Omega - \partial\Omega_a$. The lifetime in Ω of a Brownian trajectory that starts at a point $\mathbf{x} \in \Omega$ is the first passage time τ of the trajectory to the absorbing boundary $\partial\Omega_a$. The NET

$$v(\mathbf{x}) = \mathbb{E}[\tau | \mathbf{x}(0) = \mathbf{x}] \quad (\text{A.37})$$

is finite under quite general conditions [173]. As the size (e.g., the diameter) of the absorbing hole decreases to zero, but that of the domain remains finite, the NET increases indefinitely. A measure of smallness can be chosen as the ratio between the surface area of the absorbing boundary and that of the entire boundary, for example

$$\varepsilon = \left(\frac{|\partial\Omega_a|}{|\partial\Omega|} \right)^{1/(d-1)} \ll 1, \quad (\text{A.38})$$

provided that the isoperimetric ratio remains bounded,

$$\frac{|\partial\Omega|^{1/(d-1)}}{|\Omega|^{1/d}} = O(1) \text{ for } \varepsilon \ll 1. \quad (\text{A.39})$$

The NET $v(\mathbf{x})$ can be obtained by solving the Pontryagin-Andronov-Vitt (PAV) mixed boundary value problem for the Poisson equation [156, 155, 173]

$$\Delta v(\mathbf{x}) = -\frac{1}{D} \text{ for } \mathbf{x} \in \Omega \quad (\text{A.40})$$

$$v(\mathbf{x}) = 0 \text{ for } \mathbf{x} \in \partial\Omega_a \quad (\text{A.41})$$

$$\frac{\partial v(\mathbf{x})}{\partial n(\mathbf{x})} = 0 \text{ for } \mathbf{x} \in \partial\Omega_r, \quad (\text{A.42})$$

where D is the diffusion coefficient and $\mathbf{n}(\mathbf{x})$ is the unit outer normal vector to the boundary at $\mathbf{x} \in \partial\Omega$. For a circular window of radius $a \ll |\partial\Omega|^{1/2}$ (Fig. A.7)

$$\mathbb{E}\tau = \frac{|\Omega|}{4aD \left[1 + \frac{L(\mathbf{0}) + N(\mathbf{0})}{2\pi} a \log a + o(a \log a) \right]} \text{ for } a \ll |\partial\Omega|^{1/2}. \quad (\text{A.43})$$

The MFPT to the absorbing boundary at the end of the funnel of a solid of revolution obtained by rotating the symmetric planar domain (A.7) (see [84]of Section A.7) is given by

$$\bar{\tau} = \frac{1}{\sqrt{2}} \left(\frac{\ell_+}{a'} \right)^{3/2} \frac{V}{\ell_+ D} (1 + o(1)) \text{ for } a' \ll \ell_+, \quad (\text{A.44})$$

where $V = |\Omega'|$ is the volume of the domain. The NET $\bar{\tau}_{\mathbf{x} \rightarrow \partial\Omega_a}$ of a diffusing particle

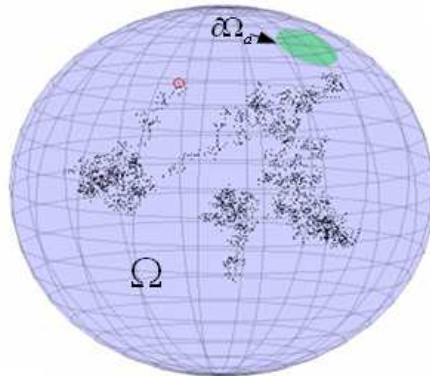


Figure A.7: **Brownian escape from a spherical window.**

from a three-dimensional domain Ω with a bottleneck in the form of a narrow circular

A.2. Detailed Description

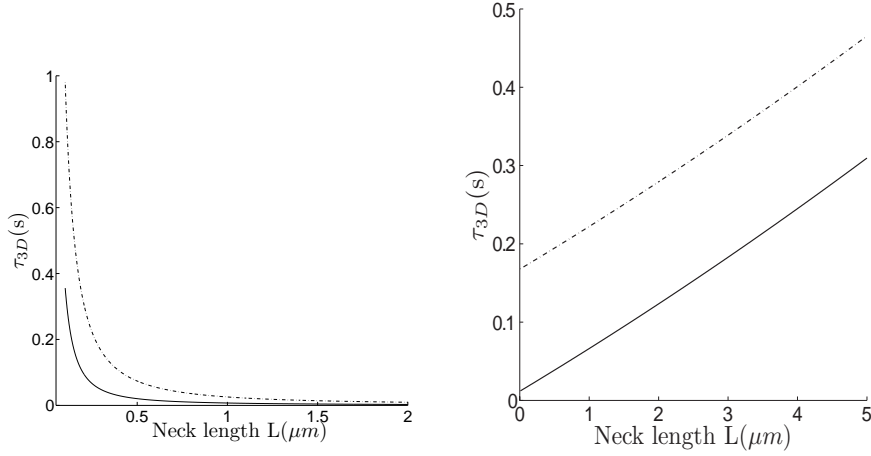


Figure A.8: **Residence time of calcium in dendritic spine.** Left: effect of the spine radius a on the exit time. right: effect of the spine length L .

cylinder of cross section area πa^2 is given by

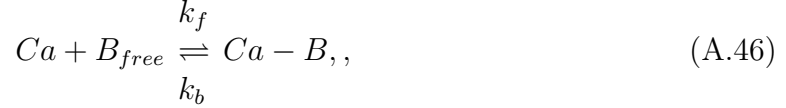
$$\bar{\tau}_{\mathbf{x} \rightarrow \partial\Omega_a} = \begin{cases} \frac{|\Omega_1|}{4aD} \left[1 + \frac{a}{\pi R} \log \frac{R}{a} \right] + \frac{O(1)}{D} + \frac{L^2}{2D} + \frac{|\Omega_1|L}{\pi a^2 D} & \text{solid spherical head of radius } R \text{ connected to the neck at a right angle} \\ \frac{|\Omega_1|}{4aD} \left[1 + \frac{(L\mathbf{x} + R\mathbf{x})}{2\pi} \left| \frac{\partial\Omega_a}{\pi} \right|^{1/2} \log \sqrt{\frac{|\partial\Omega_1|}{|\partial\Omega_a|}} + o \left(\sqrt{\frac{|\partial\Omega_a|}{|\partial\Omega_1|}} \log \sqrt{\frac{|\partial\Omega_a|}{|\partial\Omega_1|}} \right) \right] & \text{a general head connected to the neck at a right angle} \\ \frac{L^2}{2D} + \frac{|\Omega_1|L}{\pi a^2 D} & \text{a general head connected to the neck at a right angle} \\ \frac{1}{\sqrt{2}} \left(\frac{R_c}{a} \right)^{3/2} \frac{|\Omega_1|}{R_c D} (1 + o(1)) + \frac{L^2}{2D} + \frac{|\Omega_1|L}{\pi a^2 D} & \text{a general head connected smoothly to the neck by a funnel,} \end{cases} \quad (\text{A.45})$$

where R_c is the curvature at the cusp. The asymptotic expression is derived in [82]. The order 1 term can be computed for the sphere using the explicit expression of the Neumann-Green function [27]. When the spine radius is small, the leading order term for the mean exit time (which is also the rate of diffusion extrusion) was initially presented in [188]. This term accounts for the many returns of an ion between the spine neck and head [12]. This term is not present when an ion cannot return to the head once it enters the neck [108]. Because the other terms in formula A.45 diverge to infinity, their contribution cannot be neglected and they affect significantly the residence time of a diffusing particle in a dendritic spine (see Fig. A.8). We conclude from these analytical formulas that the spine connection determines the rate of extrusion. For short spines, all terms are significant.

Remarks The presence of a spine apparatus inside the spine might affect the extrusion of calcium or any other diffusing molecules. In addition, molecular binding affects calcium extrusion and the rate is no longer Poissonian.

Influence of calcium buffers on the residence time of calcium in microdomains such as dendritic spines

The residence of calcium in a spine can be influenced by other mechanisms than pure diffusion. Binding and unbinding to calcium buffers affect the time course. In that case, the entire system of partial differential equations (PDE) describing the process should be solved. Only numerical simulations are available. The generic example is



which leads to the PDE system of equations

$$\frac{\partial c}{\partial t}(x, t) = D\Delta c(x, t) - k_{in}c(x, t)B(x, t) + k_b[c-B](x, t), \quad (A.47)$$

$$\frac{\partial [c-B]}{\partial t}(x, t) = D_B\Delta c(x, t)B(x, t) + k_{in}c(x, t)B(x, t) - k_b[c-B](x, t), \quad (A.48)$$

$c-B$ is the bound calcium that can diffuse with diffusion coefficient D_B , but stays confined in the spine head, while the calcium can be extruded at pumps or at the spine neck, which translate into the following boundary conditions

$$\begin{aligned} \frac{\partial c(x, t)}{\partial n} &= 0 \text{ on } \partial\Omega_r, \\ c(x, t) &= 0 \text{ on } \partial\Omega_a, \\ \frac{\partial [c-B](x, t)}{\partial n} &= 0 \text{ on } \partial\Omega_r, \end{aligned}$$

when there is cooperativity at pumps, more elaborated boundary conditions are needed [73] and will be discussed later on. There is no general solution of such equations. If binding is fast, since $c(x, t) + [c-B](x, t) = N_0e^{-\lambda_1 t}$, the decay rate depends on the unbinding time, such that for a long enough time (so that binding occurred), the asymptotic decay rate is well approximated by a sum of two exponentials

$$c(x, t) = Ae^{-\lambda_1 t} + Be^{-k_b t}, \quad (A.49)$$

where A and B are constants.

Residence time of calcium in dendritic spines with a hydrodynamics flow

Dendritic spines can change shape in a few hundreds milliseconds [55, 88], after calcium ions flow in. This fast change of shape decreases the spine head volume. Spine motility was proposed by Blomberg and al. [15] and the fast twitching movement of the spine was anticipated by F. Crick in [32]. Spine fast contraction was attributed to actin-myosin molecules or troponin-C, which were observed inside the spine head. As in muscle cells, high concentrations of actin molecules indicate that rapid movement can follow the arrival of calcium ions. It has been proposed in

[88], that calcium ions set the spine in motion by initiating the contraction of actin-myosin (AM) as they bind at active sites. Each molecule is assumed to give rise to a local contraction. In a simplified model, all contractions add up to achieve a global contraction, neglecting anisotropic contraction due to a delay interval between each molecule contraction. Once calcium ions enter the spine, they arrive to the binding sites by diffusion and can bind there. When four calcium ions bind to a single troponin-C protein, a local contraction of the protein occurs. Adding all local contractions at a given time produces a global contraction and induces a hydrodynamic movement of the cytoplasmic fluid. Calcium trajectories are no longer pure Brownian, but contain a drift and thus the probability to reach the dendritic shaft through the spine neck is increased [88]. The model requires feedback of a flow field $\mathbf{v}(\mathbf{x}, t)$ on the velocity. The flow field can be computed using the Green's function of the spine domain [88]. Adding the effect of diffusion and hydrodynamics, the transient escape rate is not necessarily a single exponential. The concentration inside the spine follows

$$c(x, y, z, t) = C \exp \left\{ -\lambda_1 t + \frac{\bar{v}_0^2}{4D} t \right\},$$

where the hydrodynamics decay time is

$$\tau = \frac{4D}{\bar{v}_0^2}, \tag{A.50}$$

where \bar{v}_0 is the initial average velocity [88]. Figure A.3 illustrates the effect of adding a hydrodynamics drift on pure diffusion for the exploration of the spine head. Contrary to the effect of buffer, the hydrodynamics effect shifts the extrusion rate, but does not lead to a sum of exponentials.

Crowding model of a dendrite

Molecular crowding reduces diffusion and this effect can be estimated by computing the effective diffusion coefficient of a Brownian particle moving between obstacles in dimension 2. For obstacles positioned periodically, the effective coefficient of diffusion decays nonlinearly with the density of obstacles [75]. This decay also depends on the shape of the obstacles. The effective diffusion coefficient can be computed asymptotically by conformal mapping [75]. In addition, when obstacles are positioned with additional variabilities, local narrow passages, funnels or dead ends can be observed that lead to heterogeneity in the diffusion trajectories [62, 83, 84]. However due to the complexity of obstacle geometry, there is no achieved theory of diffusion with obstacles in three dimensions.

We present here a local model and numerical simulations to study calcium diffusion in a dendrite. The dendrite cytoplasmic medium is highly heterogeneous and filled with many organelles. Thus the motion of a diffusing particle is affected by many interactions with its environment. The functional consequences of these interactions are difficult to access directly experimentally due to ubiquitous pathways especially for calcium dynamics. In a reduced model of diffusion in dendrites, the one-dimensional effective diffusion equation and an effective diffusion constant accounts for the presence of heterogeneity in the medium.

Modeling diffusion in a heterogeneous dendritic cytoplasm. To characterize diffusion in a heterogeneous dendrite, containing various organelles such as mitochondria, spine apparatus, endoplasmic reticulum and other structures, one method [13] consists of coarse-graining a three dimensional cylindrical dendrite into a one-dimensional effective diffusion equation in the limit where the space between organelles is small. Diffusing ions can still move inside a dendritic domain Ω and the nature of the motion is not impaired, and is well approximated by the Smoluchowski limit of the Langevin equation [172]: a particle at position $\mathbf{X}(t)$ at time t is described by

$$\dot{\mathbf{X}} + \frac{1}{\gamma} \nabla \Phi(\mathbf{X}) = \sqrt{2D} \dot{\mathbf{w}}(t), \quad (\text{A.51})$$

where Φ is a potential per unit of mass, γ is the friction coefficient, D is the aqueous diffusion constant and $\mathbf{w}(t)$ is Gaussian white noise. The potential Φ represents the effective force on the particle. When a moving molecule hits impenetrable organelles O_i , it is reflected.

The distribution of independent molecules is characterized by the probability density function (pdf) $p(\mathbf{x}, t)$ which satisfies the Fokker-Planck equation

$$\frac{\partial p}{\partial t} = D \Delta p + \nabla \left[\frac{1}{\gamma} (\nabla \Phi(\mathbf{X})) p \right] \quad (\text{A.52})$$

in the domain $\tilde{\Omega} = \Omega \setminus \cup_i O_i$, and a zero flux condition on the organelles and the dendritic membrane $\partial \tilde{\Omega}$:

$$\mathbf{J} \cdot \mathbf{n} = -D \frac{\partial p}{\partial n} + \frac{p}{\gamma} \frac{\partial \Phi}{\partial n} = 0, \quad (\text{A.53})$$

where \mathbf{J} is the flux and \mathbf{n} the outer normal of the domain $\tilde{\Omega}$.

To account for the overall effect of crowding on diffusion, we adopt an approach based on a compartmentalization of the dendritic domain and the narrow escape theory [84], which provides the mean time for a Brownian particle to exit a domain through a small absorbing opening. The dendrite is divided into periodic compartments of length l and volume V , separated from their neighbors by a reflecting cross section, except for a small opening of radius a . This compartment should be large enough so that the organelle density is the same in each of them. The small openings allow diffusing molecules to move across compartments. In contrast to previous models where crowding has been described by spherical obstacles [13] that pose barriers to diffusing molecules, crowding is modeled as a sequence of periodic compartments and small openings at the boundaries of neighboring compartments. A compartment k starts at position x_k and ends at position x_{k+1} . The number $N_k(t)$ of particles in compartment k changes according to the net flux across the small windows. The flux is estimated by the small hole approximation (see [13] for details).

The concentration $c(x, t) = N(x, t)/V(x, t)$ satisfies

$$\frac{\partial c(x, t)}{\partial t} = \frac{4l^2 D}{V(x)} \frac{\partial}{\partial x} \left[a(x) \frac{\partial}{\partial x} c(x, t) \right]. \quad (\text{A.54})$$

Similar equations have been derived in other contexts [212, 12, 10]. When the parameters $a(x)$ and $V(x)$ are spatially independent, equation (A.54) simplifies to

$$\frac{\partial c(x, t)}{\partial t} = D_{eff} \frac{\partial^2 c(x, t)}{\partial x^2}, \quad (\text{A.55})$$

where $D_{eff} = \frac{4la}{S}D$, is the effective diffusion constant, and $V = Sl$ with S the cross-sectional area. The effective diffusion constant depends on two parameters: the compartment length l and the size of the opening a .

The model parameters are determined by (i) measuring the ratio of diffusion constants D_{eff}/D and (ii) a calibration condition of the form $l/a = 4$. The calibration condition expresses that the parameters l and a do not necessarily have direct physiological meanings, and we can thus set one parameter arbitrarily within the limits of the small hole approximation. Additional measurements of the diffusion constant will then fix the other parameter. A Brownian simulation of diffusing ions around an obstacle is presented in Fig. A.9. Other applications of reducing equations are to compute the mean time for calcium ions or diffusing molecules to travel along crowded dendrites or axons.

Calcium spread following high frequency stimulation The one dimensional effective diffusion equation presented in the last paragraph allows analyzing calcium spread originating from localized inputs such as synapses. At dendritic synapses calcium can enter through NMDA-receptors. To estimate calcium spread as a function of the synaptic input frequency, Ca^{2+} -influx was simulated in the middle of a dendritic segment (Fig. A.10) with buffers and pumps (see [13] for the reaction-diffusion equation). The different input frequencies are $f = 5, 10, 20, 50, 80$ Hz. Interestingly, for input frequencies larger than 20 Hz, the calcium signal in the dendrite reaches a stationary value. For high input frequencies (≥ 20 Hz) calcium spread does not exceed $2.5\mu\text{m}$ ($= 0.5 \times \text{FWHM}$) as measured from the input source. Buffers and pumps limit calcium spread to a few micrometers [13].

A.2.6 Calcium extrusion along a cylinder: Homogenization of hole into a killing rate

Computing the final distribution of calcium ions between two possible fates is a generic problem. It can be the proportion of bound calcium ions versus the number extruded or the fraction that reached the dendrite versus the fraction that got pumped. We present a general approach based on homogenization to reduce the complexity of this computation.

Homogenization of perforated by partially reflecting boundary

We approximate the flux through a reflecting boundary, perforated by many small independent absorbing holes [11, 10]. For diffusion, the problem can be solved using the eigenvalues of the Laplace equation in the domain Ω with mixed Neumann boundary conditions on $\partial\Omega - \partial\Omega_A$ and Dirichlet conditions on $\partial\Omega_A = \bigcup_{i=1}^N A_i$. If

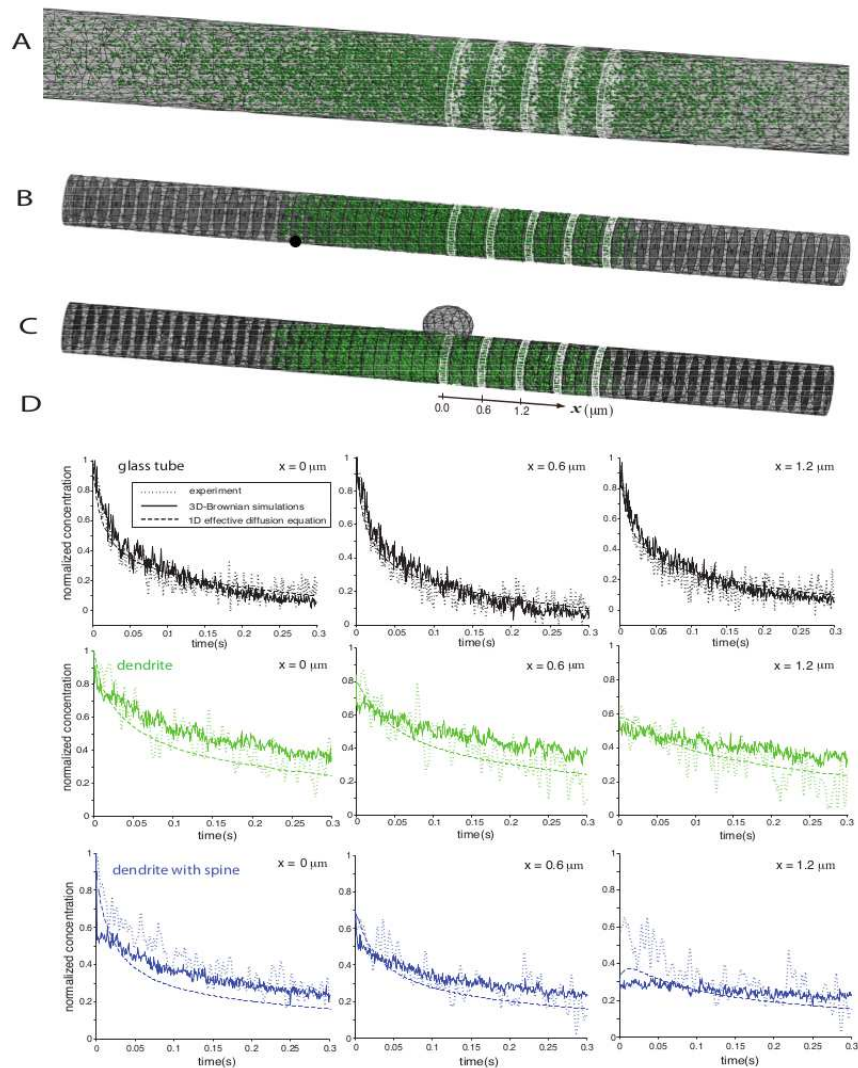


Figure A.9: **Brownian simulations of uncaging experiments.** A) Model glass pipette. Shown is the initial particle distribution as taken from the experimental data and the sampling volumes (white cylindrical disks) at different locations from the uncaging spot. (B) Compartmentalized model dendrite. (C) Compartmentalized model dendrite with attached spine (dendrite geometry as in B with spine neck radius: $0.3 \mu m$, spine neck length $0.2 \mu m$, spine head radius $0.4 \mu m$). (D) Comparison of 3D Brownian simulations with the uncaging experiments and the results derived from the solutions of the 1D effective diffusion equation. The normalized concentration profiles are shown for the glass tube (A), the dendrite (B) and the dendrite with attached spine (C) at three locations from the uncaging spot. Adapted from [13]

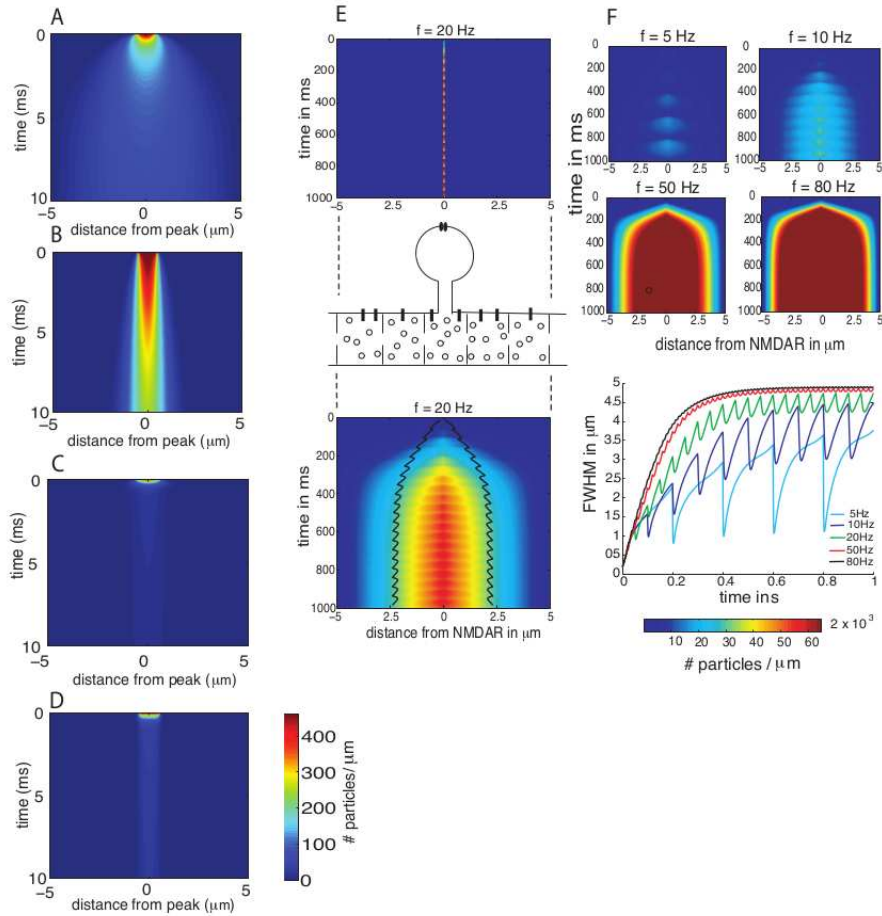


Figure A.10: **Lateral extent of calcium driven by high frequency stimulation.** A) Calcium diffusion in an aqueous solution contained in a pipette. (B) Calcium diffusion in a crowded dendrite. The initial concentration is equal to about 600 particles and evaluates to about 470 particles per micron for a dendrite. (C) Same settings as in (A) but with additional buffers (medium buffer concentration) and pumps. (D) Same settings as in (B) but with additional buffers (medium buffer concentration) and pumps. (E) Calcium was injected at 20 Hz for 1 s at the location of the NMDAR in the middle of the dendritic segment as shown in the upper and middle panel. The resulting spatiotemporal -profile in the dendrite is shown in the lower panel. (F) Spatiotemporal profiles in the dendrite for different influx frequencies at the location of the NMDAR. (G) Corresponding calcium spread in the dendrite as measured by the full width at half maximum (FWHM) of the calcium signal (adapted from [13]).

the holes A_i are sufficiently far apart, the smallest eigenvalue λ_1^A is asymptotically the sum of the eigenvalues $\lambda_1^{A_i}$ of the Laplace operator in Ω with mixed Neumann-Dirichlet boundary conditions on $\partial\Omega - A_i$ and A_i , respectively, which can be calculated from the narrow escape theory [84]. For circular holes with fixed radius ε , we have the formula

$$\lambda_1^{A_i} \approx \frac{4\varepsilon D}{|\Omega|}, \quad \lambda_1^A = \frac{4\varepsilon DN}{|\Omega|}. \quad (\text{A.56})$$

The pdf of the Brownian motion in the perforated domain relaxes to a quasi steady state and can be described by a single exponential decay in time with rate λ_1^A and a uniform quasi steady state distribution in Ω , except in boundary layers near A_i . The total absorption probability flux on the boundary, λ_1^A , is partitioned among the holes with probabilities $P_i = \frac{\lambda_1^{A_i}}{\sum_{i=1}^N \lambda_1^{A_i}}$. If the holes are distributed with surface density $n(\mathbf{x})$ on $\partial\Omega$, the normal absorption flux density is

$$\mathbf{J}(\mathbf{x}) \cdot \boldsymbol{\nu}(x) = \frac{4\varepsilon D n(\mathbf{x})}{|\Omega|}. \quad (\text{A.57})$$

The homogenization procedure consists in replacing the perforated holes by a radiation condition that preserves asymptotically the same quasi steady state distribution. We replace the leading eigenfunction and eigenvalue of the Robin problem by a Laplace equation with a small radiation function $k(\mathbf{x})$,

$$D\Delta p(\mathbf{x}) = -\lambda p(\mathbf{x}) \quad \text{for } \mathbf{x} \in \Omega \quad (\text{A.58})$$

$$D \frac{\partial p(\mathbf{x})}{\partial \nu} = -k(\mathbf{x}) p(\mathbf{x}) \quad \text{for } \mathbf{x} \in \partial\Omega. \quad (\text{A.59})$$

Matching the flux density in (A.57) and (A.59), we obtain in dimensional coordinates

$$k(\mathbf{x}) = 4\varepsilon D p_0(\mathbf{x}) n(\mathbf{x}) + O\left(\frac{\varepsilon^2}{L^2} \log \frac{\varepsilon}{L}\right). \quad (\text{A.60})$$

The quasi steady state pdf is

$$p_0(\mathbf{x}) = \frac{(1 + O(\tilde{k}_0))}{|\Omega|},$$

except in boundary layers near A_i .

After the first homogenization which consists in replacing a three dimensional diffusion with total and/or partial absorption by a reduced diffusion equation in dimension one, with a killing rate k , the case of a cylindrical geometry can be treated immediately. The one-dimensional case of a diffusion with uniform killing inside an interval [77] with reflecting and absorbing endpoints has a survival pdf of a particle satisfying the equation

$$\begin{aligned} \frac{\partial p(x, t)}{\partial t} &= -\nabla \cdot J(x, t) - kp(x, t) \\ p(L, t) &= 0, \quad p(x, 0) = \rho(x), \end{aligned} \quad (\text{A.61})$$

where the probability flux density is given by

$$J(x, t) = -D \frac{\partial}{\partial x} p(x, t) + b(x)p(x, t). \quad (\text{A.62})$$

For long time asymptotic, the solution of equation (A.61) is approximated by the first eigenfunction:

$$p(x, t) = p_0(x)e^{-\lambda_0 t} + O(e^{-\lambda_0 t}), \quad (\text{A.63})$$

normalized by

$$\int_0^L p_0(x) dx = 1. \quad (\text{A.64})$$

When the killing term k is a constant, the eigenvalue problem is

$$D \frac{\partial^2 p(x)}{\partial x^2} - k(x)p(x) = -\lambda p(x) \quad (\text{A.65})$$

$$p(L) = 0, \quad \frac{\partial p(0)}{\partial x} = 0,$$

In case that $k(x) = k = \text{const}$, the first eigenfunction and eigenvalue are

$$p_0(x) = \Omega \frac{\cos(\Omega x)}{\sin(\Omega L)}, \quad \Omega = \frac{\pi}{2DL}, \quad \lambda_0 = D \frac{\pi^2}{4L^2} + k.$$

The total flux J of killed diffusing particles is given by

$$J = \int_0^L k(x)p_0(x)dx = k.$$

Particles splitting: absorbed versus arrived

To quantify how ions split between pumps located on the surface of a cylinder and the ones that arrive at the end, we use the ratio

$$R_s = \frac{\int_{\partial\Omega_a} \mathbf{J}(\mathbf{x} | \mathbf{y}) \cdot \boldsymbol{\nu}(\mathbf{x}) dS_{\mathbf{x}}}{\int_{\Omega} k(\mathbf{x})p(\mathbf{x} | \mathbf{y}) d\mathbf{x}} = \frac{\int_{\partial\Omega_i} \Phi(\mathbf{x})dS_{\mathbf{x}} - \int_{\Omega} k(\mathbf{x})p(\mathbf{x} | \mathbf{y}) d\mathbf{x}}{\int_{\Omega} k(\mathbf{x})p(\mathbf{x} | \mathbf{y}) d\mathbf{x}}. \quad (\text{A.66})$$

that can be computed in the limit of a very thin cylinder. The flux and the killing term are computed from solving the steady state using Fokker-Planck

$$0 = D\Delta p(\mathbf{x} | \mathbf{y}) - k(\mathbf{x})p(\mathbf{x} | \mathbf{y}) \quad \text{for } \mathbf{x}, \mathbf{y} \in \Omega. \quad (\text{A.67})$$

The boundary conditions are

$$p(\mathbf{x} | \mathbf{y}) = 0 \quad \text{for } \mathbf{x} \in \partial\Omega, \mathbf{y} \in \Omega_a$$

$$\mathbf{J}(\mathbf{x} | \mathbf{y}) \cdot \boldsymbol{\nu}(\mathbf{x}) = 0 \quad \text{for } \mathbf{x} \in \partial\Omega - \partial\Omega_a - \partial\Omega_i, \mathbf{y} \in \Omega, t > 0.$$

$$\mathbf{J}(\mathbf{x} | \mathbf{y}) \cdot \boldsymbol{\nu}(\mathbf{x}) = -\Phi(\mathbf{x}) \quad \text{for } \mathbf{x} \in \partial\Omega_i.$$

The time independent flux is $\Phi(\mathbf{x}) \geq 0$. The external steady state flux of absorbed particles is

$$J_a = \int_{\partial\Omega_a} \mathbf{J}(\mathbf{x} | \mathbf{y}) \cdot \boldsymbol{\nu}(\mathbf{x}) dS_{\mathbf{x}}. \quad (\text{A.68})$$

The total inward flux is

$$J_i = \int_{\partial\Omega_i} \mathbf{J}(\mathbf{x} | \mathbf{y}) \cdot \boldsymbol{\nu}(\mathbf{x}) dS_{\mathbf{x}} = \int_{\partial\Omega_i} \Phi(\mathbf{x}) dS_{\mathbf{x}}. \quad (\text{A.69})$$

if the killing measure is uniform in the interval $[0, L]$, then $R_s(L) = \frac{1}{\cosh(bL) - 1}$,

where $b = \sqrt{\frac{N\chi}{D}}$. The case where the killing is a Dirac $k(x) = k\delta(x - x_1)$, located at a single point x_1 , and k is a constant has been treated in [77]. Interestingly, changing the distribution of killing from uniform to concentrated at one point has a drastic effect on the final repartition of ions (see fig.2 [77])

A.2.7 Calcium cascade initiating cellular activation

The molecular implementations that describe the transformation of a transient signal to cell activation is still unclear. We shall here present a threshold-based model: when the number of bound molecules equal a given number, we suppose that a cellular change is initiated. We present a Markov chain model that reduces the geometrical complexity based on the narrow escape rate formula [175].

Probability to bind a fixed number of molecules during a transient process

To illustrate the need of a multi-scale approach to bridge the molecular to the cellular scale, we recall that during Long Term Potentiation (LTP) induction, a transient calcium signal is converted into a long term change in the synaptic properties [14, 125, 118, 121]. This process specifically involves a class of kinases (CaMKII) that have complex local cooperative binding sites organized into a ring structure.

However, the first problem is to define the meaning of activation. For example, it can either be that a single binding by a $CaM(Ca)_3$ or $CaM(Ca)_4$ molecules, or several bonds, or one to six phosphorylations. Once a criteria is chosen, it becomes a computational question to estimate the probability P_k that k CamKII molecules are activated and also compute statistical quantities such as the mean number $\langle N_{act} \rangle$ of CaMKII that are activated following a transient calcium entry.

More complicated calcium patterns are also generated where calcium ions are flowing inside a synapse. In that case, it is worthwhile to compute the number of bound molecules before an arbitrary time t or the probability $P_{act}(t)$ and the mean number $\langle N_{act}(t) \rangle$ of activations before time t . These quantities are in practice difficult to compute and depend on many parameters such as the dendritic spine geometry, intrinsic property rate constants, the binding site interaction forces, their localization and so on. There are two complementary approaches:

1. **Coarse-grained Markov models:** this approach is based on the narrow escape methodology, where instead of accounting for the entire time dynamics

within the complex geometry organization of the microdomain, a Poissonian rate of arrival to small targets is used to approximate the target search and finding. Various quantities of interest such as the activation probability, the statistic for the number of bound CaMKII can be estimated [80, 35, 36, 74].

2. **Brownian simulations.** Contrary to the previous approach, it is not possible to obtain the exact dependency of the probability, rather this approach is tedious and allows estimating any moment of interest for a given set of parameters.

For a micro-structure such as a dendritic spine, there is no equilibrium, because the steady state is zero. Thus the relaxation time is the time for a diffusing particle to be extruded by diffusion, which is in the range of tens of ms, see [82]. The probability for N CaMKII to be activated and the time to induction is the mean time for this to happen during a repetitive stimulation. Because the calcium to CamKII pathways requires CaM intermediates, there a no coarse grained model yet [69]. To present the threshold method, we shall now present a simplified model where a diffusing molecule can bind to a ligand. The probability to reach a threshold has been developed in [35] and is reviewed here briefly.

Coarse-grained Markov models Traditional chemical kinetics, based on mass-action laws or reaction-diffusion equations, give an inappropriate description of the stochastic chemical reactions in micro-domains, where only a small number of substrate and reactant molecules is involved. A reduced Markovian description of the stochastic dynamics of the binding and unbinding of molecules is given in [80] and applied in [35, 36]. Specifically, consider two finite species, the mobile reactant M that diffuses in a bounded domain Ω and the stationary substrate S (e.g., a protein) that binds M . The boundary $\partial\Omega$ of the domain Ω is partitioned into an absorbing part $\partial\Omega_a$ (e.g., pumps, exchangers, another substrate that forms permanent bonds with M , and so on) and a reflecting part $\partial\Omega_r$ (e.g., a cell membrane). In this model the volume of M is neglected. In terms of traditional chemical kinetics the binding of M to S follows the law



where k_f is the forward binding rate constant, k_b is the backward binding rate constant, and S_{free} is the unbound substrate. We assume in our model of the reaction that the M molecules diffuse in Ω independently and when bound, are released independently of each other at exponential waiting times with rate k_{-1} . To calculate the average number of unbound (or bound) sites in the steady state the following reduced model is used. The number $k(t)$ of unbound receptors at time t is a Markovian birth-death process with states $0, 1, 2, \dots, \min\{M, S\}$ and transition rates $\lambda_{k \rightarrow k+1} = \lambda_k$, $\lambda_{k \rightarrow k-1} = \mu = k_{-1}$. The boundary conditions are $\lambda_{S \rightarrow S+1} = 0$ and $\lambda_{0 \rightarrow -1} = 0$. Setting $P_k(t) = \Pr\{k(t) = k\}$, the Kolmogorov equations for the

transition probabilities are given by [80]

$$\begin{aligned} \dot{P}_k(t) &= -[\lambda_k + k_{-1}(S - k)]P_k(t) + \lambda_{k+1}P_{k+1}(t) + k_{-1}(S - k + 1)P_{k-1}(t) \\ &\text{for } k = (S - M)^+ + 1, \dots, S - 1 \end{aligned} \quad (\text{A.71})$$

with the boundary equations

$$\begin{aligned} \dot{P}_{(S-M)^+}(t) &= -k_{-1}SP_{(S-M)^+}(t) + \lambda_1P_{(S-M)^++1}(t) \\ \dot{P}_S(t) &= -\lambda_S P_S(t) + k_{-1}P_{S-1}(t) \end{aligned}$$

and initial condition $P_{k,q}(0) = \delta_{k,S}\delta_{q,0}$. In the limit $t \rightarrow \infty$ the model (A.71) gives the average number

$$\langle k_\infty \rangle = \sum_{j=(S-M)^+}^S jP_j,$$

where $P_j = \lim_{t \rightarrow \infty} P_j(t)$. Similarly, the stationary variance of the number of unbound sites is $\sigma^2(M, S) = \langle k_\infty^2 \rangle - \langle k_\infty \rangle^2$, where $\langle k_\infty^2 \rangle = \sum_{j=(S-M)^+}^S j^2 P_j$.

The rates λ_k are modeled as follows. For a single diffusing molecule, the time to binding is the first passage time to reach a small absorbing portion $\partial\Omega_a$ of the boundary, which represents the active surface of the receptor, whereas the remaining part of $\partial\Omega$ is reflecting. Due to the small target and to the deep binding potential well the binding and unbinding of M to S are rare events on the time scale of diffusion [175]. This implies that the probability distribution of binding times is approximately exponential [173] with rate $\lambda_1 = 1/\mathbb{E}\tau_1$, where the NET $\mathbb{E}\tau_1$ is the MFPT to $\partial\Omega_a$. When there are S binding sites, $k(t)$ of which are unbound, there are $N = [M - S + k]^+$ free diffusing molecules in Ω , where $x^+ = \max\{0, x\}$. The arrival time of a molecule to the next unbound site is well approximated by an exponential law with state-dependent instantaneous rate (see discussion in [80])

$$\lambda_k = \frac{Nk}{\mathbb{E}\tau_1} = \frac{k(M - S + k)^+}{\mathbb{E}\tau_1}.$$

The results of the Markovian model (A.71) are

$$\begin{aligned} P_S &= \frac{1}{1 + \sum_{k=1}^{S-(S-M)^+} \frac{\prod_{i=S-k+1}^S i(M - S + i)^+}{k!(\mathbb{E}\tau_1 k_{-1})^k}} \\ \langle k_\infty \rangle &= P_S \sum_{k=S-1}^{(S-M)^+} (S - k)^+ \frac{\prod_{i=S-k+1}^S i(M - S + i)^+}{k!(\mathbb{E}\tau_1 k_{-1})^k} \\ \langle k_\infty^2 \rangle &= P_S \sum_{k=S-1}^{(S-M)^+} [(S - k)^+]^2 \frac{\prod_{i=S-k+1}^S i(M - S + i)^+}{k!(\mathbb{E}\tau_1 k_{-1})^k} \\ \sigma_S^2(M) &= \langle k_\infty^2 \rangle - \langle k_\infty \rangle^2 \end{aligned} \quad (\text{A.72})$$

(see [80] for further details).

These formulas are used to estimate the fraction of bound receptors in photo-receptor

outer segments and also to interpret the channel noise measurement variance in [80]. In [89] this analysis was used to estimate the number of bound AMPA receptors in the post-synaptic density. A similar gated Markovian model was proposed in [19]. The reduced Markovian model is used for the calculation of the mean time of the number of bound molecules to reach a given threshold T (MFTT). In a cellular context, the MFTT can be used to characterize the stability of chemical processes, especially when they underlie a biological function. Using the above Markov-chain description, the MFTT can be expressed in terms of fundamental parameters, such as the number of molecules, of ligands, and the forward and backward binding rates. It turns out that the MFTT depends nonlinearly on the threshold T . Specifically, consider M Brownian molecules that can bind to immobile targets S inside a microdomain, modeled generically by equation (A.70). The first time the number $[MS](t)$ of MS molecules at time t reaches the threshold is defined as

$$\tau_T = \inf\{t > 0 : [MS](t) = T\} \quad (\text{A.73})$$

and its expected value is $\bar{\tau}_T$. Consider the case of an ensemble of the targets initially free and distributed on the surface of a closed microdomain and assume that the backward rate vanishes ($k_{-1} = 0$) and $k_f > 0$. The dynamical system for the transition probabilities of the Markov process $MS(t)$ is similar to that above, but for the absorbing boundary condition at the threshold T , which gives (A.71) [35]. When the binding is irreversible ($k_{-1} = 0$), $\bar{\tau}_T$ is the sum of the forward rates

$$\begin{aligned} \tau_T^{irrev} &= \frac{1}{\lambda_0} + \frac{1}{\lambda_1} + \dots + \frac{1}{\lambda_{T-1}} \\ &= \frac{1}{\lambda} \sum_{k=0}^{T-1} \frac{1}{(M_0 - k)(S_0 - k)}. \end{aligned} \quad (\text{A.74})$$

In particular, when $M_0 = S_0$ and $M_0 \gg 1$, (A.74) becomes asymptotically $\tau_T^{irrev} \approx T/\lambda M_0(M_0 - T)$. In addition, when the number of diffusing molecules greatly exceeds the number of targets ($M_0 \gg S_0, T$), (A.74) gives the asymptotic formulas

$$\tau_T^{irrev} \approx \begin{cases} \frac{1}{\lambda M_0} \log \frac{S_0}{S_0 - T} & \text{for } M_0 \gg S_0, T \\ \frac{1}{\lambda S_0} \log \frac{M_0}{M_0 - T} & \text{for } S_0 \gg M_0, T \\ \frac{T}{\lambda M_0 S_0} & \text{for } M_0, S_0 \gg T. \end{cases} \quad (\text{A.75})$$

Figure A.11 shows the plot of τ_T^{irrev} for several values of the threshold T , compared to Brownian simulations in a circular disk $\Omega = D(R)$ with reflecting boundary, except at the targets.

A.2.8 Discussion and conclusion

We have summarized here biophysical models at a molecular level, mathematical analysis, and coarse-graining models to study calcium dynamics in cellular microdomains. The present approach can be implemented to better understand how

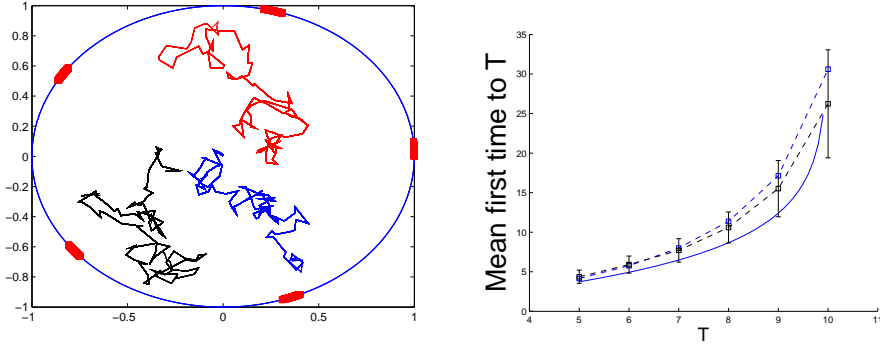


Figure A.11: **The MFTT. Left:** trajectories of diffusing molecules in a microdomain containing five binding sites on the boundary. **Right:** the time τ_T^{irrev} is plotted as a function of the threshold T . We present the Brownian simulations (dotted blue line, variance in black), the theoretical formula A.74 (dotted black line) and its approximation A.75 (continuous blue line) for a circular disk in the irreversible case ($k_{-1} = 0$). The other parameters are $S_0 = 15$, $M_0 = 10$, $\varepsilon = 0.05$, $D = 0.1\mu m^2 s^{-1}$ and the radius of the disk $R = 1\mu m$ (200 runs).

calcium dynamics can induce sophisticated processes such as Long Term Potentiation or Depression, cellular processes that are responsible for long lasting changes in physiological properties. Yet what calcium is doing at synapses still remains unclear: where calcium is accumulating, what is the number of activated CaMKII (it is not exactly clear what is the meaning of being activated: it can be that a single site is phosphorylated), and what other calcium activated molecules are important. We presented as an example of complex calcium feedback how spine twitching can be described at a molecular level. We also described Brownian and simplified simulation of calcium and the CamKII pathway. The CamKII molecule can be modeled as a simplified ring made of 6 balls. A calibration procedure is then used to determine the radius a of a sphere or disk in that matches the Smoluchowski formula. We have not reviewed the presynaptic terminal, which is a critical microdomain where calcium modulates the release of vesicles. Vesicular release is triggered by calcium entrance at specific calcium channels [90]. The exact steps from the calcium entrance to the vesicular release are still under investigation. The steps of calcium diffusion have been investigated both experimentally and numerically. In particular the distance from the channel to the vesicle is a key parameter. Channel clustering also would be interesting to investigate. The possibility that channels are not fixed and the membrane is constantly remodeled shows that this process is quite complex. Interestingly, the release probability can be modulated by 6 orders of magnitude [106, 169]. Simulations of pre-synaptic calcium are based on numerically solving partial differential equations [127, 211, 210]; however, it is hard to account for the cusp nature of the region between a vesicle and the plasma membrane [144]. Analysing diffusion in cusps can be studied by mapping locally the cusp conformally to a nonsingular domain or to use analytical computation [83, 70]. Another difficulty is to account for various varicosities, leading to divergences and a multiscale analysis should be developed. Modeling approaches are already shedding

A.2. Detailed Description

new light on the unsolved debate about the role of dendritic spines in regulating electrical versus chemical activity. It is certainly time to revisit the electrical properties of spines based on solving the full Poisson-Nernst-Planck equation. Chemical properties should consider surface receptors trafficking as a chemical reservoir.

Table A.1: Calcium entry into dendritic spines

Parameter	Description	Value
	Fraction of NMDAR-current carried by Ca^{2+}	15%
	Total Charge entering I_N (NMDAR)	$6.38 \cdot 10^{-15}$ C
	Calcium ions entering through NMDAR	≈ 3000 ions
g_N	NMDAR Conductance	0.16 nS
E_N	Equilibrium potential (NMDAR)	0 mV
$\tau_{N,1}$	NMDAR time constant	11.5 ms
$\tau_{N,2}$	NMDAR time constant	0.67 ms
	Fraction of AMPAR-current carried by Ca^{2+}	1.4%
	Total Charge entering I_A (NMDAR)	$11.51 \cdot 10^{-15}$ C
	Calcium ions entering through NMDAR	≈ 500 ions
g_A	Conductance (AMPAR)	0.3 nS
E_A	Equilibrium potential (AMPAR)	0 mV
τ_A	AMPAR time constant	0.2 ms
	Total Charge entering I_V (NMDAR)	$0.64 \cdot 10^{-15}$ C
	Calcium ions entering through VSCC	≈ 2000 ions

Bibliography

- [1] S. Andrews and D. Bray. Stochastic simulation of chemical reactions with spatial resolution and single molecule detail. *Phys. Biol.*, 1, 2004.
- [2] E. Bart, S. Bao, and D. Holcman. Modeling the spontaneous activity of the auditory cortex. *J. Comput Neurosci*, 19(3), 2005.
- [3] T.M. Bartol, D.X. Keller, J.P. Kinney, C.L. Bajaj, K.M. Harris, T.J. Sejnowski, and M.B. Kennedy. Computational reconstitution of spine calcium transients from individual proteins. *Frontiers in synaptic neuroscience*, 7(17), 2015.
- [4] L. Batsilas, A.M. Berezhkovskii, and S.Y. Shvartsman. Stochastic model of autocrine and paracrine signals in cell culture assays. *Biophys. J.*, 85, 2003.
- [5] F. Benazilla. The voltage sensor in voltage-dependent ion channels². *Physiological Reviews*, 80(2), 2000.
- [6] C.M. Bender and S.A. Orszag. *Advanced Mathematical Methods for Scientists and Engineers*. McGraw-Hill, New York, 1978.
- [7] O. Bénichou, M. Coppey, M. Moreau, P.H. Suet, and R. Voituriez. Averaged residence times of stochastic motions in bounded domains. *Europhys. Lett.*, 70(1), 2005.
- [8] A.M. Berezhkovskii, L. Dagdug, V.A. Lizunov, J. Zimmerberg, and S.M. Bezrukov. Communication: Clusters of absorbing disks on a reflecting wall: competition for diffusing particles. *J. Chem. Phys.*, 136(21), 2012.
- [9] A.M. Berezhkovskii, L. Dagdug, V.M. Vazquez, V.A. Lizunov, J. Zimmerberg, and S.M. Bezrukov. Trapping of diffusing particles by clusters of absorbing disks on a reflecting wall with disk centers on sites of a square lattice. *J. Chem. Phys.*, 138(6), 2013.
- [10] A.M. Berezhkovskii, Y.A. Makhnovskii, M.I. Monine, V.Yu. Zitserman, and S.Y. Shvartsman. Boundary homogenization for trapping by patchy surfaces. *J. Chem. Phys.*, 121(22), 2004.
- [11] H.C. Berg and E.M. Purcell. Physics of chemoreception. *Biophysical Journal*, 20(2), 1977.

- [12] A. Biess, E. Korkotian, and D. Holcman. Diffusion in a dendritic spine: The role of geometry. *Phys. Rev. E*, 76, 2007.
- [13] A. Biess, E. Korkotian, and D. Holcman. Barriers to diffusion in dendrites and estimation of calcium spread following synaptic inputs. *PLoS Comput. Biol.*, 7(10):e1002182, 2011.
- [14] T.V.P Bliss and G.L. Collingridge. A synaptic model of memory: long-term potentiation in the hippocampus. *Nature*, 361(6407), 1993.
- [15] F. Blomberg, R.S. Cohen, and P. Siekevitz. The structure of postsynaptic densities isolated from dog cerebral cortex. ii. characterization and arrangement of some of the major proteins within the structure. *J. Cell Biol.*, 74(1), 1977.
- [16] C. Börgers, G. Talei Franzesi, F.E.N LeBeau, E.S. Boyden, and N.J. Kopell. Minimal size of cell assemblies coordinated by gamma oscillations. *PLoS Comput Biol*, 8(2), 2012.
- [17] C. Börgers and N. Kopell. Synchronization in networks of excitatory and inhibitory neurons with sparse, random connectivity. *Neural Comput.*, 15:509–538, 2003.
- [18] P.C. Bressloff and S. Coombes. Dynamics of strongly coupled spiking neurons. *Neural Comput*, 12(1), 2000.
- [19] P.C. Bressloff and B.A. Earnshaw. A dynamical corral model of protein trafficking in spines. *Biophys. J.*, 96, 2009.
- [20] J. Brockhaus and K. Ballanyi. Synaptic inhibition in the isolated respiratory network of neonatal rats. *Eur J Neurosci*, 10(12), 1998.
- [21] N. Brunel and V. Hakim. Sparsely synchronized neuronal oscillations. *Chaos: An Interdisciplinary Journal of Nonlinear Science*, 19:015113, 2008.
- [22] N. Brunel and X. Wang. What determines the frequency of fast network oscillations with irregular neural discharges? I. synaptic dynamics and excitation-inhibition balance. *J Neurophysiol*, 90:415, 2003.
- [23] R.J. Butera, J. Rinzel, and J.C. Smith. Models of respiratory rhythm generation in the pre-Bötzinger complex. I. bursting pacemaker neurons. *J Neurophysiol*, 82(1), 1999.
- [24] R.J. Butera, J. Rinzel, and J.C. Smith. Models of respiratory rhythm generation in the pre-Bötzinger complex. II. populations of coupled pacemaker neurons. *J Neurophysiol*, 82(1), 1999.
- [25] M.S. Carroll and J-M. Ramirez. Cycle-by-cycle assembly of respiratory network activity is dynamic and stochastic. *J Neurophysiol*, 109(2), 2012.
- [26] H.S. Carslaw and J.C. Jaeger. Conduction of heat in solids. *Oxford University Press*, 1959.

- [27] A.F. Cheviakov, M.J. Ward, and R. Straube. An asymptotic analysis of the mean first passage time for narrow escape problems: Part II: The sphere. *SIAM Multiscale Model. Simul.*, 8(3):836–870, 2010.
- [28] C.C. Chow, J.A. White, J. Ritt, and N. Kopell. Frequency control in synchronised networks of inhibitory neurons. *J. Comput. Neurosci.*, 5:407–420, 1998.
- [29] F.C. Collins and G.E. Kimball. Diffusion-controlled reaction rates. *J. Colloid Sci.*, 4(7-8), 1949.
- [30] S. Condamin, O. Bénichou, and M. Moreau. Random walks and Brownian motion: A method of computation for first-passage times and related quantities in confined geometries. *Phys. Rev. E*, 75, 2007.
- [31] J. Crank. The mathematics of diffusion, second edition. *Oxford University Press*, 1975.
- [32] F. Crick. Do dendritic spines twitch? *Trends Neurosci.*, 5, 1982.
- [33] M. Dittrich, J.M. Patillo, J.D. King, S. Cho, J.R. Stiles, and S.D. Meriney. An excess-calcium-binding-site model predicts neurotransmitter release at the neuromuscular junction. *Biophys J*, 104(12):2751–2763, 2013.
- [34] A. Doi and J.M. Ramirez. State-dependent interactions between excitatory neuromodulators in the neuronal control of breathing. *J Neurosci*, 30(24), 2010.
- [35] K. Dao Duc and D. Holcman. Threshold activation for stochastic chemical reactions in microdomains. *Phys. Rev. E.*, 81, 2010.
- [36] K. Dao Duc and D. Holcman. Using default constraints of the spindle assembly checkpoints to estimate the associate chemical rates. *BMC Biophysics*, 5(1), 2012.
- [37] K. Dao Duc, Z. Schuss, and D. Holcman. Oscillatory decay of the survival probability of activated diffusion across a limit cycle. *Phys Rev E Stat Nonlin Soft Matter Phys.*, 89(3), 2014.
- [38] O.K. Dudko, A.M. Berezhkovskii, and G.H. Weiss. Rate constant for diffusion-influenced ligand binding to receptors of arbitrary shape on a cell surface. *J. Chem. Phys.*, 121(3), 2004.
- [39] J.R. Dunmyre, C.A. Del Negro, and J.E. Rubin. Interactions of persistent sodium and calcium-activated nonspecific cationic currents yield dynamically distinct bursting regimes in a model of respiratory neurons. *J Comput Neurosci*, 31(2), 2011.
- [40] A. Edelstein, N. Amodaj, K. Hoover, R. Vale, and N. Stuurman. Computer control of microscopes using μ manager. *Curr Protoc Mol Biol*, 14(20), 2010.

- [41] R.S. Eisenberg, M.M.Klosek, and Z. Schuss. Diffusion as a chemical reaction: Stochastic trajectories between fixed concentrations. *J. Chem. Phys.*, 102, 1995.
- [42] R. Erban and J. Chapman. Reactive boundary conditions for stochastic simulations of reaction-diffusion processes. *Phys. Biol.*, 4, 2007.
- [43] G.B. Ermentrout. Neural networks as spatio-temporal pattern-forming systems. *Reports on progress in physics*, 61:353, 1998.
- [44] G.B. Ermentrout and N. Kopell. Fine structure of neural spiking and synchronisation in the presence of conduction delays. *Proc. Natl. Acad. Sci.*, 95:1259–1264, 1998.
- [45] A.K. Roopun et al. Temporal interactions between cortical rhythms. *Front Neurosci*, 2(2), 2008.
- [46] C.A. Del Negro et al. Sodium and calcium current-mediated pacemaker neurons and respiratory rhythm generation. *J Neurosci*, 25(2), 2005.
- [47] C.A. Del Negro et al. Synaptically activated burst-generating conductances underlie a group-pacemaker mechanism for respiratory rhythm generation in mammals. *Prog Brain Res*, 187, 2010.
- [48] J. Bouvier et al. Hindbrain interneurons and axon guidance signaling critical for breathing. *Nat Neurosci*, 13(9), 2010.
- [49] M. Ainsworth et al. Rates and rhythms: a synergistic view of frequency and temporal coding in neuronal networks. *Neuron*, 75(4), 2012.
- [50] M.W. Winter et al. Glycinergic interneurons are functionally integrated into the inspiratory network of mouse medullary slices. *Eur J Physiol*, 3(458):459–469, 2009.
- [51] N. Hartelt et al. Imaging of respiratory network topology in living brainstem slices. *Molecular and Cellular Neuroscience*, 37(3), 2008.
- [52] X. Wang et al. Laser ablation of dbx1 neurons in the pre-Bötzinger complex stops inspiratory rhythm and impairs output in neonatal mice. *eLife*, 3, 2014.
- [53] J.L. Feldman and C.A. Del Negro. Looking for inspiration: new perspectives on respiratory rhythm. *Nat Rev Neurosci*, 7(3), 2006.
- [54] F. Felmy, E. Neher, and R. Schneggenburger. Probing the intracellular calcium sensitivity of transmitter release during synaptic facilitation. *Neuron*, 37(5):801–811, 2003.
- [55] M. Fischer, S. Kaech, D. Knutti, and A. Matus. Rapid actin-based plasticity in dendritic spines. *Neuron*, 20(5), 1998.

- [56] M. Flegg, J. Chapman, and R. Erban. Two regime method for optimizing stochastic reaction-diffusion simulations. *Journal of the Royal Society Interface*, 9(70), 2012.
- [57] K.M. Franks, T.M. Bartol, and T.J. Sejnowski. A monte carlo model reveals independent signaling at central glutamatergic synapses. *Biophys J.*, 83, 2002.
- [58] B. Franz, M. Flegg, J. Chapman, , and R. Erban. Multiscale reaction-diffusion algorithms: Pde-assisted brownian dynamics. *SIAM Journal on Applied Mathematics*, 73(3), 2013.
- [59] D. Freche, U. Pannasch, N. Rouach, and D. Holcman. Synapse geometry and receptor dynamics modulate synaptic strength. *PLoS ONE*, 6(10), 2011.
- [60] L.R. Gehlen, S. Nagai, K. Shimada, P. Meister, A. Taddei, and S.M. Gasser. Nuclear geometry and rapid mitosis ensure asymmetric episome segregation in yeast. *Curr. Biol.*, 21(1), 2011.
- [61] L.R. Gehlen, S. Nagaia, K. Shimada, P. Meister, A. Taddei, and S.M. Gasser. Nuclear geometry and rapid mitosis ensure asymmetric episome segregation in yeast. *Biol.*, 21:25–33, 2011.
- [62] P.K. Ghosh, P. Hänggi, F. Marchesoni, F. Nori, and G. Schmid. Brownian transport in corrugated channels with inertia. *Phys. Rev. E*, 86(2), 2012.
- [63] M.I. Glavinovi and H.R. Rabie. Monte carlo evaluation of quantal analysis in the light of ca²⁺ dynamics and the geometry of secretion. *Pflugers Arch.*, 443(1):132–45, 2001.
- [64] J.H. Goldberg, G. Tamas, D. Aronov, and R. Yuste. Calcium microdomains in aspiny dendrites. *Neuron*, 40(4), 2003.
- [65] U.F. Greber and M. Way. A superhighway to virus infection. *Cell*, 124:741–754, 2006.
- [66] I.V. Grigoriev, Y.A. Makhnovskii, A.M. Berezhkovskii, and V.Y. Zitserman. Kinetics of escape through a small hole. *J. Chem. Phys.*, 116(22), 2002.
- [67] S. Grillner. Biological pattern generation: the cellular and computational logic of networks in motion. *Neuron*, 52(5), 2006.
- [68] L.T. Grinberg, U. Rueb, and H. Heinsen. Brainstem: neglected locus in neurodegenerative diseases. *Front Neurol*, 2(42):1–9, 2011.
- [69] C. Guerrier and D. Holcman. Activation of camkii in dendritic spines : A stochastic model. *In prep.*, 2015.
- [70] C. Guerrier and D. Holcman. Search time for a small ribbon and application to vesicular release at neuronal synapses. *SIAM MMS*, In press., 2015.

- [71] Y. Han, A. Alsayed, M. Nobili, and A.G. Yodh. Quasi-two-dimensional diffusion of single ellipsoids: Aspect ratio and confinement effects. *Phys. Rev. E*, 80, 2009.
- [72] J.A. Hayes, X. Wang, and C.A. Del Negro. Cumulative lesioning of respiratory interneurons disrupts and precludes motor rhythms *in vitro*. *Proc Natl Acad Sci USA*, 109(21), 2012.
- [73] B. Hille. *Ion channels of excitable membranes, Third Edition*, volume 507. Sinauer Sunderland, MA, 2001.
- [74] D. Holcman, K. Daoduc, and K. Burrage. Successful delivery of pten in the cytoplasm escaping from micrnas degradation. *pre-print.*, 2013.
- [75] D. Holcman, N. Hoze, and Z. Schuss. Narrow escape through a funnel and effective diffusion on a crowded membrane. *Phys. Rev. E*, 84:021906, 2011.
- [76] D. Holcman, E. Korkotian, and M. Segal. Calcium dynamics in dendritic spines, modeling and experiments. *Cell calcium*, 37:467–475, 2005.
- [77] D. Holcman, A. Marchewka, and Z. Schuss. The survival probability of diffusion with trapping in cellular biology. *Phys. Rev E, Stat. Nonlin. Soft Matter Phys.*, 72(3), 2005.
- [78] D. Holcman and Z. Schuss. Modeling calcium dynamics in dendritic spines. *SIAM J. Appl. Math.*, 65(3), 2004.
- [79] D. Holcman and Z. Schuss. Stochastic chemical reactions in micro-domains. *J Chem Phys*, 122(1), 2005.
- [80] D. Holcman and Z. Schuss. Stochastic chemical reactions in microdomains. *J. Chem. Phys.*, 122, 2005.
- [81] D. Holcman and Z. Schuss. Diffusion escape through a cluster of small absorbing windows. *J. Phys. A*, 41:155001, 2008.
- [82] D. Holcman and Z. Schuss. Diffusion laws in dendritic spines. *J. Math. Neurosci.*, 1(10), 2011.
- [83] D. Holcman and Z. Schuss. Brownian motion in dire straits. *SIAM Multiscale Model. Simul.*, 10(4):1204–1231, 2012.
- [84] D. Holcman and Z. Schuss. Control of flux by narrow passages and hidden targets in cellular biology. *Phys Progr Report*, 76(7):074601, 2013.
- [85] D. Holcman and Z. Schuss. The narrow escape problem. *SIAM Rev*, 56(2):213–257, 2014.
- [86] D. Holcman and Z. Schuss. Time scale of diffusion in molecular and cellular biology. *J. Phys. A: Math. Theor.*, 47(17):173001, 2014.

- [87] D. Holcman and Z. Schuss. *Stochastic Narrow Escape in Molecular and Cellular Biology*. Springer, NY, 2015.
- [88] D. Holcman, Z. Schuss, and E. Korkotian. Calcium dynamics in dendritic spines and spine motility. *Biophys. J.*, 87(1):81–91, 2004.
- [89] D. Holcman and A. Triller. Modeling synaptic dynamics and receptor trafficking. *Biophys. J.*, 91(7), 2006.
- [90] N. Holderith, A. Lorincz, G. Katona, B. Rózsa, A. Kulik, W. Masahoki, and Z. Nusser. Release probability of hippocampal glutamatergic terminals scales with the size of the active zone. *Nature Neuroscience*, 15, 2013.
- [91] J.D. Jackson. *Classical Electrodynamics, 2nd ed.* Willey, NY, 1975.
- [92] W.A. Janczewski, A. Tashima, P. Hsu, and Y. Cui and J.L. Feldman. Role of inhibition in respiratory pattern generation. *J Neurosci*, 33(13), 2013.
- [93] J.G.R. Jefferys, R.D. Traub, and M.A. Whittington. Neuronal networks for induced ~ 40 Hz rhythms. *Trends in Neurosciences*, 19:202–208, 1996.
- [94] P.S. Kaeser, L. Deng, Y. Wang, I. Dulubova, X. Liu, J. Rizo, and T.C. Sudhof. RIM proteins tether Ca^{2+} channels to presynaptic active zones via a direct PDZ-domain interaction. *Cell*, 144(2):282–295, 2011.
- [95] K. Kam, J.W. Worrell, W.A. Janczewski, Y. Cui, and J.L. Feldman. Distinct inspiratory rhythm and pattern generating mechanisms in the preBötzinger complex. *J Neurosci*, 33(22), 2013.
- [96] K. Kam, J.W. Worrell, C. Ventalon, V. Emiliani, and J.L. Feldman. Emergence of population bursts from simultaneous activation of small subsets of prebötzinger complex inspiratory neurons. *J Neurosci*, 33(8), 2013.
- [97] E. Kandel, H. Schwartz, T.M. Jessell, and S. Siegelbaum. *Principles of Neural Science, Fifth Edition*. McGraw-Hill, NY, 2012.
- [98] Eric R Kandel, James H Schwartz, Thomas M Jessell, et al. *Principles of neural science*, volume 4. McGraw-Hill New York, 2000.
- [99] J. Karbowski and N. Kopell. Multispikes and synchronisation in a large neural network with temporal delays. *Neural Comput.*, 12:1573–1606, 2000.
- [100] S. Karlin and H. Taylor. *A Second Course in Stochastic Processes*. Academic Press, New York-London, 1981.
- [101] B. Katz and R. Miledi. The role of calcium in neuromuscular facilitation. *J Physiol*, 195:481–492, 1968.
- [102] B. KATZ and R. MILEDI. Estimates of quantal content during 'chemical potentiation' of transmitter release. *Proceedings of the Royal Society B*, 205:369–378, 1979.

- [103] D. Keller, N. Babai, O. Kochubey, Y. Han, H. Markram and F. Schürmann, and R. Schneggenburger. An exclusion zone for Ca^{2+} channels around docked vesicles explains release control by multiple channels at a CNS synapse. *PLOS Comp Biol*, 11(5):e1004253, 2015.
- [104] R.A. Kerr, T.M. Bartol, B. Kaminsky, and M. Dittrich. Fast Monte Carlo simulation methods for biological reaction-diffusion systems in solution and on surfaces. *SIAM J Sci Comput.*, 30:126–3149, 2008.
- [105] C. Koch. Biophysics of computation, information processing in single neurons. *Oxford University Press New York 10016*, 1999.
- [106] O. Kochubey, X. Lou, and R. Schneggenburger. Regulation of transmitter release by Ca^{2+} and synaptotagmin: insights from a large CNS synapse. *Trends in Neuroscience*, 34(5):237–246, 2011.
- [107] T. Kolokolnikov, M. Titcombe, and M.J. Ward. Optimizing the fundamental neumann eigenvalue for the laplacian in a domain with small traps. *European J. Appl. Math.*, 16:161–200, 2005.
- [108] E. Korkotian, D. Holcman, and M. Segal. Dynamic regulation of spine-dendrite coupling in cultured hippocampal neurons. *European J. of Neuroscience*, 20(10), 2004.
- [109] E. Korkotian and M. Segal. Spatially confined diffusion of calcium in dendrites of hippocampal neurons revealed by flash photolysis of caged calcium. *Cell Calcium*, 40(5-6), 2006.
- [110] N. Koshiya and J.C. Smith. Neuronal pacemaker for breathing visualized *in vitro*. *Nature*, 400(6742), 1999.
- [111] E.K. Kosmidis, O. Pierrefiche, and J-F. Vibert. Respiratory-like rhythmic activity can be produced by an excitatory network of non-pacemaker neuron models. *J Neurophysiol*, 92(2), 2004.
- [112] A. Kottick and C.A. Del Negro. Synaptic depression influences inspiratory-expiratory phase transition in dbx1 interneurons of the preBötzinger complex in neonatal mice. *J Neurosci*, 35(33):11606–11, 2015.
- [113] R.A. Krey, A.M. Goodreau, T.B. Arnold, and C.A. Del Negro. Outward currents contributing to inspiratory burst termination in preBötzinger complex neurons of neonatal mice studied *in Vitro*. *Front Neural Circuits*, 4, 2010.
- [114] V. Kurella, J. Tzou, D. Coombs, and M.J. Ward. Asymptotic analysis of first passage time problems inspired by ecology. *Bull. Math. Biol.*, 77(1):83–125, 2015.
- [115] T. Lagache, E. Dauty, and D. Holcman. Quantitative analysis of virus and plasmid trafficking in cells. *Phys Rev E*, 79(1), 2009.

- [116] G. Lamm and K. Schulten. Extended brownian dynamics. ii. reactive, nonlinear diffusion. *J. Chem. Phys.*, 78(5), 1983.
- [117] L.D. Landau and E. M. Lifshitz. Fluid mechanics. *Pergamon Press, Elmsford, NY*, 1975.
- [118] S.R. Lee, J. Escobedo-Lozoya, E.M. Szatmari, and R. Yasuda. Activation of camkii in single dendritic spines during long-term potentiation. *Nature*, 458, 2009.
- [119] S. Levin-Zaidman, J. Englander, E. Shimoni, A. K. Sharma, K. W. Minton, and A. Minsky. Ringlike structure of the *Deinococcus radiodurans* genome: A key to radioresistance? *Science*, 299(254), 2003.
- [120] A. Lieber, A. Leis, A. Kushmaro, A. Minsky, and O. Medalia. Quasi-two-dimensional diffusion of single ellipsoids: Aspect ratio and confinement effects. *J. Bacteriol.*, 191, 2009.
- [121] J. Lisman, R. Yasuda, and S. Raghavachari. Mechanisms of camkii action in long-term potentiation. *Nature Reviews Neuro*, 13, 2012.
- [122] J.E. Lisman, S. Raghavachari, and R.W. Tsien. The sequence of events that underlie quantal transmission at central glutamatergic synapses. *Nat Rev Neurosci*, 8:597–609, 2007.
- [123] P. Macheboeuf, A.M. Di Guilmi, V. Job, T. Vernet, O. Dideberg, and A. Dessen. Active site restructuring regulates ligand recognition in class A penicillin-binding proteins. *Proc. Natl. Acad. Sci. U.S.A.*, 102(3), 2005.
- [124] A. Majewska, A. Tashiro, and R. Yuste. Regulation of spine calcium dynamics by rapid spine motility. *J Neurosci.*, 20(22), 2000.
- [125] R.C. Malenka and R.A. Nicoll. Long-term potentiation—a decade of progress ? *Science*, 285(5435), 1999.
- [126] B.J. Matkowsky, Z. Schuss, and E. Ben-Jacob. A singular perturbation approach to kramers’ diffusion problem. *SIAM J. Appl. Math.*, 42(4), 1982.
- [127] V. Matveev, R.S. Zucker, and A. Sherman. Facilitation through buffer saturation: constraints on endogenous buffering properties. *Biophys J*, 86(5):2691–2709, 2004.
- [128] L.C. McKay, W.A. Janczewski, and J.L. Feldman. Sleep-disordered breathing after targeted ablation of preBötzing complex neurons. *Nat Neurosci*, 8(9), 2008.
- [129] C.J. Meinrenken, J.G.G. Borst, and B Sakman. Local routes revisited: the space and time dependence of the ca^{2+} signal for phasic transmitter release at the rat calyx of Held. *J Physiol*, 547(3):665–689, 2003.

- [130] A.G. Millar, H. Bradacsand, M.P. Charlton, and H.L. Atwood. Inverse relationship between release probability and readily releasable vesicles in depressing and facilitating synapses. *J. Neurosci.*, 22:9661–9667, 2002.
- [131] K.D. Miller, J.B. Keller, and M.P. Stryker. Ocular dominance column development: analysis and simulation. *Science*, 247, 1989.
- [132] S.L. Mironov. Metabotropic glutamate receptors activate dendritic calcium waves and TRPM channels which drive rhythmic respiratory patterns in mice. *J Physiol*, 586(9), 1999.
- [133] M. Missler, W. Zhang, A. Rohlmann, G. Kattenstroth, R.E. Hammer, K. Gottmann, and T.C. Südhof. α -neurexins couple ca^{2+} channels to synaptic vesicle exocytosis. *Nature*, 423:939–948, 2003.
- [134] C. Modchang, S. Nadkarni, T.M. Bartol, W. Triampo, T.J. Sejnowski, H. Levine, and W.-J. Rappel. A comparison of deterministic and stochastic simulations of neuronal vesicle release models. *Physical Biology*, 7:026008, 2010.
- [135] M.I. Monine and J.M. Haugh. Reactions on cell membranes: Comparison of continuum theory and brownian dynamics simulations. *J. Chem. Phys.*, 123, 2005.
- [136] C. Morgado-Valle and J.L. Feldman. NMDA receptors in preBötzing complex neurons can drive respiratory rhythm independent of AMPA receptors. *J Physiol*, 582(1), 2007.
- [137] M. Morschel and M. Dutschmann. Pontine respiratory activity involved in inspiratory/expiratory phase transition. *Philosophical Transactions of the Royal Society B: Biological Sciences*, 364(1529), 2009.
- [138] B. Nadler, T. Naeh, and Z. Schuss. The stationary arrival process of independent diffusers from a continuum to an absorbing boundary is poissonian. *SIAM J. Appl. Math*, 62(2):433–447, 2001.
- [139] Y. Nakamura, H. Harada, N. Kamasawa, K. Matsui, J.s. Rothman, R. Shigemoto, R.A. Silver, D.A. DoGregorio, and T. Takahashi. Nanoscale distribution of presynaptic ca^{2+} channels and its impact on vesicular release during development. *Neuron*, 85:145–158, 2015.
- [140] C.A. Del Negro and J.A. Hayes. A ,Äúgroup pacemaker,Äù mechanism for respiratory rhythm generation. *J Physiol*, 586(9), 2008.
- [141] C.A. Del Negro, J.A. Hayes, and J.C. Rekling. Dendritic calcium activity precedes inspiratory bursts in prebötzing complex neurons. *J Neurosci*, 31(3), 2011.
- [142] C.A. Del Negro, K. Kam, J.A. Hayes, and J.L. Feldman. Asymmetric control of inspiratory and expiratory phases by excitability in the respiratory network of neonatal mice *in vitro*. *J Physiol*, 587(6), 2009.

- [143] C.A. Del Negro, C. Morgado-Valle, and J.L. Feldman. Respiratory rhythm: an emergent network property? *Neuron*, 34(5), 2002.
- [144] E. Neher. Complexin: Does it deserve its name? *Neuron*, 68(5):803–6, 2010.
- [145] E. Neher and H. Taschenberger. Transients in global Ca²⁺ concentration induced by electrical activity in a giant nerve terminal. *J Physiol*, 591(13):3189–3195, 2013.
- [146] C. Nusslein-volhar. *Coming to Life - How Genes Drive Development*. Broché, 2008.
- [147] T. Oka, S. Yokota, T. Tsumori, J-G. Niu, and Y. Yasui. Glutamatergic neurons in the lateral periaqueductal gray innervate neurokinin-1 receptor-expressing neurons in the ventrolateral medulla of the rat. *Neurosci Res*, 74(2), 2012.
- [148] R.W. Pace, D.D. Mackay, J.L. Feldman, and C.A. Del Negro. Role of persistent sodium current in mouse preBotzinger complex neurons and respiratory rhythm generation. *J Physiol*, 580(2), 2006.
- [149] R.W. Pace, D.D. Mackay, J.L. Feldman, and C.A. Del Negro. Inspiratory bursts in the prebötzing complex depend on a calcium-activated non-specific cation current linked to glutamate receptors in neonatal mice. *J Physiol*, 582(1), 2007.
- [150] B. Pan and R.S. Zucker. A general model of synaptic transmission and short-term plasticity. *Neuron*, 62:539–554, 2009.
- [151] M. Penrose. *Random Geometric Graphs*. 2003.
- [152] F. Perrin. Mouvement brownien d’un ellipsoïde - I. Dispersion diélectrique pour des molécules ellipsoïdales. *J. Phys. Radium*, 5(10), 1934.
- [153] F. Perrin. Mouvement brownien d’un ellipsoïde (II). Rotation libre et dépolari-sation des fluorescences. Translation et diffusion de molécules ellipsoïdales. *J. Phys. Radium*, 7(1), 1936.
- [154] S. Pillay, M. J. Ward, A. Peirce, and T. Kolokolnikov. An asymptotic analysis of the mean first passage time for narrow escape problems: Part I: Two-dimensional domains. *SIAM Multiscale Model. Simul.*, 8(3), 2010.
- [155] L.S. Pontryagin, A.A. Andronov, and A.A. Vitt. On the statistical treatment of dynamical systems. *Noise in Nonlinear Dynamics*, 1, 1989.
- [156] L.S. Pontryagin, A.A. Andronov, and A.A. Vitt. On the statistical treatment of dynamical systems. *J. Theor. Exper. Phys. (Russian)*, 3, 1933.
- [157] J.W.S. Rayleigh. *The Theory of Sound*. Dover, NY, 1945.
- [158] W.G. Regehr. Short-term presynaptic plasticity. *Cold Spring Harb Perspect Biol*, 4:a005702, 2012.

- [159] J.C. Rekling and J.L. Feldman. PreBötzinger complex and pacemaker neurons: hypothesized site and kernel for respiratory rhythm generation. *Annu Rev Physiol*, 60(1), 1998.
- [160] J.C. Rekling, X.M. Shao, and J.L. Feldman. Electrical coupling and excitatory synaptic transmission between rhythmogenic respiratory neurons in the preBötzinger complex. *J Neurosci*, 20(3), 2000.
- [161] S.O. Rizzoli and W.J. Betz. Synaptic vesicle pools. *Nat Rev Neurosci*, 6(1), 2005.
- [162] B. Roux, B. Prod'homme, and M. Karplus. Ion transport in the gramicidin channel: Molecular dynamics study of single and double occupancy. *Biophys J.*, 68, 1995.
- [163] A. Ruangkittisakul, B. Panaitescu, and K. Ballanyi. K^+ and Ca^{2+} dependence of inspiratory-related rhythm in novel 'calibrated' mouse brainstem slices. *Respir Physiol Neurobiol*, 175(1), 2011.
- [164] J.E. Rubin, J.A. Hayes, J.L. Mendenhall, and C.A. Del Negro. Calcium-activated nonspecific cation current and synaptic depression promote network-dependent burst oscillations. *Proc Natl Acad Sci USA*, 106(8), 2009.
- [165] J.E. Rubin, N.A. Shevtsova, G.B. Ermentrout, J.C. Smith, and I.A. Rybak. Multiple rhythmic states in a model of the respiratory central pattern generator. *J Neurophysiol*, 101(4), 2009.
- [166] I.A. Rybak, J.F.R. Paton, and J.S. Schwaber. Modeling neural mechanisms for genesis of respiratory rhythm and pattern. I. models of respiratory neurons. *J. Neurophysiol.*, 77, 1997.
- [167] B.L. Sabatini, M. Maravall, and K. Svoboda. Ca^{2+} signalling in dendritic spines. *Curr. Opin. Neurobiol.*, 11(3), 2001.
- [168] V. Scheuss, H. Taschenberger, and E. Neher. Kinetics of both synchronous and asynchronous quantal release during trains of action potential-evoked EPSCs at the rat calyx of Held. *J Physiol.*, 585(2):361–381, 2007.
- [169] R. Schneggenburger, Y. Han, and O. Kochubey. Ca^{2+} channels and transmitter release at the active zone. *Cell Calcium*, 52(3-4):199–207, 2012.
- [170] R. Schneider, E. Hossy, J. Kohl, J. Klueva, D. Choquet, U. Thomas, A. Voigt, and M. Heine. Mobility of calcium channels in the presynaptic membrane. *Neuron*, 86(3):672–9, 2015.
- [171] Z. Schuss. *Theory and Applications of Stochastic Differential Equations*. Wiley Series in Probability and Statistics, New York, 1980.
- [172] Z. Schuss. Diffusion and stochastic processes: an analytical approach. *Springer NY*, 2010.

- [173] Z. Schuss. *Theory and Applications of Stochastic Processes, an Analytical Approach*. Springer series on Applied Mathematical Sciences, 170, NY., 2010.
- [174] Z. Schuss. *Brownian Dynamics at Boundaries and Interfaces in Physics, Chemistry, and Biology*. Springer series on Applied Mathematical Sciences, NY, 2013.
- [175] Z. Schuss, A. Singer, and D. Holcman. The narrow escape problem for diffusion in cellular microdomains. *Proc. Natl. Acad. Sci. USA*, 104(41), 2007.
- [176] D.J. Schwab, R.F. Bruinsma, J.L. Feldman, and A.J. Levine. Rhythmogenic neuronal networks, emergent leaders, and k-cores. *Phys Rev E*, 82(5), 2010.
- [177] V. Shahrezaei and K.R. Delaney. Brevity of the ca2 microdomain and active zone geometry prevent ca2-sensor saturation for neurotransmitter release. *J Neurophysiol*, 94:1912–1919, 2005.
- [178] G. M. Shepherd. *The Synaptic Organization of the Brain*. New York: Oxford University Press., 1974.
- [179] A. Singer, Z. Schuss, and D. Holcman. Narrow escape, part II: The circular disk. *J. Stat. Phys.*, 122(3), 2006.
- [180] A. Singer, Z. Schuss, and D. Holcman. Narrow escape, part III: Non-smooth domains and riemann surfaces. *J. Stat. Phys.*, 122(3), 2006.
- [181] A. Singer, Z. Schuss, D. Holcman, and R.S. Eisenberg. Narrow escape, part I. *J. Stat. Phys.*, 122(3), 2006.
- [182] A. Singer, Z. Schuss, A. Osipov, and D. Holcman. Partially reflected diffusion. *SIAM J. Appl. Math.*, 68, 2008.
- [183] A.V. Skorokhod. Stochastic equations for diffusion processes in a bounded region. *Theory of Probability and Applications*, 6(3):264–274, 1961.
- [184] J.C. Smith, H.H. Ellenberger, K. Ballanyi, D.W. Richter, and J.L. Feldman. Pre-Bötzing complex: a brainstem region that may generate respiratory rhythm in mammals. *Science*, 254(5032), 1991.
- [185] H.H. Subramanian, R.J. Balnave, and G. Holstege. The midbrain periaqueductal gray control of respiration. *J Neurosci*, 28(47), 2008.
- [186] T.C. Südhof. The synaptic vesicle cycle. *Annu Rev Neurosci*, 27(1), 2004.
- [187] T.C. Südhof. The presynaptic Active Zone. *Neuron*, 75(1):11–25, 2012.
- [188] K. Svoboda, D.W. Tank, and W. Denk. Direct measurement of coupling between dendritic spines and shafts. *Science*, 272(5262), 1996.
- [189] A. Taffia and D. Holcman. Dwell time of a brownian molecule in a microdomain with traps and a small hole on the boundary. *J Chem Phys*, 126(23):234107, 2007.

- [190] A. Taffia and D. Holcman. Estimating the synaptic current in a multiconductance AMPA receptor model. *Biophys J.*, 101, 2011.
- [191] K. Tai, S.D. Bond, H.R. MacMillan, N.A. Baker, M.J. Holst, and J.A. McCammon. Finite element simulations of acetylcholine diffusion in neuromuscular junctions. *Biophys. J.*, 84, 2003.
- [192] M. Thoby-Brisson and J-M. Ramirez. Identification of two types of inspiratory pacemaker neurons in the isolated respiratory neural network of mice. *J Neurophysiol*, 86(1), 2001.
- [193] N. Toporikova and R.J. Butera. Two types of independent bursting mechanisms in inspiratory neurons: an integrative model. *J Comput Neurosci*, 30(3), 2011.
- [194] R.D. Traub, D. Contreras, M.O. Cunningham, H. Murray, F.E.N. LeBeau, A. Roopun, A. Bibbig, W.B. Wilent, M.J. Higley, and M.A Whittington. Single-column thalamocortical network model exhibiting gamma oscillations, sleep spindles, and epileptogenic bursts. *J Neurophysiol*, 93:2194–2232, 2004.
- [195] R.D. Traub, D. Schmitz, J.G.R. Jefferys, and A. Draguhn. High-frequency population oscillations are predicted to occur in hippocampal pyramidal neuronal networks interconnected by axoaxonal gap junctions. *Neuroscience*, 92:407–426, 1999.
- [196] R.D. Traub, M.A. Whittington, and J.G.R. Jefferys. *Fast Oscillations in Cortical Circuits*. GR Jefferys, MA Whittington (MIT Press)., 1999.
- [197] R.D. Traub, M.A. Whittington, I.M. Stanford, and J.G.R. Jefferys. A mechanism for generation of long-range synchronous fast oscillations in the cortex. *Nature*, 383:621–624, 1996.
- [198] M. Tsodyks, K. Pawelzik, and H. Markram. Neural networks with dynamic synapses. *Neural Comput*, 10(4), 1998.
- [199] M.V. Tsodyks and H. Markram. The neural code between neocortical pyramidal neurons depends on neurotransmitter release probability. *Proc Natl Acad Sci USA*, 94(2), 1997.
- [200] H.L.F. von Helmholtz. Theorie der luftschwingungen in röhren mit offenen enden. *Crelle Bn*, 57:1–72, 1860.
- [201] M.J. Ward, W.D. Henshaw, and J.B. Keller. Summing logarithmic expansions for singularly perturbed eigenvalue problems. *SIAM J. Appl. Math.*, 53:799–828, 1993.
- [202] M.J. Ward and J.B. Keller. Strong localized perturbations of eigenvalue problems. *SIAM J. Appl. Math.*, 53:770–798, 1993.
- [203] M.J. Ward and E. Van De Velde. The onset of thermal runaway in partially insulated or cooled reactors. *IMA J. Appl. Math*, 48:53–85, 1992.

- [204] A.M. Weber, F.K. Wong, A.R. Tufford, L.C. Schlichter, V. Matveev, and E.F. Stanley. N-type Ca²⁺ channels carry the largest current: implications for nanodomains and transmitter release. *Nat Neurosci.*, 13(11):1348–1350, 2010.
- [205] J.A. White, C.C. Chow, J. Ritt, C. Soto-Trevino, and N. Kopell. Synchronization and oscillatory dynamics in heterogeneous, mutually inhibited neurons. *J. Comput. Neurosci.*, 5:5–16, 1998.
- [206] H. Wilson and J. Cowan. Excitatory and inhibitory interactions in localized populations of model neurons. *Biophys Journal*, 12:1–24, 1972.
- [207] X. Xie, J-S. Liaw nad M. Baudry, and T. Berger. Novel expression mechanism for synaptic potentiation: Alignment of presynaptic release site and postsynaptic receptor. *Proc. Natl. Acad. Sci. USA*, 94:6983–6988, 1997.
- [208] M.A. Xu-Friedman, K.M. Harris, and W.G. Regehr. Three-dimensional comparison of ultrastructural characteristics at depressing and facilitating synapses onto cerebellar purkinje cells. *J Neurosci*, 21(17):6666–6672, 2001.
- [209] W Zhang and D.J. Linden. Neuromodulation at single presynaptic boutons of cerebellar parallel fibers is determined by bouton size and basal action potential-evoked ca transient amplitude. *J Neurosci*, 29(49), 2009.
- [210] R.S. Zucker. Calcium and transmitter release. *J Physiol Paris.*, 87(1), 1993.
- [211] R.S. Zucker and W.G. Regehr. Short-term synaptic plasticity. *Annu Rev Physiol*, 64:355–405, 2002.
- [212] R. Zwanzig. Diffusion-controlled ligand binding to spheres partially covered by receptors: An effective medium treatment. *Proc. Natl. Acad. Sci. U.S.A.*, 87, 1990.

